2016

State Estimation and Dynamic Control Allocation for Over-actuated Electric Vehicles with In-wheel Motors

Boyuan Li
University of Wollongong

State Estimation and Dynamic Control Allocation for Over-actuated Electric Vehicles with In-wheel Motors

A thesis submitted in partial fulfilment of the requirements

for the award of the degree of

Doctor of Philosophy

by

Boyuan Li

from

Faculty of Engineering and Information Sciences, University of Wollongong

August 2016

Wollongong, New South Wales, Australia

CERTIFICATION

I, Boyuan LI, declare that this thesis, submitted in partial fulfilment of the requirements for the award of Doctor of Philosophy, in the school of Electrical, Computer and Telecommunications Engineering, Faculty of Engineering and Information Sciences, University of Wollongong, is wholly my own work unless otherwise referenced or acknowledged. The document has not been submitted for qualifications at any other academic institution.

Boyuan LI

August, 2016

ABSTRACT

The electrification of road vehicles is an attractive research area, as problems associated with greenhouse gas emission are now a global challenge. Particularly, electric vehicles with in-wheel steering and driving motors, (also called four-wheel-independent-steering (4WIS) and four-wheel-independent-driving (4WID) electric vehicles), can utilize redundant control actuators to achieve multiple control targets. Hence these vehicles are receiving considerable attention. This thesis aims to develop novel control allocation strategies for 4WIS-4WID electric vehicles to improve their performance and energy efficiency.

A comprehensive literature review of vehicle dynamics and various control systems is the focus of the introduction. Then various real-time vehicle state estimators are proposed and a comprehensive vehicle dynamics model is suggested for 4WIS-4WID electric vehicles. Based on the state estimators and vehicle dynamics model, the linear feedback and non-linear over-actuated control allocation methods for the primary control targets, such as handling and stability control, of 4WIS-4WID electric vehicles are suggested. Next, the application of the over-actuated control allocation method is extended into the secondary control targets, such as energy-efficient control and fault-tolerant control. The autonomous vehicle trajectory control can be achieved by applying the over-actuated control allocation method. Finally, a scaled electric vehicle is utilized in the experiment to measure vehicle states and to verify the proposed vehicle mass estimator and road slope estimator.

It can be concluded that the redundant control actuators provided by 4WIS-4WID electric vehicles are effective in achieving multiple control targets through the application of designed control allocation methods. These findings demonstrate the promising future of 4WIS-4WID electric vehicles.

ACKNOWLEDGEMENT

I wish to thank my supervisor, Prof. Haiping Du, for his enthusiastic support, professional direction, and constant encouragement that inspired me to overcome the challenges on my road of life and study.

A sincere appreciation is due to my co-supervisor Prof. Weihua Li for his constant support and help. Particular thanks are also extended to my colleagues, Jiawei Zhang and Donghong, Ning, for their kind assistance, discussion, and encouragement to finish the scaled vehicle experiment.

Finally, I would like to thank my parents for their love, education, encouragement, and financial support, and wish them happiness and good health every day.

TABLE OF CONTENT

List of figures

List of tables

List of symbols

m	The vehicle total mass
v_x	Longitudinal velocity of centre of gravity (CG)
v_y	Lateral velocity of CG
a_x	Longitudinal acceleration
a_y	Lateral acceleration
$u_i(i = fl, fr, rl, rr)$	Vehicle velocity component in the wheel plane
r	Yaw rate of C.G.
β	Body side-slip angle of C.G.
r_{ref}	Desired yaw rate in the controller
β_{ref}	Desired body side-slip angle in the controller
r_{max}	Handling limit the of maximum yaw rate
I_z	Vehicle moment of inertia about yaw axis
M	Yaw moment
l_f	Front wheel base
l_r	Rear wheel base
b_f	Front track width
b_r	Rear track width
$F_{xi}\ (i = fl, fr, rl, rr)$	The longitudinal tyre force of individual wheel
$F_{yi}\ (i = fl, fr, rl, rr)$	The lateral tyre force of individual wheel
$F_{ti}\ (i = fl, fr, rl, rr)$	Tyre traction/brake force of individual wheel
$F_{si}\ (i = fl, fr, rl, rr)$	Tyre side force of individual wheel
$x_i, y_i\ (i = fl, fr, rl, rr)$	Position of the wheel centre in the coordinate system
x_{ICR}, y_{ICR}	Position of ICR in the coordinate system
$\delta_i(i = fl, fr, rl, rr)$	Steering angle of individual wheel
I_s	Moment inertial of the steering wheel
c_s	Damping coefficient around the kingpin
k_s	Spring constant around the kingpin
k_m	Armature constant
I	Motor steering current
τ_j	Jacking torque in the steering model
t_p	The pneumatic trail
t_{p0}	The initial value of the pneumatic trail
t_m	The mechanical trail
α_{sl}	The side-slip angle when tyre lost lateral grip
R	Vehicle turning radius
D^T	The value will be either 1 (anticlockwise turning) or -1 (clockwise turning)
g	Acceleration gravity
μ_0	Nominal friction coefficient
ε_r	The constant value in the Dugoff tyre model
k_x	Tyre longitudinal deflection constant
k_y	Tyre lateral deflection constant
l	Half length of the contact patch

μ	Friction coefficient between the tyre and the road
ρ	Maximum value of the normalised traction force
$F_{zi}(i = fl, fr, rl, rr)$	Vertical load of individual wheel
$\alpha_i(i = fl, fr, rl, rr)$	The side-slip angle of individual wheel
$s_i(i = fl, fr, rl, rr)$	The longitudinal slip ratio of individual wheel
I_ω	The wheel moment of inertial
$\omega_i(i = fl, fr, rl, rr)$	The rotation speed of the individual wheel
R_ω	The radius of the wheel
C_α	The lateral stiffness of the tyre
C_s	The longitudinal stiffness of the tyre
T_{di}	The traction torque of individual wheel
T_{bi}	The brake torque of individual wheel
η_i	The energy-efficient coefficient of individual wheel
P_{Oi}	Vehicle output power in the energy consuming mode
P_{Ii}	Vehicle input power in the energy gaining mode
η_{Oi}	Output power efficiency in the energy consuming mode
η_{Ii}	Input power efficiency in the energy gaining mode
C_r	Rolling resistance
D_a	Wind drag coefficient
θ_s or θ	Road slope
h	Height of vehicle centre of gravity
$V_i(i = fl, fr, rl, rr)$	Input voltage of the in-wheel motor
φ	Vehicle yaw angle

Citation of published work

Some portions of the thesis have appeared in the following publications:

Chapter 3

B. Li, H. Du, and W. Li, "A Novel Method for Side Slip Angle Estimation of Omni-Directional Vehicles," *SAE Int. J. Passeng. Cars - Electron. Electr. Syst.* 7(2), pp.471-480, 2014, doi:10.4271/2014-01-0303.

B. Li, H. Du, and W. Li, "Comparative study of vehicle tyre-road friction coefficient estimation with a novel cost-effective method", *Vehicle System Dynamics*, 52(8), pp.1066-1098, 2014, DOI:10.1080/00423114.2014.920090.

B. Li, H. Du, and W. Li, "A novel cost effective method for vehicle tire-road friction coefficient estimation," in *2013 IEEE/ASME International Conference on Advanced Intelligent Mechatronics* (AIM), pp.1528-1533, 2013.

B. Li, J. Zhang, H. Du, and W. Li, "Two-layer structure based adaptive estimation for vehicle mass and road slope under longitudinal motion", *Measurement*, under review.

Chapter 5

B. Li, H. Du, W. Li, and Y. Zhang, "Side-slip Angle Estimation Based Lateral Dynamics Control for Omni-directional Vehicles with Optimal Steering Angle and Traction/brake Torque Distribution," *Mechatronics*, 20, pp.348-360, 2015.

B. Li, H. Du, and W. Li, "Optimal Distribution Control of Non-Linear Tire Force of Electric Vehicles With In-Wheel Motors," *Asian Journal of Control*, 18(1), pp.69-99, 2016.

Chapter 6

B. Li, H. Du, and W. Li, "Integrated dynamics control and energy efficiency optimisation for over-actuated electric vehicles", *Vehicle System Dynamics*, under review.

Chapter 7

B. Li, H. Du, and W. Li, "Fault-tolerant control of electric vehicles with in-wheel motors using actuator-grouping sliding mode controllers", *Mechanical Systems and Signal Processing*, 72-73, pp.462-485, 2016.

Chapter 8

B. Li, H. Du, and W. Li, “Trajectory control for autonomous electric vehicles with in-wheel motors based on a dynamics model approach”, *IET Intelligent Transport Systems*, 10(5), 318-330, 2016.

B. Li, H. Du, and W. Li, “A Potential Field Approach Based Trajectory Control for Autonomous Electric Vehicles with In-wheel Motors”, *IEEE Transactions on Intelligent Transportation Systems*, **DOI:** 10.1109/TITS.2016.2632710, 2016.

Chapter 9

B. Li, J. Zhang, H. Du, and W. Li, “Two-layer structure based adaptive estimation for vehicle mass and road slope under longitudinal motion”, *Measurement*, 95, 439-455, 2017.

I. INTRODUCTION

1. Background

Since the beginning of civilization, human beings have developed road vehicles. For thousands of years these were in the form of horse-powered chariots or carriages. After the industrial revolution and the emergence of the steam-powered engine, machine-powered road vehicles became available. In modern times, internal combust engine (ICE) vehicles were widely developed, but challenges like pollution from carbon-dioxide emission and problems related to safety now exist.

Currently, the issue of greenhouse gas emission is a global challenge attracting the world's attention. The Key World Energy Statistics reported that the energy demand of the global transportation system grew dramatically from 23% in 1973 to 28% in 2012 [1]. It is also suggested that the transportation sector will result in 30% growth in petroleum consumption between 2004 and 2030 in the World Energy Outlook [2]. These findings conclude that the increasing use of road vehicles will contribute to energy exhaustion and global warming.

In addition, traffic accidents of commercialized ICE automotives cause serious safety problems. An estimated 1.2 million people are killed in road crashes each year and as many as 50 million are injured all over the world. Projections indicate that these figures may increase by about 65% over the next 20 years unless prevented by new technologies [3].

The electrification of road vehicles provides an attractive solution to the problem of greenhouse gas emission and could improve vehicle safety. The use of hybrid electric vehicles (HEVs) and electric vehicles (EVs) along with the development of different electric powertrains, as an alternative to the use of conventional ICE vehicles, could reduce greenhouse gas emission and improve vehicle performance.

HEVs combine the ICE and the electric powertrain to partially replace petrol consumption by electric power. Due to the rapid improvement of electrified systems and technologies, the

trend towards pure EVs is more attractive and intensive research has been carried out in this area. EVs use an electric motor, battery, inverter and electronic control unit to replace the engine, gear box and mechanical linkage, which gives greater flexibility to the arrangement of vehicle steering and driving style.

Since the 19th century when the first automotive was invented, front wheel steering has been used to steer the vehicle in most situations. This steering technique was considered to work tolerably well without any serious inconvenience for many decades [4]. When the rear wheel is also steered, however, the delay of tyre force generation can be reduced and better responsiveness can be achieved during vehicle course changing. Thus, four-wheel steering vehicles have been widely used in the last several decades [5] [6]. It should be pointed out that the term 'four-wheel steering' here refers to the ICE vehicle with two front wheels or two rear wheels which have the same steering angle. Recently, with the emergence of technology for the in-wheel motor for EVs, the innovative four-wheel independent steering (4WIS) has been developed for which all the steering angles of the four wheels can be different [7]. This steering characteristic can greatly improve vehicle mobility and minimize the adverse effect of the side-slip angle.

A single driving motor was installed in the centre of the vehicle chassis for conventional EVs in the past. Nowadays, however, the decentralized electric powertrain arrangement is preferable due to its flexibility and improved power performance. According to the literature [8], the decentralized motor arrangement in the driving system of EVs can be classified as two in-wheel motor drive EV, four-wheel independent drive (4WID) EV and front-and-rear-wheel-independent-drive (FRID) EV (Figure I-1).

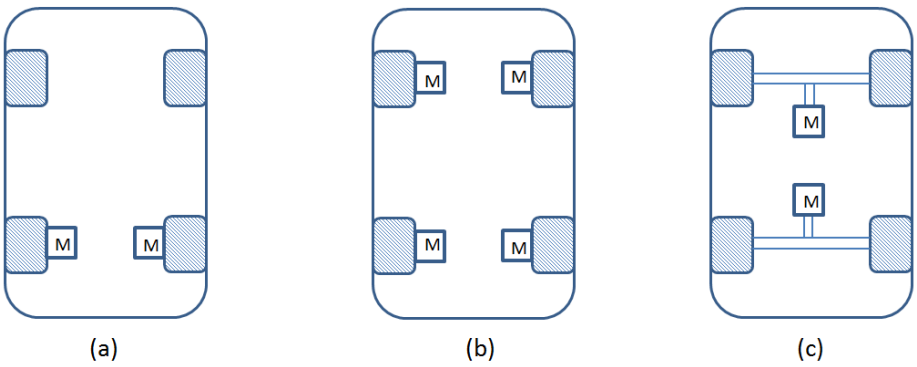

Figure I-1 Decentralized motor arrangement in the driving system of EVs: (a) two in-wheel motor drive EV (b) 4WID EV (c) FRID EV [8]

More recently, the innovative combined 4WIS and 4WID EV has been developed by equipping the in-wheel motor on each wheel [9] [10]. The four independent steering angles and four independent driving or braking torques can provide a total of eight control actuators and these redundant control actuators are advantageous in achieving multiple control targets, including handling control, stability control, energy-efficient control, and fault-tolerance control.

Vehicle control is crucial to guarantee vehicle stability and safety. The trend towards electrification of road vehicles presents advantages to the overall vehicle dynamics and performance control, and also presents challenges to the vehicle control system design due to the increased number of steering and driving actuators.

In the area of active vehicle control, three main control targets have been the focus of research papers in the last few decades: yaw rate control, side-slip angle control and combined yaw rate and side-slip angle control.

The objective of yaw rate control is primarily concerned with improving steering feel and the yaw rate tracking approach is employed to track the desired yaw rate [11] [12]. Side-slip angle control relates more to the vehicle stability and is important close to the vehicle friction limits [13]. The combined approach is usually employed by both the traction/braking and steering system to offer the benefits of improved handling feel as well as increased vehicle stability near the friction limit [14]. However, the available number of steering and driving control actuators is limited by the mechanical linkage and powertrain for the traditional ICE vehicle. 4WIS-4WID EVs are more flexible in achieving more control targets, such as energy-efficient control and fault-tolerant control, but the increased number of the controlled actuators requires more complex and advanced control strategies or actuator allocation methods.

Recent studies proposed energy-efficient control for EVs by minimizing the output power of the electric motor and maximising the regenerated brake energy [15]. However, comprehensive investigation of the combination of the vehicle dynamics controller (stability controller and handling controller) and the energy-efficient controller is still lacking.

Since EVs with in-wheel motors have more control actuators, the chance of unanticipated breakdowns of the driving or steering units can be higher than a conventional ICE vehicle.

When a conventional stability controller is applied, the fault of individual steering or driving actuators will compromise the vehicle's dynamic performance. Therefore, including the fault-tolerant controller within the vehicle dynamics controller is important for EVs with in-wheel motors.

Autonomous EVs will be commercialised in several decades and are attractive to customers due to the automated steering systems. The 4WIS-4WID EVs can take advantage of the increased number of control actuators to achieve vehicle dynamics control and automated steering control simultaneously.

2. Statement of the thesis problem

The over-actuated control problem can be defined as occurring when the number of control actuators is higher than the controlled vehicle's degree of freedom. For EVs with in-wheel driving motors and in-wheel steering motors, the number of control actuators is 8 and only two control targets – the yaw rate and body side-slip angle - are involved for the combined yaw rate and body side-slip angle controller. In this way, these redundant control actuators can be utilised to achieve other control targets, like the longitudinal velocity control, the fault-tolerant control and energy-efficient control. This thesis will focus on the over-actuated control actuator allocation and distribution problem and design optimal steering angle and traction/brake torque distributors based on desired longitudinal tyre force, lateral tyre force and yaw moment and various control targets. This represents a non-linear multi-target over-actuated optimal control allocation problem.

In order to solve this control problem, reliable and accurate real-time vehicle state information is important. In the literature, however, state estimation for traditional ICE vehicles is more extensive than for EVs with in-wheel motors. Thus, in this thesis, the real-time longitudinal velocity estimator, slip ratio estimator, friction-coefficient estimator, lateral side-slip angle estimator, vehicle mass estimator and road slope estimator for the EV with in-wheel motors were established as the first step.

When the values of vehicle states were determined, both linear and non-linear allocation methods could be used to solve the over-actuated control allocation problem for the combined handling control and stability control. Then alternative approaches could be

proposed to include the energy-efficient controller, fault-tolerant controller and autonomous vehicle steering controller into the combined handling and stability controller.

Simulations based on Matlab Simulink were used to verify the proposed control allocation methods. Finally, experimental work was also carried out to test the vehicle dynamics performance. A four-wheel driving scaled EV test platform was built to verify the mathematic vehicle dynamics modelling for comparison with the software simulation results. Various sensors, such as encoders, accelerometers and current sensors, were installed on the vehicle chassis to obtain reliable vehicle states.

3. Objectives

The main objectives of this thesis can be summarised as design and application of estimators and controllers for the 4WIS-4WID electric vehicle with in-wheel motors:

- Design of a real-time vehicle side-slip angle estimator, longitudinal velocity estimator, longitudinal slip ratio estimator, tyre-road friction-coefficient estimator and vehicle mass and road slope estimator.
- Proposal of a vehicle body dynamics model, tyre model, steering model and driving model for the 4WIS-4WID electric vehicle.
- Design of a linear feedback controller and a non-linear over-actuated control allocation method for the stability and handling control of 4WIS-4WID electric vehicle.
- Application of the over-actuated control allocation method in the energy-efficient control.
- Application of the over-actuated control allocation method in the fault-tolerant control.
- Application of the over-actuated control allocation method in the autonomous vehicle control
- Experimental verification of the proposed estimation and control method.

4. Thesis outline

A comprehensive literature review of various vehicle state estimators, vehicle dynamic modelling methods and vehicle controller design methods is found in Chapter 2. In Chapter 3 vehicle state estimators are proposed. Chapter 4 describes a vehicle dynamics model based on the 4WIS-4WID electric vehicle. A linear feedback controller and non-linear over-actuated control allocation method for the handling and stability control of the 4WIS-4WID electric vehicle based on the estimated vehicle states and vehicle dynamics model, is detailed in Chapter 5. Chapters 6 and 7 propose the application of the over-actuated control allocation method in the energy-efficiency control and fault-tolerant control, respectively. In Chapter 8, the autonomous vehicle trajectory controller design based on the over-actuated control allocation method is discussed. Chapter 9 focuses on the experimental validation of the proposed mass and road slope estimator based on a scaled electric vehicle.

II. Literature review

This thesis covers a wide range of research areas, such as the vehicle state estimation and the vehicle linear and non-linear control methods. The comprehensive literature review is essential to grasp the less focused but attracting area of the research and is helpful to push the boundary of the existing knowledge. In this section, the review about the vehicle state estimation, vehicle dynamic modelling method and the various vehicle controller design methods are presented as the preliminary study of this thesis.

1. Vehicle state estimation

Since the vehicle dynamics controller requires a number of vehicles states which are hard to be directly measured, vehicle state estimation is critical to the dynamics controller design. Vehicle longitudinal velocity, lateral velocity and side-slip angle are some important immeasurable vehicle states requiring estimator design. In this section, the studies about velocity estimator are reviewed first, followed by the review on the side-slip angle estimator. In reality, the side-slip angle β can be calculated as:

$$\boldsymbol{\beta = tan^{-1}\left(\frac{v_y}{v_x}\right)} \tag{1}$$

where v_x is the longitudinal velocity and v_y is the lateral velocity. Equation (1) suggests that the estimation of side-slip angle is related to the estimation of longitudinal velocity and lateral velocity. When the vehicle velocity and side-slip angle are available, the tyre friction force and friction coefficient can be estimated accordingly. Thus, the second part of this section is the review on the estimation of tyre force and tyre-road friction coefficient. Finally the estimation about the vehicle mass and road slope is discussed.

1) Velocity estimator

Vehicle velocity is an important value for various vehicle state estimators and dynamics controllers. In the early period, the wheel speed of non-driven wheels is used to approximate

the vehicle velocity, but it is not reliable. The actual value of velocity, however, can hardly be directly measured from the vehicle sensors and the estimation of velocity according to other vehicle states (acceleration, wheel speed or yaw rate) is a very attractive research area.

The kinematic relationships among the vehicle velocities v_x, v_y , yaw rate r and accelerations a_x, a_y are suggested as follows:

$$\dot{v}_x = rv_y + a_x \tag{a}$$

$$\dot{v}_y = a_y - rv_x \tag{b}$$

(2)

The longitudinal and lateral velocities can be obtained by integrating equation (2) if the yaw rate and accelerations are measureable. The measurement biases and noise, however, will lead to the unacceptable estimation results. Thus, the vehicle dynamics should be introduced into the model to overcome the measurement biases and noise.

In the literature, a number of earlier studies used linear approaches to estimate the vehicle velocity and vehicle state. An observer of lateral velocity was developed, which assumed that the tyre was working in the linear tyre region [16]. Tseng et al. also employed an asymptotic observer to estimate the lateral velocity and the lateral tyre force was considered as the linear function of vertical load [17]. Other earlier linear or quasi-linear approaches also only applied kinematic models without vehicle dynamics considerations [18] [19].

To improve the estimation accuracy, various nonlinear vehicle velocity observers developed. An extended Kalman filter (EKF) is developed to estimate vehicle velocity and friction coefficient [20] [21] [22]. Since a random walk is selected to model the friction force, the estimation accuracy, however, can be degraded when the tyre friction forces are time-varying during braking and driving. In addition, the non-linear vehicle dynamics model is linearized at discrete time and the model error in current state can be introduced into the estimation results. The EKF method is widely used to estimate the vehicle velocity based on the non-linear dynamics model, but the unscented Kalman filter (UKF) has shown to be the attractive alternative particularly when the system shows strong nonlinearity [23]. Zong and Deng proposed a vehicle velocity estimator for 4WID EVs based on UKF method [24]. Based on acceleration and yaw rate measurements in addition to wheel angular velocity and steering angle measurements, a non-linear velocity observer is proposed with stability guarantees [25].

Unfortunately, this research is based on the zero tyre longitudinal and lateral slip assumption and the estimation of longitudinal velocity can be deteriorated when the tyre slips are high. Recently, a non-linear vehicle velocity observer based on the Dugoff's tyre model was presented. This observer utilised the difference between the measured and estimated longitudinal acceleration, lateral acceleration and yaw rate as the feedback value with the fixed gain structure. The stability of the observer is proved by a sufficient condition in [26].

Li et al. suggested that two kinds of errors cause the challenges on the velocity observer [27]. One error is caused by the linearization of the non-linear vehicle dynamics model, while the other error is induced by the mismatch between dynamics model and actual physical vehicle motion under the combined steering and driving/braking motion. The large amounts of computation resources and time cost of the convergence of the velocity observer also present great challenge. Therefore, Li et al. considered the nonlinear characteristics of the vehicle under a complicated handling condition, such as the road ramp and load transfer. The longitudinal and lateral velocity could be estimated under different non-linear manoeuvres and the cascade system was proposed to improve the computational efficiency of the velocity observer.

With the emerging of the innovative technology of in-wheel motors, Ko et al. suggested a velocity estimator based on the concept of the effective inertial and the measurement values of motor torque, angular velocity of each wheel and acceleration for the an in-wheel EV [28]. Xin et al. proposed two vehicle velocity estimation algorithms for the in-wheel EVs; one algorithm based on the UKF was designed for the four-wheel drive condition, whereas the other algorithm based on the wheel rotational speed was designed for the two-wheel drive condition [29].

2) Tyre side-slip angle estimation

Since the side-slip angle is an important feedback value for vehicle stability control, the real-time information about the side-slip angle is critical to the performance of various control strategies. Ryu et al. used the combination of a global positioning system (GPS) and an inertial navigation system (INS) to directly measure the side-slip angle [30], and side-slip angle can also be measured by two antenna GPS [31] [32]. The GPS signal, however, may not be reliable due to disturbance in the satellite signal.

Due to the difficulty in directly measuring the side-slip angle, accurate estimation of the side-slip angle via available on-board sensors is important. So far, the methods of side-slip angle

estimation can be classified into two groups – kinematics method (direct integration method) and vehicle model method. The method of integrating the side-slip rate, which is available through the side-slip rate sensor, have the advantage of being independent of tyre properties, road friction, vehicle loading mass and other vehicle tyre properties, but is affected by error due to sensor bias, road slope and bank angle [33] [34] [35] [36]. For the vehicle model method, in order to estimate the side-slip angle, accurate information about vehicle velocity, road friction coefficient and some tyre parameters are necessary, but all of these are difficult to be directly measured [37] [38] [39] [40] [41]. We can find out the accurate estimation of the vehicle side-slip angle is closely related to the accurate estimation of velocity and friction coefficient for the model-based method. The model based method has the advantage of high accuracy in linear region, but the accuracy is not sufficient due to the saturation of tyre side force against slip angle. Stephant et al. presented a typical structure of this method based on on-board vehicle models [42]. The author stated four observers, including a linear observer based on linear vehicle model, an extended Luenberger observer, and EKF and a sliding-mode observer (SMO) based on non-linear vehicle model. In the linear regions, all proposed observers are satisfactory, while the accuracy in the nonlinear regions deteriorates due to the linearity assumption.

Piyabongkarn et al. developed the side-slip angle estimator based on the model-based method and the direct integration method to utilise the advantages of these two methods, where the model-based method played the dominant role at low frequencies and the weight of the kinematics-based method was relatively large at higher frequency [43]. This method, however, applied an open-loop observer and large estimation error may exist without the feedback signal, and it was difficult to find the best balance between the model-based estimation and kinematic-based estimation. Fukada suggested the combination of model observer and direct integration method to obtain the reliable side-slip angle, and the yaw rate feedback algorithm is applied to compensate the model error [44]. Pi et al. also suggested the close loop side-slip angle estimation method that combines the model-based method and kinematics-based method together [45]. In [45], to obtain the reliable side-slip angle, the generated side forces from model-based method and kinematics-based method are weighted and summed according to the degree of vehicle non-linear state which is determined by the fuzzy-logic procedure considering the yaw rate deviation and lateral acceleration.

In addition, Baffet et al. proposed the vehicle side-slip angle estimation process which was separated into two blocks, where one block corresponded to the vehicle body dynamics and

the other block referred to the tyre-road interface dynamics [46]. The first block contained the SMO which estimates tyre forces and yaw rate from a single-track model. In the second block, an EKF based on a side-slip angle model and a linear adaptive tyre-force model was applied for the estimation of side-slip angle and wheel cornering stiffness. For normal driving situations, lateral forces are usually considered to be linear with respect to side-slip angle and the constant cornering stiffness is assumed. However, when tyre-road friction changes or when the non-linear tyre domain is reached, wheel cornering stiffness varies. In Baffet et al.'s study, in the linear adaptive tyre-force model, a readjustment variable has been added to correct wheel cornering stiffness error when vehicle tyre enters into the non-linear region.

It is noted that a new source of information, steering torque, has been considered by recent studies. Steering torque measurement are available in electric vehicles with steer-by-wire, electric power steering, or active steering systems and total alignment moment can be determined easily if the steering torque is measurable. Since total alignment moment decreases well before the saturation of the tyre force, the information of alignment moment can be utilised to improve the vehicle stability. Nakajima conducted the earlier study and demonstrated that steering torque can enhance electronic stability control performance more than just relying on yaw rate measurements [47]. Other studies suggested that the driver steering input should be limited when the noticeable decrease in total alignment moment is detected [48] [49] [50]. These methods relied on linear observers for side-slip angle, which are not accurate when the tyre's lateral limit of adhesion is reached. All of the above methods utilised the total alignment moment as an early indication of exceeding the tyre's lateral limits, but the method of the explicit estimation of peak lateral force and tyre side-slip angle were not provided. Hsu et al. [51] [52] [53] presented a new model-based estimation method that used pneumatic trail information in measured steering torque to estimate the friction limit and lateral handling limit. The innovation of this work is the sensitivity of the pneumatic trail to tyre parameters even in the linear tyre region, which can enable early detection of peak lateral force before the friction limits are reached. Directly using the available motor currents for the estimation of individual side-slip angle of the omni-directional vehicle was also recently done in [54].

3) Tyre-road friction coefficient estimation

Since vehicle tyres are the only part that vehicle body maintains contact with the road, information about the tyre-road friction is critical to vehicle's longitudinal, lateral and roll dynamics and control. Particularly, for vehicle electronic stability control (ESC) system, if the tyre-road friction coefficient can be obtained, the yaw rate can be effectively controlled to prevent vehicle skidding with the updated information about the tyre-road friction coefficient [55] [56] [57]. For 4WD vehicles, estimation of individual tyre-road friction coefficients can help to detect which wheel needs the maximum drive torque [58]. In adaptive cruise control and collision-avoidance systems, the estimated tyre-road friction coefficient can help to adjust the braking distance in real time [59]. In winter road maintenance, estimation of tyre-road friction coefficient can be used to adjust de-icing materials on icy roads [60].

In general, the tyre-road friction coefficient μ is defined as the maximum value of the normalised traction force ρ, which is determined by the tyre longitudinal friction force, tyre lateral friction force and tyre vertical load as [61] [62]:

$$\rho = \frac{\sqrt{F_x^2 + F_y^2}}{F_z} \tag{3}$$

where F_x is the tyre longitudinal friction force, F_y is the tyre lateral friction force and F_z is the vertical load. Note that the tyre-road friction coefficient μ only relies on the road surface type, such as ice, snow, and dry asphalt, and its value is between 0 and 1. In addition, it can be seen from (3) that the tyre-road friction force is closely related to the tyre-road friction coefficient. The maximum tyre-road friction force that the tyre can generate is determined by the tyre-road friction coefficient when a particular vertical load on the tyre is given.

To obtain the information about road surfaces in real time, some studies used special sensors to directly measure the tyre-road friction coefficient. For instance, an acoustic sensor was used to 'listen to the tyre' to determine the tyre-road friction coefficient [63] [64]. An alternative method using an optical sensor was suggested to be installed at the front bumper of the car to estimate the type of road surface [65]. In addition, an optical positioning sensor was proposed to measure the displacement of the tyre contact patch relative to the wheel rim to estimate the tyre-road friction coefficient [66]. However, it is noted that all of these

methods need expensive sensors, which are not available for conventional passenger vehicles. The requirement of for dedicated sensors is one of the main disadvantages of special sensor based friction estimation method, which will be available in several years in the future.

Due to the difficulties in directly measuring the tyre friction force or tyre-road friction coefficient, in recent years some studies focused on the estimation of tyre-road friction coefficient based on the vehicle model and correct information of vehicle position, velocity, wheel speed and steering angle. Li et al. suggested there are mainly three position systems for the measurement of vehicle states: INS, GPS and magnetic positioning system (MPS) [67]. INS is the first position-navigation system used widely but mechanical inertial gyroscopes consume high power and are vulnerable to damage. Recently, the new type INSs are realized by integrated electronic-mechanical or electronic-optical sensors only [68] [69]. Because of the lacking of the moving parts, such new-type INSs outperform the conventional INS in many ways. Applications of GPS for vehicle position measurement are also widely used and the current trend is to combine INS and GPS together to achieve better estimation performance of vehicle position [70] [71]. However, GPS is relatively expensive to a passenger vehicle and it cannot be always reliable due to the change of environment such as satellite drop-outs in urban environment. In addition, magnetic sensing is also a promising technology for the vehicle-position measurement and guidance [72] [73] [74]. In addition to be directly measured, vehicle states such as velocity and side-slip angle can also be estimated by the mode-based method, which is comprehensive reviewed in sections 2.1.1 and 2.1.2.

Based on the knowledge of these vehicle states and proper vehicle dynamics model, the tyre-road friction information can be obtained accordingly. Many studies used the longitudinal vehicle dynamics model to analyse the tyre-road friction during traction/brake motion. Three main longitudinal dynamics model based methods have been proposed so far: slip slope method [61] [75] [76], individual wheel friction estimation method [62] [77], and EKF method [78] [20] [21] [79]. Specifically, Gustafsson [75] suggested a slip slope method based on the front-wheel-driving vehicle while Müller et al. [76] proposed a slip slope friction estimator only for the braking situation. Wang et al. [61] developed a slip slope method for the front wheel-, rear wheel-, and four wheel-traction or braking systems under both linear and non-linear tyre regions. Compared with Gustafsson's method and Müller's method, Wang's method greatly expanded the applicable scope for the friction coefficient identification. For the EKF method, Ray [78] [20] [21] conducted a series of studies on the vehicle state estimation and tyre-road friction coefficient estimation. First, Ray developed a 9

degree-of-freedom (DOF) vehicle dynamics model and an analytic tyre force model to simulate the real vehicle motion, and used a 5 DOF vehicle model to develop the EKF state estimator [78]. Then based on the developed EKF estimator in [78], the braking controller, using the estimated longitudinal slip ratio, was proposed [20]. Ray also suggested extended Kalman-Bucy filtering (EKBF) and Bayesian hypothesis selection method to estimate the vehicle motion and friction coefficient [21]. In this study, based on the previous studies of EKF estimator in [78] [20], the estimated vehicle states like tyre force, slip ratio and side-slip angle were compared statistically with a nominal analytic tyre model to choose the most likely friction coefficient based on the Bayesian hypothesis selection. Note that the prior knowledge of tyre parameters and tyre model was not required in Ray's studies. In addition to Ray's studies, Dakhlallah et al. [79] also suggested the estimation method for vehicle state and tyre-road friction coefficient based on EKF method. However, the vehicle dynamics model used by Dakhlallah et al. included a non-linear Dugoff tyre force model, which requires prior knowledge of tyre parameters.

Furthermore, some studies developed the friction estimation method based on both longitudinal and lateral excitations to have a wide operation range. Having adequate and rich excitations is critical for the friction estimation because we do not have the luxury of choosing the level and type of excitations in ground vehicle applications. Ahn et al. developed the integrated friction estimation method based on both the longitudinal and lateral excitations [80] [81]. Specifically, the large lateral excitation-based method is used when large lateral excitations exist, and a non-linear observer requires medium level of excitations. The longitudinal dynamics based method requires less than 2% of longitudinal slip ratio for the linear region and 30-100% of longitudinal slip ratio for the saturation region. Wang and Wang also suggested a sequential tyre cornering stiffness coefficient and tyre-road friction coefficient estimation method [82]. In this study, when the vehicle is moving along a straight line or making a slow turn when the tyre side-slip angle is small and the friction coefficient is difficult to estimate, the tyre cornering stiffness can be estimated first according to the generated additional yaw moment induced by the longitudinal tyre force difference. When the vehicle is making a fast turn with large side-slip angle, the friction coefficient can be reliable estimated with the pre-estimated cornering stiffness.

Most of the researches of the friction coefficient estimation in the literature are based on the traditional ICE vehicles, while the friction estimation method for the EVs equipped with in-wheel motors can be different. The electric parameters of the motor, such as the armature

current and voltage, are more convenient to measure and used to estimate the friction information. Xu et al. presented the research to explore the innovative friction estimation method taking advantage of the electric parameters of in-wheel motors [83]. Xu's study addressed the issue of the influence of the road condition on the electric parameters. When the road surface is changed suddenly from high-adhesion road onto the low-adhesion road, there is a sudden change of the load current drop in the electric motors, which can be used to estimate the current tyre-road friction coefficient.

4) Vehicle mass and road slope estimation

In the development of the vehicle technology, the driver's safety and the stability performance of the vehicle are the primary concerns. It is well known that various vehicle control decisions can be further improved if the vehicle parameters are known. Particularly, if the road slope ahead is known, the road slope can be used as an input for the driving control system to improve the vehicle energy efficiency [84]. Vehicle mass is usually needed in the engine management and driving control system to improve the fuel consumption and driving performance. Since the mass of a typical passenger vehicle may be changed when the passengers get on or get off the vehicle, the identification of the vehicle mass is important. In addition, a number of studies proposed control method to minimise the fuel consumption of the heavy vehicle [85] [86] and the knowledge of the vehicle mass reduction related to fuel consumption is important. It has been also proved that the vehicle mass estimation without the knowledge of road slope is not accurate due to the error caused by the unacceptable level [87]. The dynamic performance of a vehicle on a steep downhill can be improved in terms of the hill holding and traction control when the information of the vehicle mass and road slope is simultaneously available [88]. Thus, the real-time information of vehicle mass and road slope is important to vehicle's safety and stability control.

Many studies in the literature applied the sensor-based method to obtain the road slope information [89] [90]. This, however, may lead to the extraneous hardware and wiring complexity, which is not desirable for the automotive industry [91]. The application of inclinometer may be acceptable to measure the real-time value of road slope, but the measurement noise of the inclinometer when the vehicle is moving may seriously impair the measurement performance [92].

Compared with the sensor-based method, the model-based parameter estimation method has advantages because the measurement sensor is not required. In recent years, the simultaneously estimation of the vehicle mass, road slope and other vehicle parameters by the model-based method is extensively focused. The traditional recursive least square (RLS) estimation method is quite straightforward and easy to implement to estimate the vehicle parameters [61] [93]. However, the major drawback of this method is not reliable when the measurement noise is considered. The real-time estimation of the vehicle parameters can be also considered as the adaptive control of a non-linear system with unknown parameters. In conventional adaptive controller, the tracking of the reference trajectory is focused and the parameters estimation error is not guaranteed to converge to zero because of the lacking of the excitation [94]. In order to achieve the parameter convergence, the finite-time (FT) identification method was proposed and the true parameter estimate is obtained at any time instant when the excitation condition is satisfied [95]. The drawback of the FT method, however, is to check the invertibility of the matrix online and compute the inverse matrix when appropriate. Adetola and Guay developed a novel adaptive compensator to guarantee the exponential convergence of the parameter estimation error and the persistent excitation (PE) can be satisfied according to the rate indicated by the close-loop system's excitation instead of the checking of the invertibility of the matrix [96]. Mahyuddin et al. proposed the adaptive observer to estimate the vehicle mass and road slope simultaneously [97]. This adaptive estimator guarantees the FT convergence due to the added sliding mode term and the PE condition can be satisfied if the defined filtered regressive matrix is positive defined. However, the accurate estimation of each parameter relies on the carefully turning of the adaptive gain and the coupling effect of each estimated parameter is significant. In addition, [97] also applied the observer to produce the observer error for updating parameters and this may lead to the increasing computational effort and the adding of the sliding term may also increase the computational effort. Yang et al. proposed the adaptive parameter estimator without the adaptive state observer and the road slope, vehicle mass, rolling resistance coefficient, viscous friction coefficient and aerodynamic drag coefficient can be estimated simultaneously [84]. In contrast to [97], the construction of observer or predictor is evaded in Yang's method and the computational efficiency is improved. The PE condition can be achieved by calculating the minimum eigenvalue of regression matrix. However, the problem of the coupling effect of each estimated parameter still exists in this method.

2. Vehicle dynamics modelling for 4WIS-4WID EVs

For the traditional vehicle, the vehicle dynamics model mainly includes the body dynamics model, tyre model, steering model and driving model. The comprehensive vehicle dynamics model can be used as the plant for the controller design and parameter estimator design. In addition, the design of the controller and estimator also requires the accurate and comprehensive vehicle dynamics model.

1) Vehicle body dynamics model

Abe [98] or Karnopp [99] developed the basic equations of motion based on a coordinate system fixed on the body of a moving vehicle:

$$mv_x\frac{d\beta}{dt}+2\left(C_{\alpha f}+C_{\alpha r}\right)\beta+\left\{mv_x+\frac{2}{v_x}\left(l_fC_{\alpha f}-l_rC_{\alpha r}\right)\right\}r=2C_{\alpha f}\delta_f \quad \text{(a)}$$

$$2\left(l_fC_{\alpha f}+l_rC_{\alpha r}\right)\beta+I\frac{dr}{dt}+\frac{2\left(l_f^2C_{\alpha f}+l_r^2C_{\alpha r}\right)}{v_x}r=2l_fC_{\alpha f}\delta_f \quad \text{(b)}$$

(4)

where v_x is the vehicle longitudinal velocity. $C_{\alpha f}$ is the front tyre cornering stiffness and $C_{\alpha r}$ is the rear tyre cornering stiffness. m is the vehicle mass and I_z is the vehicle moment of inertial. β is the vehicle body side-slip angle and r is the vehicle yaw rate. l_f and l_r are the front and rear wheel base lengths. δ_f is the input steering angle.

Equation (4) describes the vehicle lateral motion and yaw motion, and the longitudinal velocity is considered as the constant value. Thus, these equations can only be used to describe the vehicle steady state turning motion without traction or braking. The constant cornering stiffness is applied to present the lineal relationship between the side-slip angle and tyre lateral force without the considering of the tyre non-linear characteristic. In addition, these equations only consider the two front wheel steering and the steering angles of rear wheels are fixed as zero.

Lam et al. [7] proposed a vehicle dynamics equation for a 4WIS vehicle:

$$\sum_{i=fl,fr,rl,rr}F_{xi}=m\left(\dot{v}_x-v_yr\right) \quad \text{(a)}$$

$$\sum_{i=fl,fr,rl,rr} F_{yi} = m(\dot{v}_y + v_x r) \quad \text{(b)}$$

$$l_f(F_{yfl} + F_{yfr}) - l_r(F_{yrl} + F_{yrr}) + \frac{T_f}{2}(F_{xfl} - F_{xfl}) + \frac{T_r}{2}(F_{xrl} - F_{xrr}) = I_z \dot{r}$$

(c)

(5)

The forces F_{xi} and F_{yi} are related to the traction force F_{ti} and tyre lateral force F_{si} of each wheel:

$$F_{xi} = F_{ti} \cos \delta_i - F_{si} \sin \delta_i \quad \text{(a)}$$

$$F_{yi} = F_{ti} \sin \delta_i + F_{si} \cos \delta_i \quad \text{(b)}$$

(6)

In [7], the Magic formula tyre model is also applied to describe the non-linear relationship between lateral tyre force and the side-slip angle of each wheel.

Boada et al. [100] also developed a more complicated vehicle dynamics model considering the roll motion and traction or brake motion of the vehicle in addition to longitudinal motion, lateral motion and yaw motion. The vehicle dynamics model used the Dugoff tyre model to describe the non-linear relationship between the tyre force and side-slip angle. This dynamics model can be considered as the basic vehicle dynamics model for the 4WIS-4WID EVs, and the steering model and the driving model based on the electric motor should also be considered.

2) Vehicle tyre model

Tyre is the only contact part the vehicle interacts with the road. In the literature there are mainly two kinds of tyre models: a physical tyre model and an empirical tyre model. The physical tyre model can theoretically describe the tyre characteristics with less accuracy, while an empirical tyre model is the curve fitting results of the actual tyre data.

a) <u>Physical tyre model</u>

The brush model is a simple physical tyre model consisting of a row of elastic bristles called the tread element. The top of the tread element is attached to the base of the wheel and the bottom one is attached to the ground. The relative slip between the top and bottom of the element can generate the lateral slip and tyre forces [101].

Deur [102] proposed the LuGre tyre model, which is a more complicated physical tyre model that considers the decreasing effect of friction [103]. This tyre model is a linear model for pure cornering condition and the model parameters are described by the function of static curve slope parameters.

The non-linear Dugoff tyre model, which can well describe the non-linear tyre characteristic of combined longitudinal and lateral tyre force and the effect of friction circle, is proposed in [104].

The Dugoff tyre model can be classified as two stages according to the defined value λ: when $\lambda > 1$, the tyre has not reached the sliding boundary point and when $\lambda < 1$, the tyre reaches the sliding boundary point and starts to slide away. The defined value λ is the reciprocal function of the combined slip s_R which considers both the longitudinal slip ratio and the lateral slip angle.

According to [104], the Dugoff tyre model is the mathematical simplification of the analytical Fiala tyre model under some reasonable simplifying assumptions in the analysis of the tyre mechanics. In [104], the tyre force curve derived from the experimental data obtained by an on-road tyre dynamometer and the curve derived from the simulation results of the tyre data obtained by the Dugoff tyre model are shown to agree. This proves that the Dugoff tyre model can accurately represent the actual vehicle tyre characteristics.

In addition, a number of researches also focused on the modelling of the physical or analytical tyre model in the literature. Guo and Lu [105] proposed a UniTire model for the vehicle dynamics model, which is a unified non-steady and non-linear semi-physical tyre model. Based on the UniTire model, Xu et al. [106] suggested a combined tyre model for cornering and braking. Zhou et al. [107] developed a three plane multi-spoke tyre model for transient tyre behaviour, while Lacombe [108] suggested an on-road analytical model to describe the tyre force and moment. An innovative non-linear tyre observer was proposed by Canudas-de-Wit et al. [109] to describe the road friction. Yamazaki et al. [110] also estimated the friction between the tyre and the road based on the tyre brush model. To analyse vehicle performance during a crash, a new detailed model has been evaluated [111]. In addition, to effectively analyse vehicle behaviour during extreme cornering, Lu et al. [112] proposed a tyre model that considers the effect of camber.

b) *An empirical tyre model*

The Magic formula model is a widely used empirical tyre model [101]. Similar to other empirical tyre models, the Magic Formula model is the curve fitting results of actual tyre data that can accurately describe the behaviour of a certain type of tyre. However, the coefficient of the Magic Formula model (B, C, D and E) should be changed when the type of the tyre is changed, and the Magic Tyre model cannot describe how a tyre's physical parameters affecting its output tyre force.

In addition, a semi-empirical tyre model was developed to simulate vehicle normal driving in [113], and Guo and Ren [114] developed the Unified Semi-Empirical High accuracy tyre model with less parameters. The EKF is also widely used to filter the vehicle test data that is used to obtain the empirical tyre model: Best [115] obtained a tyre model from the test data by the EKF, while Dihua et.al [116] proposed tyre corning models with parameters obtained from the experiment and the cornering force was also estimated from the test data by the EKF [117].

Due to the obvious disadvantages of the lacking of the physical meaning, the empirical tyre model is not focused in this thesis. However, the pure physical tyre model is too complex for the vehicle modelling and consequently the semi-physical Dugoff tyre model is selected to achieve the trade-off between the physical model and empirical model.

3) *The model of in-wheel steering motor*

Abe suggested the steering dynamics equation for the traditional front wheel steering ICE vehicle can be presented as follows [98]:

$$I_s\ddot{\delta} + c_s\dot{\delta} + k_s(\delta - \delta_\alpha) = 2\xi C_{\alpha f}\left(\beta + \frac{l_f r}{v_x} - \delta\right) \tag{7}$$

where I_s is the moment of inertial of the front wheel. c_s and k_s are the damping coefficient and spring constant around the kingpin. δ_α is the driver's steering angle at the steering shaft and δ is the steering angle of the vehicle wheel. ξ is the total alignment moment, which is the

sum of the pneumatic trail t_p and mechanical trail t_m. The mechanical linkage, such as the gear box and tyre rod, is also considered in this model.

For the model of in-wheel steering motor, the electric motor is applied to generate the steering torque and four in-wheel motors are installed on each wheel to achieve the 4WIS characteristic. Hsu at al. proposed the steering dynamics model for in-wheel motor [52]:

$$I_s\ddot{\delta} + c_s\dot{\delta} = \tau_a + \tau_j + k_m I \tag{8}$$

where k_m is the armature constant and I is the motor steering current. τ_a is total aligning moment of each wheel, which is described by the following equation:

$$\tau_a = -(t_m + t_p)F_{si} \tag{9}$$

In the P1 vehicle developed by Stanford University, a steer-by-wire vehicle with independent front-wheel steering mechanism, the actual mechanical trail t_m changes between different steering angles, and the improved steering geometry design provides the relative constant value $t_m = 33\ mm$ [118]. F_{si} is the vehicle lateral side force of each wheel and can be obtained from the vehicle model. As defined in equation (9), the pneumatic trail t_p starts at t_{p0} and decreases to zero as the slip angle increases. t_{p0} can be considered as the half length of the tyre road contact length a [101]. t_p can be derived analytically as a parabolic pressure distribution, however this is less accurate in practice and the simple representation of the force model is chosen instead [51]:

$$t_p = \begin{cases} t_{p0} - \dfrac{t_{p0}C_\alpha}{3} I_f |\tan\alpha_i|, & if\ |\alpha_i| \le \alpha_{sl} \\ 0 & else \end{cases} \tag{10}$$

where α_{sl} is the slip angle α_i at which the tyre has lost lateral grip. C_α is the cornering stiffness.

τ_j is the jacking torque, which is the reaction torque produced by the vertical tyre force and suspension travel as a function of steering angle δ.

4) The model of in-wheel driving motor

In most of the vehicle dynamics model, such as Boada et al.'s study [100], the wheel dynamics equation can be obtained as follows:

$$I_\omega \dot{\omega}_i = -R_\omega F_{xi} + T_i \tag{11}$$

where $i = fl, fr, rl, rr$, which represents the front left, front right, rear left and rear right wheel, respectively.

T_i presents the driving torque or the steering torque applied on each wheel. For the conventional vehicle, the traction torque can be roughly calculated from engine torque by considering the reduction. The engine torque is normally obtained from the measurement of engine fly-wheel speed. To improve the accuracy of measurement, high-resolution rotational motion sensors are utilised [119]. For the conventional vehicle with hydraulic braking system, the brake torque can be calculated from the measurement of oil pressure by pressure sensors in the hydraulic system [120]. These torque measurement signals are available through CAN bus. In addition, with emerging technology of in-wheel driving motor in EV, the traction/brake torque can be easily and accurately measured and controlled from the current of driving motors [83].

3. Vehicle controller design

In this section, linear and non-linear control algorithms for the over-actuated control allocation problem are reviewed first, and then the applications of the control algorithm on the vehicle dynamics in the literature are discussed. These applications include the vehicle handing and stability control, energy-efficient control, fault-tolerant control and autonomous control.

1) Control algorithm

Johansen and Fossen made a clear definition on the over-actuated control allocation problem [121]. It states that the design of the controller for the over-actuated control problem is divided into several levels. In the high level controller, the control algorithm is designed to compute a virtual control input τ_c. This virtual control input is often selected as the number

of forces and moments equalling to the number of the model freedom. The following dynamics model can be used to describe a wide range of mechanical system:

$$\dot{x} = f(x,t) + g(x,t)\tau \quad \text{(a)}$$

$$\boldsymbol{y} = \boldsymbol{l}(\boldsymbol{x},\boldsymbol{t}) \quad \text{(b)}$$

(12)

where $f(x,t)$, $g(x,t)$ and $l(x,t)$ are system functions and $x \in R^n$ is the state vector. t is the time and $y \in R^m$ is the output vector. τ is the virtual input vector that equals to the high-level control value τ_c.

After that, a control allocation algorithm is designed to map the virtual control input τ_c into individual effector forces or moments by the following static effector model:

$$\tau = h(u,x,t) = B(x,t)u$$

(13)

where h and B are functions and $u \in R^p$ is the actual control input. Because the system is the over-actuated system, $p > m$, which means the number of the actual control input u is larger than the number of the virtual control input τ_c.

Finally, for each individual effector and actuator, a separate low-level controller is designed to make the individual actuator achieve the desired control value.

In the literature, various methods have been proposed to solve the over-actuated control problem. Many studies considered the linear effector model where the control effectiveness matrix B describes the linear relationship between the actual control input u and virtual control input τ_c. A number of researches proposed the unconstrained linear control allocation method which neglected any saturation and rate constraints of the input values [122] [123] [124]. The allocation cost function can be formulated as the following equation:

$$\min_{u \in R^p} \frac{1}{2}(u - u_p)^T W (u - u_p)$$

Subject to $\tau_c = Bu$

(14)

where $W \in R^{p \times p}$ is the positive definite weighting matrix and u_p is the desired control input. If B has the full rank, the optimization problem (14) can be solved by weighted least-square method:

$$u = (I - CB)u_p + C\tau_c \tag{15}$$

where

$$C = W^{-1}B^T(BW^{-1}B^T)^{-1} \tag{16}$$

The above method of the generalised inverses can not guarantee the constraints on the input are satisfied. Some researchers proposed the redistributed pseudo-inverse method to solve the control allocation problem [125] [126]. In the first step, the unconstrained control allocation problem is solved. If the constraints are satisfied, no further actions are required. Otherwise, the unconstrained input vector $\bar{u}$ is projected into the admission set to satisfy the constraints and is re-computed by a reduced pseudo-inverse algorithm. The daisy chaining method is the alternative method in addition to the redistributed pseudo-inverse method [127] [128] [129]. This method groups the actuators and effectors into two or more groups which are ranked with different priorities. If one or more effectors or actuators in a group saturates, the whole group is frozen and the optimization will continue in the group with less priority.

The direct allocation method [130] suggested that when the allocated actuator input calculated from the pseudo-inverse method satisfied the input constraints, no further action is required. Otherwise another control input value would be calculated based on the following equation:

$$\max_{\alpha \leq 1} \alpha, \qquad \text{subject to } Bu = \alpha\tau_c, \quad \alpha\tau_c \in \mathbb{A} \tag{17}$$

where $\alpha \in [0,1]$. $\mathbb{A}$ presents the constraints of the virtual control input. However, solving this problem is not trivial when the dimension of u is large.

Linear programming (LP) method is a powerful approach to minimise the error between the allocated input value and the desired one [131] [132] [133] [134]. Specifically, the following 1-norm control allocation problem can be solved by LP method:

$$\min_{u,s}\left(\sum_{i=1}^{m} q_i|s_i| + \sum_{j=1}^{p} w_j|u_j|\right)$$

(18)

subject to $Bu = \tau_c + s$, $u_{min} \le u \le u_{max}$, $\Delta u_{min} \le u - u_l \le \Delta u_{max}$. s_i is the slack variables which ensure that a feasible solution always exists. u_l is the control value from the last sampling instant.

Define the following auxiliary variables:

$$s_i^+ = \begin{cases} s_i & s_i \ge 0 \\ 0 & s_i \le 0 \end{cases}$$

$$s_i^- = \begin{cases} -s_i & s_i \le 0 \\ 0 & s_i \ge 0 \end{cases}$$

$$u_i^+ = \begin{cases} u_i & u_i \ge 0 \\ 0 & u_i \le 0 \end{cases}$$

$$u_i^- = \begin{cases} -u_i & u_i \le 0 \\ 0 & u_i \ge 0 \end{cases}$$

(19)

The control allocation problem in (18) can be transferred in the following linear program:

$$\min_{u^+,u^-,s^+,s^-} \begin{bmatrix} w^T & w^T & q^T & q^T \end{bmatrix} \begin{bmatrix} u^+ \\ u^- \\ s^+ \\ s^- \end{bmatrix}$$

(20)

subject to $\begin{bmatrix} B & -B & -I & I \end{bmatrix} \begin{bmatrix} u^+ \\ u^- \\ s^+ \\ s^- \end{bmatrix} = \tau_c$,

$$\begin{bmatrix} I & -I & 0 & 0 \\ -I & I & 0 & 0 \end{bmatrix} \begin{bmatrix} u^+ \\ u^- \\ s^+ \\ s^- \end{bmatrix} \ge \begin{bmatrix} max(u_{min}, \Delta u_{min} + u_l) \\ -min(u_{max}, \Delta u_{max} + u_l) \end{bmatrix}.$$

The commonly used numerical methods for LP include the simplex method, active set method and interior-point method [135]. Bodson suggested that LP based methods were often

used for a small number of effectors, while quadratic program (QP) based methods tended to use all the effectors but with small control values [132].

When the 2-norm is chosen in the cost function, the control allocation problem becomes the QP that can be solved by numerical QP methods [136] [137] [138]. Consider the following 2-norm control allocation problem:

$$\min_{u,s}\left(\sum_{i=1}^{m} q_i s_i^2 + \sum_{j=1}^{p} w_j u_j^2\right) \tag{21}$$

subject to $Bu = \tau_c + s$, $u_{min} \le u \le u_{max}$, $\Delta u_{min} \le u - u_l \le \Delta u_{max}$. This can be transferred into a standard QP problem:

$$\min_{u,s}[u^T \quad s^T] H \begin{bmatrix} u \\ s \end{bmatrix} \tag{22}$$

subject to $[B \quad -I]\begin{bmatrix} u \\ s \end{bmatrix} = \tau_c$, $\begin{bmatrix} I & 0 \\ -I & 0 \end{bmatrix}\begin{bmatrix} u \\ s \end{bmatrix} \ge \begin{bmatrix} max(u_{min}, \Delta u_{min} + u_l) \\ -min(u_{max}, \Delta u_{max} + u_l) \end{bmatrix}$,

$H = 2\mathrm{diag}(w_1, \dots, w_p, q_1, \dots q_m)$.

QPs are often solved by active set method, interior-point method and fixed-point method [135] [136] [139]. Active set method can improve the guess of the optimal active set at each iteration and find how the active set needs to be changed in order to obtain the better optimal solution [135]. Interior-point methods apply a barrier function instead of the inequality constraints to prevent the solutions going into the infeasible region [135]. Active set method is beneficial from that the initial values can take the advantages from the solution from previous sample, which is known as warm start. However, interior-point method is difficult to achieve the warm start procedure and is widely applied in the larger-scale problems [138].

When the control allocation problem includes a non-quadratic cost function, a non-linear effector model or the constraint sets are not polyhedral, the control allocation problem cannot be easily solved by the above linear LP methods or QP methods. In [139], a numerical method similar to sequential quadratic programming (SQP) was proposed to solve this kind of problem by locally approximating the cost function by a quadratic cost function and linearised constraints. However, strong non-linear control allocation problem may result in

non-convex cost functions or constraints functions that may make the optimization get stuck in local minimums and severely degenerate the performance.

2) Applications of the control algorithms in the vehicle dynamics

a) Vehicle handling and stability control

(1) Vehicle yaw rate control

To improve the vehicle steering feel or handling performance, the studies on the yaw rate controller are widely focused.

The application of active steering system is the main trend of these studies, including some work on the active drive line and suspension. The active system can provide benefits on two regions: limited handling condition and normal driving condition. In the limit handling studies, the retention of stability under severe manoeuvres is the prime issue. For the normal driving studies, Millsap and Law concentrated on two important measures, the steering sensitivity at lateral acceleration and steering wheel torque gradient [140]. Steering sensitivity indicates how much the vehicle responds to the steer angle input. They proposed the Variable Ratio Electric Steering system (VRES) to overcome the compromise between the steering sensitivity and torque gradient over the speed range. However, this research work is based on quasi-steady-state measurements and the steering feel is also greatly influenced by the transient behaviour.

Feedforward and feedback control strategies were suggested for yaw rate control under steering manoeuvres. The feedforward controller can transiently increase the steering angle and reduce the time lag between the input and output response of the vehicle system. The feedback controller uses the simple vehicle model to generate the desired yaw rate and then the desired value is fed through a first-order lag to generate the demanded yaw rate. The feedback controller requires less steering control effort and shows good side-slip behaviour on icy surface. Furthermore, the additional steering angle can also be generated by the controller to assist the braking-based stability control system on the vehicle to improve the yaw rate response and stability under braking condition.

Kremer and Hackl from Bosch showed a good overview of Active Front Steering (AFS), where the additional front steering angle is actuated by a motor that drives the ring gear of a planetary gear connected in line with the steering column [141]. Ackermann et al. used an

additional positive feedback element from the yaw rate to steering angle, which can remove the yaw dynamics from driver's control. This system can successfully deal with the unexpected yaw disturbance like cross-wind and split-u surface, but the performance in severe lateral motion is questionable [142]. Ackermann also argued that the steering actuator bandwidth and saturation are the key limiting factors in achieving the desired yaw dynamics [142]. Segawa et al. extended some concepts for the feedforward and feedback yaw rate controller by introducing the Variable Gain Steering (VGS) ratio and D* strategy in [11]. VGS ratio was used in the feedforward controller to be scheduled with speed and the D* strategy was applied as the feedback controller. D* strategy suggested that the lateral acceleration and yaw-speed component of lateral acceleration had the separate feedback control gains. The experiment results in [11] showed that D* strategy could reduce the lag in the system and improve the path following on low friction surface. Kojo et al. described the practical implementation of VGS system in Toyota [143]. Simulation and field test data in [143] showed that there were different optical steering ratios for the disturbance rejection and course tracking. There are also some other studies that focus on how active steering control affects the vehicle handling, but these studies do not address the human factor issue [144].

In addition to the active steering control strategy, the feedforward-feedback yaw rate control can also utilise braking, driveline and suspension system. Matsumoto et al. [145] described the Brake Force Distribution (BFD) control on Nissan and the significant details on BWM's direct stability control system are also provided ([146] [147] [148] [149] [150]). Although there are significant advantages when using brake for yaw control, the vehicle longitudinal performance is compromised. Naito et al. presented the 4WD torque split mechanism [151] and Matsuno et al. suggested the Variable Torque Distribution (VTD) system for the yaw rate control to improve handling on dry roads and stability on slippery roads [12]. In addition, Motoyama et al. indicated that the left/right torque split showed the great potential for improving vehicle cornering performance [152]. Smakman investigated that the vertical wheel load could offer some benefits to the improvement of the yaw rate response [153].

The yaw rate control is achieved by the model reference feedback yaw rate controller, which attempts to push the vehicle non-linear behaviour into the linear bicycle behaviour. Active braking system offers the most power for generating corrective yaw moment, but has disadvantage over the longitudinal acceleration demand. Thus, the yaw rate control relies more on active steering control to improve the driver's subjective view of handling feel in the normal driving condition.

(2) Vehicle stability control

The vehicle side-slip angle is the critical control value for vehicle stability control. Early studies about side-slip angle are dominated by linear feedforward active rear-wheel steering (ARS) systems ([154] [155] [156] [157]). The feedforward value is obtained by calculating the 2 DOF bicycle model equations of zero side-slip angle at steady state. Many of these early studies examined the vehicle dynamics in the linear range of handling, but side-slip stability is more critical in the non-linear range. Shibahata et al. showed a non-linear analysis of steady-state performance of Direct Yaw-moment Control (DYC) systems (beta-method), which indicates the stability margin under different side-slip angles and steering angles [158]. This DYC algorithm decouples the roll motion from lateral motion, which includes the differential braking between left and right wheel, Roll Moment Distribution (RMD) and active rear wheel steering. Left and right differential braking can control the side-slip angle over a full range of vehicle motion, while RMD is only used for the large lateral acceleration more than 4 m/s^2. ARS is only effective at small side-slip angle. The steady-state beta-method assumes zero dynamics jump from one vehicle state to another and the beta-phase plane analysis is suggested by the researchers to increase the fidelity of the analysis [159]. In this study, the rate of side-slip angle is plotted against the side-slip angle, which shows much more information on the dynamic response, like side-slip angle damping and nature frequency. In addition, this plot can further used to ensure the side-slip behaviour stays in the control boundaries.

Some studies explored the effect of integrating several controllers for side-slip angle control. For instance, Smakman suggested that the braking intervention has the most important effect on the vehicle lateral dynamics, but it compromises the driving demands [153]. Wheel load control has the advantage of contributing little to the vehicle longitudinal dynamics, but the high moment required cannot be generated. Thus, Smakman suggested that the wheel load control was applied normally until the vehicle reached saturation and the brake intervention was applied. This research also suggested that the effect of wheel load variation was minimal when the lateral acceleration was greater than 0.3 g. Selby et al. and He et al. explored the integration of active braking/driving system with the AFS system to delay intervention in the longitudinal dynamics significantly [160] [161].

Motivated by the robust control of nonlinearities, mismodelling and parameter variations, Abe et al. ([13] [162] [163] [164]) and Furukawa and Abe [165] applied sliding mode control (SMC) to track the desired side-slip angle response.

(3) Integrated vehicle handling and stability control

Two main approaches are suggested for this problem: the control system with only one actuator and the system with two or more actuators. The controlling of two target values with only one actuator is implemented by H_{inf} control. Firstly, the vehicle yaw-sideslip response is shaped to first-order dynamics and then the side-slip angle is controlled by the conventional zero-sideslip law. A comprehensive theoretical study on this work about AFS is presented [166] [167].

The integrated yaw rate and side-slip angle control with more than one actuators is implemented by both linear and non-linear control strategy. Nagai et al. ([14] [168] [169]) presented the combined feed-forward and feedback control, and Kleine and Van Niekerk [170] used 4WS controller with both AFS and rear wheel steering to achieve the integrated control. Smakman used the heuristic integration strategy and involved the shift of authority between wheel-load control and brake control [153]. Selby, He and Cooper et al. applied the similar approach for braking-steering control, driveline-steering control and driveline-wheel-load control [160] [161] [171]. These combined controllers all showed better estimation performance than the combined stand-alone controllers.

However, most of above studies are based on traditional ICE vehicles, and the controller performance is constrained by the limitation of the actuators. For active steering control, the controlled steering angle is limited by the mechanical steering linkage, while the direct yaw moment control is constrained by the limited longitudinal tyre force difference between the left and right wheels. With the innovative technique of in-wheel steering motors and in-wheel driving motors, these limitations can be overcome, and recently there has been some research aiming to improve vehicle handling and stability. For example, Chen and Wang designed and evaluated electric differentials for over-actuated electric ground vehicles with in-wheel driving motors [172]. The energy-efficient control allocation (EECA) method was designed for the longitudinal speed tracking control of an electric vehicle with two pairs of in-wheel driving motors in [15], where three different EECA methods, i.e., adaptive-EECA, KKT-based EECA and rule-based EECA were presented. The adaptive-EECA takes into

consideration the power consumption of the individual in-wheel motor, but global optimization cannot be reached at every time step and only trends in the optimal direction. KKT-based EECA can obtain globally optimal torque distribution in real time and consume the least energy. The rule-based method uses a simple fixed ratio to dictate the torque distribution by *a priori* knowledge, and of the three methods, this consumed the most energy. In [173], a passive actuator fault-tolerant control was also applied to control the 4WID EV. These studies did comprehensive research into motion and power consumption control on EVs with in-wheel driving motors, but little research has been done on lateral vehicle motion and 4WIS vehicles. In [174] and [175], a vehicle lateral motion controller for 4WID and front wheel steering EVs was proposed and the controller made use of the combined active front wheel steering and direct yaw moment control through in-vehicle networks with real-time message priority scheduling. To realise the desired control target, an optimum torque allocation algorithm using the quadratic forms as the cost function was adopted in [174]. This algorithm can be solved as a QP problem with constraints. The first term of the cost function was the error between the demanded yaw moment and the actual yaw moment, while the second term of the cost function was a 'penalised term' used to adjust the longitudinal forces of the four wheels by taking into consideration of the tyre force margin. Demirci and Gokasan developed the adaptive stability control of a 4WIS-4WID EV, but the front wheels and the rear wheels had the same steering angle [9]. In Demirci and Gokasan's paper, according to the controlled yaw moment which was calculated by the sliding mode yaw moment observer in the upper level, the steering angle and driving torque of each wheel was distributed in the lower level by solving a non-linear optimization problem. The main problem of the above-mentioned methods is that they need to solve a very complex optimization problem. Ando and Fujimoto, instead, used a linear longitudinal and lateral tyre force distribution method for the direct yaw-moment controller, and the optimal value can be solved by the linear equation in every time step [176].

Researchers, especially from European countries, also consider the combined yaw rate and body side-slip angle control as a part of the vehicle global chassis control (GCC). Various approaches to GCC have been proposed but the main difficulty is to consider the possible combination of different actuator configurations. Some studies used a given combination of actuators, and the controllers were designed and calibrated for each single actuator configuration [177] [153] [178]. Some other studies explored the full synergetic potential of the available actuators. For example, in [179], each wheel was assumed to be individually

steered and driven, and this requires the allocation of tyre force within their friction limit. The allocation method included a feedforward and feedback flatness-based tracking controller which was used to determine the virtual control command, and an inverse static subsystem, which was used to convert the virtual control command into the actual control command. The inverse static subsystem required a simple tyre model so that it could be inverted analytically, but this model is not accurate enough to represent the actual vehicle motion. Similarly, a vehicle motion controller which was designed based on feedback linearization of a simple vehicle model was developed, and a control allocation-like method was used to distribute the generalised forces to the wheel forces in [180]. In addition, a model inversion-based feedforward optimal control method with direct allocation of the actuator commands was proposed with high-gain feedback in [181]. The major improvement of these studies compared with [179] is the introduction of the control allocation method because the desired control targets can be achieved by the actual actuators with different solutions. In [181], the allocation problem was proposed as an optimization problem with linear constraints. In [180], the allocation problem was solved by using a sampled constrained least-square linearized optimization method. Bajcina and Kouhi [182] also suggested an innovative redundant feedforward control scheme for the GCC systems using a single–wheel actuated powertrain with independent steering and driving/braking. Based on a simple iterative structure with a Lagrange-multiplier, the analytic expression for the optimal allocation of longitudinal and lateral tyre friction force was obtained. This study was further extended into a fault-tolerant distributed feedback GCC system in [183].

Over the past several decades, various automotive companies have also carried out intensive research into the GCC or the integrated vehicle dynamics control (IVDC). The years between the 1980s and the 1990s was the beginning stage of IVDC. In 1987, Toyota presented its concept car, the FXV-II, which integrated air suspension, 4WS, engine control, gearbox ratio control, 4WD and an anti-lock braking system (ABS) [184]. In 1991, Toyota also developed its Sorarer model, which integrated 4WS, ABS and a traction control system (TCS) [185]. Since the mid-1990s when the electronic stability program (ESP) was developed, there has been rapid development of IVDC. Continental proposed its original differential braking and engine interventions in the ESP, and the active front steering was introduced in the second generation of ESP [186]. Bosch developed VDC, which is a new active safety system for road vehicles to control dynamic vehicle motion in emergency situations. This system regulates the engine torque and wheel brake pressure using traction control components [187].

Lexus 64, developed by Toyota, used integrated vehicle dynamics management to manage the ABS, traction control, active braking intervention and steering system at the same time. Recently, automotive suppliers such as Delphi, Bosch, Continental and TRW have extended integrated chassis control to whole vehicle control, and have covered all the subsystems of the controller in a single frame, including the driving assist system (cruise control), the active safety system (electronic stability control) and the passive safety system (supplemental restraint system) [188]. Conti Automotive also carried out some research on the integrated motion control of EVs [189].

b) *Vehicle energy-efficient control*

For the 4WIS-4WID electric vehicles, multiple control targets can be achieved due to the redundant control actuators utilised. In addition to the handling and stability control targets which have been in the focus in the above sections, energy efficiency is also a highly important control target due to the limited energy on-board in EVs. Much research has been done to improve the efficiency from the point of view of motor design [190] [191], motor control algorithms [192] [193] and power electronics [194] [195]. Wang et al. proposed a longitudinal motion controller to improve the energy efficiency of the four in-wheel brushless DC (BLDC) motors by allocating different driving torques among the four motors in two different operation modes: the driving mode and the braking mode, with different energy-efficient formulations defined as [196]:

$$J = \min \quad \sum_{i=fl,fr,rl,rr} \frac{\omega_i T_{di}}{\eta_i} \qquad \text{in driving mode} \quad \text{(a)}$$

$$J = \max \quad \sum_{i=fl,fr,rl,rr} \omega_i T_{bi}\, \eta_i \qquad \text{in braking mode} \quad \text{(b)}$$

(23)

where J is the optimisation cost function of the total power output of the battery in the driving mode and the total input power to the inverter in the braking mode. T_i is the driving or braking torque of each wheel, and $i = fl, fr, rl, rr$, which represents the front left, front right, rear left and rear right wheel, respectively. ω_i and η_i are the wheel angular velocity and energy-efficient coefficient of each wheel.

Based on the similar energy-efficient formulation in (23), Gu et al. also proposed the energy-efficient control of the individual wheel driving motor based on the longitudinal motion, and

proved that equal distribution of all the driving torques can achieve optimal energy efficiency [197]. However, the in-wheel motor of a permanent magnetic synchronous motor (PMSM) was selected to be used in this study and the motor efficiency map was different from the BLDC motor.

The above studies mainly focused on the control allocation of the vehicle during longitudinal motion, but the controller design will be more complex during combined longitudinal and lateral motion. This is because vehicle handling and stability are also critical issues to be considered in addition to the energy efficiency. As the redundant actuators can be used in the control system, the control allocation of the EV can achieve multiple control targets such as handling control, stability control and energy-efficient control.

In [198], the desired vehicle understeer characteristic, which was expressed as a function of the dynamic steering wheel angle δ and lateral acceleration a_y, was analysed and optimised off-line to achieve energy-efficient control. In addition, four other objective functions for the control allocation were compared. These included: the minimisation of the total power output, the minimisation of the standard deviation of individual tyre longitudinal slip ratio with respect to the average slip, the minimisation of the total longitudinal slip power loss and the minimisation of the average combined tyre force coefficient. In [199], it was also suggested that there was a variety of cost functions for control allocation optimisation which related to the tyre slip, the actuator effort and power loss when the vehicle cornering motion was considered. An off-line procedure was first applied to minimise the total motor power loss in [199]. Then a simple on-line method was used to approximate the results of the off-line optimisation into the on-line torque allocation function. Three different motor types were demonstrated to achieve the reduction of the power loss by using an off-line procedure in [200]. This method, however, cannot be directly applied to on-line applications in real-time because of the high computational cost. Chen and Wang [201] considered the vehicle's longitudinal dynamics, lateral dynamics and yaw dynamics. In their study, the planar motion controller had a two-layer structure. In the upper layer, the virtual control law is obtained by a dynamic SMC in order to achieve robust control of the vehicle stability. In the lower level controller, the optimisation targets of the energy efficiency and virtual control law in the upper level can be achieved by adaptive control, but this whole control system is based on the linear vehicle planer motion model, which is usually applicable in the moderate velocity and small steering angle situation, and the non-linear tyre characteristic is neglected.

c) *Vehicle fault-tolerant control*

Compared with conventional vehicles, the probability of an in-wheel motor fault is a crucial issue due to the system complexity and large number of control actuators. The in-wheel motor fault may be caused by mechanical problems, over-heating of the motors or a fault associated with the motor drivers [202]. In addition, uneven road conditions can cause the individual wheel to lose contact with the road, thus losing friction force and this can cause a fault in an individual wheel. The fault of the in-wheel motor compromises the vehicle's dynamic control performance when conventional controllers are applied, so the design of the fault-tolerant controllers for EVs is especially important.

Previously, to improve the robustness of the vehicle traction control, the model following control (MFC) approach has been proposed. This only required the input information of vehicle torque and wheel rotation speed [203] [204] [205]. Then the maximum transmissible torque estimation (MTTE) approach was developed to further improve the robust control performance of MFC [206]. Recently, a fault-tolerant control method based on MTTE has been suggested using a proportional-integral (PI) type disturbance observer [207], but this method only concerned the uncertainties of the mathematical model and sensor faults and did not focus on the failure of one specific wheel.

Driving actuator failure could be handled using the well-known H_∞ robust control method, but the dynamic performance of the vehicle under healthy conditions was also compromised [208]. To overcome this disadvantage, various active fault-tolerant controllers (AFTC) have been proposed based on the application of a fault detection and isolation (FDI) module [209] [210]. According to the fault severity, different control structures and control parameters are selected after the fault is detected. In [211], two control structures in the AFTC approach were proposed to achieve the fault-tolerant control of an induction-motor affected by a speed-sensor fault. The first control structure was the PI controller for the healthy mode and the second controller was the H_∞ robust controller for the faulty mode.

This means, however, that specific controller strategies can be implemented only after the fault has been detected and therefore fault diagnosis is important for fault-tolerant control. In the literature, a number of fault diagnosis control strategies for conventional ground vehicles have been suggested, but these control methods are not for EVs [212] [213] [214]. Several fault diagnosis methods for EVs have been proposed [215] [216], but motor failures are hard

to diagnose using only the current and voltage sensors in the in-wheel motor. In [202] and [217], the faulty wheel could be identified by estimating the individual motor control gain without the knowledge of the specific tyre-road friction coefficient.

Apart from the fault of a sensor or a fault caused by the disturbance and model uncertainty, much study has been done into the failure of the specific in-wheel motor. A control method has been proposed in which the faulty wheel and its opposite side wheel were isolated but this degrades the performance and stability of the vehicle [218]. Wenbo et al. proposed a control strategy to enhance the performance of the vehicle in a small turn or at low speed, but conditions where the vehicle is moving in a sharp turn or at high speed were not discussed [219]. Xin et al. classified the control strategy into the failure-driving mode, which guaranteed the vehicle continued moving and the failure-stopping mode, which stopped the vehicle [220]. In [202], a SMC was implemented as the high level controller to achieve the desired longitudinal velocity, lateral velocity and yaw rate, then the four driving torques of each wheel could be generated to achieve these values. An adaptive-control-based passive fault-tolerant controller was also designed to maintain vehicle stability and track the desired vehicle motion [217]. Wang and Wang also introduced an improved passive fault-tolerant controller which grouped the actuators having similar effects on the control of the system into one sub-system [173]. This control method was promising due to the direct distribution of the high-level control targets to each of the group of actuators in the lower level.

The adaptive control method, however, has the problem of high computational cost compared with the SMC method. For this reason many see SMC control in fault-tolerant control of 4WID vehicles as quite promising. In order to achieve better control performance, however, SMC needs large control gains and this will cause a large chattering effect. Alipour et al. suggested the proportional-integral sliding mode control (PISMC) strategy to improve the fault-tolerant control performance of the traditional SMC so that a smaller control gain could be selected and the chattering effect could be reduced [221]. Although the SMC control gain can be reduced significantly, however, the improvement of the actual dynamics control performance over the traditional SMC is not assured. Song et al. applied terminal sliding mode control (TSMC) to achieve the finite-time convergence and quick responsiveness on the terminal sliding manifold [222]. If the SMC method is applied in a 4WID vehicle to achieve multiple control targets, the control effort is allocated into the driving actuators of four wheels. One big problem is the coupling effect between different control targets and grouping the driving actuators is one of the solutions to solve this problem. For instance, the

two front wheels can be considered as one group in order to control the body side-slip angle only, while the two rear wheels can also be regarded as one group in order to achieve the desired yaw rate. In this way, the control actuators related to the body side-slip angle will not have a strong effect on the control performance of the yaw rate. Except for [221] however, it appears that few researchers have examined the grouping of the driving actuators. Actuators having a similar control effect were grouped in [221], but this was not related to the coupling effect between different control targets.

3) Autonomous vehicle control

In recent years, intensive research has been done into autonomous vehicles. The ultimate goal of automated driving is to reduce accidents caused by human error and improve safety. In addition, full automation can significantly improve the road capacity and diminish air pollution because of a more efficient use of fuel [223]. Autonomous vehicles can perform different automated driving manoeuvres such as lane following, lane changing, merging, splitting, platooning, and overtaking and these have been extensively studied. In 1997, California's Partners for Advanced Transit Highways (PATH) team developed the DEMO'97 fully automated control vehicles, in order to test the platooning, lane keeping, lane changing, platoon split and merge manoeuvres [224]. Recently, autonomous vehicles including passenger vehicles [225] [226] and trucks [227] have been demonstrated in the Grand Cooperative Driving Challenge 2011 (GCDC 2011). Platooning demonstrations proved the technical feasibility of implementing such a technique on the existing roads. Some EU-funded projects, such as Cybercars [228], HAVEit [229] and ECOVISION [230], also focused on automated driving difficulties such as adaptive cruise control, lane keeping, and lane changing.

Until now, the automated steering angle control was focused on autonomous vehicles. According to [231], there are two ways to design the steering controllers: imitating human drivers and using the dynamics model of the car. The first case does not require detailed knowledge of vehicle dynamics because the algorithm mimicking human driver behaviour is the key to control. The vehicle dynamics method, however, requires detailed knowledge of the dynamics of the car. In [231], the automatic-steering control architecture, based on a combination of fuzzy logic and proportional-integral-derivative (PID) controller, was

proposed to control the vehicle motion like a human driver. This control method only included the position control of the steering wheel, while the control of the steering wheel's angular velocity was also considered in [232].

The automated steering, however, can only improve the vehicle's lateral motion. In recent years, autonomous vehicles have been designed to follow the longitudinal-lateral trajectories that optimize safety, speed, driver comfort, fuel consumption and obedience to the traffic rules. In [233], the trajectory planning for the autonomous vehicle was done using a two-step algorithm. The first step defined the feasible manoeuvres with respect to the environment. The output of this step was a target group of manoeuvres in the longitudinal direction (acceleration and decelerating) and lateral direction (lane changes). In the second step, these possible trajectories are evaluated in more detail and the trajectories are optimised. The output of this step is the recommended vehicle state in the desired trajectory, like position, heading, speed and acceleration.

The vehicle trajectory can be optimised in various scenarios by considering the multiple optimization targets and the environment. Overtaking is one of the most complex manoeuvres for road vehicles. It is a composition of two consecutive manoeuvres: lane change followed by a specific path parallel to the overtaken vehicle, and again, a lane change to the position in front of the overtaken vehicle. Petrov and Nashashibi suggested a mathematical model and adaptive controller to control the autonomous vehicle in this scenario [223]. This mathematical model was composed of a general kinematic model for the overtaking vehicle and the relative intervehicle kinematics model during the overtaking manoeuvre. Lin et al. also suggested an active collision avoidance system (CAS) for autonomous vehicles in the vehicle overtaking scenario [234]. In this study, the vehicle trajectory error dynamics model was included in the CAS. The above studies only applied the vehicle kinematic model or the limited dynamics model to describe the vehicle motion in the overtaking scenario. This may be suitable at low speed and in-doors but it is not suitable for the vehicle in the high speed out-door condition. Thus, the comprehensive vehicle dynamics description and control of autonomous vehicles are required in the real road condition.

For traditional ICE vehicles, only one steering control input and one driving input are used to achieve multiple control targets, and this limits control performance. With the development of the innovative technology of EVs with in-wheel steering and driving motors, 4WIS and 4WID can be achieved. In this way, more control inputs are available for the longitudinal and

lateral motion control and there are redundant control inputs in the control system. These redundant control inputs can be utilised in the autonomous control to achieve longitudinal dynamics control, lateral dynamics control and yaw dynamics control in addition to the kinematic motion control.

For the autonomous control of the robot such as the holonomic omni-directional robot, the longitudinal position, lateral position and yaw angle can be independently controlled and the desired trajectory can be easily tracked [235]. However, when the on-road EV is considered, even the 4WIS-4WID vehicle has strong coupling effect between the longitudinal motion, lateral motion and yaw motion, which is a big challenge for the trajectory tracking of the EV. Thus, the automation control of steering angle and driving torque of the vehicle should be undertaken separately to alleviate the strong coupling effect between them. For instance, the driving torque controller is used to control the states of longitudinal motion and yaw motion such as longitudinal position and yaw rate, while the steering angle controller is utilised to control the vehicle lateral motion.

In addition to the above direct trajectory tracking method, the potential field method is also quite attracting in the research area of the autonomous steering control. The steering control method based on the potential fields can form a steering corridor with a desired tracking error tolerance and the vehicle can be steered smoothly with smaller control effort compared with the direct trajectory tracking method. The total potential normally includes the attractive potential to reach the desired position and repulsive potential to avoid the obstacle. Jaradat et al. utilised the fuzzy model and TSK model to develop the total attractive and repulsive potential force applied on the autonomous mobile robot [236]. Khatib presented a unique real-time obstacle avoidance approach for the mobile robot based on the artificial potential field method [237]. In addition, Pan et al. used the fuzzy controller to improve the artificial potential field method and safeguarded the reliability of the path planning and path smoothness [238]. Ge and Cui proposed the dynamic motion planning method for the mobile robot where the target and obstacle are moving by using the potential field method [235].

The potential field method is advantageous to control the vehicle to follow a more smooth trajectory and to decrease the total control effect compared with the strictly trajectory following method. Thus, the potential field method is quite attractive for the autonomous control of the on-road EV with limited mobility and high velocity. The above papers about the potential field method, however, are mainly focused on the mobile robot and the virtual

longitudinal and lateral control forces are required to achieve the control trajectory. In the area of the on-road vehicle, the longitudinal motion, lateral motion and yaw motion are highly coupled and only tracking the virtue forces can hardly achieve the desired trajectory.

One possible way to control the trajectory of the on-road vehicle is to achieve the desired yaw angle instead of the tracking of the virtual forces or the desired position. Park and Gerdes proposed the trajectory control method by tracking the desired yaw angle based on the on-road vehicle dynamics model. Then, according to the desired vehicle motion, the actual actuators are allocated by equally using the friction capability of each tyre [239]. However, the yaw angle depends on time and the desired road trajectory and road boundary depend on positions. In order to achieve the desired trajectory by using the yaw angle control, the time-dependent real-time vehicle states should be transferred into the position-dependent desired trajectory and road boundary.

4. Summary

This section extensively focuses on the literature review about the vehicle state estimation, 4WIS-4WID vehicle dynamics modelling and the various controller design methods. In the current literature, many studies have addressed on the state estimation and control of the traditional two-wheel vehicle, but the state estimation and control allocation method, especially the over-actuated control allocation method, of 4WIS-4WID electric vehicle are less focused. Based on this background information, this thesis proposes the estimation methods for vehicle states, the 4WIS-4WID electric vehicle modelling and various control strategies in the following sections.

III. Vehicle state estimation method

Vehicle state estimations are the important preliminary studies for the modelling and control of the 4WIS-4WID EVs with in-wheel motor, since these estimations can provide important vehicle state values which are hard to measure in real situation. In this section, the studies on the estimation of the lateral side-slip angle, the estimation of the longitudinal velocity and tyre-road friction coefficient, and the estimation of the vehicle mass and road slope are extensively focused.

1. Estimation of lateral side-slip angle

Based on the vehicle dynamics model in [100], the lateral side-slip angle estimator is proposed. The proposed side-slip angle estimator mainly includes two parts: the total aligning moment estimator and the side-slip angle estimator as shown in Figure III-1.

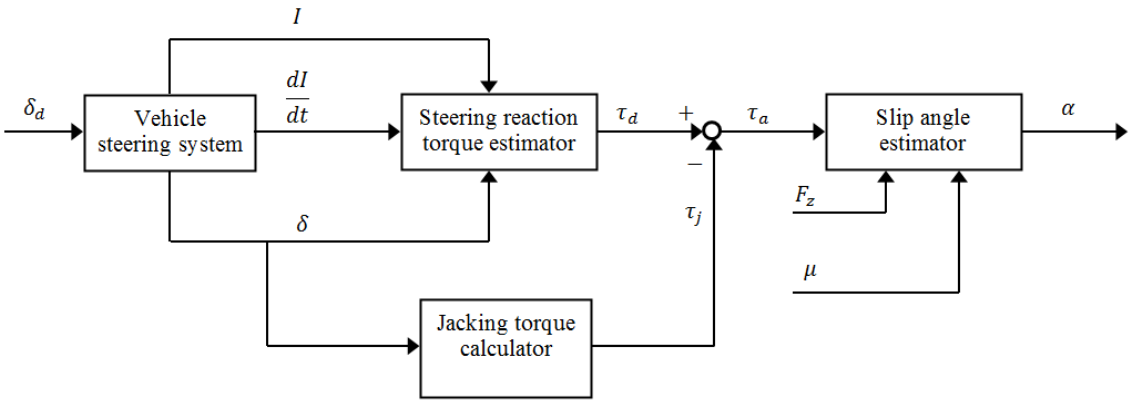

Figure III-1 The working process of side-slip angle estimator

First, the driver suggests the desired steering angle to the vehicle steering system according to the intended manoeuvre, and then the steering system will track the desired steering angle by appropriately controlling the current i in the steering motor, which is proportional to the required steering motor torque τ_{act}. As the steering motor current i and steering angle θ can be measured, the state space model in equation (26) is used to estimate the steering reaction

torque τ_d of each wheel. Then the total alignment torque τ_a is obtained by subtracting the jacking torque τ_j from τ_d. With the inputs of the total aligning moment τ_a, vertical load F_z and tyre-road friction coefficient μ, the side slip angle estimator (equation (32)) is used to estimate the side-slip angle α.

The proposed side-slip angle estimator only needs the measurement inputs of steering current and steering angle, which are all easy to obtain from the in-wheel steering motors. The only requirement of this proposed side-slip angle estimator is that the tyre-road friction coefficient and vertical load need to be available in advance. Friction coefficient can be determined by the vehicle longitudinal friction estimation method proposed in section 3.2 in real time and the vertical load can be considered as the static load when the vehicle load transfer effect is neglected.

1) Total aligning moment estimator

The total aligning moment is an important value to determine the wheel side-slip angle. However, it is hard to be directly measured, and therefore the total aligning moment estimator for each individual wheel is proposed in this paper.

The following relationships between steering reaction torque τ_d and steering motor current i are assumed:

$$\tau_d = -\tau_{act} = -k_m i \quad \rightarrow \quad \dot{\tau}_d = -\dot{\tau}_{act} = -k_m \dot{i} \tag{24}$$

Note that equation (24) is just assumed relationship between steering motor torque τ_{act} and steering reaction torque τ_d, and will be used in the estimation of the total aligning moment.

According to steering model (8) and equation (24), the following state-space equation is built:

$$\dot{x} = A_{cts} x + B_{cts} I \tag{25}$$

Where $x = \begin{bmatrix} \delta \\ \dot{\delta} \\ \tau_d \end{bmatrix}$, $A_{cts} = \begin{bmatrix} 0 & 1 & 0 \\ 0 & -\frac{c_s}{I_s} & \frac{1}{I_s} \\ 0 & 0 & 0 \end{bmatrix}$, $B = \begin{bmatrix} 0 & 0 \\ \frac{k_m}{I_s} & 0 \\ 0 & k_m \end{bmatrix}$, $I = \begin{bmatrix} i \\ \dot{i} \end{bmatrix}$

An observer for estimating the steering reaction torque τ_d is then proposed as:

$$\dot{\hat{x}} = A_{cts}\hat{x} + B_{cts}I + L\tilde{x}$$

$$= \hat{A}_{cts}\hat{x} + \hat{B}_{cts}\hat{I}$$

(26)

Where $\hat{x} = \begin{bmatrix} \hat{\delta} \\ \dot{\hat{\delta}} \\ \hat{\tau}_d \end{bmatrix}$, $\tilde{x} = \begin{bmatrix} \tilde{\delta} \\ \dot{\tilde{\delta}} \\ \tilde{\tau}_d \end{bmatrix}$, $\tilde{\delta} = \delta - \hat{\delta}$. The observer gain is selected $L = \begin{bmatrix} l_1 & 0 & 0 \\ 0 & 0 & 0 \\ l_2 & 0 & 0 \end{bmatrix}$ so that only the steering angle error $\tilde{\delta}$ is used to improve the estimation performance of steering angle and steering reaction torque.

$$\hat{A}_{cts} = \begin{bmatrix} -l_1 & 1 & 0 \\ 0 & -\frac{c_s}{I_s} & \frac{1}{I_s} \\ -l_2 & 0 & 0 \end{bmatrix}, \hat{B}_{cts} = \begin{bmatrix} 0 & 0 & l_1 \\ \frac{k_m}{I_s} & 0 & 0 \\ 0 & k_m & l_2 \end{bmatrix}, \hat{I} = \begin{bmatrix} i \\ \dot{i} \\ \delta \end{bmatrix}$$

The output of the estimator is:

$$\hat{y} = C\hat{x}$$

$$= \begin{bmatrix} 1 & 0 & 0 \\ 0 & 1 & 0 \\ 0 & 0 & 1 \end{bmatrix} \begin{bmatrix} \hat{\delta} \\ \dot{\hat{\delta}} \\ \hat{\tau}_d \end{bmatrix}$$

(27)

It can be seen that in this observer, the inputs are measured steering motor current, the derivative of the steering motor current and measured steering angle, which are all available for the steer-by-wire vehicle in practice. The outputs are estimated steering angle, the derivative of the estimated steering angle and estimated steering reaction torque τ_d. The matrix C is selected as the full rank so that all these three output values can be obtained and successfully estimated. Note that $\dot{\tilde{\delta}}$ and $\tilde{\tau}_d$ do not affect the estimation because they are multiplied by 0, and therefore, are neglected finally. The observer gains l_1, l_2 can be chosen by the pole placement method based on the observer characteristic equation of:

$$det[sI - (A_{cts} - LC)]$$

$$= det\left\{ \begin{bmatrix} s & 0 & 0 \\ 0 & s & 0 \\ 0 & 0 & s \end{bmatrix} - \left(\begin{bmatrix} 0 & 1 & 0 \\ 0 & -\frac{c_s}{I_s} & \frac{1}{I_s} \\ 0 & 0 & 0 \end{bmatrix} - \begin{bmatrix} l_1 & 0 & 0 \\ 0 & 0 & 0 \\ l_2 & 0 & 0 \end{bmatrix} \begin{bmatrix} 1 & 0 & 0 \\ 0 & 1 & 0 \\ 0 & 0 & 1 \end{bmatrix} \right) \right\}$$

(28)

To make one of the roots to be far from the zero in the negative direction, $s = -35$ is defined. We can also select $\xi = 0.8$ and $\omega_n = 10$ to make sure the stability of the system, so $s^2 + 16s + 100$ is defined. Therefore:

$$det[sI - (A_{cts} - LC)] = (s + 35)(s^2 + 16s + 100) = 0$$

(29)

After solving equation (29), the observer gains are obtained as: $l_1 = 29$, $l_2 = 14000$.

The total alignment moment τ_a can be calculated by subtracting jacking torque τ_j from estimated steering reaction torque τ_d:

$$\tau_a = \hat{\tau}_d - \tau_j = \hat{\tau}_d - c_1\delta^2 + c_2\delta + c_3$$

(30)

2) Side-slip angle estimation

When the total alignment moment is estimated, equation (9) can be used to obtain the relationship between the total alignment moment τ_a and the side-slip angle α.

t_p is determined in equation (10). The lateral tyre force F_y can be determined by the tyre model. Dugoff tyre model can present the effect of the longitudinal force on the lateral tyre force, but the inputs of vehicle chassis velocity and longitudinal slip ratio are required. Fiala's tyre model has less parameters and measured inputs to be considered, which is considered here to describe the lateral tyre force [101]:

$$F_y = -C_\alpha \tan\hat{\alpha} + \frac{C_\alpha^2}{3}|\tan\hat{\alpha}|\tan\hat{\alpha}\, I_f - \frac{C_\alpha^3}{27}\tan^3\hat{\alpha}\, I_f^2$$

(31)

According to equation (10), α_{sl} is also quite large, which is 34.2 degree when $\mu = 0.9$, $F_z = 7550$ N and cornering stiffness $C_\alpha = 30000$. Thus, the condition that the tyre has lost the lateral grip can be neglected and the slip angle can be approximated by the following equation according to equations (10) and (31):

$$\tau_a = -\left(t_m + t_{p0} - \frac{t_{p0}C_\alpha}{3}|\tan\hat{\alpha}|I_f\right)\left(-C_\alpha \tan\hat{\alpha} + \frac{C_\alpha^2}{3}|\tan\hat{\alpha}|\tan\hat{\alpha}\, I_f - \frac{C_\alpha^3}{27}\tan^3\hat{\alpha}\, I_f^2\right)$$

(32)

This side-slip angle estimator only needs the input value of total alignment moment, which is estimated in section 3.1.1. The other vehicle states, like the vehicle chassis velocity and yaw rate, are not required.

It can be seen from Figure III-2 that when the side-slip angle is within the range (-0.35, 0.2) rad, the aligning moment is monotonically corresponded to the side-slip angle, which means the side-slip angle can be solely solved by equation (32). However, if the side-slip angle is not within (-0.35, 0.2) rad, the aligning moment will correspond to multiple side-slip angles, which suggests that equation (32) cannot be used to solve the side-slip angle.

Therefore, this side-slip angle estimator can only work well when the side-slip angle is within (-0.35, 0.2) rad. Nevertheless, this range is sufficient to cover most of the required vehicle manoeuvres in practice.

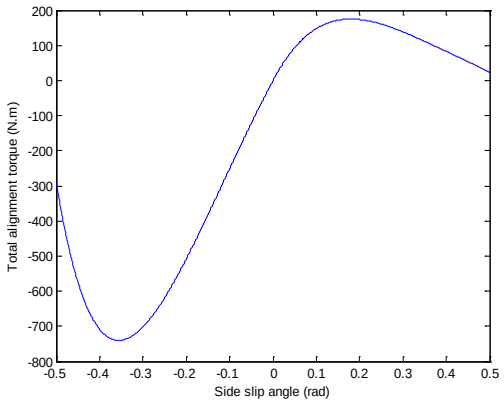

Figure III-2 Relationship between side slip angle and total aligning moment

3) Simulation results

In this section, the side-slip angle estimation performance is tested with the input steering current and steering angle. The simulation parameters are shown in Table III-1. It is noted that these fundamental vehicle parameters would be used throughout the whole thesis and will not be shown again in the following tables.

Table III-1 Simulation parameters in the side-slip angle estimator [100]

m	Mass	1298.9 kg
l_f	Distance of c.g. from the front axle	1 m
l_r	Distance of c.g. from the rear axle	1.454 m
b_f	Front track width	1.436 m
b_r	Rear track width	1.436 m
C_s	Longitudinal stiffness of the tyre	50000 N/unit slip
I_z	Vehicle moment of inertial about yaw axle	1627 kgm^2
R_ω	Wheel radius	0.35 m
I_ω	Wheel moment of inertial	2.1 kgm^2
l_1	Observer gain	29
l_2	Observer gain	14000
μ	Friction coefficient	0.9
ε_r	Road adhesion reduction factor	0.015 s/m
C_α	Cornering stiffness of the tyre	30000 N/unit slip
J_{eff}	Inertial coefficient	4
b_{eff}	Damping coefficient	88
k_m	Armature constant	0.053
t_m	Mechanical trail	0.028 m
t_{p0}	Pneumatic trail	0.05 m

Firstly, the test vehicle is moving with the simple J turn with the steering angle of 6 degree for the traditional front wheel steering vehicle. For the 4WIS-4WID vehicle in this research, the turn radius is 23.43 m to generate the same steering angle as the front wheel steering vehicle, and the steering angle of each wheel is 2.52 degree for front left wheel, 2.372 degree for front right wheel, -3.66 degree for rear left wheel and -3.44 degree for rear right wheel. In all the simulations, the initial velocity of the vehicle is 5 m/s and the road friction coefficient is assumed as 0.9. The estimated side-slip angles are shown in Figure III-3. For comparison, the estimation results obtained by another two existing methods based on traditional front wheel steering vehicle: Hsu's method [52] [51] and EKF method [78] [20] [21], are also presented. Only simulation results of front left and rear left tyre are shown, because when the steering angle is small the difference between left and right tyre side-slip angle can be neglected.

As the initial velocity is relatively slow in the first simulation, now the velocity is increased to 10 m/s in the second set of simulation and the simulation results are shown in Figure III-4. We can clearly see the proposed method shows good estimation performance.

The traditional side-slip angle estimation methods like Hsu's method and EKF method rely on the measurement vehicle states like acceleration, velocity and yaw rate. The accuracy of these measured values is affected by the system noise and environment disturbance. The new proposed estimation method needs the measured inputs of steering angle and steering current, which also have the measurement noise for the steering current and steering angle. Therefore, in the third case, Figure III-5 shows the slip angle estimation results when measurement noise is considered. For the traditional methods, the lateral acceleration measurement noise is considered (random noise with variance of 0.01). For the new proposed method, the measurement noise of steering current is considered (random noise with variance of 0.01). The results show that the proposed method is robust to the measurement noise.

In the above conducted simulations, the traction or brake torque is assumed to be zero. However, the vehicle is under the combined steering and braking motion at the beginning of turning, while the vehicle is turning and accelerating at the end of turning. Now the combined traction and steering motion is simulated here to further test the estimation performance of these side-slip angle estimation methods. The traction torque is applied from 0s to 20s (25 N.m) on all the four wheels and the estimated side-slip angle is shown in Figure III-6 in this case.

When the extremely large steering angle is applied on the vehicle, the estimated side-slip angle is not accurate due to the non-linear tyre characteristic caused by large steering angle. However, for the omni-directional vehicle, each wheel can be independently steered to have smaller side-slip angle and better estimation performance. In Figure III-7, front wheel steering angle of 1 rad (57.3degree) is applied on the traditional front wheel steering vehicle. This means that the turn radius of vehicle is approximate 2.454 m for the omni-directional vehicle. According to [7], the steering angles of the four wheels of omni-directional vehicle are 29.94 degree for the front left wheel, 17.5 degree for the front right wheel, -39.95 degree for the rear left wheel and -24.63 degree for the rear right wheel. In this simulation, the steering angle is large and consequently the difference of the left and right tyre slip angle is also large. Thus all the side-slip angles of the four wheels have been compared here.

According to Figure III-7, the proposed estimator has better estimation performance compared with the existing methods when the large steering angle is applied. This scenario is like that the vehicle is turning in the narrowed space in traffic congestion in big city. The traditional two wheel vehicle model cannot successfully estimate the side-slip angle, while the 4WIS vehicle model can successfully get the results.

To show the estimation results more clearly, the root mean square error obtained from Figure III-3-Figure III-7 are summarized in Table III-2. According to Table III-2, it is also proved that the proposed side-slip angle estimator has better estimation performance than the existing estimation methods in all the simulations.

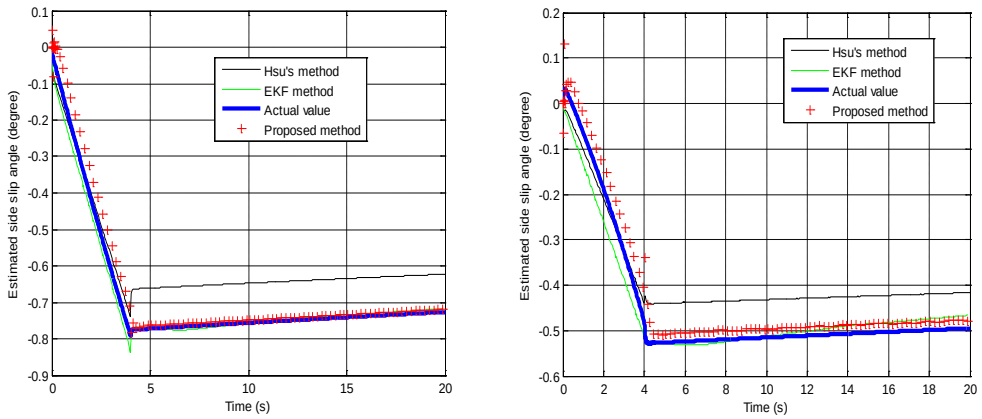

(a) (b)

Figure III-3 Comparison of the estimated side slip angle with the actual value in the simple turning condition (a) front left wheel (b) rear left wheel

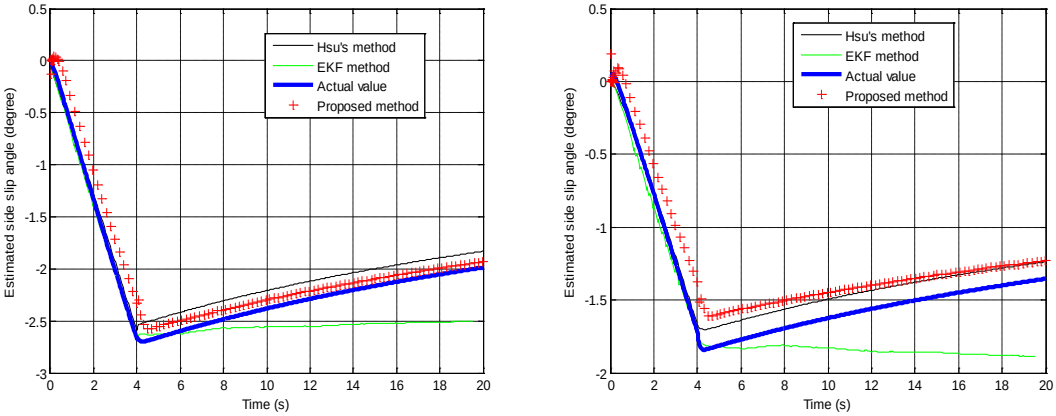

(a) (b)

Figure III-4 Comparison of the estimated side slip angle with the actual value in the simple turning condition when velocity is increased (a) front left wheel (b) rear left wheel

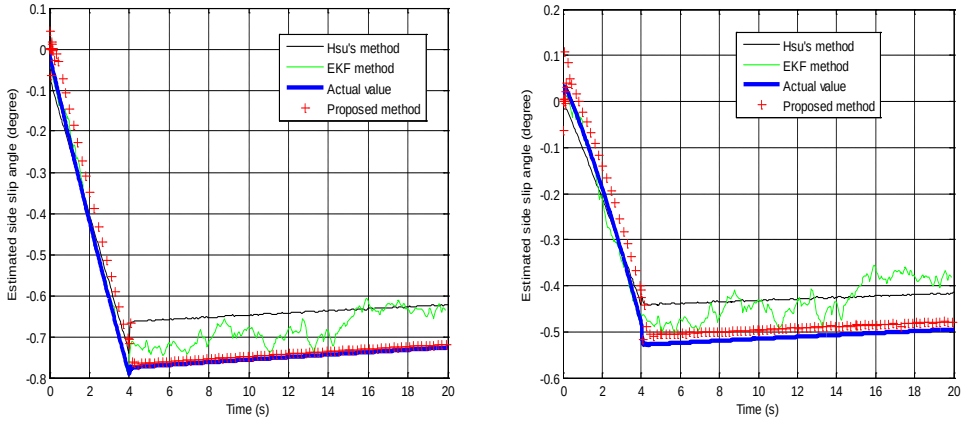

(a) (b)

Figure III-5 Comparison of the estimated side slip angle with the actual value in the simple turning condition when measurement noise is considered (top figure) front left wheel (bottom figure) rear left wheel

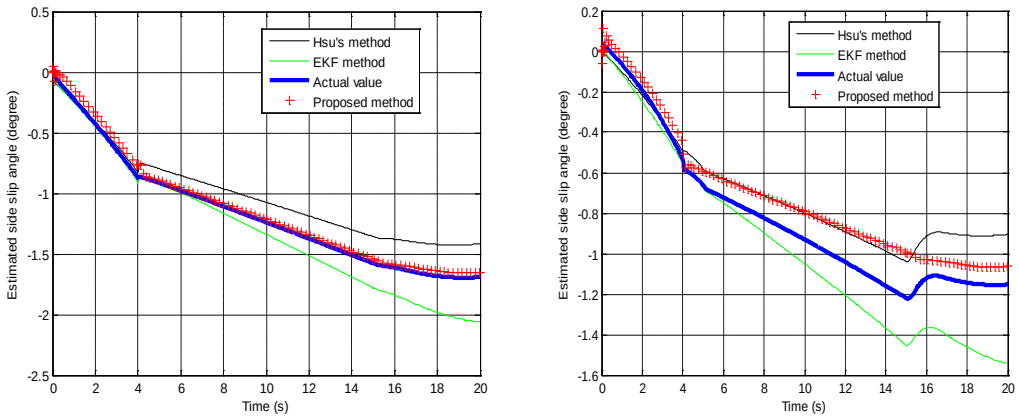

(a) (b)

Figure III-6 Comparison of the estimated side slip angle with the actual value (a) front left wheel (b) rear left wheel when combined steering and traction motion is considered

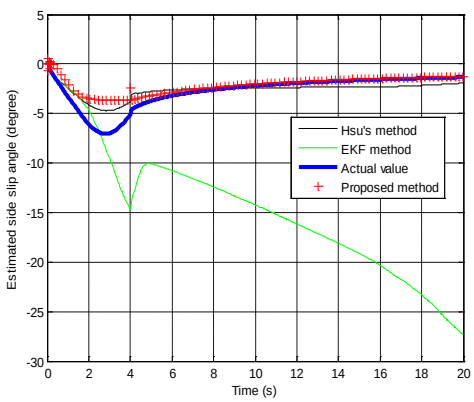

(a)

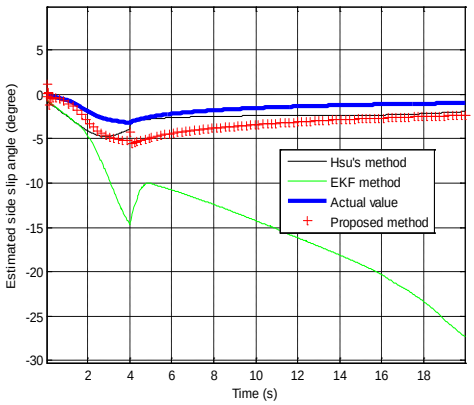

(b)

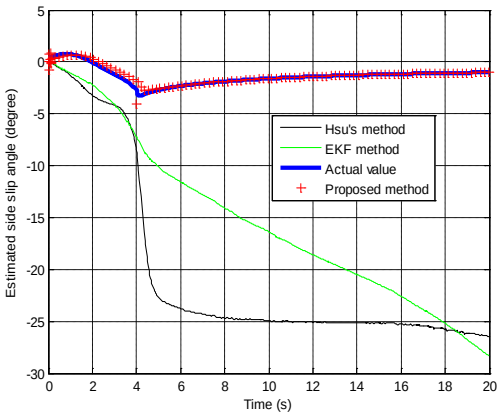

(c)

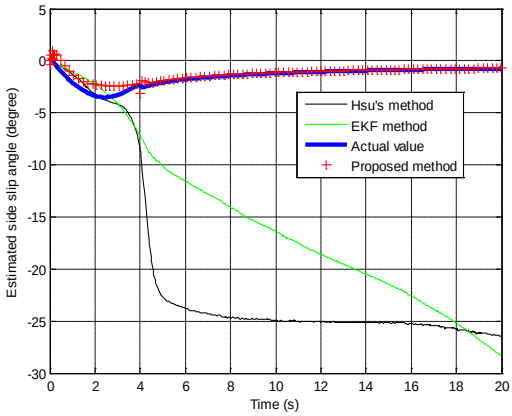

(d)

Figure III-7 Comparison of the estimated side slip angle with the actual value when the large steering angle is applied (a) front left wheel (b) front right wheel (c) rear left wheel (d) rear right wheel

Table III-2 The root mean square (RMS) error of the proposed estimation method and two existing estimation methods (unit: degree)

Simulation 1: Simple turning motion			
	Hsu's method	EKF method	Proposed method
Front wheel	0.0745	0.0224	0.0374
Rear wheel	0.063	0.0129	0.0347
Simulation 2: Simple turning motion with increased velocity			
Front wheel	0.0802	0.3495	0.0974
Rear wheel	0.0745	0.338	0.0802
Simulation 3: Considering the measured noise			
Front wheel	0.0745	0.0483	0.0374
Rear wheel	0.063	0.063	0.0347
Simulation 4: Combined steering and traction motion			
Front wheel	0.1432	0.1833	0.0365
Rear wheel	0.1375	0.1833	0.0974
Simulation 5: Large steering angle turning			
Front left wheel	1.22	12.35	0.573
Front right wheel	1.22	12.35	1.415
Rear left wheel	20.82	15.67	0.126
Rear right wheel	20.82	15.67	0.229

4) Conclusion

A novel side-slip angle estimator is proposed for the 4WIS-4WID vehicle and the simulation results are presented to compare with the existing methods in this paper. It shows that the proposed side-slip angle estimator for the 4WIS-4WID electric vehicle with in-wheel steering motor is more accurate and reliable than the existing estimation methods. The inputs of the estimator are the steering motor current and steering angle, which are easy to be accurately measured and controlled. In addition, when the steering angle is large, the proposed estimator which is based on a 4WIS vehicle model shows better estimation performance than the traditional methods which are based on a two-wheel vehicle model.

2. Estimation of longitudinal velocity and friction coefficient

A novel cost effective vehicle longitudinal velocity and tyre-road friction coefficient estimation method during the pure longitudinal motion is presented in this section. From the available ABS system, CAN bus and longitudinal accelerometer, the wheel angular speed measurement, traction/brake torque measurement and longitudinal acceleration measurement are available. Particularly for the conventional vehicle, the traction torque can be roughly calculated from engine torque by considering the reduction. The engine torque is normally obtained from measurement of engine fly-wheel speed. To improve the accuracy of measurement, high-resolution rotational motion sensors are utilised [240]. For the conventional vehicle with hydraulic braking system, the brake torque can be calculated from the measurement of oil pressure by pressure sensors in the hydraulic system [241]. These torque measurement signals are available through CAN bus. In addition, with emerging technology of in-wheel driving motor in EV, the traction/brake torque can be easily and accurately measured and controlled from the current of driving motors [83]. A number of studies have used the input traction torque and brake torque to estimate the tyre-road friction coefficient. These studies have been verified by the real experiment utilising the real vehicles, like the Volvo XC90 sport utility vehicle, with the torque measurement available on the CAN bus [62] [77] [242]. As the measurement of traction/brake torque may contain certain measurement noise, to reduce the effect of the torque measurement noise and improve the velocity estimation accuracy, a new observer is proposed with using the measured acceleration value as feedback signal and choosing appropriate feedback control gain to guarantee the convergence of the observer. The vehicle absolute velocity and slip ratio are estimated by this observer without using the expensive GPS, and the tyre longitudinal force and tyre-road friction coefficient of each wheel can be estimated accordingly. This method will produce a better estimation performance compared to the above discussed three methods.

There are mainly three steps in this proposed friction estimation method: (1) estimation of the longitudinal velocity and slip ratio; (2) estimation of the tyre longitudinal force; and (3) estimation of friction coefficient using the results obtained from the first two steps.

1) Vehicle longitudinal dynamics model

Only the vehicle longitudinal motion is considered for the longitudinal velocity and friction coefficient estimator. The schematic diagram of the vehicle longitudinal motion model is

shown in Figure III-8. When the vehicle is under acceleration, the vehicle longitudinal dynamics model and wheel dynamics model are described as:

$$\dot{v}_x = \frac{1}{m}\left(F_{xf} + F_{xr}\right) - C_r g - \frac{D_a v_x^2}{m} + g\sin\theta \quad \text{(a)}$$

$$\dot{\omega}_f = \frac{1}{I_\omega}\left(-F_{xf}R_\omega + T_{df}\right) \quad \text{(b)}$$

$$\dot{\omega}_r = \frac{1}{I_\omega}\left(-F_{xr}R_\omega + T_{dr}\right) \quad \text{(c)}$$

(33)

Where the wheel rolling resistance $C_r mg$, wind drag force $D_a v_x^2$ and road gradient $g\sin\theta$ are considered. T_{df} and T_{dr} are the traction torques applied on front and rear wheel, respectively. F_{xf} and F_{xr} are front wheel and rear wheel longitudinal tyre forces. m denotes the vehicle mass and v_x shows the vehicle longitudinal velocity. ω_f and ω_r are the front wheel and rear wheel angular velocities. I_ω denotes the wheel moment of inertia and R_ω is the wheel radius. When the vehicle is in braking mode, the vehicle dynamics model is described as:

$$\dot{v}_x = \frac{1}{m}\left(F_{xf} + F_{xr}\right) - C_r g - \frac{D_a v_x^2}{m} + g\sin\theta \quad \text{(a)}$$

$$\dot{\omega}_f = \frac{1}{I_\omega}\left(-F_{xf}R_\omega - T_{bf}\right) \quad \text{(b)}$$

$$\dot{\omega}_r = \frac{1}{I_\omega}\left(-F_{xr}R_\omega - T_{br}\right) \quad \text{(c)}$$

(34)

Where T_{bf} and T_{br} are the braking torques applied on front and rear wheel, respectively.

The Magic Formula tyre model is employed in this study to represent the nonlinear tyre characteristic, which is defined as:

$$F_{xf,r} = Dsin\{Carctan[Bs_{f,r} - E\{Bs_{f,r} - arctan(Bs_{f,r})\}]\}$$

(35)

Where B, C, D, E are all curve fitting coefficients in the Magic Formula tyre model. Particularly, $D = \mu F_z$, which is directly related to the vertical load F_z and the tyre-road friction coefficient μ.

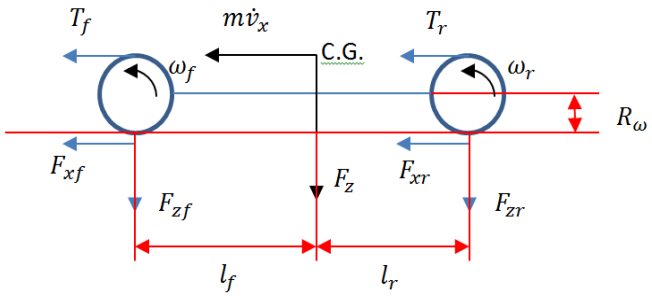

Figure III-8. Schematic diagram of vehicle longitudinal motion model.

2) Estimation of the vehicle longitudinal velocity and slip ratio

First, some assumptions on the longitudinal velocity observer are made.

Assumptions: The longitudinal acceleration, traction or brake torque and wheel angular velocity are measurable. The road gradient is also known. The lateral vehicle motion is neglected.

These assumptions are reasonable because the longitudinal acceleration can be obtained by the accelerometer and the traction or brake torque is available from the CAN bus of the vehicle system. The wheel angular velocity can be measured from the wheel speed sensor, while a longitudinal accelerometer and a vertical accelerometer can be used together to measure the road gradient [62]. As this paper is based on a vehicle longitudinal dynamics model that is applicable during vehicle acceleration and deceleration, the lateral motion is neglected.

The following vehicle longitudinal dynamic equations from the model (33)(34) are used for the observer design:

$$\dot{v}_x = \frac{T_{df}+T_{dr}-I_\omega(\dot{\omega}_f+\dot{\omega}_r)}{mR_\omega} - C_r g - \frac{D_a v_x^2}{m} + g\sin\theta \qquad \text{during acceleration} \qquad \text{(a)}$$

$$\dot{v}_x = \frac{-(T_{bf}+T_{br})-I_\omega(\dot{\omega}_f+\dot{\omega}_r)}{mR_\omega} - C_r g - \frac{D_a v_x^2}{m} + g\sin\theta \qquad \text{during braking} \qquad \text{(b)}$$

(36)

A nonlinear observer is designed to estimate the vehicle velocity as follows:

$$\dot{\hat{v}}_x = \left(\frac{T_{df} + T_{dr}}{mR_\omega}\right) \cdot Sat\left(\hat{v}_x - R_\omega \omega_f\right) - \frac{I_\omega\left(\dot{\omega}_f + \dot{\omega}_r\right)}{mR_\omega} - C_r g - \frac{D_a \hat{v}_x^2}{m} + g \sin\theta$$

$$+K_a \left[\left(\left(\frac{T_{df}+T_{dr}}{mR_\omega}\right) Sat\left(\hat{v}_x - R_\omega \omega_f\right) - \frac{I_\omega(\dot{\omega}_f+\dot{\omega}_r)}{mR_\omega} - C_r g - \frac{D_a \hat{v}_x^2}{m}\right) - a_x\right]$$

during acceleration (a)

$$\dot{\hat{v}}_x = \left(\frac{T_{bf} + T_{br}}{mR_\omega}\right) \cdot Sat\left(\hat{v}_x - R_\omega \omega_f\right) - \frac{I_\omega\left(\dot{\omega}_f + \dot{\omega}_r\right)}{mR_\omega} - C_r g - \frac{D_a \hat{v}_x^2}{m} + g \sin\theta$$

$$+K_a \left[\left(\left(\frac{T_{bf}+T_{br}}{mR_\omega}\right) Sat\left(\hat{v}_x - R_\omega \omega_f\right) - \frac{I_\omega(\dot{\omega}_f+\dot{\omega}_r)}{mR_\omega} - C_r g - \frac{D_a \hat{v}_x^2}{m}\right) - a_x\right]$$

during braking (b)

(37)

Where $T_{df}, T_{dr}, T_{bf}, T_{br}$ and ω_f, ω_r are all the inputs of the observer, which are measurable. a_x is the measured acceleration, which is used as the feedback value to make the observer converge with the designed feedback gain K_a. $Sat(x)$ is a nonlinear filter function, which is defined as:

$$Sat(x) = \begin{cases} 1, & x > d \\ -1, & x < -d \\ \dfrac{x}{d}, & else \end{cases}$$

(38)

Where $x = \hat{v}_x - R_\omega \omega_f$ and $d = 0.1$. d is a small value which is used to prevent numeric oscillations between the value -1 and 1 [243].

The insight behind the nonlinear filter function (38) is that it acts like a bang-bang controller where the output v_x will converge to the input $R_\omega \omega_f$ in steady state when there is no traction or brake torque applied. By defining the estimation error variable as $\tilde{v}_x = v_x - \hat{v}_x$, the error dynamics equations can be obtained by subtracting (37) from (36) as:

$$\dot{\hat{v}}_x = \left(\frac{T_{df}+T_{dr}}{mR_\omega}\right)(1-Sat(x)) - \frac{D_a(v_x^2-\hat{v}_x^2)}{m} - K_a\left[\left(\left(\frac{T_{df}+T_{dr}}{mR_\omega}\right)Sat(x) - \frac{I_\omega(\dot{\omega}_f+\dot{\omega}_r)}{mR_\omega} - C_r g - \frac{D_a\hat{v}_x^2}{m}\right) - a_x\right]$$

during acceleration (a)

$$\dot{\hat{v}}_x = \left(\frac{T_{bf}+T_{br}}{mR_\omega}\right)(-1-Sat(x)) - \frac{D_a(v_x^2-\hat{v}_x^2)}{m} - K_a\left[\left(\left(\frac{T_{bf}+T_{br}}{mR_\omega}\right)Sat(x) - \frac{I_\omega(\dot{\omega}_f+\dot{\omega}_r)}{mR_\omega} - C_r g - \frac{D_a\hat{v}_x^2}{m}\right) - a_x\right]$$

during braking (b)

(39)

As the measured acceleration is $a_x = \frac{T_{df}+T_{dr}-I_\omega(\dot{\omega}_f+\dot{\omega}_r)}{mR_\omega} - C_r g - \frac{D_a v_x^2}{m}$ (while acceleration) and $a_x = \frac{-(T_{bf}+T_{br})-I_\omega(\dot{\omega}_f+\dot{\omega}_r)}{mR_\omega} - C_r g - \frac{D_a v_x^2}{m}$ (while braking), thus, the error dynamics equation of the observer can be re-arranged as follows:

$$\dot{\tilde{v}}_x = -\left(\frac{T_{df}+T_{dr}}{mR_\omega}\right)(Sat(x)-1) - (1+K_a)\frac{D_a(v_x+\hat{v}_x)}{m}\tilde{v}_x - K_a\left[\left(\frac{T_{df}+T_{dr}}{mR_\omega}\right)(Sat(x)-1)\right]\tilde{v}_x$$

during acceleration (a)

$$\dot{\tilde{v}}_x = -\left(\frac{T_{bf}+T_{br}}{mR_\omega}\right)(Sat(x)+1) - (1+K_a)\frac{D_a(v_x+\hat{v}_x)}{m}\tilde{v}_x - K_a\left[\left(\frac{T_{bf}+T_{br}}{mR_\omega}\right)(Sat(x)+1)\right]\tilde{v}_x$$

during braking (b)

(40)

Hence, with the condition that $K_a > 0$, we have $t \to \infty$, $\tilde{v}_x \to 0$, $Sat(x) \to 1$ when acceleration and $Sat(x) \to -1$ when braking and $\dot{\tilde{v}}_x \to 0$. Therefore, the observer can ensure stable estimation of vehicle velocity. The structure of the propose observer is shown in Figure III-9.

The detailed stability proof of the proposed velocity estimator by using the Lyapunov method is presented as follows:

Define the Lyapunov function as:

$$V = \frac{1}{2}s^2 = \frac{1}{2}\tilde{v}_x^2 > 0$$

(41)

The time derivative of the Lyapunov function can be obtained as:

$$\begin{aligned}\dot{V} = s\dot{s} = \tilde{v}_x\dot{\tilde{v}}_x \\ &= -\left(\frac{T_{df}+T_{dr}}{mR_\omega}\right)(Sat(x)-1)\tilde{v}_x - (1+K_a)\frac{D_a(v_x+\hat{v}_x)}{m}\tilde{v}_x^2 \\ &- K_a\left[\left(\frac{T_{df}+T_{dr}}{mR_\omega}\right)(Sat(x)-1)\right]\tilde{v}_x^2\end{aligned}$$

during acceleration (a)

$$\begin{aligned}\dot{V} = s\dot{s} = \tilde{v}_x\dot{\tilde{v}}_x = \\ &= -\left(\frac{T_{bf}+T_{br}}{mR_\omega}\right)(Sat(x)+1)\tilde{v}_x - (1+K_a)\frac{D_a(v_x+\hat{v}_x)}{m}\tilde{v}_x^2 \\ &- K_a\left[\left(\frac{T_{bf}+T_{br}}{mR_\omega}\right)(Sat(x)+1)\right]\tilde{v}_x^2\end{aligned}$$

during braking (b)

(42)

It is noted that in equation (42), $Sat(x) \to 1$ when acceleration and $Sat(x) \to -1$ when braking, so this equation can be rewritten as:

$$\dot{V} = -(1+K_a)\frac{D_a(v_x+\hat{v}_x)}{m}\tilde{v}_x^2$$

during acceleration (a)

$$\dot{V} = -(1+K_a)\frac{D_a(v_x+\hat{v}_x)}{m}\tilde{v}_x^2$$

during braking (b)

(43)

In equation (43), since $K_a > 0$ and the longitudinal velocity value is always positive $v_x + \hat{v}_x > 0$, the derivative of the Lyapunov function is always less than zero and the proposed velocity estimator is stable.

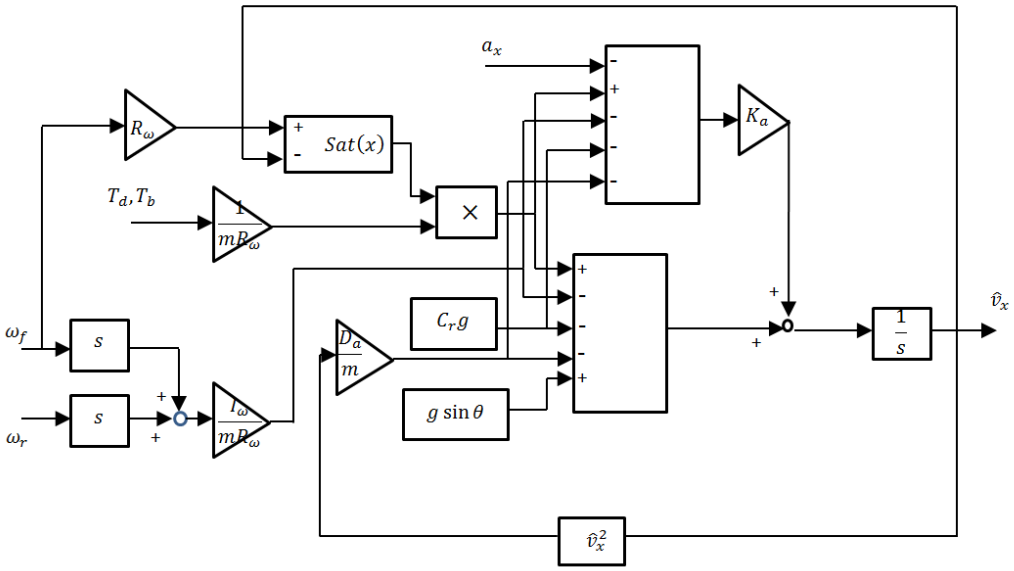

Figure III-9. Structure of the proposed vehicle velocity observer.

After the longitudinal velocity is estimated, the vehicle longitudinal slip ratio $s_{f,r}$ is obtained from the measured wheel angular speed and estimated longitudinal velocity by the as follows:

$$s_{f,r} = \frac{R_\omega \omega_{f,r} - v_x}{R_\omega \omega_{f,r}} \quad \text{during acceleration} \quad \text{(a)}$$

$$s_{f,r} = \frac{R_\omega \omega_{f,r} - v_x}{v_x} \quad \text{during braking} \quad \text{(b)}$$

(44)

3) Estimation of the vehicle longitudinal force

In this subsection, the vehicle longitudinal tyre force will be estimated instead of using expensive sensors to measure it. The vehicle acceleration can be utilised as the measurement information to update the error gain and improve the estimation accuracy. Therefore, this estimation method is cost effective and reliable. In addition, this estimator can estimate the front and rear tyre force individually.

Assumptions: Vehicle longitudinal slip ratio is available from the results of above section and longitudinal acceleration is measurable. Tyre lateral force is neglected.

According to equation (44), the tyre longitudinal slip ratio can be determined if the vehicle velocity can be accurately estimated. Then the front longitudinal tyre force and rear longitudinal tyre force can be estimated in equation (45).

$$F_{xf} = ks_f \tag{a}$$

$$F_{xr} = k\frac{F_{zr}}{F_{zf}}s_r \tag{b}$$

(45)

where k is the ratio between the tyre force and tyre slip ratio. To improve the estimation accuracy, this ratio will be updated in real time according to the error between the measured acceleration and the total estimated longitudinal tyre force. This is given by:

$$e = \left(\hat{F}_{xf} + \hat{F}_{xr}\right) - (ma_x + C_r mg + D_a v_x^2 - mg\sin\theta)$$

(46)

The block diagram of the tyre force estimator is shown in Figure III-10. It can be seen that k indicates the longitudinal stiffness of the tyre and will be updated according to the measured acceleration. In this way, the relationship between the estimated tyre force and slip ratio is no longer a simple linear relationship with a constant value but a nonlinear relationship. K_e is the control gain which is used to adjust the value of k according to the error e. C_s is the tyre longitudinal stiffness in the linear tyre region, which is a constant value.

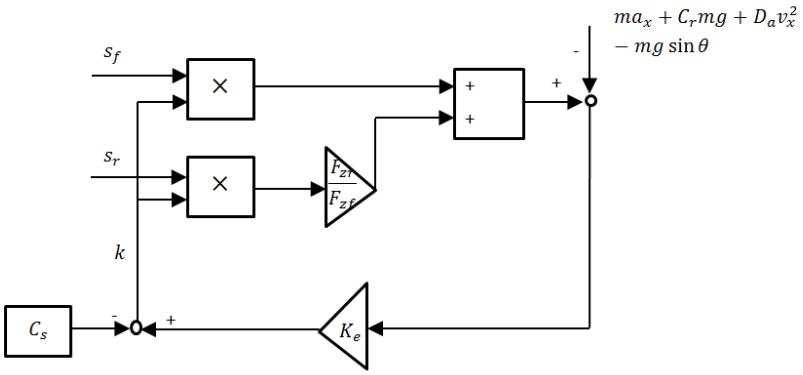

Figure III-10 Block diagram of the improved individual tyre force estimator.

4) Estimation of friction coefficient

The slip slope k_r is determined according to the RLS algorithm in [61]. When the slip slope k_r is estimated, based on the experimental data in the simulation, the tyre-road friction coefficient can be estimated by the following equation:

$$\mu = ak_r + b \tag{47}$$

where a is the proportional constant and b is the bias constant. The linear first-order curve fitting equation (47) is used in this study and the simulation results have shown that the linear equation is adequate to successfully estimate the results. In the future, the higher-order curve fitting equation or even nonlinear relationship may be applied if it is required.

In practice, a low-pass signal filter [61] is used to accommodate the measurement noise for acceleration. The estimation performance of the proposed friction estimator is improved in the simulation when the filter is applied, which will be shown in Table III-4 and Table III-5 in next section.

5) Simulation results

To validate the effectiveness of the proposed method, numerical simulations will be conducted. The parameters used in the simulations are the same as the parameters given in Table III-3.

Table III-3. Simulation results in the friction-coefficient estimator **[100]**

D_a	Wind drag coefficient	0.4176
C_r	Rolling resistance coefficient	1.5
θ	Road gradient	0.00001 rad
K_a	Control gain	800000 (140 when measurement noise of acceleration is considered)
K_e	Control gain	80000 (140 when measurement noise of acceleration is considered)
B	Magic formula tyre parameter – stiffness factor	20

C	Magic formula tyre parameter – shape factor	1.5
D	Magic formula tyre parameter – peak factor	μF_z
E	Magic formula tyre parameter – curvature factor	-0.5
a	Proportional constant	0.03
b	Bias constant	0.1

In the first test, the traction torque is applied as in Figure III-11 and the initial velocity is also 1 m/s. The actual friction coefficient is set as 0.9 in the vehicle dynamics model.

Figure III-12 compares the actual vehicle velocity with the estimated vehicle velocity, which proves that the improved nonlinear observer in equation (37) can effectively estimate the vehicle absolute velocity.

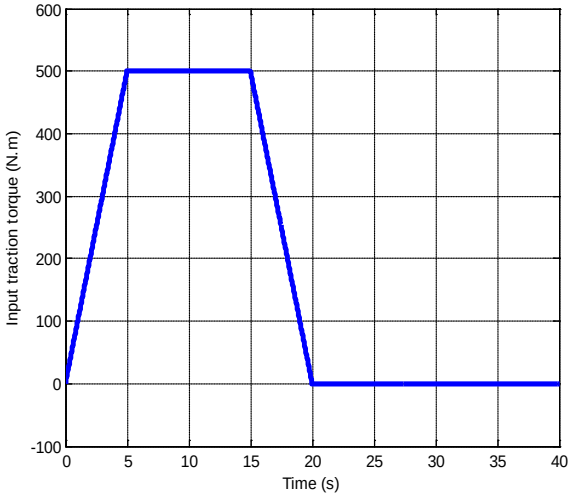

Figure III-11. Vehicle input traction torque applied on front and rear wheel.

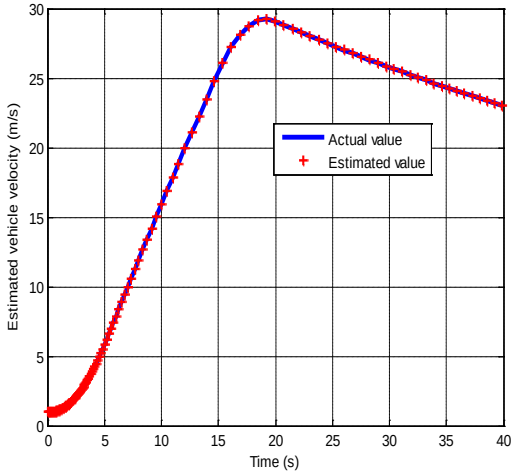

Figure III-12. Comparison of the estimated vehicle absolute velocity.

Figure III-13 shows the tyre force estimation of the proposed estimator compared to the actual tyre force. This result proves that the force estimation result of the proposed estimator is acceptable. Note that in the following figures, all the points in the simulation are presented to clearly show the simulation results.

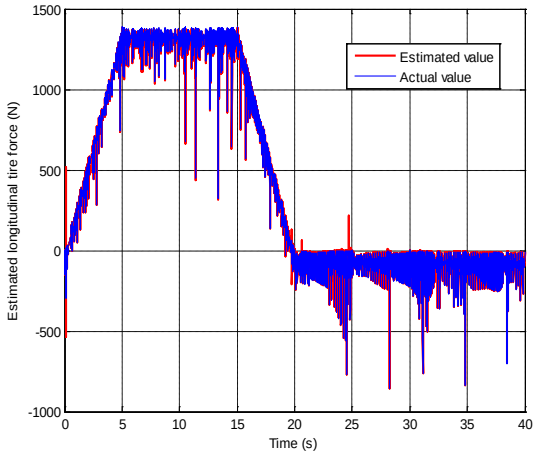

Figure III-13. Comparison of the estimated front tyre longitudinal forces.

The estimation of friction coefficient is shown in Figure III-14. It can be seen that the proposed estimator shows good estimation performance.

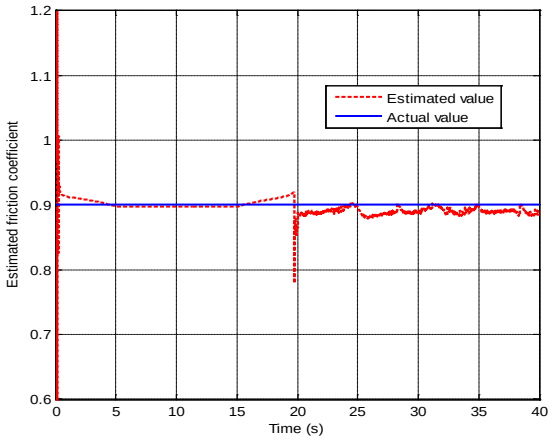

Figure III-14. Comparison of the estimated tyre-road friction coefficients of front tyre.

If the actual friction coefficient is changed from 0.9 to 0.5 at 10s (for example, the vehicle is moving from the normal road into the sand road), the estimated tyre forces and friction coefficients are shown in Figure III-15 and Figure III-16, respectively.

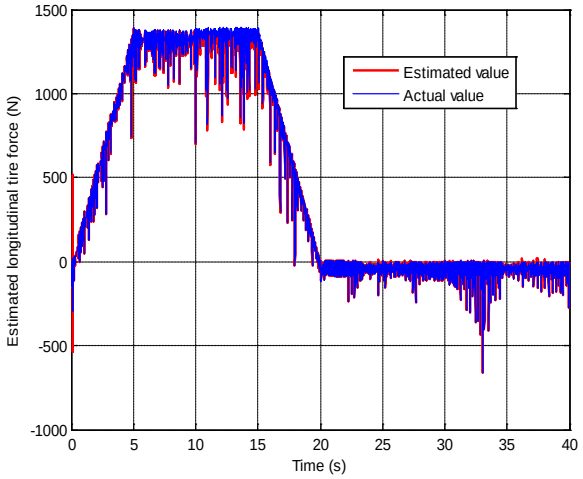

Figure III-15. Comparison of the estimated front tyre forces when the actual tyre-road friction coefficient is changed.

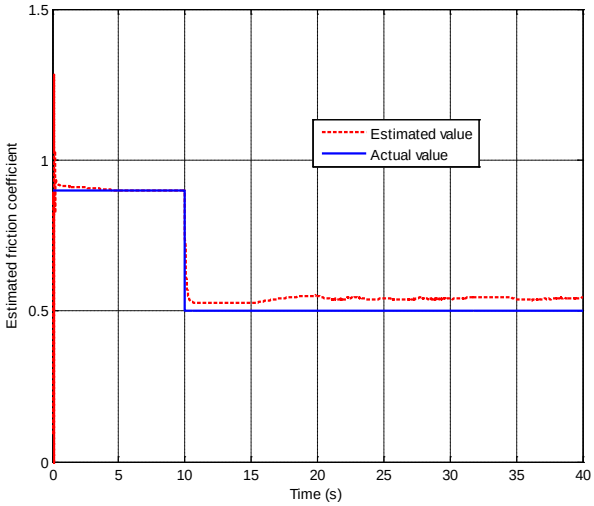

Figure III-16. Comparison of the estimated front tyre friction coefficients when the actual tyre-road friction coefficient is changed.

According to Figure III-16, it can be seen that the newly proposed estimation method achieves good performance on the estimation of the friction coefficient. Note that these figures also suggest that the estimation performance is compromised when the friction coefficient is changed from 0.9 to 0.5 during 10 to 15 seconds compared with Figure III-14. However, this disadvantage can be neglected during the whole time range of vehicle motion and the RMS error shown in Table III-4 and Table III-5 is not significantly affected by this disadvantage.

If the measurement noise of longitudinal acceleration is considered, the estimated tyre forces and friction coefficients are shown in Figure III-17 and Figure III-18, respectively.

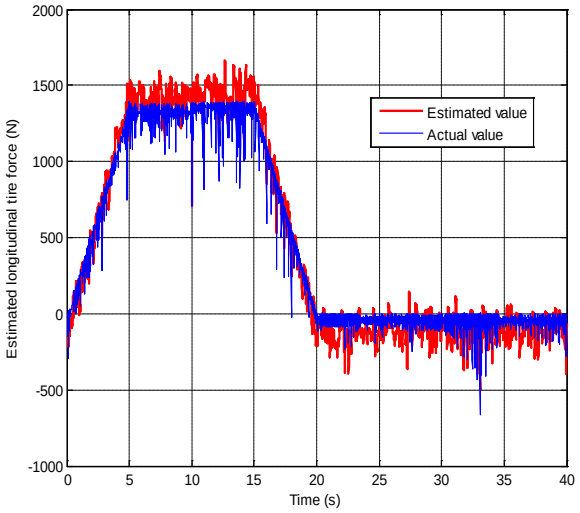

Figure III-17. Comparison of the estimated front tyre forces when the measurement noise of longitudinal acceleration is considered

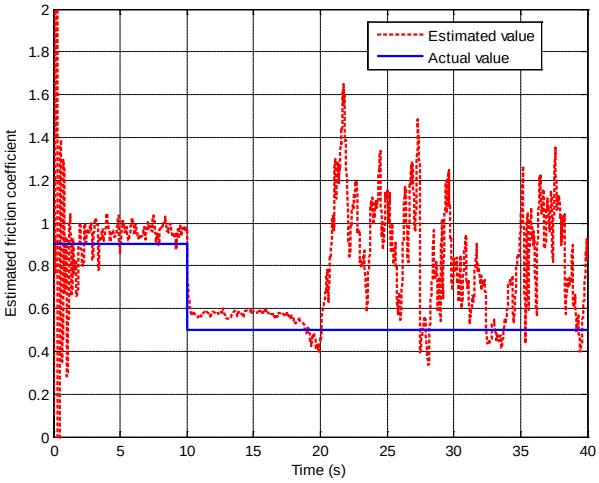

Figure III-18. Comparison of the estimated tyre-road friction coefficients of front tyre when the measurement noise of longitudinal acceleration is considered.

According to Figure III-17, when the longitudinal acceleration measurement is not reliable, the proposed method can still improve the estimation performance of tyre force by decreasing the feedback control gain about the acceleration and relying more on the torque measurement. For the friction coefficient estimation, the estimation performance can be improved by directly using the GPS to measure the vehicle velocity to obtain the slip ratio since the using of acceleration measurement to estimate the velocity is not reliable.

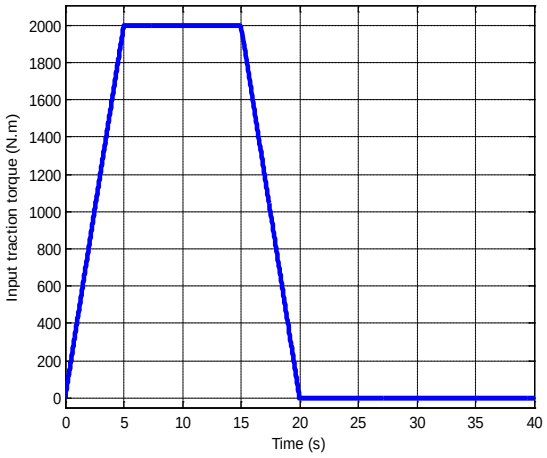

Figure III-19. Large input traction torque of front and rear wheel for investigation of estimation performance in nonlinear tyre region.

If the large traction torque is applied (same as Figure III-19) so the vehicle is operating in the nonlinear tyre region, the estimated tyre forces and friction coefficients are shown in Figure III-20 and Figure III-21, respectively.

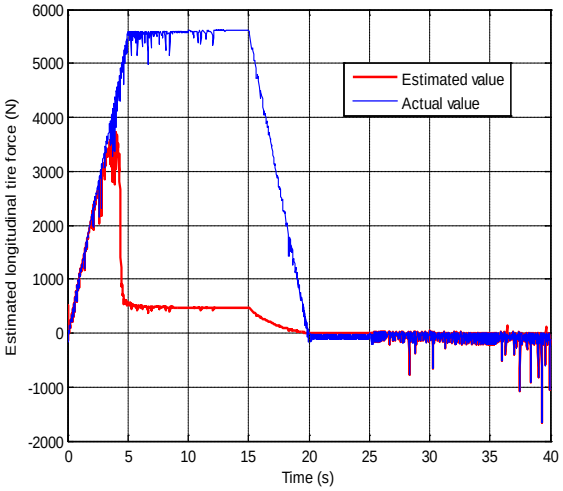

Figure III-20. Comparison of the estimated front tyre forces when the large input traction torque is applied.

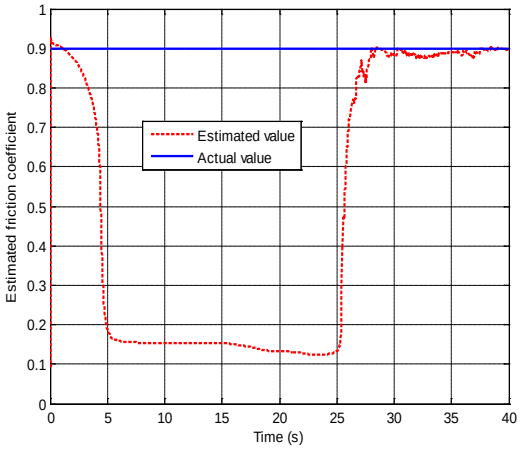

Figure III-21. Comparison of the estimated tyre-road friction coefficients of front tyre when the large input traction torque is applied.

According to Figure III-20 and Figure III-21, the estimated tyre force and friction coefficient are not accurate when the large traction torque is applied because the tyre is working in the non-linear tyre region. Although the proposed estimator can update the longitudinal stiffness, the estimator is still based on the linear relationship between the tyre force and slip ratio, which cannot accurately represent the non-linear relationship between them. Figure III-20 suggests that the estimator can accurately estimate the front tyre force when it is not larger

than about 3800 N. However, this novel estimator can find the accurate friction coefficient immediately when the tyre begins to work in the linear region after 25 s.

In addition, road gradient can also be changed (from 0.00001 to 0.01) to test the robustness of estimation performance of the proposed estimator. According to Figure III-22 and Figure III-23, the proposed estimation method has good estimation performance even when the road gradient is increased.

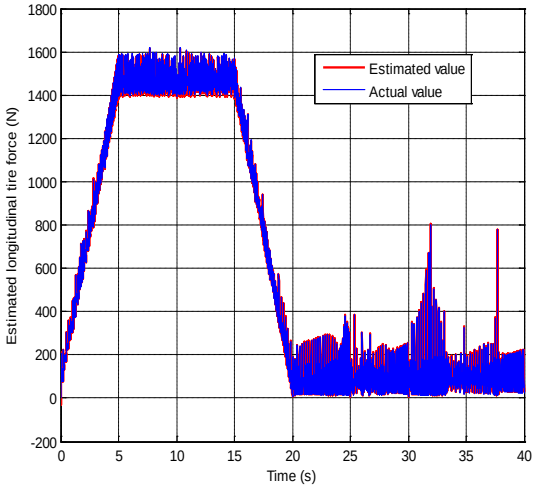

Figure III-22. Comparison of the estimated front tyre forces when the road gradient is considered.

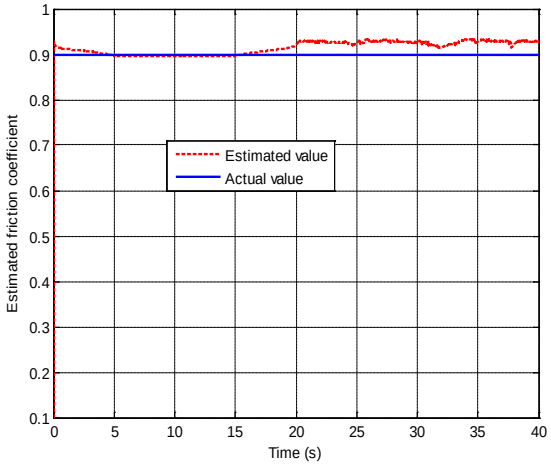

Figure III-23. Comparison of the estimated front tyre-road friction coefficients when the road gradient is considered.

Finally, the combined traction and brake motion is applied to evaluate the estimation performance of estimator. Figure III-24 and Figure III-25 also suggest that the proposed estimator has better performance.

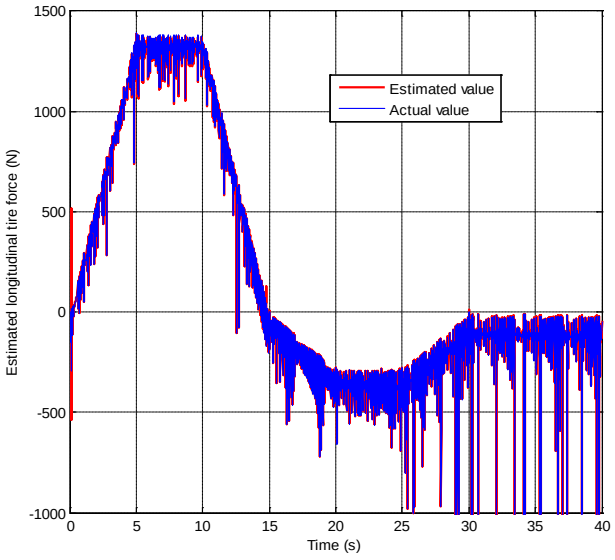

Figure III-24. Comparison of the estimated front tyre forces when considering the combined traction and brake motion.

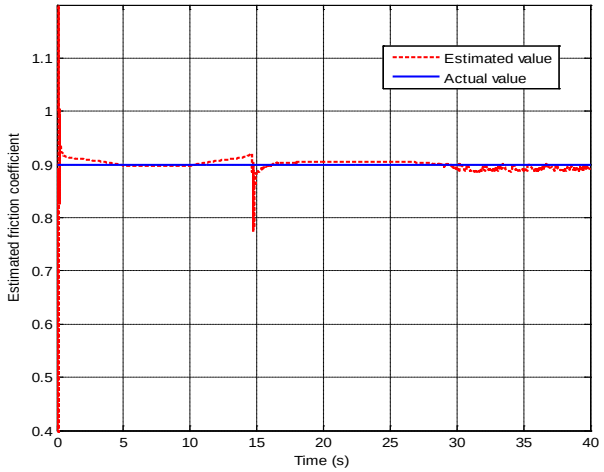

Figure III-25. Comparison of the estimated front tyre-road friction coefficients when considering the combined traction and brake motion.

To compare the results more clearly, the RMS value of estimation error of the proposed method is compared with other existing methods. The comparison results are shown in Table

III-4 and Table III-5 for the front tyre force and the tyre-road friction coefficient, respectively. For brevity, the slip slope method is called Method 1 in Table III-4 and Table III-5 [61]. The Algorithm 1 of the individual wheel tyre-road friction coefficient estimation method is called Method 2 in the following tables [62]. The Algorithm 2 of the individual wheel tyre-road friction coefficient estimation method is called Method 3 in the following tables [62]. The EKF based friction estimation method is also presented to compare with other estimation methods [21].

Table III-4. RMS of estimation error of front tyre force (unit: N)

Scenarios	Method 1	Method 2	Method 3	EKF method	Proposed method
Simple turning condition	44.67	76.58	45.44	48.05	8.738
Changed friction coefficient	38.84	57.88	39.54	40.58	10.56
Considering the measurement noise of acceleration	124.68	58.94	124.72	112.58	92.7
Large traction torque	439.75	127.62	55.43	440.15	1305
Considering the road gradient	42.88	117.3	44.15	53.09	3.283
Combined traction and brake motion	55.11	103.7	57.33	58.28	7.5838

Table III-5. RMS of estimation error of front tyre-road friction coefficient

Scenarios	Method 1	Method 2	Method 3	EKF method	Proposed method
Simple turning condition	0.0186	0.4229	0.8465	0.7045	0.0421
Changed friction coefficient	0.028	0.2774	0.8871	0.7269	0.0481
Considering the measurement noise of acceleration signal	2.033	0.2774	2.703	1.247	1.905
Large traction torque	0.3	0.7005	0.3624	2.126	0.2635
Considering the road gradient	0.0195	0.4842	0.1817	0.2083	0.0233
Combined traction and brake motion	0.0175	0.422	0.7832	0.6482	0.0388

6) Conclusion

It is confirmed from the simulation results that the novel friction coefficient estimation method shows good performance in the normal, in the friction coefficient variation, in the road gradient changing and in the combined traction and braking condition simulations when compared with other existing methods. When the measurement noise is considered, the proposed method still has the acceptable performance. However, this estimation method cannot work well when the tyre is working in the extreme non-linear tyre region. The non-linear tyre region is highly undesirable and many current studies are trying to design the advanced control strategies to prevent the vehicle from working in the non-linear tyre region. Nevertheless, the non-linear tyre condition is inevitable and more advanced vehicle state estimators are needed to tackle this issue by incorporating more comprehensive non-linear vehicle dynamics model in the future. Table III-4 and Table III-5 also show that the estimation performance is improved when the filter is applied at the scenario of considering the measurement noise of acceleration signal. Compared with Method 1, the proposed method has better estimation results of tyre force and the worse estimation results of friction coefficient.

This is because that Method 1 uses the direct measurement velocity from GPS to calculate the slip ratio, while the proposed method uses the estimation of velocity to calculate the slip ratio. The estimate velocity can compromise the estimation results of slip ratio and friction coefficient.

3. Two-layer vehicle parameter estimator

In this section, the proposed two-layer adaptive parameter estimator is presented. The two-layer structure is used in the study to clearly classify the slowly changed parameters and fast changed parameters. The estimator in the first layer is applied to estimate the slowly changed parameters including vehicle mass, moment of inertia and road slope on the smooth road. Then the real-time adaptive velocity observer is applied to estimate the fast changed parameters, like road slope on the uneven road, by assuming the slowly changed parameters are available from the first layer. Only the fast changed parameters need to be estimated in every time step and the slowly changed parameters can be assumed as the constant known values when they are not changed. Therefore, the proposed estimators can estimate less parameters in real-time compared with traditional methods, which is proved to be able to reduce the computational burden. The detailed structure of the two-layer adaptive estimator is presented in Figure III-26.

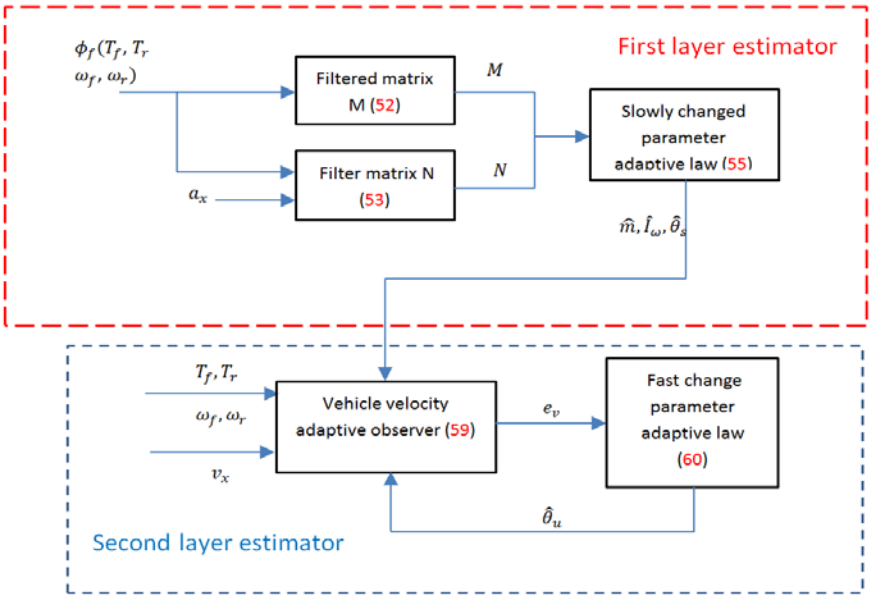

Figure III-26. The structure of the two-layer adaptive estimator

1) Vehicle slowly changed parameter estimator in the first layer

In the first layer, the adaptive parameter estimator is proposed by referring to [84]. This adaptive estimator is based on the vehicle dynamics model (36) and the vehicle mass and wheel moment of inertial can be estimated simultaneously. Particularly, for the road slope, if the vehicle is moving on the smooth road, the road slope can be considered as the slowly changed parameter θ_s estimated in the first layer in this section. If the vehicle is moving on the uneven road, however, the road slope changes abruptly and can be considered as the fast changed parameter θ_u, which will be estimated in the next section.

Compared with the traditional vehicle state observer, the proposed parameter estimator only uses two filtered matrices to determine the estimated parameters and the construction of vehicle state observer or predictor is evaded.

Assumptions: The various vehicle parameter estimators proposed below require the measured values of longitudinal acceleration, traction torque and wheel angular velocity. The longitudinal acceleration, traction or brake torque and wheel angular velocity are measurable. The lateral vehicle motion is neglected.

Assume the road slope is zero and equation (36) can be rewritten as the following equation:

$$\dot{v}_x = \frac{I_\omega}{m}\frac{-\dot{\omega}_f - \dot{\omega}_r}{R_\omega} + \frac{1}{m}\frac{T_f + T_r}{R_\omega} + g\sin\theta_s$$

(48)

where θ_s represents the slope of the smooth road.

Assume $\phi = \begin{bmatrix} \frac{-\dot{\omega}_f - \dot{\omega}_r}{R_\omega} & \frac{T_f + T_r}{R_\omega} & g \end{bmatrix}$ and $\delta = \begin{bmatrix} \frac{I_\omega}{m} \\ \frac{1}{m} \\ \sin\theta_s \end{bmatrix}$, equation

(48**)** can be written as:

$$\dot{v}_x = \phi\delta$$

(49)

It is noted that the vector ϕ requires the measurement values of the front wheel angular acceleration $\dot{\omega}_f$, rear wheel angular acceleration $\dot{\omega}_r$ and total input driving torque. The wheel angular acceleration is very hard to measure and can only be obtained by differentiating the measured wheel angular velocity. However, the derivative of the wheel angular velocity will cause large error due to the measurement noise. Thus, filters are applied to overcome the measurement noise.

$$k\dot{\omega}_{ff} + \omega_{ff} = \omega_f, \omega_f(0) = 0$$

(50)

$$k\dot{\omega}_{rf} + \omega_{rf} = \omega_r, \omega_r(0) = 0$$

(51)

where ω_{ff} and ω_{rf} are the filtered values of measured front wheel angular velocity and rear wheel angular velocity, respectively. k is the positive constant and this value can be adjust to determine the cut-off frequency of the filter. Similarly, a filter is applied for the measured driving torque T_f or T_r and the filtered driving torques can be presented as T_{ff} and T_{rf}. Thus, the filtered vector $\phi_f = \begin{bmatrix} \frac{-\dot{\omega}_{ff} - \dot{\omega}_{rf}}{R_\omega} & \frac{T_{ff} + T_{rf}}{R_\omega} & g \end{bmatrix}$.

Then the filtered matrix $M \epsilon R^{5\times5}$ and vector $N \epsilon R^{5\times1}$can be defined as:

$$\dot{M} = -lM + \phi_f^T\phi_f, M(0) = 0$$

(52)

$$\dot{N} = -lN + \phi_f^T a_x, N(0) = 0$$

(53)

where a_x is the measured vehicle acceleration. M can be considered as the matrix related to measurement input vector ϕ, and N can be considered as the matrix related to the longitudinal acceleration. The auxiliary vector $W \epsilon R^{3\times1}$ can be considered as the error between the measured acceleration a_x and $\phi\hat{\delta}$, which is obtained as:

$$W = M\hat{\delta} - N$$

(54)

The adaptive law for the estimated parameter can be presented as the constant gain ($\Gamma > 0$) multiplied by the auxiliary error vector W:

$$\dot{\hat{\delta}} = -\Gamma W$$

(55)

We can choose the Lyapunov function $V_1 = \frac{1}{2}\tilde{\delta}^T\Gamma^{-1}\tilde{\delta}$ to prove the stability of the proposed vehicle mass and wheel moment of inertial estimator. The derivative of Lyapunov function V_1 can be calculated as:

$$\dot{V}_1 = \tilde{\delta}^T\Gamma^{-1}\dot{\tilde{\delta}} = \tilde{\delta}^T W = -\tilde{\delta}^T M\tilde{\delta}$$

(56)

When the repressor vector ϕ is PE, the fact $\lambda_{min}(M) > \sigma > 0$ is true. When $\mu_1 = \frac{2\sigma}{\lambda_{max}(\Gamma^{-1})}$ is a positive constant, equation (56) can be rewritten as:

$$\dot{V}_1 = -\tilde{\delta}^T M\tilde{\delta} \leq -\mu_1 V_1$$

(57)

Equation (57) can guarantee V_1 converge to zero exponentially. $\tilde{\delta} = \delta - \hat{\delta}$.

It is noted that the estimated parameters in the first layer is the slowly changed parameters and consequently the adaptive law only needs to implement when the parameter is changed. For example, the vehicle mass is changed when passengers get on or get off the vehicle. If these parameters are not changed after they have been identified, they are assumed to be known as the constant value. In this way, the computation of the estimation algorithm in the whole vehicle moving process is avoided and the computational efficiency is improved.

2) Vehicle fast changed parameter estimator in the second layer

In the second layer estimator, the slowly parameters estimated in the first layer are assumed to be known and only the real-time values of the fast change parameters are required to be estimated. In this way, the coupling effect between the estimated parameters in the first layer and the second layer is prevented. In addition, the suggested real-time adaptive velocity observer is suitable for the online estimation of the fast changed parameters, such as the road slope in this study.

In [97], the adaptive observer can be written as the following form:

$$\dot{\hat{x}} = A\hat{x} + B_1 u_1 + B_2 \varphi \hat{\theta} + L(y - C\hat{x}) \quad \text{(a)}$$

$$y = Cx \quad \text{(b)}$$

(58)

According to vehicle dynamics equation (36), equation (58) can be rewritten as:

$$\dot{\hat{v}}_x = \frac{\hat{I}_\omega\left(-\dot{\omega}_f - \dot{\omega}_r\right)}{\hat{m}R_\omega} + \frac{T_{f,r}}{\hat{m}R_\omega} + \hat{\theta}_u g + L(v_x - \hat{v}_x)$$

(59)

where $A = 0$, $B_1 = \left[\frac{\hat{I}_\omega}{\hat{m}R_\omega} \quad \frac{1}{\hat{m}R_\omega}\right]$, $u_1 = \begin{bmatrix} -\dot{\omega}_f - \dot{\omega}_r \\ T_{f,r} \end{bmatrix}$, $B_2 = 1$, $\varphi = g$, $\hat{\theta} = \hat{\theta}_u$, $C = 1$. Thus, this adaptive observer requires the measurement values of wheel acceleration, the wheel driving torque and the actual longitudinal velocity. To make sure the stability and convergence of the observer, the matrix $Q = -(A_c^T P + P A_c)$ $(A_c = A - LC, P = 1)$ should be positive defined. Thus, $L = 1$ is chosen. The road slope $\hat{\theta}_u$ can be updated by the following adaptive law:

$$\dot{\hat{\theta}}_u = r_s \varphi e_v$$

(60)

where $e_v = v_x - \hat{v}_x$. r_s is the adaptive gain, which can be chosen as 1.

The observer's stability and convergence behaviour can be analysed by using the following Lyapunov function candidate:

$$V_2 = \frac{1}{2}e_v^2 + \frac{g\tilde{\theta}_u^2}{2r_s}$$

(61)

The derivative of the Lyapunov function V_2 can be calculated as follows from

(48) and (59):

$$\dot{V}_2 = e_v\left(\frac{I_\omega(-\dot{\omega}_f - \dot{\omega}_r)}{mR_\omega} + \frac{T_{f,r}}{mR_\omega} + \theta_s g - \frac{I_\omega(-\dot{\omega}_f - \dot{\omega}_r)}{mR_\omega} - e_{m1} - \frac{T_{f,r}}{mR_\omega} - e_{m2} - \hat{\theta}_u g - Le_v\right) - \frac{g}{r_s}\tilde{\theta}_s r_s e_v$$

$$= -Le_v^2 - e_v(e_{m1} + e_{m2})$$

(62)

where $e_{m1} = \frac{\hat{I}_\omega(-\dot{\omega}_f - \dot{\omega}_r)}{\hat{m}R_\omega} - \frac{I_\omega(-\dot{\omega}_f - \dot{\omega}_r)}{mR_\omega}$ and $e_{m2} = \frac{T_{f,r}}{\hat{m}R_\omega} - \frac{T_{f,r}}{mR_\omega}$, which reflect the estimation error of vehicle mass and wheel moment of inertial in the first layer parameter estimator. $\tilde{\theta}_s = \theta_s - \hat{\theta}_s$. According to equation (62), when the vehicle mass and wheel moment of inertial are estimated accurately, e_{m1} and e_{m2} are close to zero. Then according to this, the derivative of V_2 is always negative and the proposed observer is stable. When the estimation error of the vehicle mass and wheel moment of inertial exists, the stability performance of the observer will impair.

It is also noted that the vehicle longitudinal velocity v_x is actually hard to measure. The longitudinal velocity can be obtained by directly integrating the measured acceleration, but the measured acceleration has large random error which will great impair the integration results. In this study, the longitudinal velocity can be calculated from the wheel angular speed, which is reasonable during the smooth road and small longitudinal slip condition. This means $v_x = \omega_f R_\omega = \omega_r R_\omega$, where the front and rear wheel angular velocity are assumed as the same. In order to achieve the persistent excitation, the vehicle should be accelerated with large enough driving torque in the whole time, which leads to the large acceleration $\dot{v}_x$. Although the large tyre slip may impair the velocity measurement, large acceleration in the whole time range can still significantly benefit the parameter estimation results, which is clearly shown in the simulation and experiment results.

3) Simulation results

In the simulation, the estimation performance of vehicle mass and wheel moment of inertia in the first layer is presented first. Then based on these estimated parameters, the estimation results of the estimated road slope in the second layer are presented. To simulate the actual vehicle motion, the parameters from a typical vehicle are applied here, which is shown in Table III-6.

Table III-6. Simulation model parameters [100]

B	Magic formula tyre parameter – stiffness factor	20
C	Magic formula tyre parameter – shape factor	1.5
D	Magic formula tyre parameter – peak factor	μF_z
E	Magic formula tyre parameter – curvature factor	-0.5
Γ	Adaptive gain in the first layer	$\begin{bmatrix} 10 & 0 \\ 0 & 10 \end{bmatrix}$

In the first set of simulations, the vehicle is moving along the straight line with the initial velocity of 10 m/s. The road slope is assumed as zero and the road friction coefficient is 0.9. At 10 seconds, the vehicle mass is increased due to the change of load. The actual road slope is zero at the beginning and the value changes into 0.02 rad after 10 seconds. The vehicle input driving torque is shown in Figure III-27. The proposed estimator in the first layer is only implemented at the beginning of the vehicle motion and when the slowly changed parameters are changed after 10 seconds.

Figure III-28 and Figure III-29 suggest the good estimation results of vehicle mass, wheel moment of inertia and road slope when the estimator is implemented at the beginning and after 10 seconds when the vehicle mass and road slope are changed in Section 3.3.1.

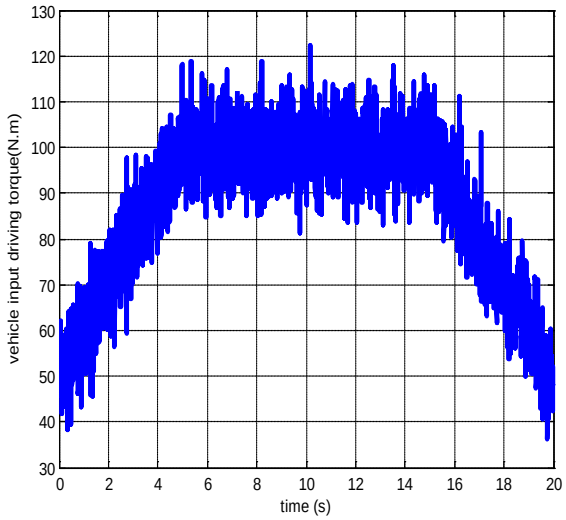

Figure III-27. Vehicle input driving torque

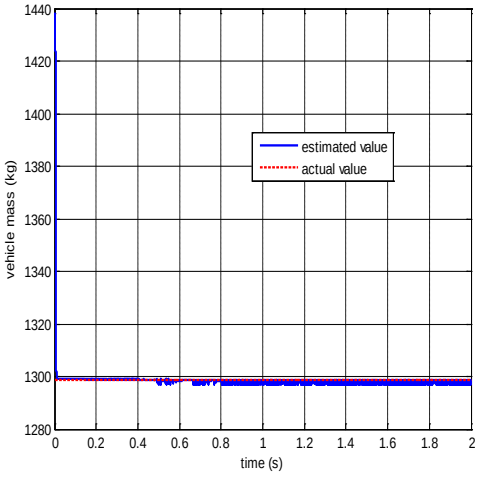

(a) vehicle mass

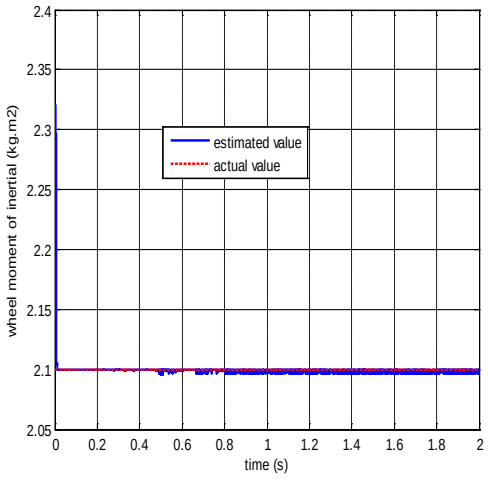

(b) wheel moment of inertial

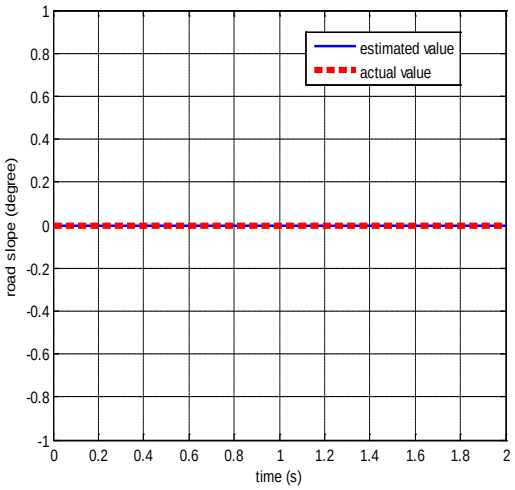

(c) road slope

Figure III-28. The estimated vehicle parameters at the beginning in the first set of simulations.

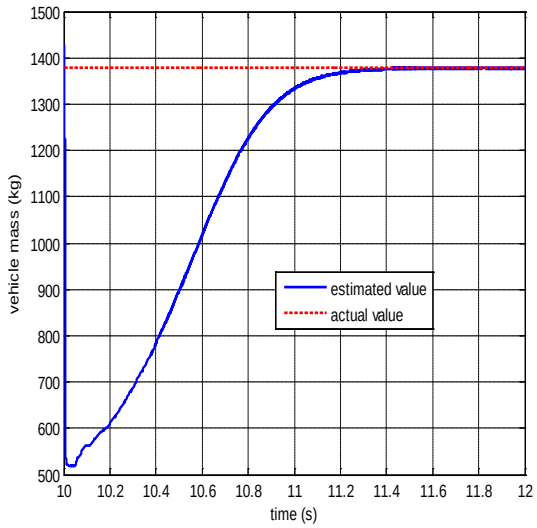

(a) vehicle mass

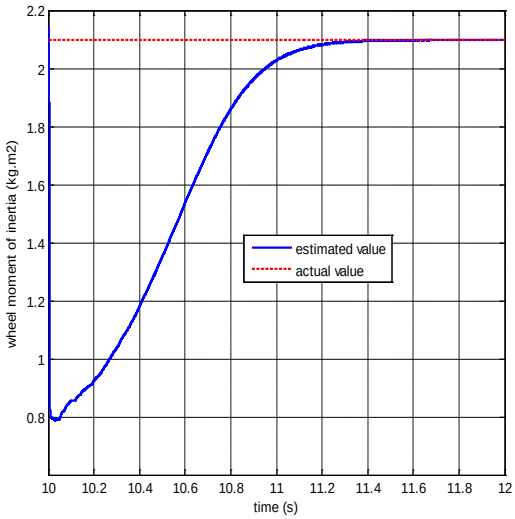

(b) wheel moment of inertial

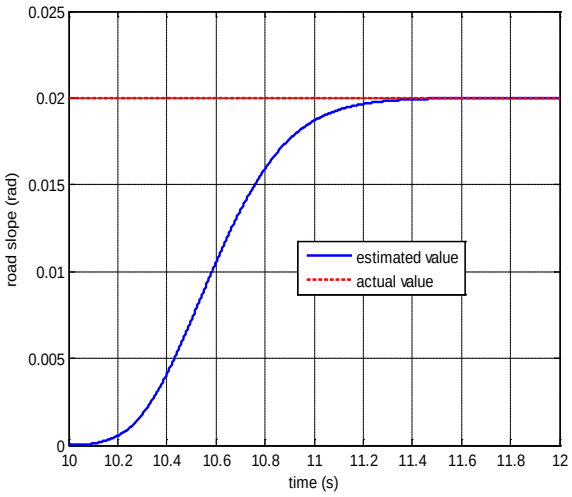

(c) road slope

Figure III-29. The estimated vehicle parameters after 10 seconds in the first set of simulations.

In the first set of the simulations, all the measured inputs are ideal values, which is not realistic due to the existence of the measurement noise. In the second set of simulation, the measured wheel velocity has the random noise with the variance of 0.01 and the input torque has the random noise with the variance of 0.1. The measured vehicle acceleration has the random noise with the variance of 0.001. Figure III-30 presents the estimated vehicle mass

and wheel moment of inertia when the proposed parameter estimator is implemented at the beginning. The measurement noise does not significantly impair the estimation performance. In Figure III-31, when the proposed estimator is implemented after 10 seconds, the estimation results are still not impaired by the measurement noise. This proves the robustness of proposed parameter estimator and the advantageous over the traditional RLS estimation method.

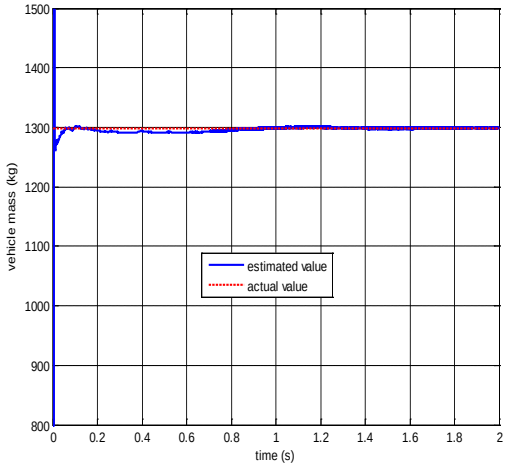

(a) vehicle mass

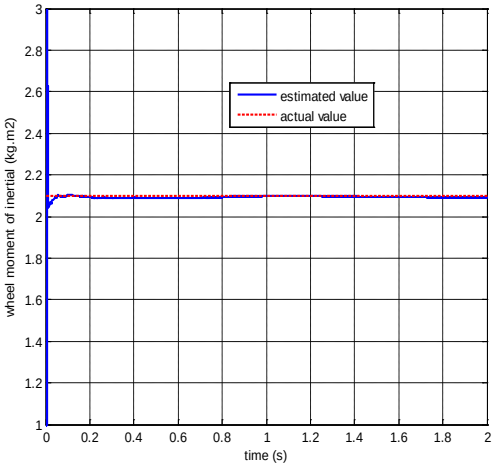

(b) wheel moment of inertial

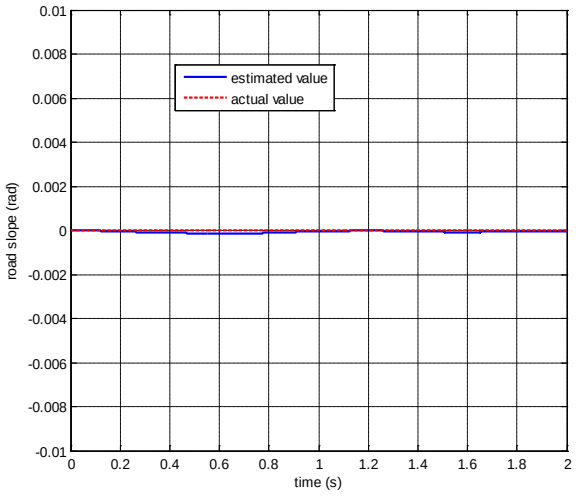

(c) road slope

Figure III-30. The estimated vehicle parameters at the beginning in the second set of simulations.

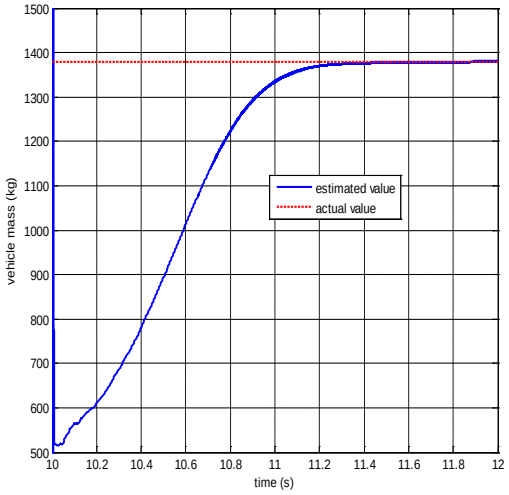

(a) vehicle mass

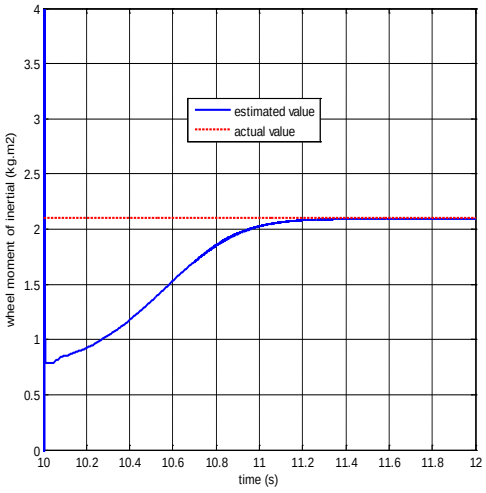

(b) wheel moment of inertial

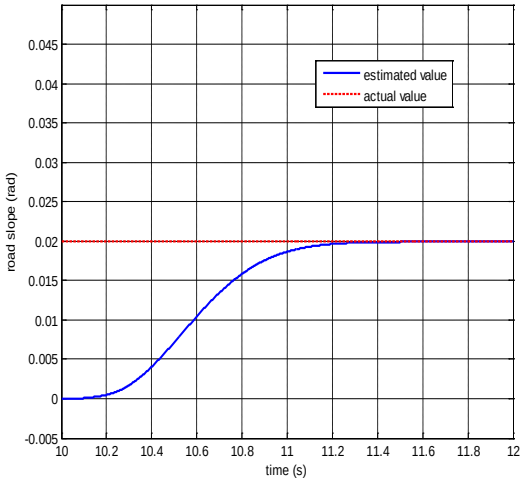

(c) road slope

Figure III-31. The estimated vehicle parameters after 10 seconds in the second set of simulations.

When the vehicle mass and wheel moment of inertia are determined in the road with actual road slope value of zero, these parameters can be input into the adaptive velocity observer in the second layer to estimate the road slope when the actual road slope is quite large, which is shown in the third set of simulations. The vehicle initial velocity, tyre-toad friction coefficient and the vehicle input driving torque are all the same as the first set of simulations. The same measurement errors are applied as the conditions in the second set of simulations. The actual road slope, however, is different from the previous simulations and is fast changed due to the uneven road. The estimated road slope is shown in Figure III-32 and this result

suggests that the adaptive observer in the second layer can successfully estimate the road slope even the measurement noise exists.

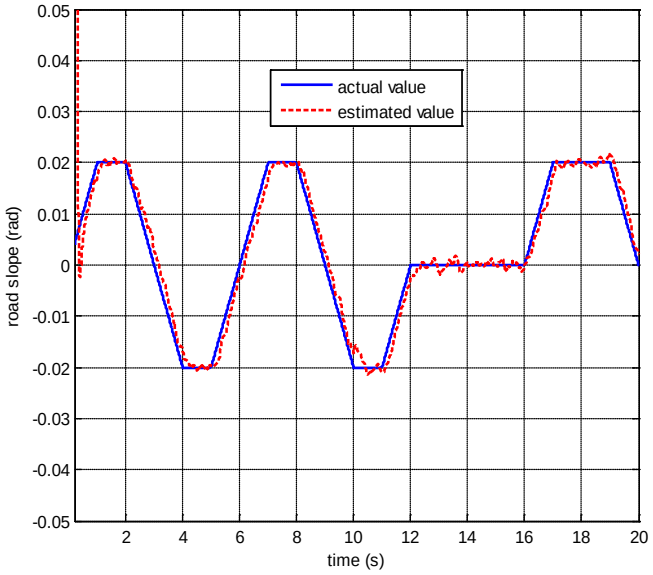

Figure III-32. The estimated vehicle road slope in the third set of simulations.

4) Conclusion

This section proposes the two-layer vehicle parameter adaptive estimation method. In the first layer, the slowly changed vehicle parameters are estimated by an adaptive law. Once successfully estimated, these parameters can be assumed as the constant values unless they are abruptly changed. In the second layer, by assuming the slowly changed parameters are available from the first layer, the real-time values of the fast changed parameters are estimated by an adaptive velocity observer. Simulations are implemented to verify the proposed parameter estimators and the major findings can be summarised as follows:

(1) The proposed two-layer adaptive parameter estimator can successfully determine the slowly changed parameter and the fast changed parameter.

(2) The two-layer hierarchical structure of the proposed estimator has the advantage of the separation of the estimation of the fast changed parameters and the slowly changed parameters and the coupling effect between them can be alleviated.

4. Summary

In this section, various vehicle state estimation methods, such as the side-slip angle estimation, the velocity estimation, friction coefficient estimation and mass and road slope estimation, are proposed for the 4WIS-4WID EVs and these estimated state values can provide important real-time feedback information for the proposed over-actuated controller in this thesis.

IV. Vehicle dynamics modeling

1. Vehicle dynamics model

In this thesis, a 4WIS and 4WID vehicle model as shown in Figure IV-1 is utilised to describe the dynamics motion of the EV with in-wheel steering and driving motors [100]. This model is used to present the actual vehicle motion and validate the performance of the proposed various over-actuated control allocation method. The equations of motion of this model are described as follows:

Longitudinal motion:

$$m\dot{v}_x = mv_y r + \left(F_{xfl} + F_{xfr} + F_{xrl} + F_{xrr}\right) \tag{a}$$

Lateral motion:

$$m\dot{v}_y = -mv_x r + \left(F_{yfl} + F_{yfr} + F_{yrl} + F_{yrr}\right) \tag{b}$$

Yaw motion:

$$I_z\dot{r} = l_f\left(F_{yfl} + F_{yfr}\right) - l_r\left(F_{yrl} + F_{yrr}\right) + \frac{b_f}{2}\left(F_{xfl} - F_{xfr}\right) + \frac{b_r}{2}\left(F_{xrl} - F_{xrr}\right) \tag{c}$$

(63)

where v_x, v_y, r are the vehicle longitudinal velocity, lateral velocity, and yaw rate, respectively. $F_{xfl}, F_{xfr}, F_{xrl}, F_{xrr}$ are the vehicle front left, front right, rear left and rear right longitudinal tyre forces, respectively, and $F_{yfl}, F_{yfr}, F_{yrl}, F_{yrr}$ are the vehicle front left, front right, rear left and rear right lateral tyre forces, respectively. l_f and l_r are the front and rear wheel base lengths, while b_f and b_r are the front and rear track widths. I_z and m are the moment of vehicle inertia in terms of yaw axis and vehicle mass. In order to simplify the vehicle model and improve computational efficiency, the vehicle roll dynamics are neglected in this study.

The tyre traction or brake force and side force are defined as F_{ti} and F_{si}, respectively, which can be related to the longitudinal and the lateral tyre forces by the steering angle δ_i as follows:

$$F_{xi} = F_{ti}\cos\delta_i - F_{si}\sin\delta_i$$

$$F_{yi} = F_{ti}\sin\delta_i + F_{si}\cos\delta_i \tag{64}$$

where $i = fl, fr, rl, rr$, which represents the front left, front right, rear left and rear right wheel, respectively. δ_i represents the steering angle of each vehicle wheel. It should be noted that all the steering angles mentioned in this thesis indicate the steering angles of the vehicle wheels.

In the proposed vehicle model in Figure IV-1, the Ackermann steering characteristic is assumed. According to [244], in the case of traditional vehicles, the desired steering angles for the Ackermann steering cannot be achieved for a number of reasons, such as the wheel side slipping, tyre elasticity, kingpin inclination and camber angles. The actual steering angles are also constrained by the mechanical linkage, but in an EV with in-wheel motors, the actual steering angle can be controlled according to the desired steering angle by adjusting the steering torque of the steering motor. The accurate control of the individual steering angle without the constraint of mechanical linkage can compensate for the resultant steering angle error caused by above suggested reasons and achieve almost 100% Ackermann steering. However, this 100% can only be achieved in the low speed condition. When the vehicle is cornering at high speed, the vehicle can not achieve the Ackermann steering due to the large individual wheel side-slip angle and the vehicle should have the small steering angle input.

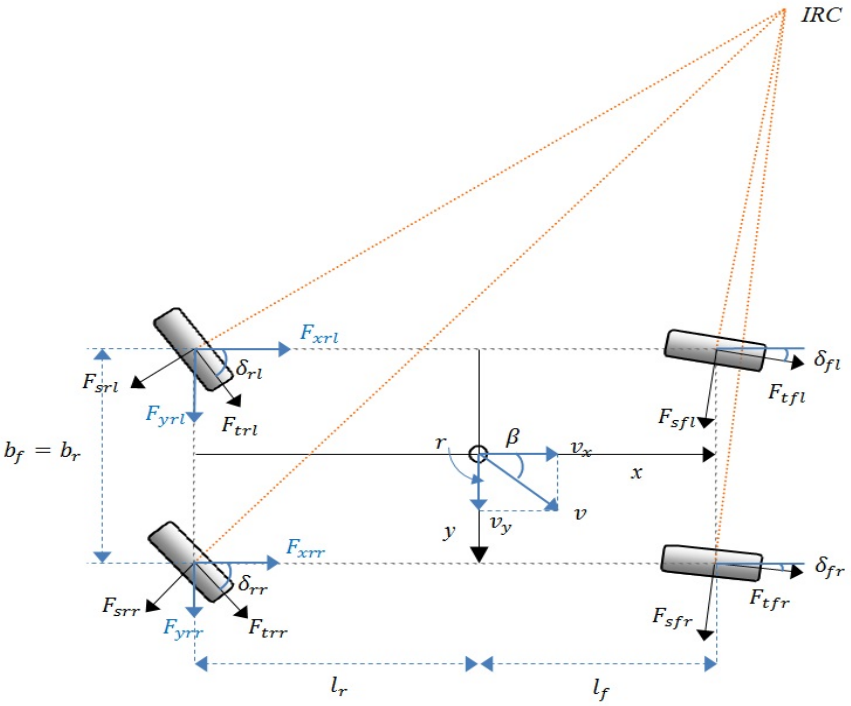

Figure IV-1. 4WS-4WD vehicle dynamics model, where *IRC* represents the instantaneous centre of rotation.

2. Vehicle tyre model

The non-linear Dugoff tyre model, which can well describe the non-linear tyre characteristic of combined longitudinal and lateral tyre force and the friction circle effect [104] is used in this study and described by:

$$\lambda_i = \frac{\mu F_{zi}(1 - s_i)}{2\sqrt{C_s^2 s_i^2 + C_\alpha^2 \tan^2 \alpha_i}}$$

$$f(\lambda_i) = \begin{cases} \lambda_i(2 - \lambda_i), & \lambda_i < 1 \\ 1, & \lambda_i \geq 1 \end{cases}$$

$$F_{si} = \frac{C_\alpha \tan \alpha_i}{1 - s_i} f(\lambda_i)$$

$$F_{ti} = \frac{C_s s_i}{1 - s_i} f(\lambda_i)$$

(65)

where μ is the tyre-road friction coefficient. C_s is the longitudinal slip stiffness and C_α is the lateral cornering stiffness. C_s and C_α can be represented by the following equations:

$$C_s = 2l^2 w k_x \tag{a}$$

$$C_\alpha = 2l^2 w k_y \tag{b}$$

(66)

where l is the half-length of the contact patch and w is the width of the contact patch. k_x and k_y are the tyre longitudinal deflection constant and lateral deflection constant related to the tyre property, respectively. In [104], it is suggested that the range of lateral cornering stiffness is between 26689 N/rad and 62275 N/rad and the range of longitudinal slip stiffness is between 22241 N/unit slip and 177929 N/unit slip, which corresponds to the range of that of real tyres. The parameters of C_s (50000 N/unit slip) and C_α (30000 N/rad) used in this study are those used in [100]. These parameters correspond to a typical vehicle and are also within the range of the values of real tyres suggested in [104]. s_i is the longitudinal slip ratio, and α_i is the lateral slip angle. ε_r is a constant value, and u_i is the vehicle velocity component in the wheel plane which is defined for each wheel as:

$$u_{fl} = \left(v_x + \frac{1}{2} b_f r\right) \cos \delta_{fl} + \left(v_y + l_f r\right) \sin \delta_{fl}$$

$$u_{fr} = \left(v_x - \frac{1}{2} b_f r\right) \cos \delta_{fr} + \left(v_y + l_f r\right) \sin \delta_{fr}$$

$$u_{rl} = \left(v_x + \frac{1}{2} b_r r\right) \cos \delta_{rl} - \left(l_r r - v_y\right) \sin \delta_{rl}$$

$$u_{rl} = \left(v_x - \frac{1}{2} b_r r\right) \cos \delta_{rr} - \left(l_r r - v_y\right) \sin \delta_{rr}$$

(67)

The friction coefficient μ can be presented by the following equation:

$$\mu = \mu_0 \left(1 - \varepsilon_r u_i \sqrt{s_i^2 + \tan^2 \alpha_i}\right)$$

(68)

where μ_0 is the nominal friction coefficient, which is assumed to be 0.9 in the simulation in order to represent good cement road conditions. ε_r is the friction reduction factor scaling the reduction effluence of the sliding velocity $u_i\sqrt{s_i^2 + \tan^2 \alpha_i}$, which is quite small value (0.015 s/m). F_{zi} is the vertical load of each wheel, which can be calculated as follows [245]:

$$F_{zfl} = \frac{m}{l_f + l_r}\left(\frac{1}{2}gl_r - \frac{1}{2}(\dot{v}_x - v_y r)h - \frac{l_r}{b_f}(\dot{v}_y + v_x r)h\right)$$

$$F_{zfr} = \frac{m}{l_f + l_r}\left(\frac{1}{2}gl_r - \frac{1}{2}(\dot{v}_x - v_y r)h + \frac{l_r}{b_f}(\dot{v}_y + v_x r)h\right)$$

$$F_{zrl} = \frac{m}{l_f + l_r}\left(\frac{1}{2}gl_f + \frac{1}{2}(\dot{v}_x - v_y r)h - \frac{l_f}{b_r}(\dot{v}_y + v_x r)h\right)$$

$$F_{zrl} = \frac{m}{l_f + l_r}\left(\frac{1}{2}gl_f + \frac{1}{2}(\dot{v}_x - v_y r)h + \frac{l_f}{b_r}(\dot{v}_y + v_x r)h\right)$$

(69)

where h is the height of the vehicle CG above the ground, and g is the acceleration of gravity.

According to [104], the Dugoff tyre model is the mathematical simplification of the analytical Fiala tyre model under some reasonable simplifying assumptions in the analysis of the tyre mechanics. In [104], the tyre force curve derived from the experimental data obtained by an on-road tyre dynamometer and the curve derived from the simulation results of the tyre data obtained by the Dugoff tyre model are shown to agree. This proves that the Dugoff tyre model can accurately represent the actual vehicle tyre characteristics.

According to equation (65), the Dugoff tyre model can be classified as involving two stages according to the defined value λ: when $\lambda > 1$, the tyre has not reached the sliding boundary point and when $\lambda < 1$, the tyre reaches the sliding boundary point and starts to slide away. The defined value λ is the reciprocal function of the combined slip s_R which considers both the longitudinal slip ratio and the lateral slip angle.

3. Traction or brake dynamics model

Since one important feature of 4WID-4WIS EVs is the ability to perform independent traction or brake motion for each wheel, each wheel is integrated with an in-wheel traction or brake motor. The wheel rotation dynamics is described by the following equations:

$$I_\omega \dot{\omega}_i = -R_\omega F_{ti} + T_{di} \quad \text{during traction} \quad \text{(a)}$$

$$I_\omega \dot{\omega}_i = -R_\omega F_{ti} - T_{bi} \quad \text{during braking} \quad \text{(b)}$$

(70)

where I_ω is the wheel moment of inertia and ω_i is the angular velocity of each wheel. R_ω is the wheel radius and T_{di} is the traction torque of each wheel and T_{bi} is the brake torque of each wheel.

The input of the wheel rotation dynamics model is the traction or brake torque and the output of the model is the wheel angular velocity. According to the difference between the vehicle absolute velocity and wheel angular velocity, the vehicle longitudinal slip ratio s_i can be calculated as follows:

$$s_i = \frac{\omega R_\omega - v_x}{max(v_x, \omega R_\omega)}$$

(71)

4. Actuator constraints

For the 4WIS-4WID vehicle, the limitation of the steering angle is between -90 degrees and 90 degrees ($\delta_{max} = 90$), which is larger than the traditional vehicle [115]. The maximum driving torque of the individual wheel for the electric vehicle is 100 N.m [206]. Thus, the steering and driving actuator constraints can be presented as:

$$-T_{max} \leq T_i \leq T_{max} \quad \text{(a)}$$

$$-\delta_{max} \leq \delta_i \leq \delta_{max} \quad \text{(b)}$$

(72)

5. Summary

In this chapter, the vehicle body dynamics model, tyre model, steering model and driving model for the 4WIS-4WID EV are proposed. Based on this vehicle dynamics model, the over-actuated control allocation method for various control targets can be designed.

V. Design of the over-actuator controller for the 4WIS-4WID electric vehicle

Based on the proposed vehicle dynamics model in Chapter 4, the over-actuated controller for the 4WIS-4WID EV can be designed accordingly. The vehicle states, such as velocity, side-slip angle and friction-coefficient, are important feedback values for the controller design have been successfully estimated in Chapter 3. In the vehicle dynamics control, the primary control targets are vehicle handling control (yaw rate control) and vehicle stability control (body side-slip angle control).

1. Two-level linear feedback control allocation method

For 4WID-4WIS EVs, four steering actuators and four electric driving motors mounted in wheels can be used for vehicle yaw rate control (vehicle handling control) and body side-slip angle control (vehicle stability control). The main aim of vehicle yaw rate control is to minimize the difference between the actual yaw rate and the desired yaw rate by adjusting the steering angles through four steering actuators and adjusting the traction/brake torques through four driving motors. To successfully adjust the eight actuators, we develop a two-level optimal control allocation method (hierarchical control structure). The first level (high level) is to allocate the additionally controlled individual tyre longitudinal force and the lateral force according to the tracking error of the yaw rate. The second level (low level) is to decide the steering angle and driving or braking torque according to the allocated longitudinal and lateral forces of the individual wheel. Similarly, the main aim of vehicle side-slip angle control is to minimize the difference between the actual side-slip angle and the desired side-slip angle by adjusting the individual control actuator of each wheel, which is similar to the vehicle handling control method.

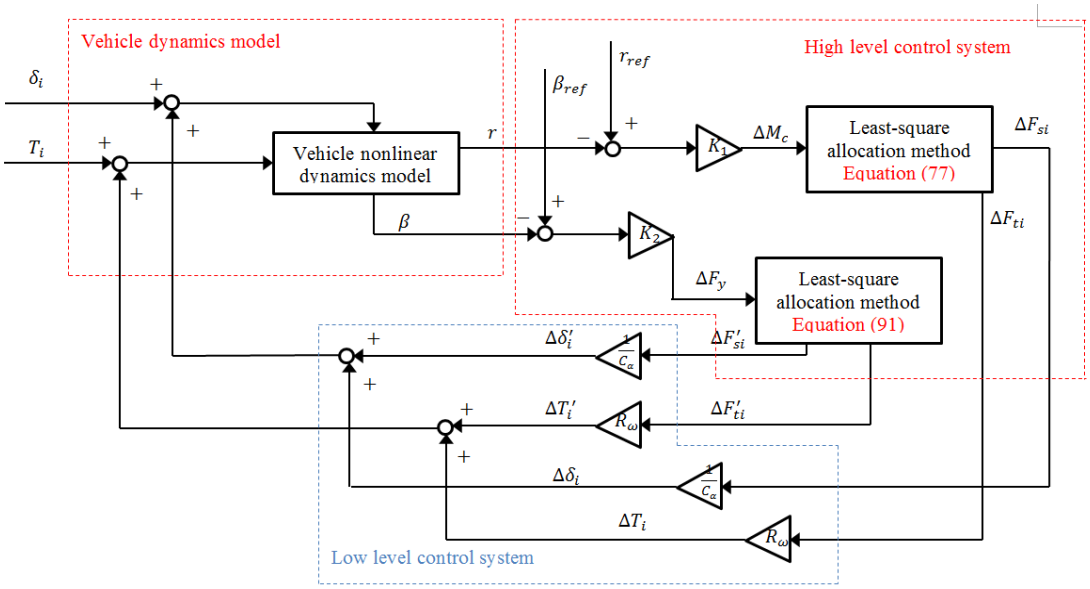

Figure V-1. The block diagram of two-level control allocation method

In total, eight actuators are available for control allocation and the control allocation method consists of a two-level yaw rate controller and a two-level slip angle controller:

1) High level longitudinal and lateral tyre force distribution module for yaw rate controller

Based on the desired vehicle dynamics model, the yaw rate reference r_{ref} is defined and the additional control yaw moment ΔM_c, which will be generated by changing the longitudinal and lateral tyre forces and is used to adjust the yaw moment to compensate the difference between the actual yaw rate and the desired yaw rate, for the yaw rate controller is obtained according to the yaw rate error as:

$$\Delta M_c = K_1 \tilde{r} = K_1 (r_{ref} - r) \tag{73}$$

where r is the actual vehicle yaw rate and r_{ref} is the desired yaw rate. K_1 is the control gain for the yaw rate controller, which will be tuned by a trial and error method.

The desired yaw rate can be calculated by the following equation [100]:

$$r_{ref} = \frac{v_x \delta_f}{(l_f + l_r)(1 + P v_x^2)} \tag{74}$$

where $P = -\frac{m}{2(l_f+l_r)^2}\frac{C_{\alpha f}(l_f-l_r)}{C_{af}C_{ar}}$, which is defined as the stability factor. $C_{\alpha f}$ and $C_{\alpha r}$ are the front tyre and rear tyre cornering stiffness, which is assumed as the same value C_α in this research.

Note in equation (74), the measurement value of longitudinal velocity v_x is required and this value is assumed to be known in this study. The estimation of the longitudinal velocity can be found in section 3.2.1. The high level control system relies on the inputs of steering angle of each wheel ($\delta_{fl}, \delta_{fr}, \delta_{rl}, \delta_{rr}$), traction or brake torque of each wheel ($T_{fl}, T_{fr}, T_{rl}, T_{rr}$), measured actual yaw rate, and yaw acceleration. The signals of steering angles and traction or brake torques are available for the 4WIS-4WID vehicle with in-wheel steering motors and in-wheel driving motors. Yaw rate and yaw acceleration can be obtained through the inertial measurement unit (IMU).

For the 4WID-4WIS EV, the relationship between the tyre force of each individual wheel and the total tyre force or yaw moment is expressed in equations (63). In the high level yaw rate control system, the additional yaw moment will be calculated based on the feedback value of the yaw rate tracking error (73) and the additional total longitudinal and lateral forces will be zeros to avoid influence on longitudinal and lateral motions. Thus, equation (63) is now modified as:

$$A \cdot \Delta F = B \tag{75}$$

where

$$A=\begin{bmatrix} \cos\delta_{fl} & \cos\delta_{fr} & \cos\delta_{rl} & \cos\delta_{rr} \\ \sin\delta_{fl} & \sin\delta_{fr} & \sin\delta_{rl} & \sin\delta_{rr} \\ \frac{b_f}{2}\cos\delta_{fl}+l_f\sin\delta_{fl} & -\frac{b_f}{2}\cos\delta_{fr}+l_f\sin\delta_{fr} & \frac{b_r}{2}\cos\delta_{rl}-l_r\sin\delta_{rl} & -\frac{b_r}{2}\cos\delta_{rr}-l_r\sin\delta_{rr} \\ -\sin\delta_{fl} & -\sin\delta_{fr} & -\sin\delta_{rl} & -\sin\delta_{rr} \\ \cos\delta_{fl} & \cos\delta_{fr} & \cos\delta_{rl} & \cos\delta_{rr} \\ l_f\cos\delta_{fl}-\frac{b_f}{2}\sin\delta_{fl} & l_f\cos\delta_{fr}+\frac{b_f}{2}\sin\delta_{fr} & -l_r\cos\delta_{rl}-\frac{b_r}{2}\sin\delta_{rl} & -l_r\cos\delta_{rr}+\frac{b_r}{2}\sin\delta_{rr} \end{bmatrix}$$

$$\Delta F=\begin{bmatrix} \Delta F_{tfl} \\ \Delta F_{tfr} \\ \Delta F_{trl} \\ \Delta F_{trr} \\ \Delta F_{sfl} \\ \Delta F_{sfr} \\ \Delta F_{srl} \\ \Delta F_{srr} \end{bmatrix}, B=\begin{bmatrix} 0 \\ 0 \\ \Delta M_c \end{bmatrix},$$

ΔF_{ti} and ΔF_{si} $(i = fl, fr, rl, rr)$ are the changes in traction/brake force and side force used to generate the required yaw moment ΔM_c. The relative individual tyre forces ΔF_{ti} and ΔF_{si} are used here (not the absolute value of tyre forces) because they are the additional tyre forces used to generate the required yaw moment, which is calculated from the yaw rate tracking error in equation (73) and is used to compensate for the difference between the actual yaw rate and the desire yaw rate.

To distribute the additional tyre forces according to the required yaw moment in equation (75), the square sum of the product of friction coefficient μ and the work load of each wheel will be used as the performance cost function J [246]:

$$J_{min}=\frac{\rho_1\Delta F_{tfl}^2+\rho_5\Delta F_{sfl}^2}{\mu^2F_{zfl}^2}+\frac{\rho_2\Delta F_{tfr}^2+\rho_6\Delta F_{sfr}^2}{\mu^2F_{zfr}^2}+\frac{\rho_3\Delta F_{trl}^2+\rho_7\Delta F_{srl}^2}{\mu^2F_{zrl}^2}+\frac{\rho_4\Delta F_{trr}^2+\rho_8\Delta F_{srr}^2}{\mu^2F_{zrr}^2} \tag{76}$$

subject to:

$$\sum_{i=fl,fr,rl,rr}\Delta F_{ti}\cos\delta_i-\sum_{i=fl,fr,rl,rr}\Delta F_{si}\sin\delta_i=0 \tag{a}$$

$$\sum_{i=fl,fr,rl,rr}\Delta F_{ti}\sin\delta_i+\sum_{i=fl,fr,rl,rr}\Delta F_{si}\cos\delta_i=0 \tag{b}$$

$$\left(\frac{b_f}{2}\cos\delta_{fl} + l_f\sin\delta_{fl}\right)\Delta F_{tfl} + \left(-\frac{b_f}{2}\cos\delta_{fr} + l_f\sin\delta_{fr}\right)\Delta F_{tfr}$$
$$+ \left(\frac{b_r}{2}\cos\delta_{rl} - l_r\sin\delta_{rl}\right)\Delta F_{trl} + \left(-\frac{b_r}{2}\cos\delta_{rr} - l_r\sin\delta_{rr}\right)\Delta F_{trr}$$
$$+ \left(l_f\cos\delta_{fl} - \frac{b_f}{2}\sin\delta_{fl}\right)\Delta F_{sfl} + \left(l_f\cos\delta_{fr} + \frac{b_f}{2}\sin\delta_{fr}\right)\Delta F_{sfr}$$
$$+ \left(-l_r\cos\delta_{rl} - \frac{b_r}{2}\sin\delta_{rl}\right)\Delta F_{srl} + \left(-l_r\cos\delta_{rr} + \frac{b_r}{2}\sin\delta_{rr}\right)\Delta F_{srr} = \Delta M_c \quad \text{(c)}$$

$$(F_{ti} + \Delta F_{ti})^2 + (F_{si} + \Delta F_{si})^2 \leq \mu^2 F_{zi}^2 \quad \text{(d)}$$

In equation (76), the denominator of the cost function J is the vertical tyre load of the individual wheel. The larger the value of the individual wheel vertical tyre load and friction coefficient, the larger the potential individual tyre forces which can be generated. $\rho_1 - \rho_9$ represent the weighting factors of individual tyre forces. The smaller the weighting factors of the individual tyre forces, the larger the value of the tyre forces which can be distributed in the optimization process. There are a number of ways to solve the optimization problem described by equation (76).

The common method to solve this problem is by using QP to solve the allocation of controlled tyre force at each time step. However, there are a number of non-linear and linear constraints (76)(a-d) in the QP problem which require large computational effort. To realize the real-time tyre force allocation and significantly reduce the computation time, the direct analytical solution of the control allocation problem by the least-square solution can be obtained by the following equation:

$$\Delta F = W^{-1}A^T(AW^{-1}A^T)^{-1}B \quad (77)$$

where A, B can be found in equation (75), which are related to the constraints (76)(a-c) and these constraints are included in the optimized least-square solution.

The weighting matrix W, which describes the cost function J, is determined as follows:

$$W = diag\left(\frac{\rho_1}{\mu^2 F_{zfl}^2}, \frac{\rho_2}{\mu^2 F_{zfr}^2}, \frac{\rho_3}{\mu^2 F_{zrl}^2}, \frac{\rho_4}{\mu^2 F_{zrr}^2}, \frac{\rho_5}{\mu^2 F_{zfl}^2}, \frac{\rho_6}{\mu^2 F_{zfr}^2}, \frac{\rho_7}{\mu^2 F_{zrl}^2}, \frac{\rho_8}{\mu^2 F_{zrr}^2}\right)$$

(78)

The friction circle constraint (76)(d) is neglected in the least-square solution. This is reasonable because the vertical load in the denominator of the cost function J has considered the friction circle. If the specific tyre has small vertical load because of the load transfer effect or decrease of the tyre-road friction coefficient, the denominator of the cost function of the specific tyre is small and any further increase in the tyre force in the numerator will further increase the value of the cost function.

The optimization problem requires the real-time value of vertical load information of each wheel. The vertical load can be calculated from equation (69) in each time step. In equation (69), all the parameters are assumed to be known and the longitudinal and lateral accelerations $\dot{v}_x$ and $\dot{v}_y$ can be measured by the IMUs.

2) Low level individual wheel steering angle and driving or brake torque distribution module

In Section 5.1.1, the required longitudinal tyre force and lateral tyre force are distributed according to the desired yaw rate. The next step is to use suitable steering angle and driving torque to generate the required tyre forces.

In the linear tyre region, the relationship between the longitudinal or lateral force of the tyre and its longitudinal slip ratio or lateral slip angle is linear, and the changing of steering angle and driving torque is also linearly related to the tyre lateral slip angle and the longitudinal slip ratio. Thus, the steering angle and driving torque required to improve the vehicle handling performance can be easily calculated.

Specifically, the relationship between the changed longitudinal tyre force ΔF_{ti} and the changed traction/brake torque ΔT_i can be derived according to the wheel dynamics equation (70).

In the steady state, the changed driving/braking force is determined by the changed traction or brake torque:

$$\Delta T_i = R_\omega \Delta F_{ti}$$

(79)

The relationship between the changed side tyre force ΔF_{si} and the changed side-slip angle $\Delta\alpha_i$ can be assumed as the linear relationship:

$$\Delta F_{si} = C_\alpha \Delta\alpha_i$$

(80)

The relationship between slip angle α_i and steering angle δ_i can be derived according to the kinematic equation of the side-slip angle of each wheel:

$$\alpha_{fl} = \delta_{fl} - atan\left(\frac{v_y + l_f r}{v_x - \frac{1}{2} b_f r}\right)$$

$$\alpha_{fr} = \delta_{fr} - atan\left(\frac{v_y + l_f r}{v_x + \frac{1}{2} b_f r}\right)$$

$$\alpha_{rl} = \delta_{rl} + atan\left(\frac{l_r r - v_y}{v_x - \frac{1}{2} b_r r}\right)$$

$$\alpha_{rr} = \delta_{rr} + atan\left(\frac{l_r r - v_y}{v_x + \frac{1}{2} b_r r}\right)$$

(81)

The longitudinal velocity, lateral velocity and yaw rate are assumed as constants when the small adjusted tyre force is applied in the linear region. Thus, the following assumption is suggested:

$$\Delta\delta_i = \Delta\alpha_i$$

(82)

Then the changed side tyre force is calculated by the changed steering angle as follows:

$$\Delta F_{si} = C_\alpha \Delta\alpha_i = C_\alpha \Delta\delta_i$$

(83)

In the non-linear tyre region, the changing of steering and driving or braking actuators is not related in a linear fashion to the changed tyre force, but the steering and traction or brake

actuators can be adjusted according to the yaw rate feedback in real time to guarantee that the desired yaw rate is tracked. If all eight actuators are utilised, the workload of individual actuators is less than when fewer actuators are utilised (as in front wheel steering and rear wheel driving vehicles). This shows the advantage of an over-actuated vehicle compared to a conventional vehicle and this will be shown in the simulation as well.

If the longitudinal slip ratio or lateral side-slip angle of the individual actuator is so large that the tyre force reaches its friction limit, further increase of the steering angle or the traction or brake torque will impair the vehicle dynamics response. This is because the tyre friction force has reached its maximum value and the tyre force will decrease with the increase of the longitudinal slip ratio or lateral slip angle. Hsu et al. suggested the maximum slip angle α_{sl} when the tyre has lost lateral grip according to Fiala's tyre model as [52]:

$$\alpha_{mi} = \tan^{-1}\left(\frac{3\mu F_{zi}}{C_\alpha}\right) \qquad (i = fl, fr, rl, rr) \tag{84}$$

Similarly, the maximum longitudinal slip ratio s_{mi} can also be calculated according to Fiala's tyre model. Therefore, according to the estimated individual wheel slip angle, slip ratio and their friction limits, weighting factors $\rho_1 - \rho_8$ in equation (78) can be used to adjust the workload of each actuator to prevent the maximum slip angle or longitudinal slip being reached. The default values of $\rho_1 - \rho_8$ are 0.001, which mean all eight actuators are used. According to the slip angle and longitudinal slip ratio performance, if one of the actuators reaches the friction limit, the weighting factor of this actuator will be set as 1, which means this actuator is unused. $\rho_1 - \rho_8$ are defined by the following equations:

$$\rho_1 = \begin{cases} 1 & s_{fl} > s_{mfl} \\ 0.001 & s_{fl} \le s_{mfl} \end{cases}$$

$$\rho_2 = \begin{cases} 1 & s_{fr} > s_{mfr} \\ 0.001 & s_{fr} \le s_{mfr} \end{cases}$$

$$\rho_3 = \begin{cases} 1 & s_{rl} > s_{mrl} \\ 0.001 & s_{rl} \le s_{mrl} \end{cases}$$

$$\rho_4 = \begin{cases} 1 & s_{rr} > s_{mrr} \\ 0.001 & s_{rr} \le s_{mrr} \end{cases}$$

$$\rho_5 = \begin{cases} 1 & a_{fl} > a_{mfl} \\ 0.001 & a_{fl} \le a_{mfl} \end{cases}$$

$$\rho_6 = \begin{cases} 1 & a_{fr} > a_{mfr} \\ 0.001 & a_{fr} \le a_{mfr} \end{cases}$$

$$\rho_7 = \begin{cases} 1 & a_{rl} > a_{mrl} \\ 0.001 & a_{rl} \le a_{mrl} \end{cases}$$

$$\rho_8 = \begin{cases} 1 & a_{rr} > a_{mrr} \\ 0.001 & a_{rr} \le a_{mrr} \end{cases}$$

(85)

The side-slip angle of each wheel is estimated by the side-slip angle estimator described in Section 3.1. The estimation of the vehicle longitudinal velocity, longitudinal slip ratio and friction coefficient has been suggested in Section 3.2. Therefore, in this paper, the longitudinal vehicle velocity, longitudinal tyre slip ratio and tyre-road friction coefficient are simply assumed to be known.

To be more accurate, the calculation of tyre forces and the limitations of steering actuators and electric motors must also be considered by the following:

$$I_\omega \dot{\omega}_i = T_i + \Delta T_i - R_\omega (F_{ti} + \Delta F_{ti})$$

(86)

where $-T_{max} \le T_i + \Delta T_i \le T_{max}$ and $-\delta_{max} \le \delta_i + \Delta\delta_i \le \delta_{max}$.

For the 4WIS-4WID electric vehicle, the limitation of the steering angle is between -90 degrees and 90 degrees ($\delta_{max} = 90$), which is larger than the traditional vehicle [115]. The maximum driving torque of the individual wheel for the electric vehicle is 100 N.m [206].

3) Stability control of vehicle body side-slip angle

When considering the side-slip angle control, based on the desired vehicle body side-slip angle β_{ref}, the adjusted total lateral control force ΔF_y can be calculated as:

$$\Delta F_y = K_2 (\beta_{ref} - \beta)$$

(87)

where β is the estimated side-slip angle and β_{ref} is the desired side-slip angle. K_2 is the control gain for the side-slip angle controller.

Note that vehicle body side-slip angle β can be calculated according to the estimated front left wheel slip angle a_{fl} as:

$$a_{fl} = \beta + \frac{l_f r}{v_x} - \delta_{fl} \tag{88}$$

And the desired vehicle body slip angle is assumed to be zero [100]:

$$\beta_{ref} = 0 \tag{89}$$

The measurement value of longitudinal velocity v_x in equation (88) is required and this value is assumed to be known in this study according to the estimation methods in Section 3.2.

Similar to equation (75), the individually controlled tyre forces can be allocated to generate the required total lateral tyre force ΔF_y by equation (90) in the high level controller. The relative individual tyre forces ΔF_{ti} and ΔF_{si} are used in equation (90) (not the absolute value of tyre force) because the total controlled lateral force is calculated from the relative body slip angle error in equation (87), which can be considered as the relative total lateral tyre force tracking error.

$$A \cdot \Delta F' = B' \tag{90}$$

where $\Delta F' = \begin{bmatrix} \Delta F_{tfl}' \\ \Delta F_{tfr}' \\ \Delta F_{trl}' \\ \Delta F_{trr}' \\ \Delta F_{sfl}' \\ \Delta F_{sfr}' \\ \Delta F_{srl}' \\ \Delta F_{srr}' \end{bmatrix}$, $B' = \begin{bmatrix} 0 \\ \Delta F_y \\ 0 \end{bmatrix}$

Similar to Section 5.1.1, the distributed individual tyre force to control the lateral force error can be calculated by the following least-square solution:

$$\Delta F' = W^{-1}A^T(AW^{-1}A^T)^{-1}B' \tag{91}$$

When the individual tyre side force is distributed, the individual wheel steering angle $\Delta\delta_i$ for side-slip angle control can be simply calculated according to equation (83) in the low level controller.

When considering yaw rate and side-slip angle control together, both ΔF and $\Delta F'$ will be considered to calculate the required additional traction torque and steering angle.

4) Simulation results

In this section, the manoeuvres of combined road type changing and steering are presented to test the performance of the optimal control distribution method. This is because these manoeuvres are more challenging for the drivers and a handling controller and a stability controller are required. The initial tyre-road friction coefficient is 0.9. The simulation parameters are the same as Table III-1.

In the first set of simulations, the vehicle is moving like the traditional front wheel steering and rear wheel drive vehicle. The initial velocity of the vehicle is 20 m/s and the front wheel steering angle $\delta_f = 5$ degree, which is presented in Figure V-2. Figure V-3 shows the vehicle yaw rate and side-slip angle response when only yaw rate controller is implemented, while Figure V-5 presents the dynamics responses when the combined yaw rate and side-slip angle controller is utilised. Figure V-4 and Figure V-6 present the adjusted steering angle and traction or brake torque of each wheel for the above two situations. The desired vehicle responses and the actual vehicle responses without the controller are also presented for comparison. In addition, to verify the effectiveness of the proposed method, the simulation results of two other existing combined yaw rate and body side-slip angle control methods in the literature are also presented. The first method (Method 1) is the vehicle stability and fault-tolerant control method, based on a combined active front wheel steering and rear wheel steering, while the function of fault-tolerant control is neglected in this comparison study [58]. In Method 2, the feedforward type of tyre force distribution method for motion control of a full drive-by-wire electric vehicle is presented [59]. The control targets are vehicle stability

control and tyre energy dissipation control, while the lateral one is neglected in this comparison study.

In Figure V-3, the yaw rate response controlled by the proposed yaw rate controller and Method 1 show their advantage over Method 2, but the body side-slip angle response show a big disadvantage. When the proposed combined yaw rate and side-slip angle controller is utilised in Figure V-5, both the yaw rate response and the side-slip angle response are improved and show overall advantage over other existing methods. This illustrates the advantage of combined yaw rate and side-slip angle controller.

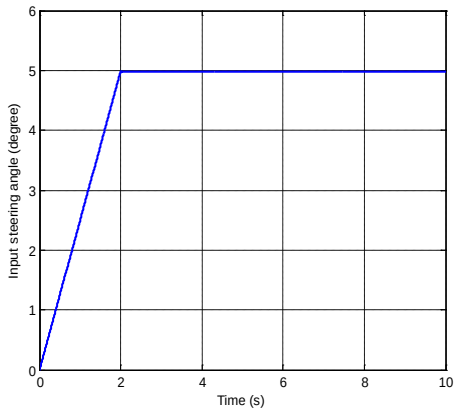

Figure V-2. Vehicle input steering angle

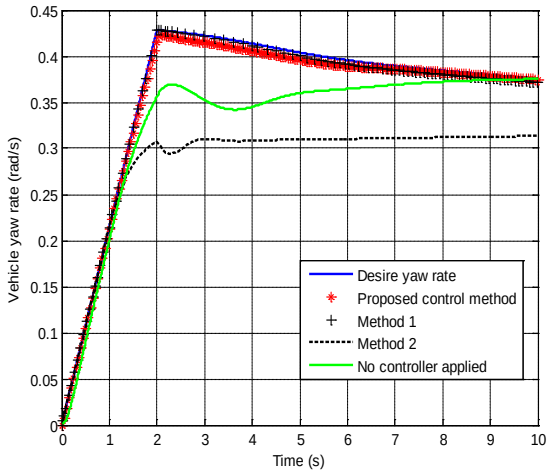

(a) Yaw rate of CG.

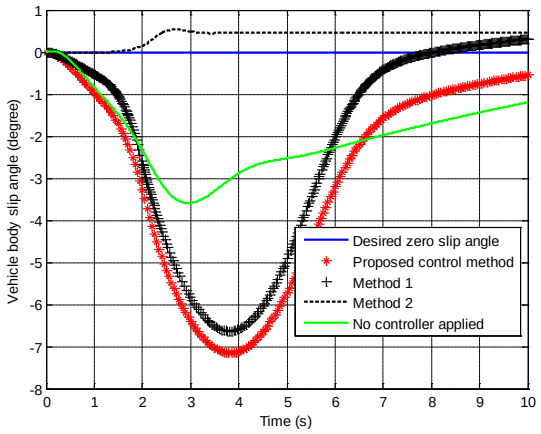

(b) Side-slip angle of CG.

Figure V-3. Vehicle dynamics response when yaw rate controller is applied.

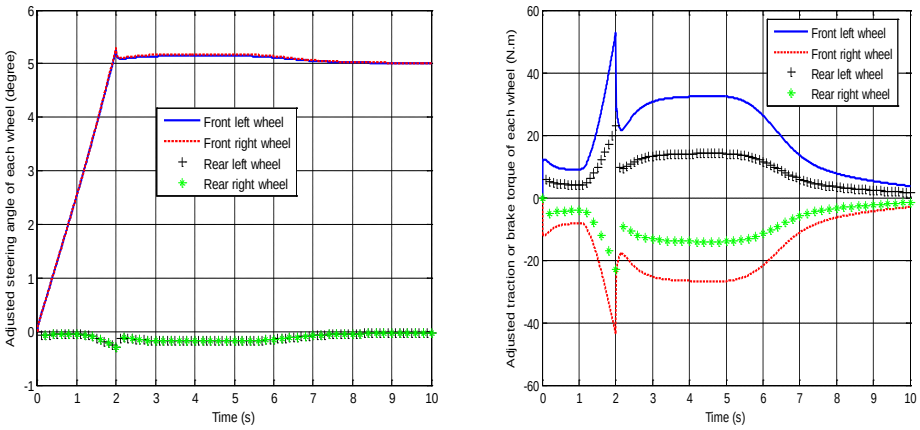

Figure V-4. Adjusted individual wheel steering angle (left figure) and traction or brake torque of each wheel (right figure)

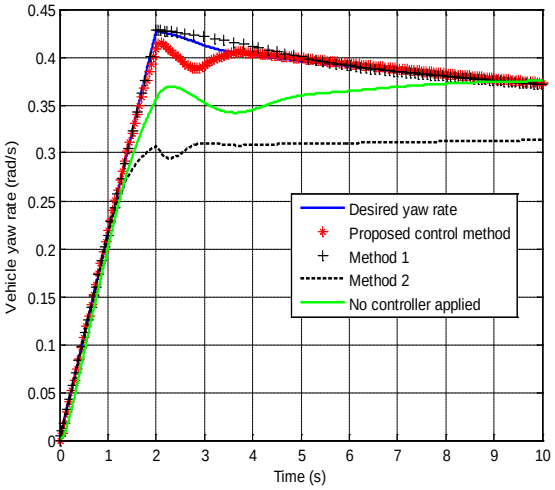

(a) Yaw rate of CG.

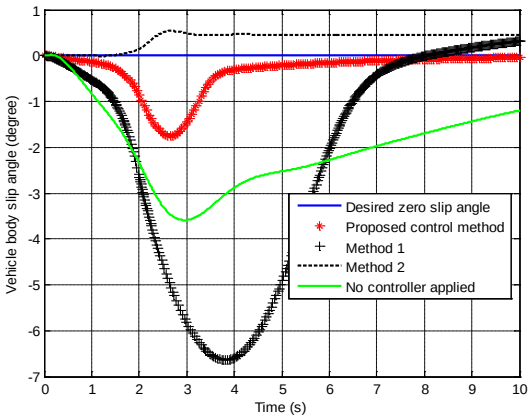

(b) Side-slip angle of CG.

Figure V-5. Vehicle dynamics response when combined yaw rate and slip angle controller is applied.

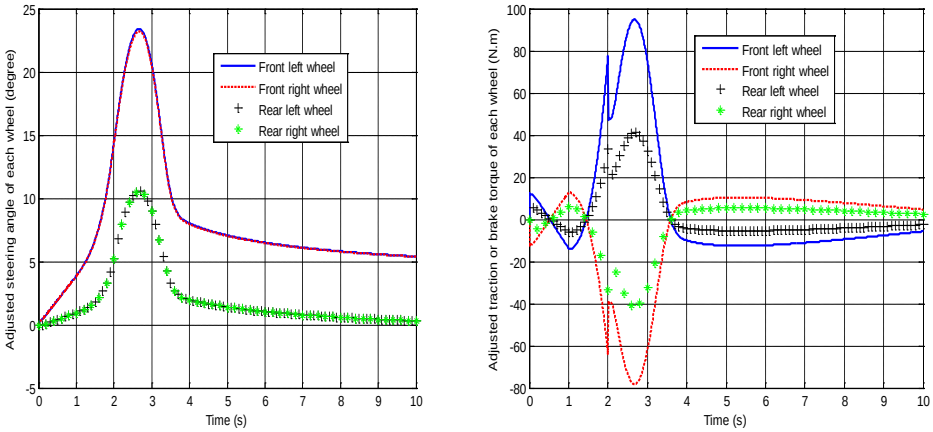

Figure V-6. Adjusted individual wheel steering angle (left figure) and traction or brake torque of individual wheel (right figure)

The first set of simulations simulate the yaw rate control and side-slip angle control for traditional vehicle motion with a small steering angle, all of which has been extensively studied [176] [246], but there are fewer studies on the yaw control and side-slip angle control of a 4WIS-4WID vehicle with large steering angle and a high non-linear characteristic. This kind of motion can improve the mobility of the vehicle in narrow metropolitan spaces, as presented in the following second set of simulations.

In the second set of simulations, the test vehicle is moving in a J-turn with a front wheel steering angle of 1 rad (approximate 57.3 degree) for the traditional vehicle. For the 4WIS-4WID electric vehicle, the individual wheel steering angles are 29.94 degrees for the front left wheel, 17.5 degrees for the front right wheel, -39.95 degrees for the rear left wheel and -24.63 degrees for the rear right wheel. The vehicle's initial velocity is 5 m/s and the friction coefficient is changed from 0.9 into 0.5 in 5 seconds. The input values are shown in Figure V-7.

To compare this with the conventional front wheel steering and rear wheel drive vehicle, conventional vehicle performance when only utilising open-loop front wheel steering is denoted as "No controller applied" in Figure V-8. For the proposed combined control strategy, all four wheel steering angles and four wheel traction/brake torques (8 actuators) are used to control the vehicle. The vehicle dynamics responses controlled by the proposed controller are shown in Figure V-8 and the adjusted values of the actuators are presented in Figure V-9. For the purpose of comparison, the simulation results of dynamics performance of Method 1 and Method 2 are also presented in Figure V-8.

In Figure V-8, the yaw rate response and the side-slip angle response show a large advantage over other methods when the proposed controller is applied. This suggests that the proposed optimal actuator force distributor can successfully track the desired yaw rate and improve the side-slip angle response especially in the large steering angle moving condition for the 4WIS-4WID vehicle.

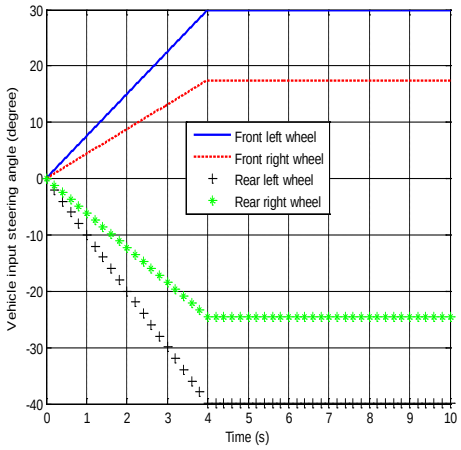

(a) Input steering angle

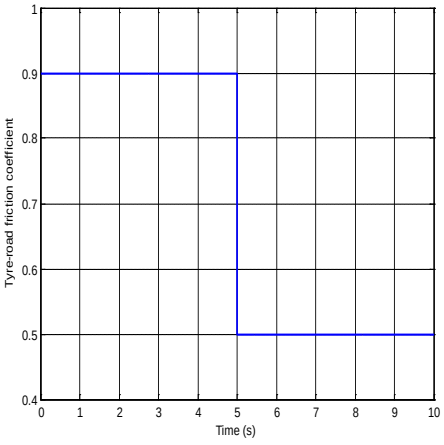

(b) Changed friction coefficient

Figure V-7. Vehicle input steering angle (left figure) and input driving torque (right figure) in the second set of simulation.

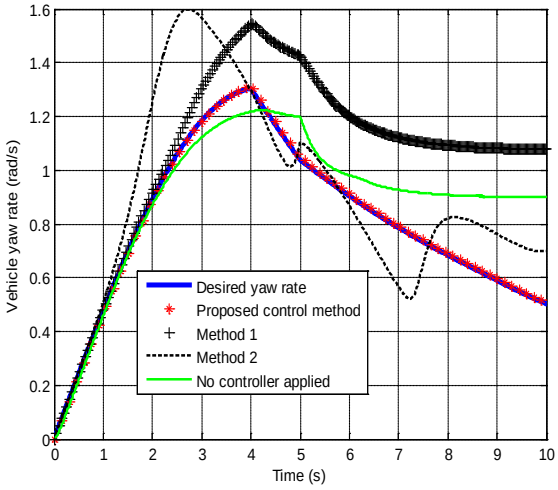

(a) Yaw rate of C.G.

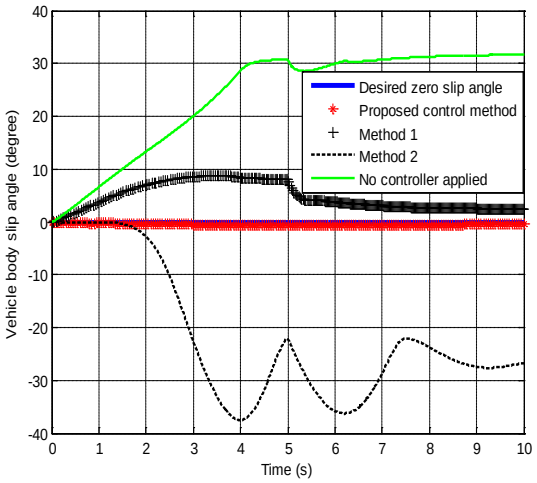

(b) Side-slip angle of CG.

Figure V-8. Comparison of vehicle dynamics responses in the second set of simulation.

5) Conclusion

In conclusion, the simulation results prove that the proposed controller can successfully track the desired yaw rate and side-slip angle and show advantages over the other two existing control methods both in the scenario of large radius turning for the traditional vehicle and that of small radius turning for the 4WIS-4WID EV.

The yaw rate feedback controller based on controlling the additional yaw moment is proved to be able to accurately track the desired yaw rate, but the body side-slip angle response is compromised. Thus, a body side-slip angle feedback controller based on controlling additional total lateral tyre force is proposed and the combined yaw rate and body side-slip angle controller shows good control of both the yaw rate response and the body side-slip angle response. This study proves that adding yaw rate control and side-slip angle control results in an overall improvement in total performance.

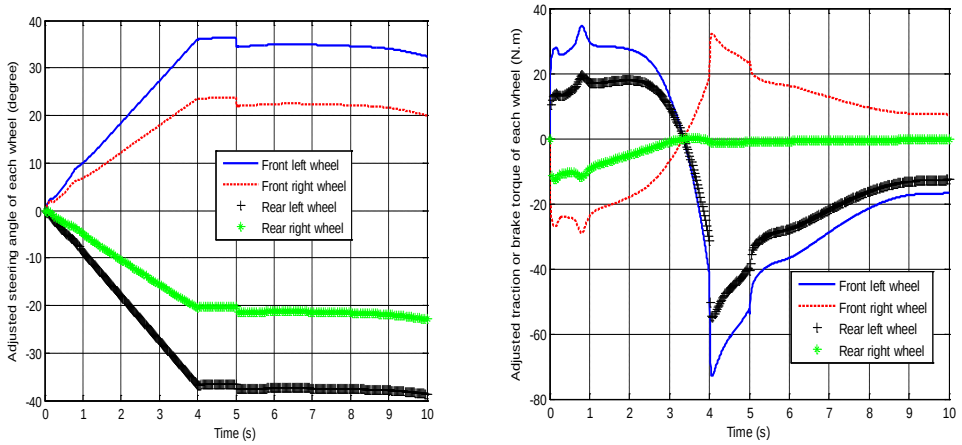

(a) Adjusted steering angle (b) Adjusted traction or brake torque

Figure V-9. Adjusted steering angle (left figure) and traction or brake torque (right figure) of four wheels in the second set of simulation.

2. Two-level non-linear control allocation method

In the above section, linear feedback method is applied to tracking the desired yaw rate and body side-slip angle. The linear feedback method, however, need to manually tune the feedback control gain and is less robust to the non-linear characteristic of the system. This section proposes the two-level non-linear control allocation method where the genetic algorithm is applied to automatically tune the feedback control gain and the robustness of the controller is improved. According to the desired control targets, the upper level controller is used to determine the ideal distributed tyre force for each wheel and the lower level controller aims to map the desired tyre force of each wheel to the control command of each driving or steering actuator. Figure V-10 shows the block diagram of the whole tyre force optimal distribution control system.

For traditional vehicles, the driver's steering input is directly connected to the steering wheel, while the driver's acceleration pedal is linked to the throttle of the engine and the brake pedal is connected to the brake system. For EVs with in-wheel motors, a new control system can be designed so that the driver is only required to determine the virtual input steering angle, and traction or braking torque, and the control allocation method can automatically control the individual actuators based on the virtual control inputs. The control system can guarantee the stability and handling of the vehicle. This can significantly decrease the driver's workload and the vehicle dynamics performance can be improved by this automatic control system.

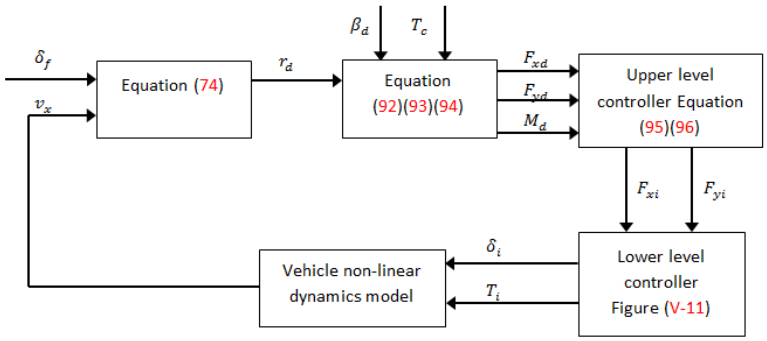

Figure V-10. Block diagram of the control allocation system.

1) Design of tyre longitudinal force and lateral force controller in the upper level

In the upper level, a tyre force controller is designed to obtain the optimal longitudinal and lateral forces for each wheel according to the desired vehicle yaw rate and body side-slip angle. In addition, in order to avoid severe loading on an individual tyre during vehicle motion, the workload of each individual wheel must be minimised.

The yaw rate control aims to improve vehicle handling. The desired yaw rate r_d can be calculated by equation (74). v_x is the vehicle longitudinal velocity, which, here, we assume to be known.

Body side-slip angle control can improve vehicle stability and the desired body side-slip angle is zero ($\beta_d = 0$) [100]. The desired total longitudinal force F_{xd}, total lateral force F_{yd} and yaw moment M_d can be determined based on the desired yaw rate and body slip angle as:

$$M_d = I_z \dot{r}_d \tag{92}$$

$$F_{yd} = mv_x\left(\dot{\beta}_d + r_d\right) = mv_x r_d \tag{93}$$

$$F_{xd} = \frac{T_c}{R_w} \tag{94}$$

where T_c is the driving input from the driver. In (93), the total desired lateral tyre force F_{yd} is determined by $mv_x\left(\dot{\beta}_d + r_d\right)$ [247]. We have assumed that the desired body side-slip angle β_d is equal to zero and consequently the derivative of the desired body side-slip angle $\dot{\beta}_d$ also equals zero. Thus, F_{yd} is determined by $mv_x r_d$. In this system, the driver is only required to determine the virtual input steering angle δ_f and the virtual driving torque T_c. Then the upper level control system will automatically calculate the desired yaw rate and body side-slip angle, and consequently the desired total longitudinal force, total lateral force and total yaw moment can be determined.

It should be noted that if the driver wants to maintain a constant velocity when turning, the desired total longitudinal force F_{xd} must be zero and the longitudinal vehicle velocity v_x in equations (92)(93)(94) is the constant value of the initial velocity. This is because when the vehicle is turning at a constant velocity, the motion is a uniform circular motion. The longitudinal acceleration is zero, and the lateral acceleration is the centripetal acceleration in the uniform circular motion. Accordingly, the total longitudinal force F_{xd} should be zero, and the total lateral tyre force F_{yd} provides the centripetal force. This means the control system will automatically adjust the driving actuators to maintain zero total longitudinal tyre force when turning.

In summary, the cost function of the upper level controller is defined as:

$$J_1 = \frac{a}{2}\sum_{i=1}^{4}\frac{F_{xi}^2 + F_{yi}^2}{F_{zi}^2} + \frac{b}{2}\left(F_{xd} - \left(F_{xfl} + F_{xfr} + F_{xrl} + F_{xrr}\right)\right)^2 + \frac{c}{2}\left(F_{yd} - \left(F_{yfl} + F_{yfr} + F_{yrl} + F_{yrr}\right)\right)^2 +$$

$$\frac{d}{2}\left(M_d - \left(l_f\left(F_{yfl}+F_{yfr}\right) - l_r\left(F_{yrl}+F_{yrr}\right) + \frac{b_f}{2}\left(F_{xfl}-F_{xfr}\right) + \frac{b_r}{2}\left(F_{xrl}-F_{xrr}\right)\right)\right)^2$$

(95)

where a,b,c and d are four scaling factors which determine the weight of each term. The range of each scaling factor is between 0 and 1. The larger the value of the scaling factor, the greater the weight of the corresponding term in the cost function. In the default setting, all the scaling factors are assumed to be 1, since the four terms are assumed to have equal priority, and each value of the scaling factor can be decreased so that the corresponding term has less weight. When F_{xd}, F_{yd} and M_d are determined, the objective cost function (95) has eight variables (F_{xi} and F_{yi}). The minimised value can be obtained by calculating the partial differential of the objective function as:

$$\frac{\partial J_1}{\partial F_{xfl}}=0, \frac{\partial J_1}{\partial F_{xfr}}=0, \frac{\partial J_1}{\partial F_{xrl}}=0, \frac{\partial J_1}{\partial F_{xrr}}=0, \frac{\partial J_1}{\partial F_{yfl}}=0, \frac{\partial J_1}{\partial F_{yfr}}=0, \frac{\partial J_1}{\partial F_{yrl}}=0, \frac{\partial J_1}{\partial F_{yrr}}=0$$

(96)

Equation (96) calculates the optimal distributed tyre forces along the x and the y-axes.

2) Design of tyre longitudinal slip ratio and lateral slip angle controllers in the lower level

In the upper level, the desired tyre forces are obtained according to the driver's virtual steering input δ_f and virtual driving input T_c. When the desired longitudinal and lateral tyre forces are determined, the next problem is how to most accurately map the desired tyre forces into the actual inputs of the steering angle and driving torque of each actuator. It should be noted that the driver cannot directly control the individual steering and driving actuators of each wheel in this study and these actual steering and driving actuators are controlled by the proposed two-level distribution control system.

Before mapping the tyre forces into the command of each individual actuator, the tyre forces must be mapped into the directions along the tyre (traction or brake force F_{ti}) and perpendicular to the tyre (side force F_{si}) according to equation (64) as:

$$F_{ti} = \frac{F_{xi}+F_{yi}}{(1+\tan\delta_i)\cos\delta_i} \quad \text{(a)}$$

$$F_{si} = \frac{F_{yi} - F_{xi}\tan\delta_i}{\sin\delta_i + \frac{\tan\delta_i}{\cos\delta_i}} \quad \text{(b)}$$

(97)

Suzuki et al. used the simple linear relations between the steering angle, driving torque and side force F_{si} or traction or brake force F_{ti} as shown in equations (98)(99). [247]

$$F_{sfl} = -C_a\left(\beta + \frac{l_f r}{v_x} - \delta_{fl}\right)$$

$$F_{sfr} = -C_a\left(\beta + \frac{l_f r}{v_x} - \delta_{fr}\right)$$

$$F_{srl} = -C_a\left(\beta - \frac{l_r r}{v_x} - \delta_{rl}\right)$$

$$F_{srr} = -C_a\left(\beta - \frac{l_r r}{v_x} - \delta_{rr}\right)$$

(98)

$$T_i = R_w F_{ti}$$

(99)

In equation (98), β is the vehicle body side-slip angle.

For the linear model, however, the distributed steering and driving actuators cannot accurately obtain the desired tyre force when the tyre is working in the non-linear tyre region. Thus, new slip ratio and the slip angle controllers of each individual wheel are proposed in this section to deal with the non-linear characteristics of the tyre. Specifically, a PI slip ratio controller and a PI slip angle controller are designed for each wheel. The PI longitudinal slip ratio controller is defined as follows:

$$\Delta T_i = K_{sip}(s_{id} - s_i) + K_{sii}\int (s_{id} - s_i)$$

(100)

where ΔT_i is the adjusted driving torque of each wheel, which is added into the distributed driving torque T_i obtained from the linear model (99). s_i represents the actual slip ratio obtained from the vehicle dynamics model and s_{di} represents the desired slip ratio

considering non-linear tyre characteristics. K_{sip} is the proportional control gain and K_{sii} is the integral control gain.

It should be noted that based on the theory of PID (proportional, integral, and derivative) controllers, the simple P controller, the PI controller and the PID controller have all been considered and tested in this study. Doing this, however, showed that the PI controller could decrease the convergence steps more efficiently than the P controller, and the PID controller was only marginally better than the PI controller. For these reasons, the PI controller is used here.

The PI lateral slip angle controller is presented as:

$$\Delta\delta_i = K_{aip}(a_{id} - a_i) + K_{aii}\int(a_{id} - a_i) \tag{101}$$

where $\Delta\delta_i$ is the adjusted steering angle of each wheel, which is added into the distributed steering angle δ_i calculated from the linear model (98). a_i represents the actual side-slip angle of the individual wheel obtained from the vehicle dynamics model and a_{di} represents the desired side-slip angle of the individual wheel when considering the non-linear tyre characteristics. K_{aip} is the proportional control gain and K_{aii} is the integral control gain.

It should be noted that the desired wheel side-slip angle and slip ratio are calculated by the inverse Dugoff tyre model (102) according to equation (65), and the actual values of the side-slip angle and the slip ratio are obtained from the vehicle dynamics model and assumed to be known in this study. Note that the desired slip ratio $s_{di}(t)$ and slip angle $a_{di}(t)$ at the current time instance need the information from previous samples $s_{di}(t-1)$ and $f(\lambda)(t-1)$.

$$s_{di}(t) = \frac{F_{ti}(t)\left(1-s_{di}(t-1)\right)}{C_s f(\lambda)(t-1)} \tag{a}$$

$$a_{di}(t) = \tan^{-1}\frac{F_{si}(t)\left(1-s_{di}(t-1)\right)}{C_a f(\lambda)(t-1)} \tag{b}$$

(102)

Estimation of the longitudinal velocity, longitudinal slip ratio, friction coefficient and lateral side-slip angle of the vehicle has been done previously in section 3.1 and 3.2. Thus, in this

paper, the longitudinal velocity of the vehicle, the longitudinal slip ratio and lateral side-slip angle of the tyre are assumed to be known.

Figure V-11 shows the whole system diagram of the longitudinal slip ratio and lateral side-slip angle PI controllers in the lower level control system, which are described by equation (102). When the PI controllers are applied, the controlled steering and driving actuators will interact with the vehicle motion according to the non-linear dynamics model.

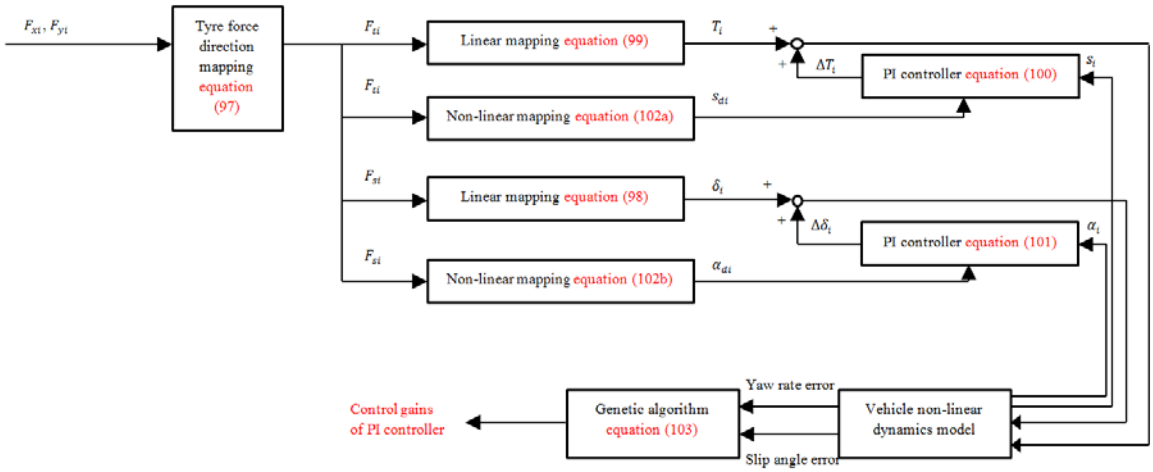

Figure V-11. Block diagram of the lower level distribution control system.

3) Application of GA to determine the control gains of PI controllers

In the slip ratio and side-slip angle controllers, there are a total of 16 feedback control gains which must be determined. These control gains are difficult to find by trial-and-error. GA is applied here to optimally determine the control feedback gains. GA originated from the computer science field of artificial intelligence, which is a type of search heuristics which mimics the process of natural selection. GA can significantly improve the searching efficiency and fast determine the feedback control gains, which shows advantageous over traditional searching algorithm. For the use of GA, a solution domain and the fitness function are required. For the proposed PI slip ratio and side-slip angle controllers, the solution domain of the control gains is defined as positive. The fitness function J_2 is determined by the following equation:

$$J_2 = \sum_{t=0}^{T} \left(A e_{yaw\_rate}^2 + B e_{slip\_angle}^2 \right)$$

(103)

where e_{yaw_rate} represents the difference between the desired yaw rate and the actual yaw rate when the non-linear control method is applied. e_{slip_angle} represents the difference between the desired zero body side-slip angle and the actual vehicle body side-slip angle when the non-linear control method is applied. A and B are the scaling factors of the yaw rate error and slip angle error. The range of the scaling factors is between 0 and 1. The default value of A and B is 1. This value can be decreased so that the corresponding term has less weight in the optimal cost function J_2.

Simulations of vehicle motion are conducted to calculate the fitness function and the optimal solution can be determined after a number of fitness functions have been calculated and evaluated. Specifically, based on the solution domain, the initial random populations, which are the control gains of the PI controllers, are generated first. The fitness of each solution is then evaluated based on equation (103) and the most suitable parents are selected. Then the child solutions are created from the selected parents using single point crossover and the children solutions are subjected to the crossover and mutation operations. Finally, the parent generation is replaced by the child generation and the evaluation cycle continues until the termination criterion is met and the results of control gains are determined [248]. In this study, the termination criterion is that either the maximum generation is reached or the tolerance of the fitness function is met. Figure V-12 shows the whole working procedure of GA.

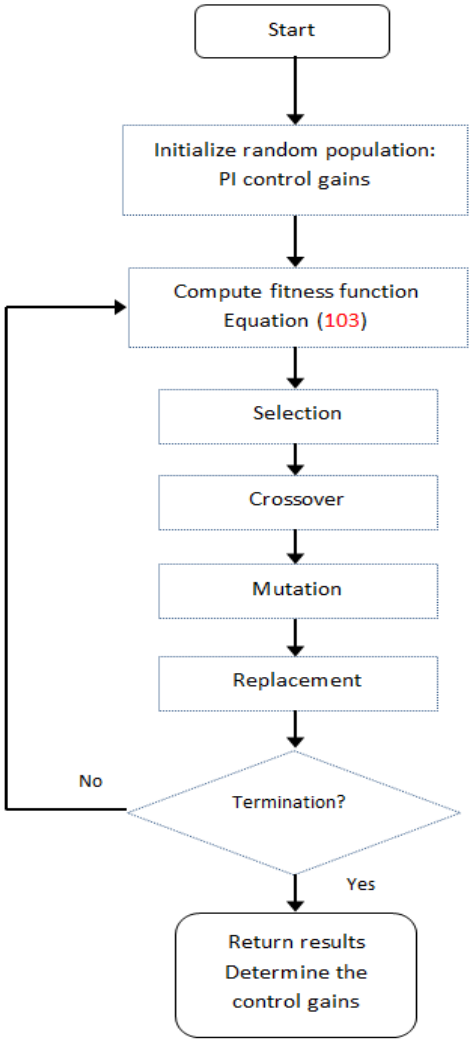

Figure V-12. Flow chart of GA.

4) Simulation results

To test the dynamics performance of the suggested optimal non-linear control allocation method, numerical simulations are conducted in various vehicle moving conditions. The parameter values used in the simulations are listed in Table V-1. First, the preliminary simulations are conducted to determine the 16 control gains of the PI controllers using GA. Then, simulations are conducted to test the control performance under various conditions.

Table V-1. Parameter values used in simulations of nonlinear control allocation method. [100]

A	Scaling factor of yaw rate error in the fitness function of	1

	genetic algorithm	
B	Scaling factor of body slip angle error in the fitness function of genetic algorithm	1
a	Scaling factors in the cost function of upper level controller	1
b	Scaling factors in the cost function of upper level controller	1
c	Scaling factors in the cost function of upper level controller	1
d	Scaling factors in the cost function of upper level controller	1

a) *Preliminary simulations to determine the control gains*

In the GA, the domain of the proportional control gain is (0, 100) and the domain of the integral control gain is (0, 100). The population is set as 50 and the generation is 150. To calculate the fitness function, the conditions of the preliminary simulations must be chosen. These must be chosen carefully since it is expected that the control gains determined in the preliminary simulations can apply to the controllers used in various vehicle moving conditions. In this study, three sets of preliminary simulations are conducted at different initial longitudinal velocities in order to determine the control gains, which are 10 m/s, 12.5 m/s and 15 m/s. Based on these three preliminary simulations, only the vehicle dynamics performance with the velocity between 10 m/s and 15 m/s is examined in this simulation section as examples. Vehicle motion with velocity beyond this range can be analysed using a similar approach but is not to be discussed in this paper.

In the first preliminary simulation, the initial velocity is 10 m/s and the friction coefficient is 0.9. The vehicle is performing a J-turn manoeuvre and the steering input is shown in Figure V-13.

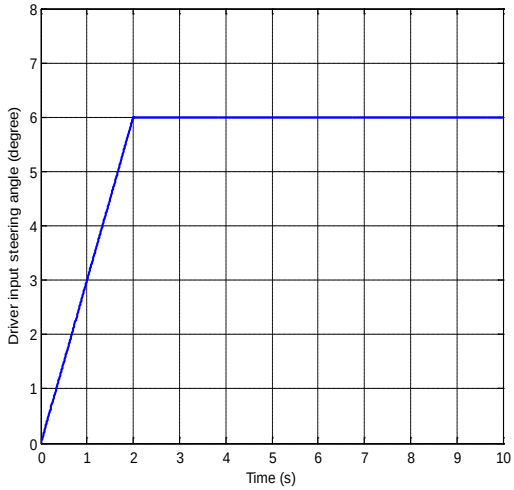

Figure V-13. Driver's input steering angle during a J-turn manoeuvre.

As the generation number increases, cost function J_2 in equation (103) decreases, as shown in Figure V-14. The finally determined control gains are shown in Table V-2.

Table V-2. Determined PI control gains in the first preliminary simulation

K_{sflp}	3.6991	K_{sfrp}	1.1656
K_{sfli}	2.4235	K_{sfri}	7.0466
K_{srlp}	5.4314	K_{srrp}	7.0470
K_{srli}	3.7549	K_{srri}	2.4243
K_{aflp}	3.5468	K_{afrp}	1.5596
K_{afli}	13.8790	K_{afri}	14.9479
K_{arlp}	6.0527	K_{arrp}	2.1615
K_{arli}	0.0567	K_{arri}	6.3381

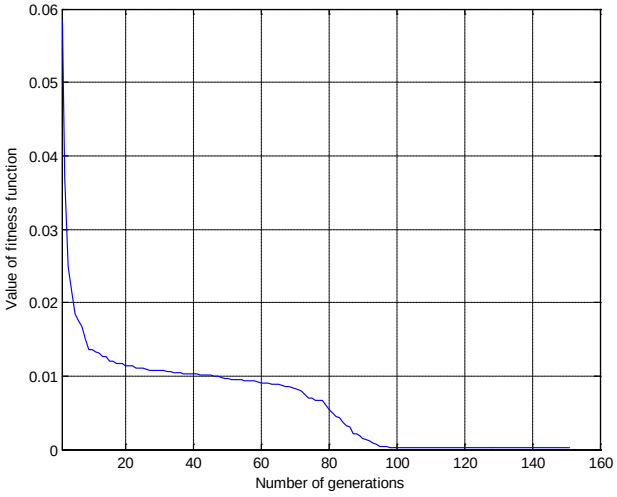

Figure V-14. The evolution of cost function $\boldsymbol{J_2}$.

In the same manner, the second and third preliminary simulations are conducted and the PI control gains are summarised in Table V-3 and Table V-4.

Table V-3. Determined PI control gains in the second preliminary simulation

K_{sflp}	9.3171	K_{sfrp}	5.6386
K_{sfli}	8.8754	K_{sfri}	7.2875
K_{srlp}	12.2399	K_{srrp}	8.1320
K_{srli}	9.9795	K_{srri}	11.8256
K_{aflp}	17.4289	K_{afrp}	17.2962
K_{afli}	24.3627	K_{afri}	18.8589
K_{arlp}	0.8027	K_{arrp}	4.5018
K_{arli}	0.6040	K_{arri}	0.3321

Table V-4. Determined PI control gains in the third preliminary simulation

K_{sflp}	3.8171	K_{sfrp}	4.6622
K_{sfli}	4.7184	K_{sfri}	4.6527
K_{srlp}	2.4899	K_{srrp}	7.2317
K_{srli}	1.9046	K_{srri}	3.1343
K_{aflp}	4.6789	K_{afrp}	9.6797
K_{afli}	1.0952	K_{afri}	13.8589
K_{arlp}	5.2920	K_{arrp}	4.3330
K_{arli}	6.9648	K_{arri}	0.0103

Figure V-14 shows the total control error as it changes with the vehicle velocity by using three different groups of control gains in the simulation of simple J-turning. The steering input of the simulation is the same as Figure V-13. The total control error is actually the value of fitness function J_2 which is defined in equation (103). According to Figure V-15, the three groups of PI controller gains can all control the vehicle yaw rate and body slip angle well when the velocity is between 10 m/s and 15 m/s. However, each specific group of control gains is better at controlling performance within a specific range of vehicle velocity. The PI control gains in Table V-2 can achieve the best control performance between 10 m/s and 11.5 m/s. The control gains in Table V-3 and Table V-4 can achieve the best control performance during the velocity range $[11.5 \quad 13.5]$ m/s and $[13.5 \quad 15]$ m/s respectively. During the transition between any two adjacent velocity ranges, the abrupt change of control gains may deteriorate the control performance. To prevent this kind of problem, the interpolation

method can be used. For example, during the transition velocity around 11.5 m/s, the total transition range is assumed to be 0.5 m/s (from 11.25m/s to 11.75 m/s) and the control gains used in the transition period can be calculated as follows:

$$K_T = \frac{11.75 - v_x}{0.5} K_1 + \frac{v_x - 11.25}{0.5} K_2 \tag{104}$$

where K_T is the group of control gains used in the transition period. K_1 and K_2 are groups of control gains given in Table V-3 and Table V-4 respectively.

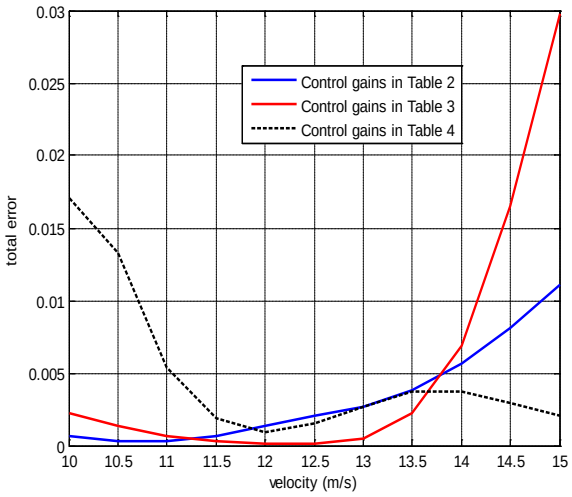

Figure V-15. The total control error with respect to vehicle velocity and control gains.

b) *Simulation results of the control allocation method*

Once the control gains of the PI controllers have been determined, the optimal non-linear vehicle dynamics controller with the optimal control gains can be tested under various driving conditions.

First, the vehicle performs a J-turn at an initial velocity of 15 m/s. The PI control gains in Table V-4 can be used and the friction coefficient is 0.9. The driver's input steering angle is the same as in Figure V-13. The vehicle yaw rate response and body side-slip angle response are shown in Figure V-16 and Figure V-17, respectively. For the purpose of comparison, the simulation result of the linear optimal control allocation method using equations (98)-(99) is

also presented. The simulation performance is also presented when no optimal tyre force distribution method is applied. When no tyre force controller is applied, the driver's input steering angle is directly applied to the two front wheels of the vehicle and the driver's input driving torque is equally distributed to the two rear wheels, which is similar to the traditional front wheel steer and rear wheel drive vehicle.

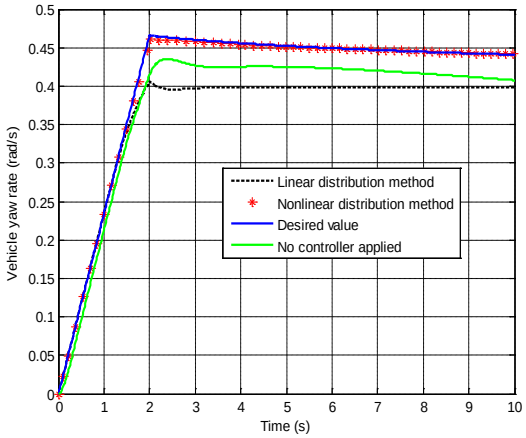

Figure V-16. The vehicle yaw rate response in the J-turn simulation.

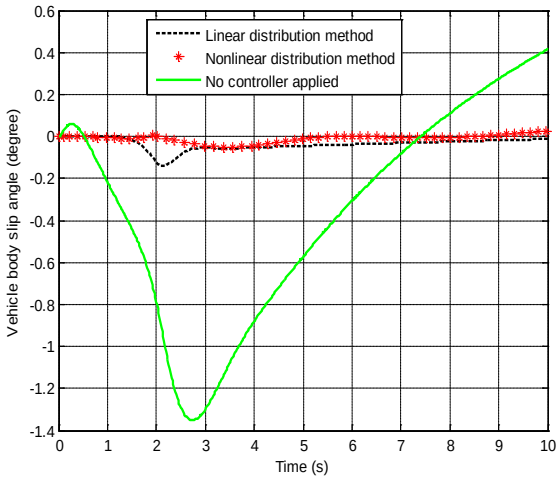

Figure V-17. The vehicle body side-slip angle in the J-turn simulation.

According to Figure V-16 and Figure V-17, the linear tyre force distribution method performs well in controlling the body side-slip angle, but the yaw rate response is compromised. This is because the linear method assumes a linear vehicle dynamics relationship, and the non-linear tyre characteristic is neglected. To achieve the desired tyre force, a larger side-slip angle or slip ratio of the individual wheel is required if the non-linear tyre characteristic is

considered. Thus, the output yaw rate obtained from the linear method is smaller than the desired value because a smaller individual slip ratio and side-slip angle is achieved. The non-linear method considers the non-linear tyre characteristic and consequently the yaw rate achieves the desired value. The body side-slip angle response in the non-linear method is equal to that achieved in the linear method, but, as explained above, the yaw rate performance of the non-linear method is far better.

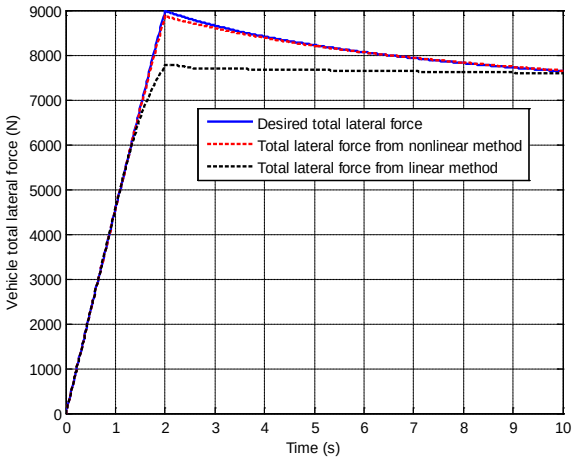

Figure V-18. The total lateral tyre force in the J-turn simulation.

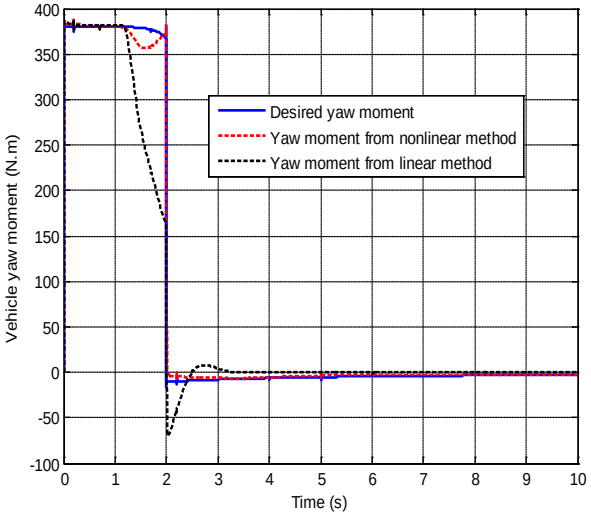

Figure V-19. The yaw moment in the J-turn simulation.

In Figure V-18 and Figure V-19, the non-linear method proposed in this study can achieve the desired total lateral tyre force and yaw moment. According to equations (92) and (93), if the desired total lateral tyre force and yaw moment are achieved, the desired yaw rate and

body side-slip angle can be achieved, as shown in Figure V-16 and Figure V-17. When the linear method is applied, the total lateral tyre force and yaw moment cannot reach the desired value because of the non-linear tyre characteristic. This means that the desired yaw rate cannot be achieved. This is shown in Figure V-16. It should be noted that there is a small difference between the total lateral force and yaw moment controlled by the non-linear method and the desired values at 2 seconds, as shown in Figure V-18 and Figure V-19, and this causes the small difference between the yaw rate controlled by the non-linear method and the desired value in 2 seconds in Figure V-16. In Figure V-20 and Figure V-21, the individual wheel side-slip angle controller and the slip ratio controller are proved to successfully achieve the desired values in the non-linear method.

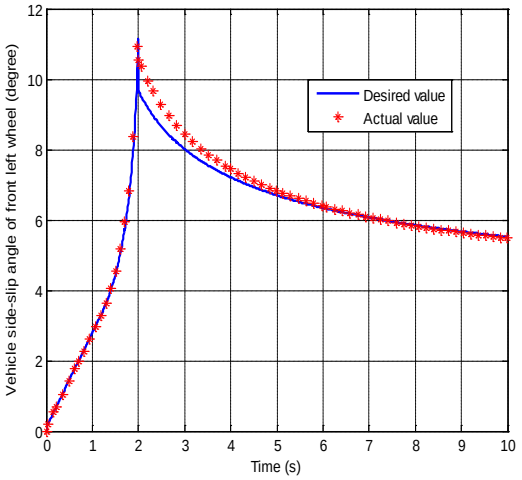

(a)

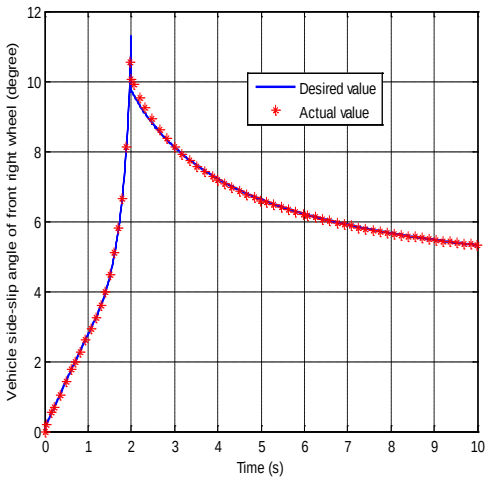

(b)

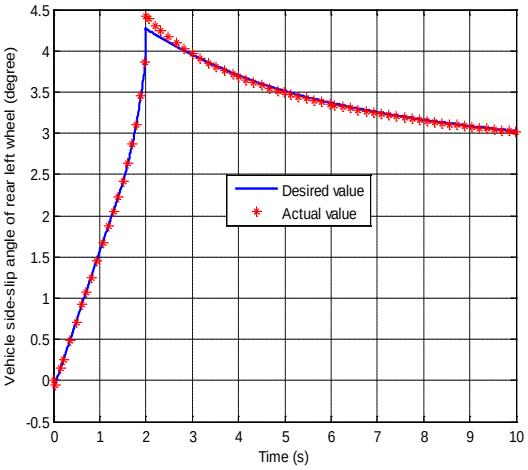

(c)

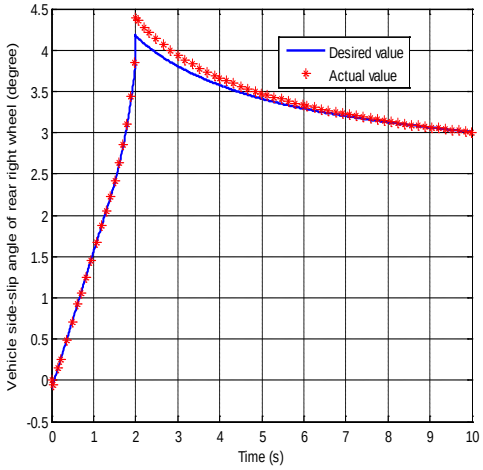

(d)

Figure V-20. The individual wheel side-slip angle in the J-turn simulation controlled by the non-linear method: (a) front left wheel (b) front right wheel (c) rear left wheel (d) rear right wheel.

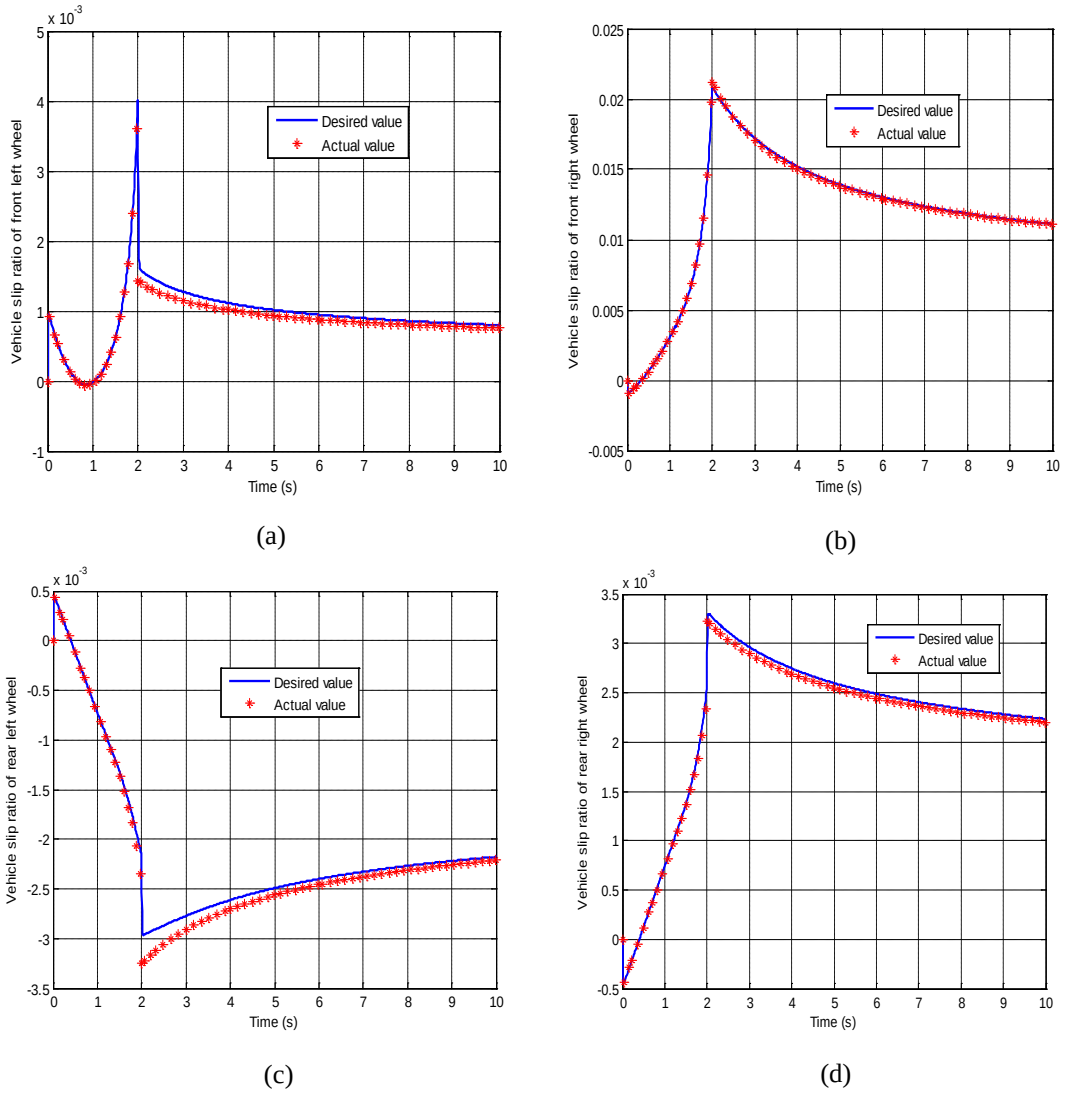

Figure V-21. The individual wheel slip ratio in the J-turn simulation controlled by the non-linear method: (a) front left wheel (b) front right wheel (c) rear left wheel (d) rear right wheel.

The second simulation is the lane change motion. The initial vehicle velocity is changed to 10 m/s and the PI control gains in Table V-2 are used. The friction coefficient is the same as simulation 1. The driver's input steering angle is shown in Figure V-22.

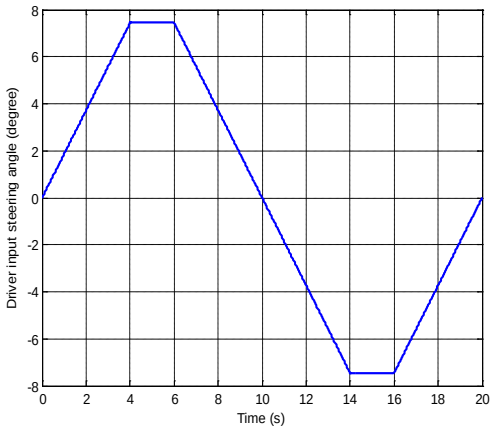

Figure V-22. Driver's steering input in the lane change simulation.

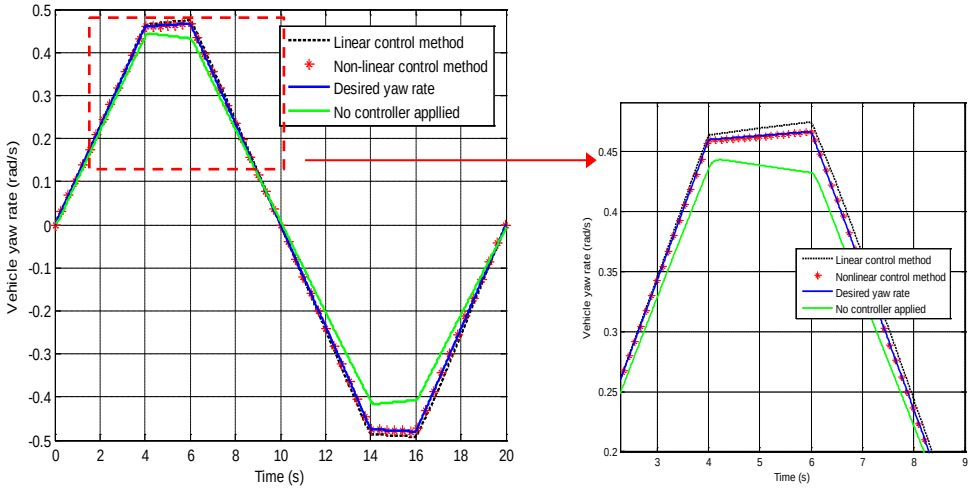

Figure V-23. The vehicle yaw rate response in the lane change simulation.

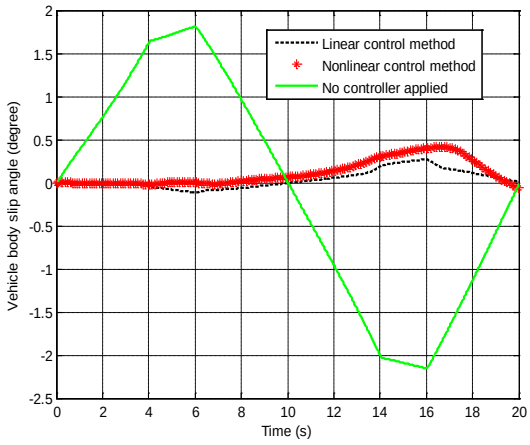

Figure V-24. The vehicle body side-slip angle in the lane change simulation.

Figure V-23 and Figure V-24 show the simulation results of yaw rate and body side-slip angle. We can see in Figure V-23 and Figure V-24 that the linear method and non-linear method both have good performance in terms of yaw rate and body side-slip angle control. In Figure V-23, the non-linear method can achieve accurate yaw rate control, but the yaw rate control performance of the linear method is a little compromised. It is noted that the vehicle body side-slip angle control performance of the non-linear method is not as good as the linear method in Figure V-24. This is because the PI control gains used in the simulation of Figure V-24 are determined based on the J-turn manoeuvre at 10 m/s as given in Table V-2. Although the simulation of Figure V-24 is for the lane change motion, the compromised control performance is acceptable and the control gains determined in the J-turn manoeuvre are proved to successfully apply to the lane change motion under the same vehicle velocity condition.

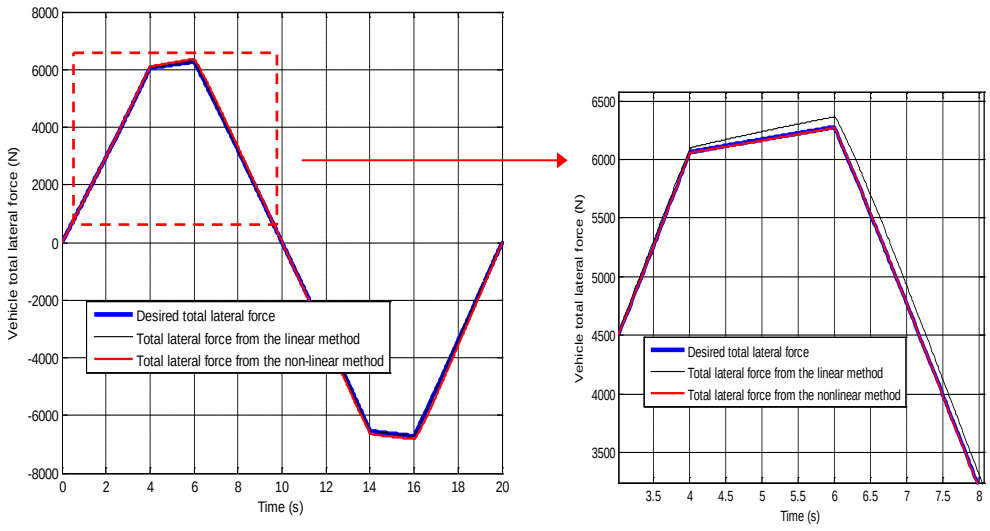

Figure V-25. The total lateral tyre force in the lane change simulation.

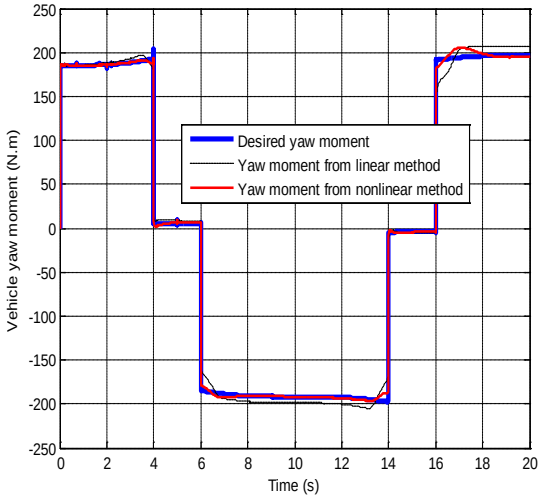

Figure V-26. The vehicle yaw moment in the lane change simulation.

Figure V-25 and Figure V-26 suggest that the non-linear method has the better performance of achieving the desired total lateral tyre force and yaw moment compared with linear method, which proves to have better yaw rate control performance in Figure V-23. It is noted that the controlled yaw moment of non-linear method between 16 and 18 seconds in Figure V-26 has small disturbance, which causes the increased body side-slip angle controlled by the non-linear method around 16 seconds in Figure V-24. Figure V-27 and Figure V-28 show that the desired individual wheel side-slip angle and slip ratio can be well tracked using the non-linear method.

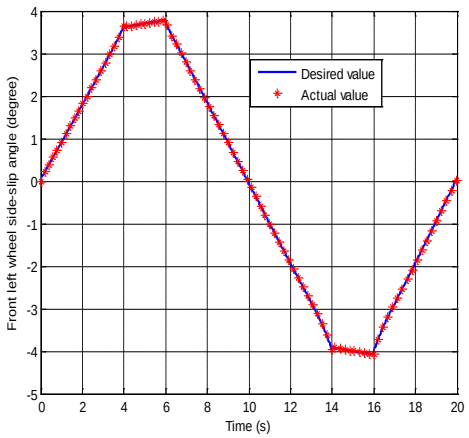

(a)

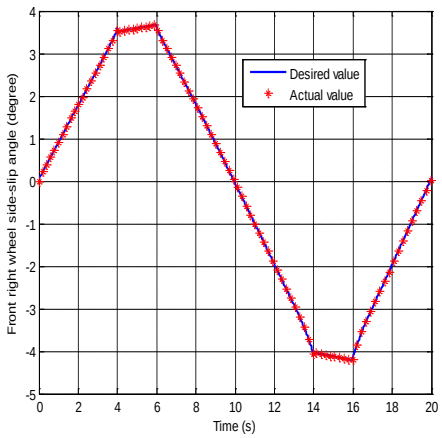

(b)

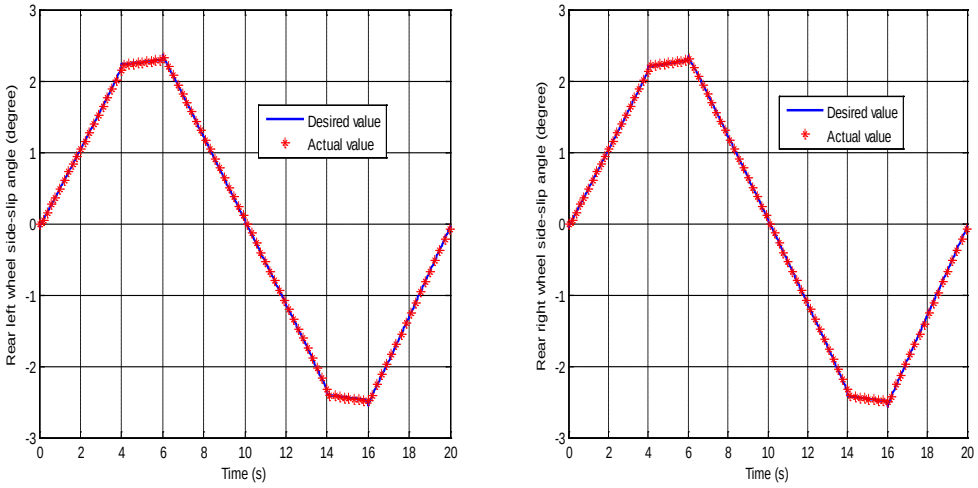

(c) (d)

Figure V-27. The individual wheel slip angle in the lane change simulation controlled by the non-linear method: (a) front left wheel (b) front right wheel (c) rear left wheel (d) rear right wheel.

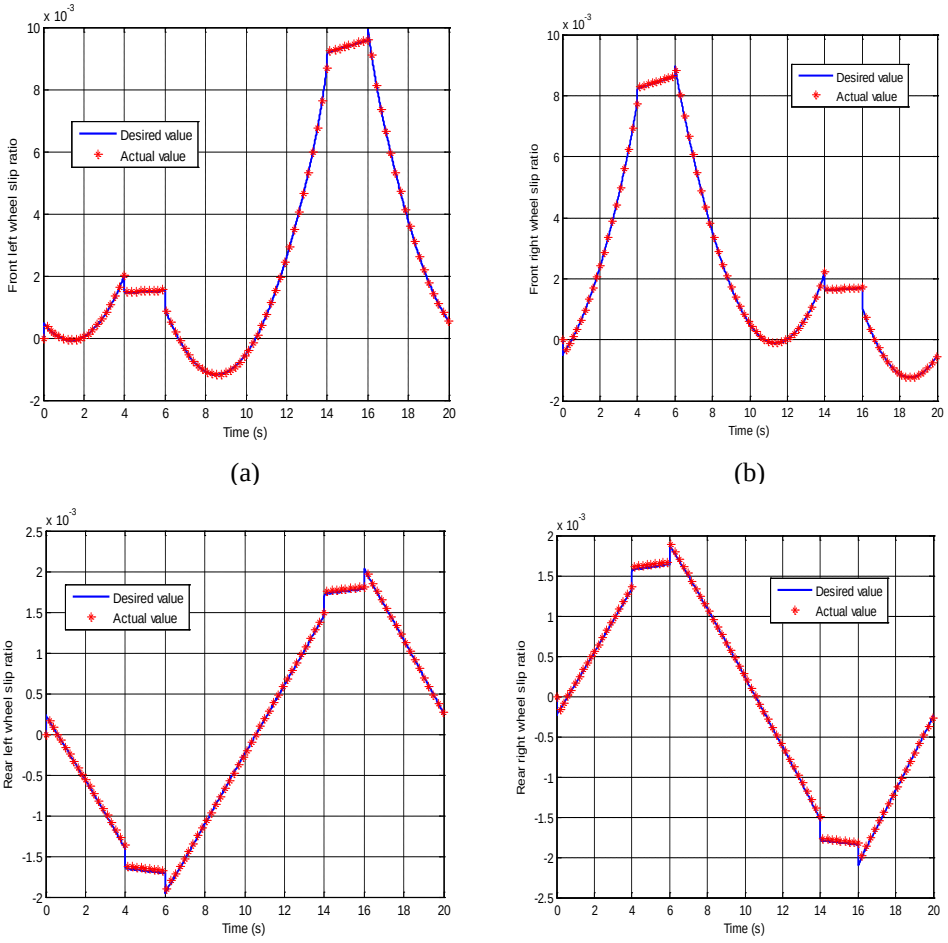

(a) (b)

(c) (d)

Figure V-28. The individual wheel slip ratio in the lane change simulation controlled by the non-linear controller: (a) front left wheel (b) front right wheel (c) rear left wheel (d) rear right wheel.

The third simulation is the combined traction and steering motion. The initial velocity of the vehicle is 10 m/s and the control gains in Table V-2 are used. The friction coefficient is still 0.9. The driver is still performing the J-turn manoeuvre, but the acceleration pedal is also pushed simultaneously. The input steering angle is the same as Figure V-13 and the input driving torque is shown in Figure V-29.

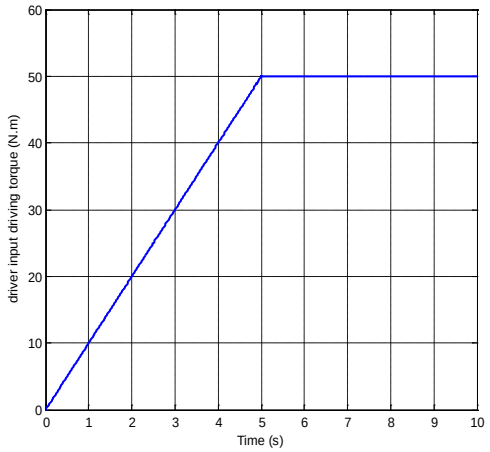

Figure V-29. The input driving torque during the combined driving and steering motion.

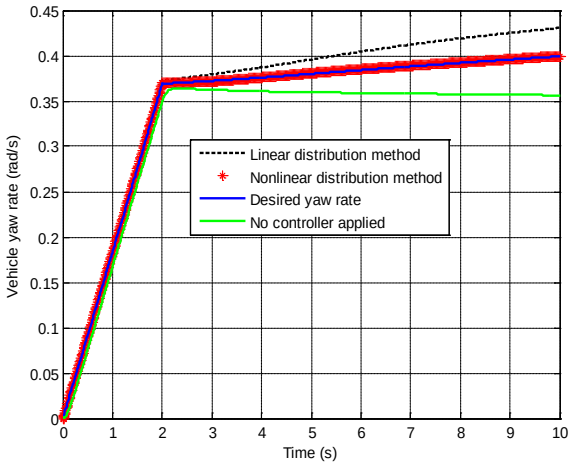

Figure V-30. The vehicle yaw rate response during the combined driving and steering motion.

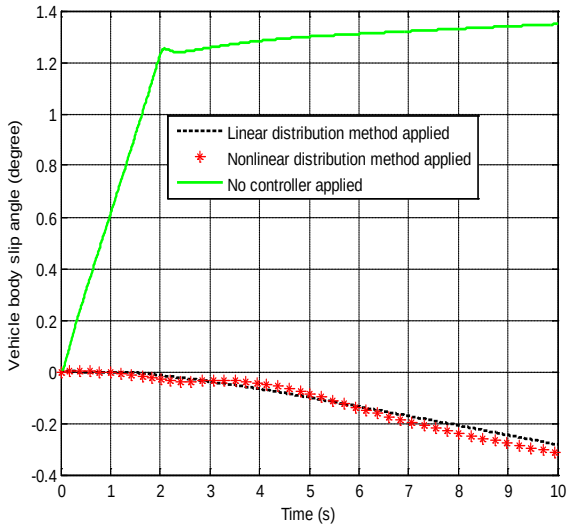

Figure V-31. The vehicle body slip angle response during the combined driving and steering motion.

Figure V-30 and Figure V-31 show the vehicle yaw rate and body side-slip angle responses. The desired yaw rate is increased, since the driver's input traction torque is applied and vehicle longitudinal velocity is increased. The non-linear method can achieve the desired yaw moment and yaw rate. For the linear method, the distributed tyre side-slip angle is larger than the desired value, which causes the larger distributed lateral force and yaw rate. For the no controller applied situation, the yaw rate response does not increase with time but even decreases. This is because even when traction torque is applied, the increased longitudinal velocity caused by the increased driving force cannot overcome the decreased velocity caused by the vehicle turning without the distribution of the controlled tyre force. In addition, the linear method and non-linear method both have the good control performance of body side-slip angle.

Figure V-32 and Figure V-33 show that non-linear method achieve good control performance of total lateral tyre force and yaw moment, which leads to the good control performance of yaw rate and body side-slip angle. The linear method has larger distributed total lateral tyre force and the consequently yaw rate control performance is compromised. Figure V-34 and Figure V-35 also demonstrate that the desired individual wheel side-slip angle and slip ratio can be achieved using the non-linear method.

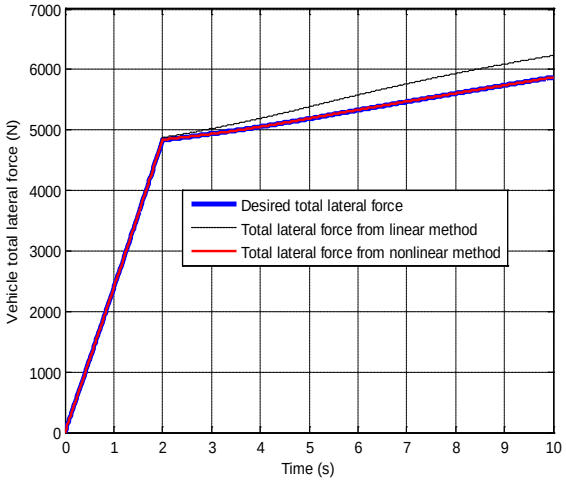

Figure V-32. The vehicle total lateral tyre force during the combined driving and steering motion.

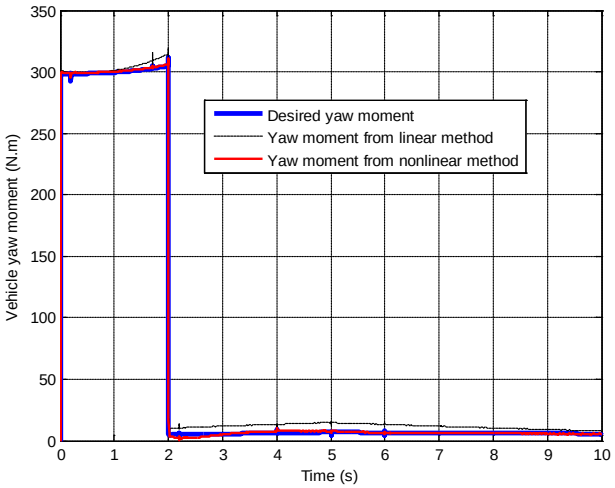

Figure V-33. The vehicle yaw moment during the combined driving and steering motion.

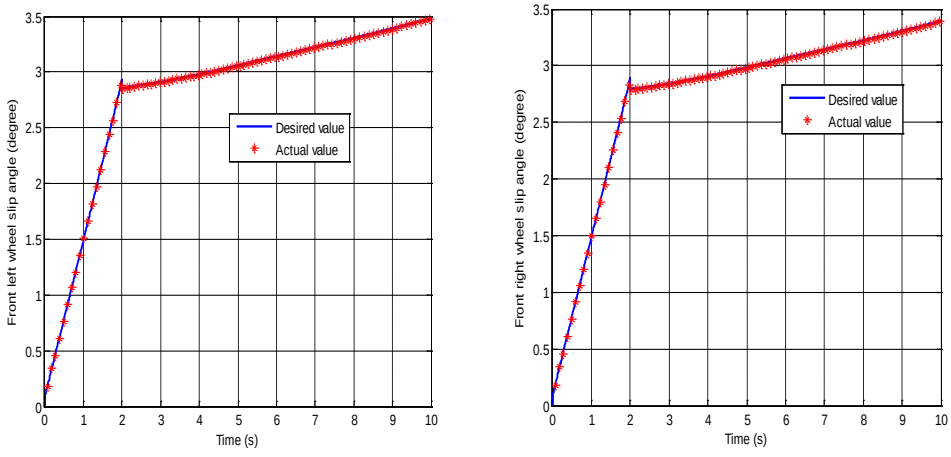

(a) (b)

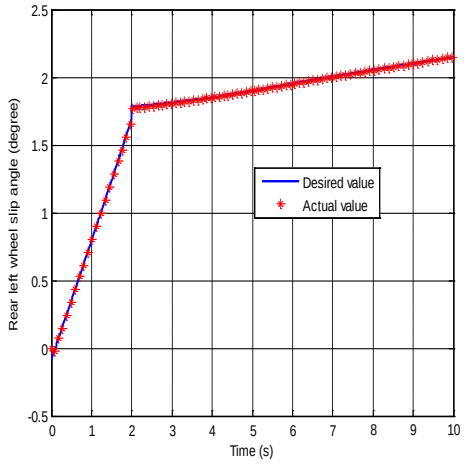

(c)

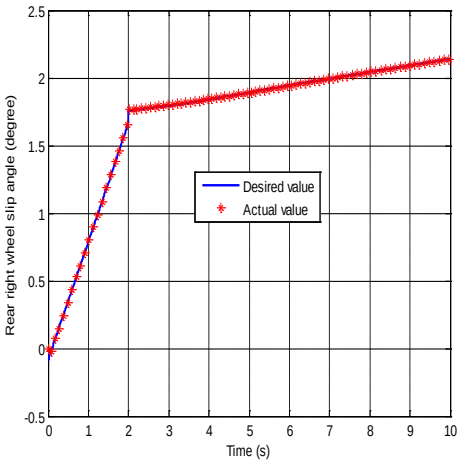

(d)

Figure V-34. The individual wheel slip angle controlled by the non-linear method during the combined driving and steering motion: (a) front left wheel (b) front right wheel (c) rear left wheel (d) rear right wheel.

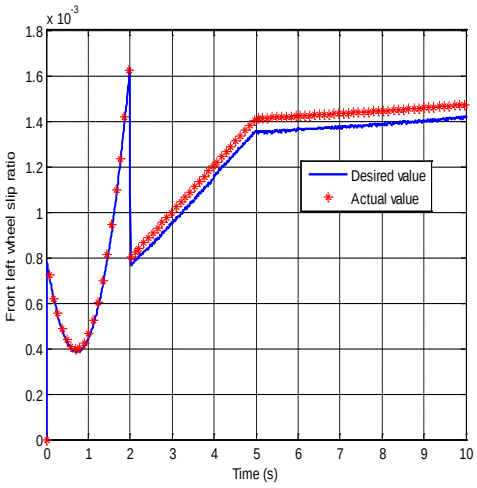

(a)

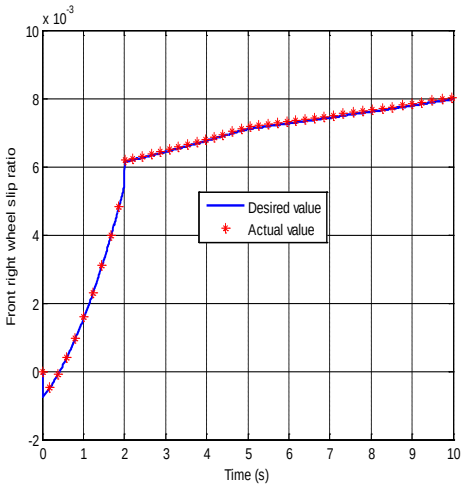

(b)

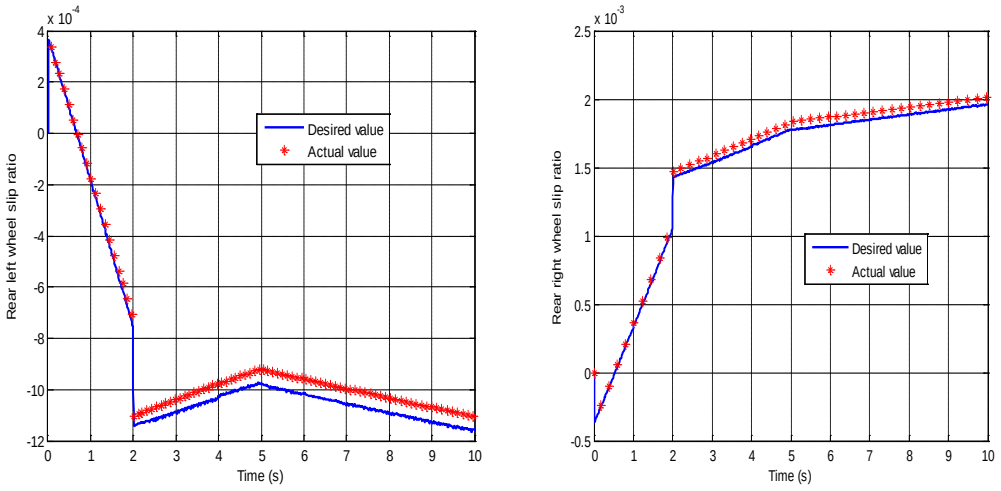

(c) (d)

Figure V-35. The individual wheel slip ratio of the vehicle controlled by the non-linear method during the combined driving and steering motion: (a) front left wheel (b) front right wheel (c) rear left wheel (d) rear right wheel.

The split surface road condition can be referred to the split of road surface between front and rear parts of the vehicle [249] or the split of road surface between the left and right wheels of the vehicle [250]. To examine the simulation performance under the condition of the split of road surface between front and rear of the vehicle, the friction coefficient is assumed to be changed from 0.9 to 0.7 at 5 seconds in the third simulation. The simulation responses of yaw rate and body side-slip angle in Figure V-36 and Figure V-37 prove that the desired vehicle dynamics performance can be well achieved. Alternatively, to evaluate the control performance under the condition of the split of road surface between the left and right wheels of the vehicle, the friction coefficient of the left wheel is assumed as 0.9 and the friction coefficient of the right wheel is 0.7. The simulation results in Figure V-38 and Figure V-39 suggest that the proposed non-linear controller can achieve the good yaw rate and body side-slip angle responses, although the yaw rate response is a little compromised due to the split surface.

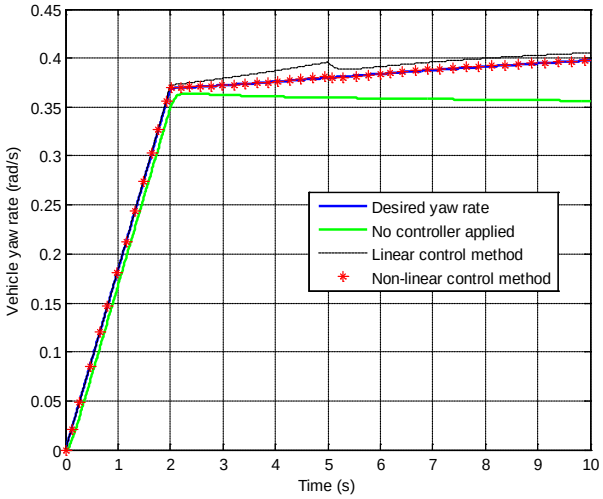

Figure V-36. The vehicle yaw rate response during the combined driving and steering motion under split surface road condition – the split of road surface between front and rear of the vehicle.

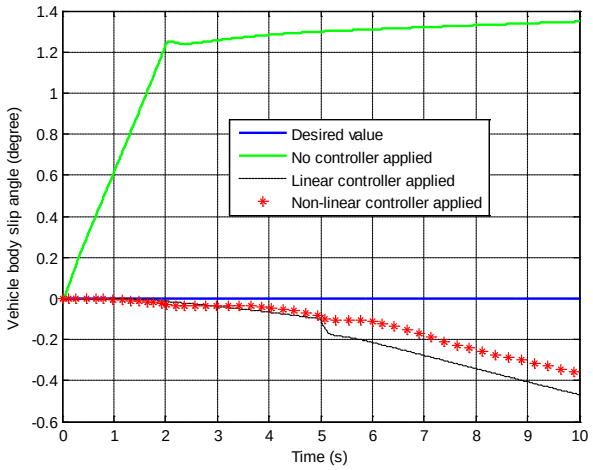

Figure V-37. The vehicle body slip angle response during the combined driving and steering motion under split surface road condition – the split of road surface between front and rear of the vehicle.

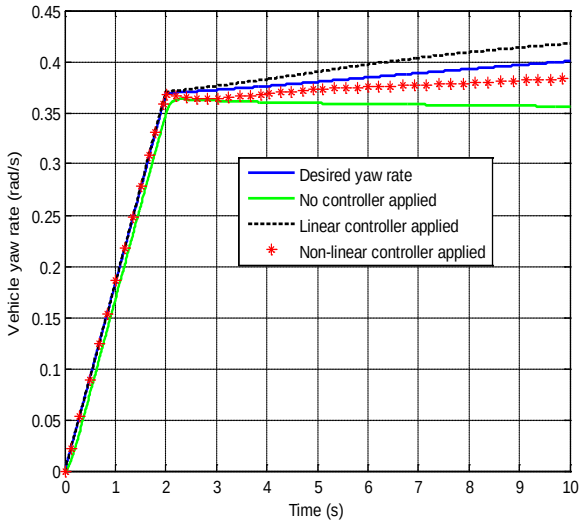

Figure V-38. The vehicle yaw rate response during the combined driving and steering motion under split surface road condition – the split of road surface between left and right wheels.

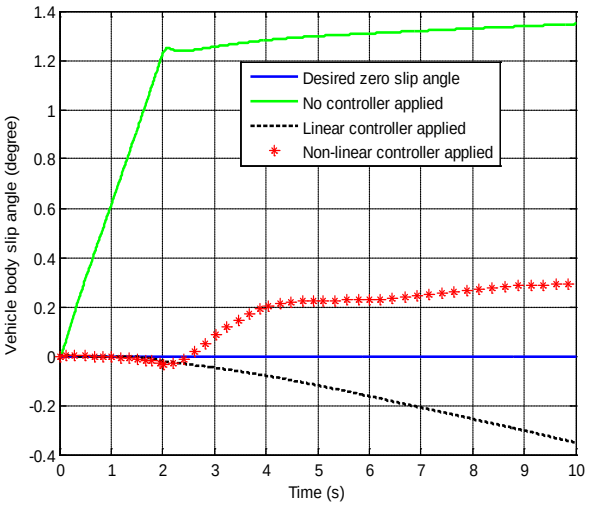

Figure V-39. The vehicle body slip angle response during the combined driving and steering motion under split surface road condition – the split of road surface between left and right wheels.

The RMS errors of the yaw rate response and body side-slip angle response (compared with desired yaw rate and side-slip angle) of both linear and non-linear methods are summarised in Table V-5 and Table V-6. In Table V-5, the linear method has worse yaw rate tracking performance compared with the no controller applied situation in most of the simulations. This is because in the linear method, the desired lateral tyre forces are achieved by linear mapping of the steering angles, and the distributed steering angles are different from the desired ones due to the non-linear tyre characteristics. Due to this error, the RMS yaw rate

error of the linear method is relatively large. In the no controller applied situation, the required steering angles are directly applied to the two front wheels of the vehicle and consequently the RMS error is relatively small compared with the linear method. In the case of non-linear controller, the desired tyre forces can be achieved by taking into consideration the non-linear tyre characteristics and this results in a much better yaw rate tracking performance compared with the linear control and no controller applied situations. From Table V-6, it can be seen that both linear and non-linear methods have good body side-slip angle control performance compared with the no controller applied situation. This proves that the desired body side-slip angle can be tracked well when the desired tyre forces are achieved using the non-linear method.

Table V-5. The RMS errors of yaw rate by different methods.

	No controller applied	*Linear distribution method*	*Non-linear distribution method*
Simulation 1	0.0184	0.0598	0.0018
Simulation 2	0.0078	0.0107	0.002
Simulation 3	0.0096	0.0196	8.1896×10^{-4}
Simulation 3 *Split of the road surface between front and rear parts of vehicle*	0.069	0.0084	0.00062264
Simulation 3 *Split of road surface between left and right wheels*	0.0272	0.0164	0.0091

Table V-6. The RMS errors of body side-slip angle by different methods.

	No controller applied	*Linear distribution method*	*Non-linear distribution method*
Simulation 1	0.0102	8.3032×10^{-4}	3.4437×10^{-4}
Simulation 2	0.023	0.0019	0.0032
Simulation 3	0.0211	0.0024	0.0027
Simulation 3 *Split of the road surface between front and rear parts of vehicle*	0.0221	0.0037	0.0027
Simulation 3 *Split of road surface between left and right wheels*	0.0221	0.003	0.0033

5) Conclusion

In conclusion, the simulation results verify that:

1) In all the simulations of the J-turn, lane change and combined traction and J-turn manoeuvres, the non-linear method considers the non-linear tyre characteristic and consequently the controlled yaw rate and body side-slip angle track the desired values more accurately.

2) The RMS errors of the yaw rate and body slip angle responses in all the simulations also suggest that the non-linear method has good yaw rate and body side-slip angle tracking performance.

3) PI control gains can be determined offline in the preliminary simulations. During the actual vehicle motion, these PI control gains are already available for various vehicle velocity conditions. According to the velocity range of a particular vehicle, the corresponding group of PI control gains is selected. These PI control gains are robust in a simple J-turn motion, lane change motion and combined steering and driving motion (on the split surface road) within a certain range of vehicle velocity, as have been proven in the simulations. If there is a large change in vehicle velocity, the pre-determined PI control gains can be quickly switched.

4) The GA is proved to successfully determine a large number of control gains simultaneously at reasonable computation cost. Since the GA is the optimal search method in the area of artificial intelligence, it has a faster convergence rate and a lower computational cost than the conventional mathematical optimisation method.

5) The individual wheel slip ratio and side-slip angle PI controllers can successfully achieve the whole vehicle body side-slip angle and optimal yaw rate control. This suggests that when the desired slip ratio and side-slip angle of individual wheels are achieved by the lower level PI controllers, the desired individual tyre force, yaw rate and body side-slip angle in the upper controller can be achieved. In this way, the two-level control system proposed in this study can successfully achieve the desired control targets.

3. Summary

In this chapter, both linear and non-linear over-actuated control allocation method for the vehicle stability control and handling control are suggested. These primary control targets are vital to the vehicle dynamics performance. In the following chapters, additional control targets, such as energy-efficient control, fault-tolerant control and autonomous vehicle control, are focused to present the extensive application of the over-actuated controller.

VI. Application of the over-actuator controller in the energy-efficient controller for the 4WIS-4WID electric vehicle

The 4WIS-4WID EV has the advantage of redundant actuators which can be utilised to not only achieve the primary control goals of vehicle handling and stability, but can also realise the important goal of energy efficiency optimisation.

Based on a review of the current literature, it can be seen that one of the most important questions to be considered for the simultaneous dynamics control and energy efficiency optimisation for over-actuated EVs is the cost function because control performance and energy efficiency have to be compromised.

To deal with this question, this chapter first defines two criteria based on the tyre working region and the steering angle to categorise the vehicle motion status into linear pure longitudinal motion and non-linear motion or turning motion including non-linear straight line motion, lane change, cornering, and fish hook manoeuvres, etc.

Then for different motion status, different cost functions are developed. In this chapter, minimisation of the total power loss and the achievement of the desired driving force are selected as the control targets during the linear pure longitudinal motion. In the non-linear motion or turning motion, the desired yaw rate, desired vehicle body side-slip angle and minimisation of the total power loss are three control targets, and desired yaw rate and body side-slip angle are chosen as the primary targets because of the importance of vehicle handling and stability performance. Based on the defined optimisation targets, the desired longitudinal and lateral tyre forces and yaw moment are then optimally distributed to the wheel driving and steering torques.

Finally numerical simulations are used to verify the effectiveness of the proposed strategies. The simulation results show that the proposed strategies can provide better dynamics control performance with less energy consumption compared with the existing approach.

The main contributions of this chapter are: (1) the vehicle planar dynamics model that includes the non-linear Dugoff tyre model and considers the vehicle load transfer effect is applied to better evaluate the control performance during the high velocity turning scenario; (2) based on the different vehicle motion status identified by two criteria, different vehicle

control targets and control structures can be selected; (3) in the proposed two-layer control structure, individual tyre forces are allocated in the upper level by achieving the primary and secondary control targets. Because of the mapping error between the allocated tyre force and the actual output of an individual actuator in the lower level controller, the linear yaw rate feedback controller and body side-slip angle feedback controller are applied to guarantee the primary control targets.

1. Motion status detection

Vehicles undertaking different motions are driven under different conditions and the control objectives for these will be different. For over-actuated EVs, when the vehicle is undertaking a linear pure longitudinal motion, the energy efficiency will be the only control target to be considered. However, when the vehicle's lateral motion becomes large enough or the vehicle's tyre is working in the non-linear tyre region, the vehicle handling and stability performance become the primary control targets and the vehicle energy efficiency becomes the secondary control target.

To deal with different control objectives, different control strategies will also need to be developed. In this research, the real-time optimal control of the individual longitudinal force will be applied when only the linear pure longitudinal motion is what is considered. During non-linear motion or turning motion, a two-level control strategy is proposed to achieve handling control, stability control and energy-efficient control. In the upper level, the target individual wheel longitudinal and lateral tyre forces are calculated according to the desired control targets. Then the actual individual steering and driving actuators are controlled according to the target individual tyre force in the lower level.

Before applying this control strategy, the threshold that determines the transition point between the linear pure longitudinal motion and the non-linear motion or turning motion must be defined. The following criteria are used to determine this transition point.

Criterion 1

When the vehicle tyre works in the linear tyre region, vehicle handling and stability performance are less important than the energy efficiency. According to the Dugoff tyre model used in this research (65), when $\lambda_i > 1$, the tyre is working in the linear tyre region. This condition can also be represented by following inequality:

$$\frac{\sqrt{(C_s s_i)^2 + (C_\alpha \tan\alpha)^2}}{1 - s_i} \leq \frac{1}{2}\mu F_{zi}$$

(105)

In general, the side-slip angle of each wheel is difficult to measure directly, and hence many different estimation methods have been proposed. In this thesis, the side-slip angle is estimated by a side-slip angle estimator described in Section 3.1. The estimation of the vehicle longitudinal velocity, longitudinal slip ratio and friction coefficient has been suggested in Section 3.2. In this section, the longitudinal vehicle velocity, longitudinal tyre slip ratio and tyre-road friction coefficient are simply assumed to be known. Using the estimation results of the individual wheel side-slip angle and slip ratio, the inequality (105) can be used to examine Criterion 1.

Criterion 2

In addition to working in the linear tyre region, the lateral acceleration of the vehicle in linear pure longitudinal motion must be small enough to ignore. The following equation suggests that the vehicle's lateral acceleration is related to the input steering angle of the vehicle wheel and the longitudinal velocity:

$$\dot{v}_y = \frac{v_x^2}{Rg} = \frac{v_x^2 \delta}{g(l_f + l_r)}$$

(106)

where *R* is the vehicle turning radius, which is determined by the steering angle and vehicle base length. Figure VI-1 shows the plot of the vehicle lateral acceleration versus the input steering angle in a group of simulations using the vehicle dynamics model given in Chapter 4. As can be seen in Figure VI-1, the lateral acceleration is limited to the small value of 0.3 m/s^2 when the steering angle is less than 0.02 rad under various vehicle longitudinal velocity conditions. If the steering angle is larger than 0.02 rad, the lateral acceleration increases by a large amount when the longitudinal velocity is high. Thus, we assume that when the steering angle of the vehicle wheel is less than 0.02 rad, the vehicle lateral motion can be ignored.

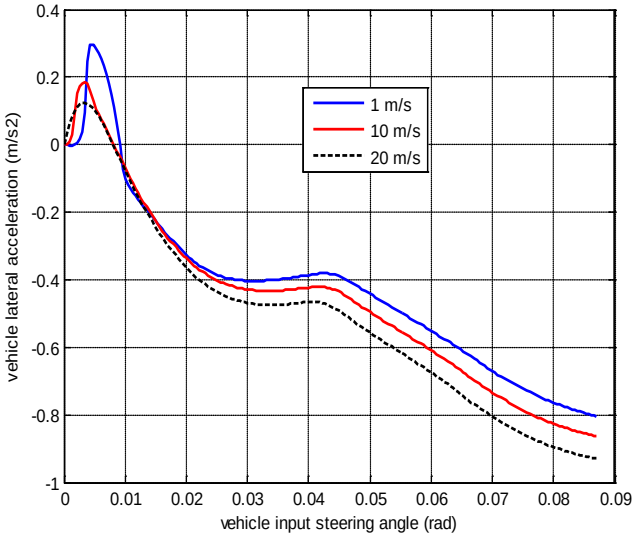

Figure VI-1. Vehicle lateral acceleration versus input steering angle.

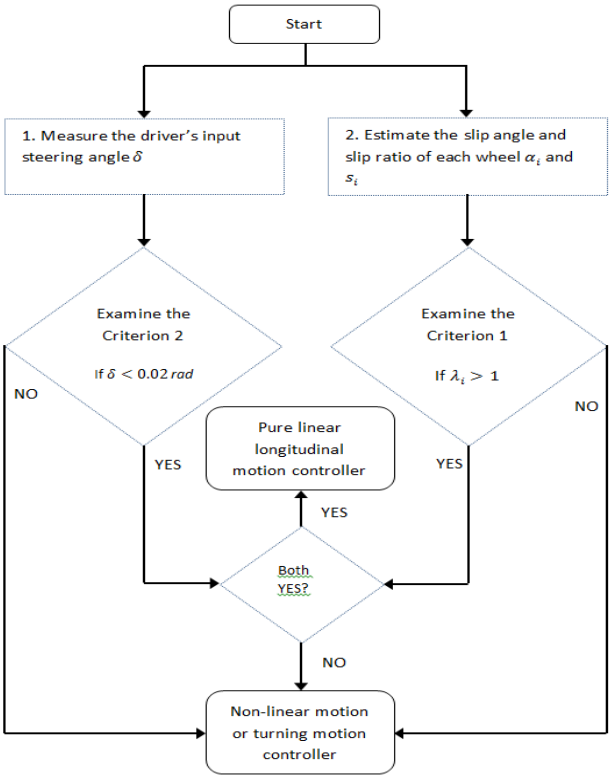

Figure VI-2. Linear pure longitudinal motion status detection.

Figure VI-2 shows the flow chart of the motion status detection method. The vehicle motion is pure linear longitudinal motion only when both the requirements of Criterion 1 and Criterion 2 are satisfied, and in this case the energy efficiency will be the primary control

target. When the tyre is working in the non-linear region and the steering angle is small, the stability of the vehicle is the major concern. When the steering angle is large and the tyre is working in the linear region, the handling of the vehicle plays a more important role. When the steering angle is large and the tyre is working in the non-linear region, both the vehicle stability and handling are primary control targets.

2. Energy consumption model

For EVs, the energy consumption models of the in-wheel driving motors are generally divided into two parts: pure energy consumption in driving mode and energy regeneration in braking mode based on the assumption that the energy can be partially re-gained through the regenerative braking function. The model which is widely used in the literature for the total power of in-wheel motors, P_m, can be described by the following equation by subtracting the total input power to the converter from the total output power of the battery [15].

$$P_m = \sum_{i=1}^{4} \frac{P_{Oi}}{\eta_{Oi}} - \sum_{i=1}^{4} P_{Ii}\,\eta_{Ii} \tag{107}$$

where P_{Oi} is the output power in the energy consuming mode and P_{Ii} is the input power in the energy gaining mode of the ith in-wheel motor, which are related to the driving torque T_{di}, braking torque T_{bi} and wheel angular velocity ω_i of the ith in-wheel motor as:

$$P_{Oi} = T_{di}\omega_i \tag{a}$$

$$P_{Ii} = T_{bi}\omega_i \tag{b}$$

(108)

where η_{Oi} is the output power efficiency in the energy consuming mode and η_{Ii} is the input power efficiency in the energy gaining mode of the ith in-wheel motor, which can be represented by the following relationships:

$$\eta_{Oi} = p_1 T_d^4 + p_2 T_d^3 + p_3 T_d^2 + p_4 T_d + p_5 \tag{a}$$

$$\eta_{Ii} = p_6 T_b^3 + p_7 T_b^2 + p_8 T_b + p_9 \tag{b}$$

(109)

where $p_1 - p_9$ are coefficients obtained by curve fitting of the actual experimental data from an in-wheel BLDC motor [15]. Figure VI-3 presents the relationship between the power efficiency and the driving or braking torque. The blue line shows the relationship between the output power efficiency from the battery and the driving torque. The red line shows the relationship between the input power efficiency to the inverter and the braking torque. It is noted that different types of motors may have different curve fitting representations based on different experimental data. In this paper, equation (109) is used due to the available coefficient values.

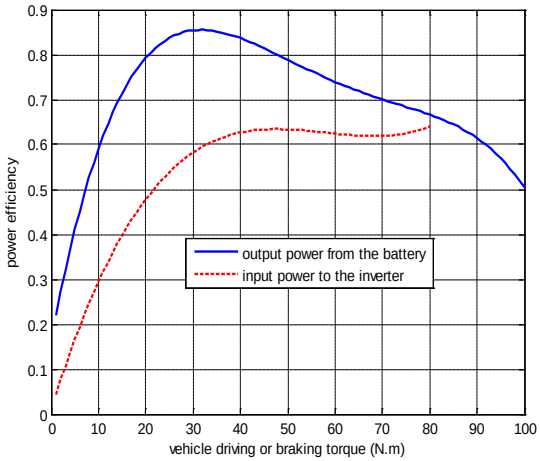

Figure VI-3. The power efficiency when the driving or braking torque is changed within its operation range.

It should be noted that the measurement of the output power of the motor or the input power to the converter (P_{Oi} or P_{Ii}) requires the information about the driving or braking torque (T_{di} or T_{bi}) and the vehicle angular velocity ω_i, which are all easy to be measured from the current of the electric in-wheel motor and the encoder sensor.

In addition, the power loss contributing to the tyre lateral side-slip P_α and the power loss related to the tyre longitudinal slip P_s can be described by equation (110) and equation (111), respectively [198]:

$$P_\alpha = \sum_{i=fl,fr,rl,rr} |F_{si} u_i \tan \alpha_i| \tag{110}$$

$$P_s = \sum_{i=fl,fr,rl,rr} |F_{ti} u_i s_i|$$

(111)

The total tyre power loss P_{tyre} due to the tyre lateral and longitudinal slip can be calculated by adding up the values of P_α and P_s as:

$$P_{tyre} = P_\alpha + P_s$$

(112)

According to equation (112), the total tyre lateral power loss is related to the lateral tyre force and lateral side-slip angle. Since the absolute value of the lateral tyre force is increasing with the increase of the absolute value of the lateral side-slip angle, we can simply conclude that the total lateral tyre power loss can be minimised by minimising the individual lateral tyre force.

Similarly, according to equations (110)(111), the total longitudinal power loss of the tyre is related to the longitudinal tyre force and longitudinal slip ratio. Because the absolute value of the longitudinal tyre force is also increasing with the absolute value of the longitudinal slip ratio, the total longitudinal power loss of the tyre can be minimised by minimising the individual longitudinal tyre force.

In the following proposed optimal tyre force distributor (113), in the cornering condition and the least-square allocation method for the yaw rate feedback controller (77) and body slip angle feedback controller (91), the minimising of the distributed individual tyre force is the optimal control target, which can guarantee the minimisation of the total power loss of the tyre.

3. Control strategy for linear pure longitudinal motion

In the linear pure longitudinal motion, it is assumed that there is either little or no steering input applied and the tyre is working in the linear region according to Criterion 1 and Criterion 2. In this case, only vehicle longitudinal dynamics and wheel dynamics are considered, and the cost function of CA problem can be represented as follows:

$$\min_{F_{xi}} P_c$$

(113)

subject to:

$$F_{xd} = F_{xfl} + F_{xfr} + F_{xrl} + F_{xrr} \tag{a}$$

$$M_d = \frac{b_f}{2}\left(F_{xfl} - F_{xfr}\right) + \frac{b_r}{2}\left(F_{xrl} - F_{xrr}\right) \tag{b}$$

where F_{xd} is the total desired longitudinal tyre force, which is determined according to the driver's input driving torque or brake torque. Due to the pure longitudinal motion condition, the desired yaw moment M_d in (113)(b) should be zero. After the desired individual longitudinal tyre force F_{xi} is obtained, the individual driving or braking torque can be controlled to achieve the desired longitudinal tyre force using the following equations.

$$T_{di} = F_{xi}R_\omega \qquad F_{xi} \geq 0 \tag{114}$$

$$T_{bi} = |F_{xi}|R_\omega \qquad F_{xi} < 0 \tag{115}$$

In this case, the desired tyre force can be perfectly achieved because the tyre is working in the linear region according to *Criterion 1*. Therefore, this optimal distribution method is an open-loop control method without any feedback information.

In this study, an in-wheel BLDC electric motor is applied. It has been suggested [198] that the maximum driving torque T_{dmax} is 100 N.m and the maximum regenerative brake torque T_{bmax} is 80 N.m. According to equations (114)(115), the constraints of the allocated longitudinal tyre force can be presented by the following equation as an additional constraint in the optimisation problem (113):

$$-\frac{T_{bmax}}{R_\omega} \leq F_{xi} \leq \frac{T_{dmax}}{R_\omega} \tag{113 (d)}$$

Now, P_c can be calculated according to equations (107)-(109) as:

$$P_c = \sum_{i=1}^{4} \frac{F_{xi}R_\omega\omega_i}{\eta_{Oi}} \qquad F_{xi} \geq 0 \tag{116}$$

$$P_c = \frac{1}{\sum_{i=1}^{4}|F_{xi}|R_\omega\omega_i\eta_{Ii}} \qquad F_{xi} < 0 \tag{117}$$

Equations (116)(117) are proposed to maximise the regenerative braking power and minimise the output driving power, and minimisation of the total motor power P_m can be achieved.

The lateral tyre force and steering angle are all approximated as zeros in the pure longitudinal motion condition. Thus, tyre longitudinal force F_{xi} is used instead of F_{ti} to calculate the driving torque T_{di} or braking torque T_{bi} in equations (113) (d) and (114)-(117). It is noted that when the steering angle is not too large (no more than 10 degrees) in the cornering condition in Section 6.4, the effect of the steering angle on power consumption can still be neglected and P_c is still calculated by equations (116)(117).

To obtain the optimisation solution, a variety of optimisation methods can be found in the literature. In this paper, the Matlab function, Fmincon, is used to solve the problem of (113). Fmincon can be utilised to minimise any formation of the cost function under both linear and non-linear constraints. When there is only linear pure longitudinal motion, only linear constraints are considered when searching for the optimal tyre force distribution with small computational effort.

4. Control strategy for non-linear motion or turning motion

When the vehicle is turning, the vehicle lateral dynamics must be the primary concern and the primary control target must be the handling and stability performance while the secondary control target is the optimisation of energy efficiency. This is because in such a situation, vehicle safety is what is critical.

Vehicle cornering motion control is a complex optimisation problem, so a two-level control strategy is proposed in this study to solve this problem. In the upper level, the desired longitudinal and lateral tyre forces are calculated by the optimisation algorithm according to the desired control targets. Then, in the lower level, the individual steering and driving/braking torques are mapped from the desired tyre force of each wheel. And then the additional controlled steering angle and driving/braking torque of each wheel are calculated from the linear feedback controllers based on the yaw rate error and body side-slip angle error. Figure VI-4 shows the overview of the proposed integrated energy efficiency and dynamics control strategy in the lateral motion condition.

It should be noted that when the proposed integrated controller is working under the conditions of non-linear longitudinal motion, the desired total lateral force F_{yd} and yaw moment M_d can be assumed as zeros in this two-level control strategy.

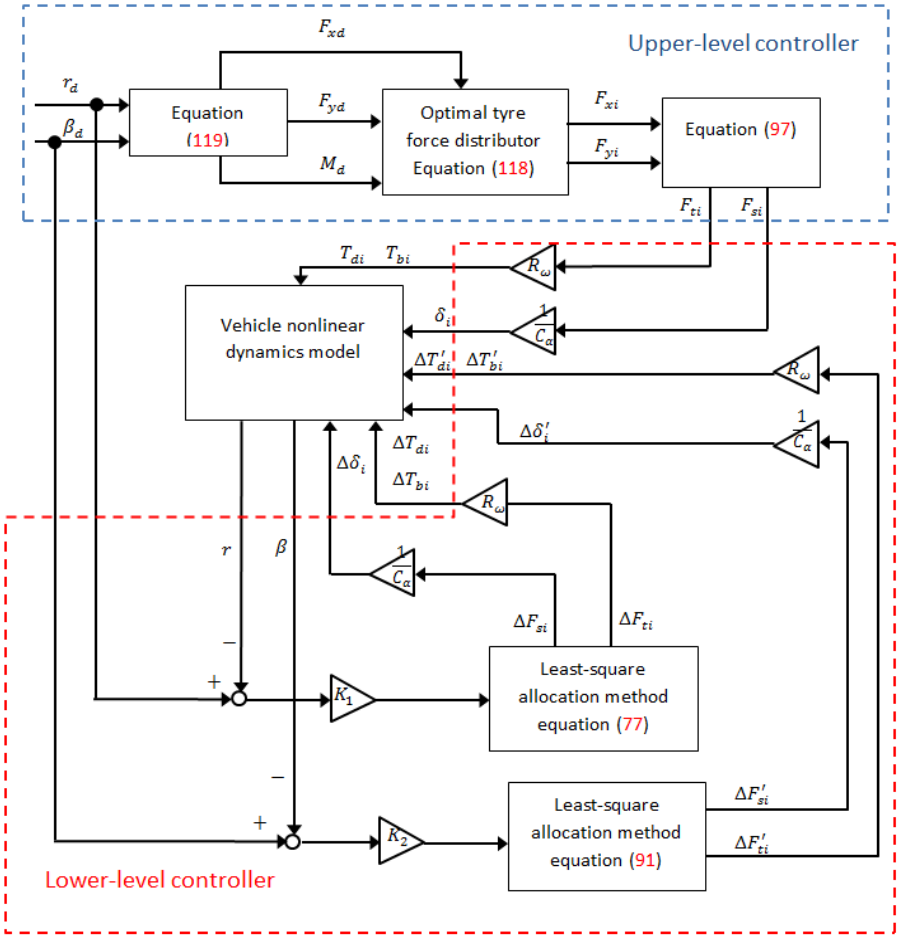

Figure VI-4. A two-level integrated controller for vehicle turning motion.

1) Upper level control

In the upper level control, the desired individual tyre lateral force and longitudinal force are calculated according to the optimal cost function. The cost function for this control allocation problem can be represented as follows:

$$\min_{F_{xi},F_{yi}} \frac{a_1}{2}\sum_{i=1}^{4}\frac{F_{xi}^2+F_{yi}^2}{(\mu F_{zi})^2}+a_2P_c \tag{118}$$

subject to:

$$F_{xd} = F_{xfl} + F_{xfr} + F_{xrl} + F_{xrr} \quad \text{(a)}$$

$$F_{yd} = F_{yfl} + F_{yfr} + F_{yrl} + F_{yrr} \quad \text{(b)}$$

$$M_d = l_f\left(F_{yfl} + F_{yfr}\right) - l_r\left(F_{yrl} + F_{yrr}\right) + \frac{b_f}{2}\left(F_{xfl} - F_{xfr}\right) + \frac{b_r}{2}\left(F_{xrl} - F_{xrr}\right) \quad \text{(c)}$$

$$F_{xi}^2 + F_{yi}^2 \leq \mu F_{zi}^2 \quad \text{(d)}$$

$$-\frac{T_{bmax}}{R_\omega} \leq F_{xi} \leq \frac{T_{dmax}}{R_\omega} \quad \text{(e)}$$

where a_1, a_2 are the scaling factors for the two optimisation terms. P_c is represented by equation (116)(117). The first term of the cost function (118) is about the minimising of the workload of longitudinal and lateral forces of each tyre, and the second term of the cost function (118) corresponds to the total motor power consumption. The first term relates to the energy efficient control of the tyre friction power loss and the second term relates to the energy efficient control of the total motor power. The primary control target about handling and stability performance will be achieved by finding the required tyre force of each wheel to satisfy the equality constraints (118)(a-c) and inequality constraint (118)(d). The constraint (118)(f) roughly suggests the maximum and minimum value of the distributed longitudinal tyre force. Although the actual available allocated driving torque or braking torque may be affected by the steering angle of each individual wheel and mapping error from the distributed tyre force to the actuators, constraint (118)(d) can be still considered as the reasonable longitudinal tyre force allocation boundary in the optimisation problem (118) in the upper level controller. Then the actual allocated driving or brake toque of each wheel can be limited to within the detailed boundary in the lower level controller. The vehicle lateral distributed tyre force of each wheel is limited by the boundary that combines constraints (118)(d) and (118)(e).

The desired total longitudinal force F_{xd}, total lateral force F_{yd} and yaw moment M_d can be determined based on the desired yaw rate and slip angle as follows :

$$M_d = I_z \dot{r}_d \quad \text{(a)}$$

$$F_{yd} = m v_x\left(\dot{\beta}_d + r_d\right) = m v_x r_d \quad \text{(b)}$$

$$F_{xd} = \sum_{i=1}^{4} F_{xi} = \sum_{i=1}^{4} \frac{T_{di} - T_{bi}}{R_\omega} \quad \text{(c)}$$

(119)

where r_d is the desired yaw rate, which can be calculated by the following equation [100] similar to equation (74):

$$r_d = \frac{v_x \delta_f}{(l_f + l_r)(1 + P v_x^2)} \qquad \text{when } |r_d| < r_{max} \tag{a}$$

$$r_d = r_{max} \qquad \text{when } |r_d| > r_{max} \tag{b}$$

(120)

where $r_{max} = \frac{\mu g}{v_x}$, which presents the handling limit the of maximum yaw rate due to the tyre friction limit [251]. v_x is the vehicle longitudinal velocity, which is assumed to be known in this study as noted in *Remark 1*. δ_f is the front wheel steering angle, and we assume that the steering angles of front left wheel and front right wheel are same in the ideal condition, that is $\delta_{fl} = \delta_{fr} = \delta_f$. β_d is the desired vehicle body side-slip angle, of which value reflects the vehicle stability. The desired body side-slip angle is generally defined as zero ($\beta_d = 0$) [100].

Non-linear constraint (118)(d) describes the friction circle, which means that the maximum longitudinal force and maximum lateral force the individual tyre can generate are constrained in an ellipse circle. However, this non-linear constraint will greatly increase the computational effort. Castro et al. suggested this non-linear inequality can be approximated by the N half-spaces [252]:

$$C \begin{bmatrix} F_{xi} \\ F_{yi} \end{bmatrix} \leq D \mu F_{zi}$$

(121)

where $C \in R^{N \times 2}$, $D \in R^N$ are matrices that characterise the half-spaces. One may see that, as the number of half-space N is increased, the friction circle constraints can be approximated with increasing accuracy. However, during the actual implementation of the controller, N can not be too large, as the computational effort will greatly increase.

Although the non-linear constraint (118)(d) has been linearized, the optimisation problem (118) is still a time consuming optimisation problem. In the simulation, the Fmincon function in Matlab is utilised to solve this problem, but relatively long computational time is required. For real application, a computationally efficient algorithm needs to be developed and/or fast

computer software needs to be used to implement the algorithm. This, however, is beyond the scope of this paper.

2) Lower level control

When the desired longitudinal and lateral tyre forces are determined in the upper level, the next problem is how to map the desired tyre forces into the actual steering angle and driving torque of each individual actuator optimally. The linear mapping method is widely used to achieve this target. The detailed explanation of this linear mapping method can be found in Section 5.2.2.

However, the distributed steering and driving actuators cannot accurately generate the desired tyre force when the tyre is working in the non-linear tyre region. This problem can be solved by measuring the actual tyre forces and using them as feedback information to adjust the control of the steering and driving actuators. As the tyre forces are difficult to measure in practice, the alternative feedback values of yaw rate and body side-slip angle are used instead in this paper. Although this alternative method has the problem of mapping from the yaw rate error and body side-slip angle error to the additionally controlled tyre forces, which is a time consuming and complex process, the advantage of this approach is that the control target of handling and stability performance can be directly and perfectly tracked and the computation speed of this approach is also fast enough to realise real-time control according to the simulation.

Thus, effective proportional feedback controllers of the vehicle body side-slip angle and yaw rate are used to overcome the yaw rate control error and body side-slip angle control error caused by the non-linear tyre characteristic. The detailed explanation of the design linear feedback yaw rate controller and body side-slip angle controller can be found in equations (73)-(78) and equations (87)-(91) in Section 5.1, respectively.

The non-linear or turning motion control allocation method has a complex two-layer hierarchical control structure. In the upper level controller, the cost function (118) is minimised under three equality constraints and two inequality constraints. These three equality constraints are actually three feedforward virtual control laws calculated from the desired yaw rate and body side-slip angle. These equality constraints guarantee these primary control targets. The cost function (118) includes two secondary control targets: the minimisation of the total tyre force workload (power loss due to tyre friction) and the minimisation of the total power consumed by the driving motor. The scaling factors a_1 and

a_2 have default values of 1 and these values can be adjusted in different conditions. Due to the non-linear characteristic of the vehicle model, however, the allocated desired tyre forces cannot be perfectly allocated to the individual actuator. For this reason, in order to further improve the primary control targets of vehicle stability and handling, two parallel feedback controllers are proposed in the lower level control system: a yaw rate proportional feedback controller and a body side-slip angle proportion feedback controller.

Although various optimisation algorithms can be used to solve the optimisation problems (113) and (118), the Matlab embedded function 'Fmincon' is used to solve the problems because 'Fmincon' can be widely applied for the linear, quadratic or sum of square cost function under linear or non-linear equality and inequality constraints. This embedded optimisation function can balance the optimisation efficiency and design flexibility. Although the suggested optimisation problems (113) and (118) only have linear constraints, the non-linear constraints are still applicable if users want to add additional modifications.

In the 'Fmincon' function, there are four optimisation options: 'active set', 'interior-point', 'trust-region-reflective' and 'sequential quadratic programming (SQP)'. The default algorithm is 'interior-point', which can be classified as a large-scale algorithm. This kind of algorithm uses a linear algorithm that does not need to store or operate on a full matrix, and this can significantly reduce the size of the required memory and computational speed. In contrast, 'active set' and SQP can be classified as the medium-scale algorithm that internally creates full matrices and uses dense linear algebra, which can be time consuming. Although 'trust-region-reflective' method can also be classified as a large-scale algorithm, this algorithm has the strict requirement of the constraints and objective function, which limits the application of this method. In the simulation part, the simulation results of the 'active set', 'interior-point' and 'SQP' algorithms are compared to find the most suitable algorithm for the proposed EECA method.

In the actual implementation of the proposed EECA control method, a switcher must be designed to achieve the smooth transition between the controllers under the pure longitudinal condition and under the cornering condition. It can be seen that the major difference between the controllers in pure longitudinal condition and in the cornering condition is the application of the linear yaw rate feedback controller and the linear body side-slip angle feedback controller in the lower level controller in the cornering condition. In the upper level controller in the cornering condition, if the driver's input steering angle is close to zero, the desired total

lateral tyre force and yaw moment are zero and this is similar to the pure longitudinal condition. Thus, a scaling factor p is applied to multiply the controlled individual tyre force ΔF in equation (75) from the yaw rate feedback controller and $\Delta F'$ in equation (90) from the body slip angle feedback controller:

$$\Delta F = p\Delta F \tag{122}$$

$$\Delta F' = p\Delta F' \tag{123}$$

If Criterion 1 and Criterion 2 are both satisfied, $p = 0$; otherwise, $p = 1$.

5. Simulation results

To test the dynamic performance of the suggested integrated dynamics control and energy efficiency optimisation method, numerical simulations are conducted under various conditions. The parameter values used in the simulations are listed in Table VI-1.

Table VI-1. Parameter values used in simulations. [100]

a_1	Scaling factor of the lateral motion energy-efficient controller	1
a_2	Scaling factor of the lateral motion energy-efficient controller	1
h	height of the vehicle centre of gravity	0.533 m
K_1	Proportional gain in actuator distribution yaw rate controller	20000
K_2	Proportional gain in actuator distribution slip angle controller	1000000

1) The simulation results of pure longitudinal motion

In the first set of simulations, the vehicle is moving along the straight lane to test the energy-efficient control performance during linear pure longitudinal motion. The initial vehicle velocity is 15 m/s and the friction coefficient is assumed as 0.9 in this set of simulations. The driver's total input driving torque is shown in Figure VI-5 as the large driving torque condition and the small driving torque condition.

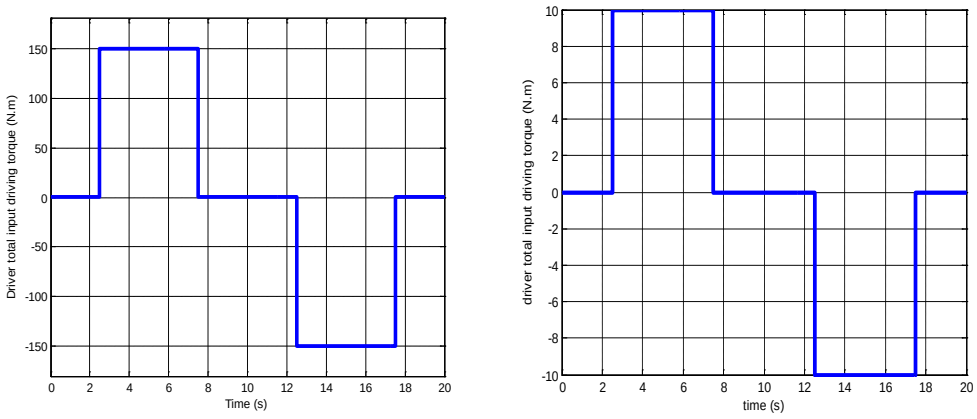

(a) large torque condition (b) small torque condition

Figure VI-5. Driver's total input driving torque in the simulation of linear pure longitudinal motion.

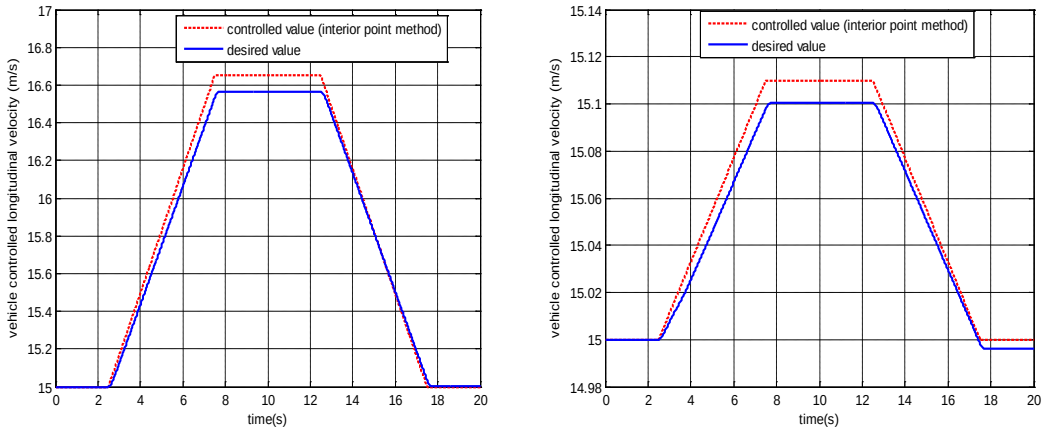

(a) large torque condition (b) small torque condition

Figure VI-6. The controlled vehicle longitudinal velocity in the linear pure longitudinal motion.

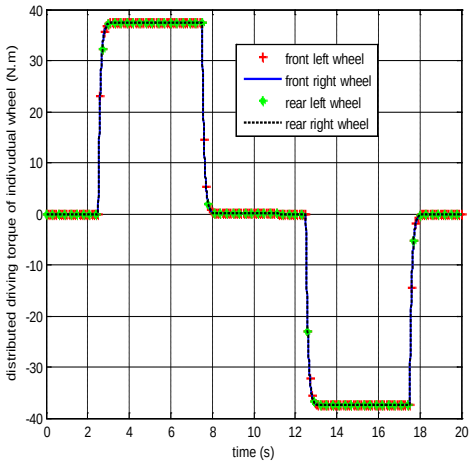

(a) large torque condition (interior point)

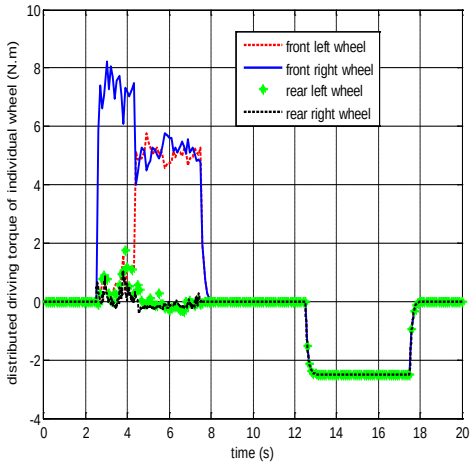

(b) small torque condition (interior point)

Figure VI-7. The distributed driving torque of the individual wheels in the linear pure longitudinal motion.

The algorithms of the ‘interior point’, ‘active set’ and ‘SQP’ in the optimisation function ‘Fmincon’ are compared in the simulations. As can be seen in Figure VI-6, the controlled vehicle longitudinal velocity can achieve the desired velocity value under both large and small driving torque conditions. The optimisation result of the distributed driving torque and braking torque of each wheel is shown in Figure VI-7. Under the medium and high driving torque conditions in Figure VI-7(a), the equal distribution of the driving torque and braking torque is the optimal method. In Figure VI-7(b), however, the optimisation method suggests that the two front wheels are responsible for the major driving workload and the braking torque is equally distributed in the small torque demand condition. It should be noted that only the torque distribution of the ‘interior point’ method is presented in Figure VI-6 and Figure VI-7. The total output power of the four-wheel optimal distribution under both large and small torque conditions is shown in Figure VI-8, which includes the total motor driving power and the total tyre power loss. To clearly present the power efficiency of each method, the root mean square (RMS) values of the power consumption of each method are presented in Table VI-2. All the three optimisation algorithms consume a similar motor driving power under the conditions of large driving torque demand, but the power consumption is different when there is small driving torque demand. The ‘interior point’ method has the best total power saving performance under conditions where there is small torque applied. It should be noted that the torque distribution in Figure VI-7(a) is perfectly overlapped due to the same energy efficiency map applied. In the real situation, the individual driving motor may have slightly different energy efficiency maps even if the same types of motors are applied. This

study, however, only shows the ideal conditions for theoretical analysis and this minor problem is not considered here.

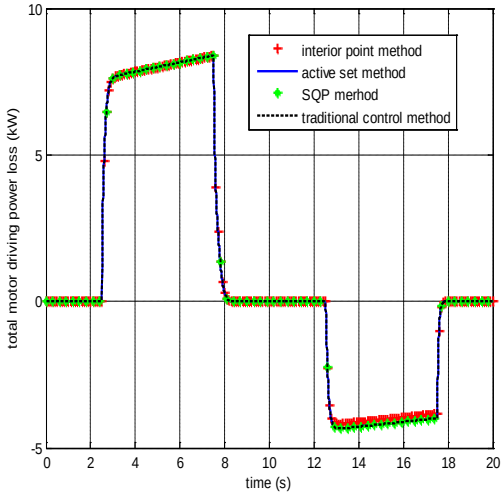

(a) total driving output power - large torque

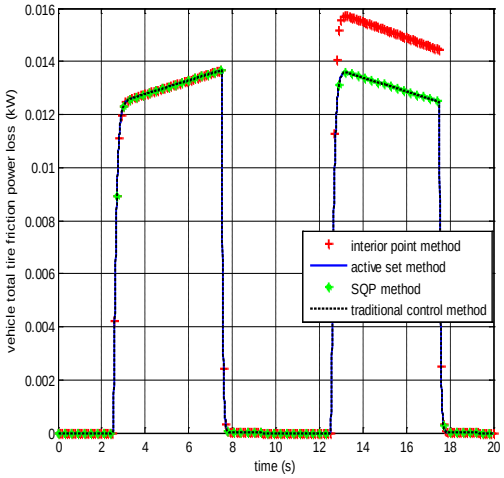

(b) total tyre power loss – large torque

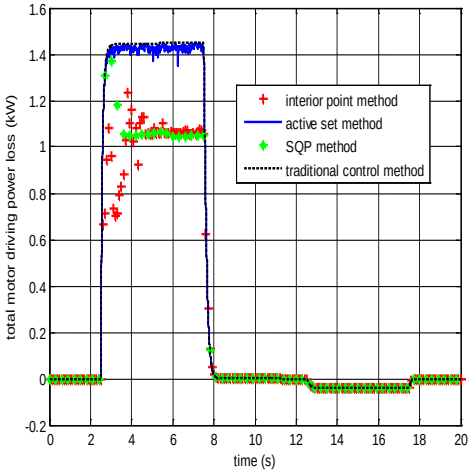

(c) total driving output power – small torque

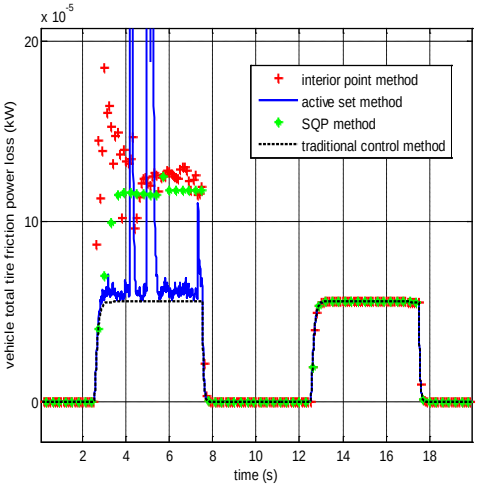

(d) total tyre power loss - small torque

Figure VI-8. The vehicle output power in simulation of the pure longitudinal motion.

2) The simulation results of vehicle cornering motion

Linear pure longitudinal motion is a simple control allocation scenario, and only the four driving/braking actuators are utilised. When the vehicle is cornering, the control targets of handling, stability and energy efficiency must all be achieved. In addition to four driving/braking control actuators, four steering control actuators are used to achieve the control targets. In the second set of simulations, the vehicle is performing a simple J-turn

manoeuvre with the steering angle of 5 degrees (Figure VI-9) under the initial velocity of 15 m/s. There is no driving or braking torque applied in the vehicle cornering motion. The controlled yaw rate and body slip angle of three different algorithms (‘interior point’, ‘active set’ and ‘SQP’) in the Matlab embedded function ‘Fmincon’ in the proposed integrated dynamics control and energy efficiency optimisation method are compared with the desired values in Figure VI-10 and Figure VI-11, respectively. The simulation results of a traditional vehicle dynamics controller are also presented for comparison. In the traditional vehicle dynamics controller, the linear feedback stability controller and handling controller in [31] are applied, but the energy efficiency optimal cost function in equation (118) is not included. For the sake of brevity, we are calling the proposed integrated dynamics control and energy efficiency optimisation method the ‘interior point method’, ‘active set method’ and ‘SQP method’ in contrast to the traditional vehicle dynamics control method which we call the ‘traditional control method’. Figure VI-10 and Figure VI-11 suggest that both the traditional control method and integrated control method can achieve the desired yaw rate accurately. The ‘SQP method’ and the ‘active set method’ can achieve better body slip angle control performance than the ‘interior point’ method. This proves that the primary control goals can be achieved by the proposed integrated control method when the vehicle is doing a cornering motion.

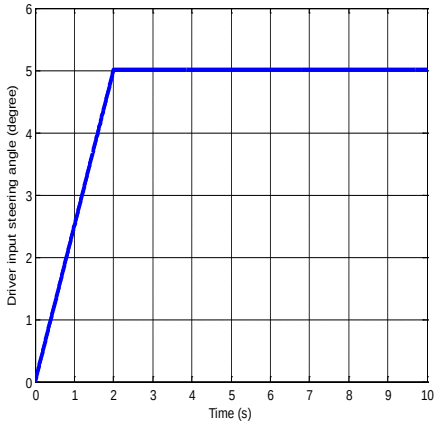

Figure VI-9. Driver’s input steering angle in the second simulation of cornering motion.

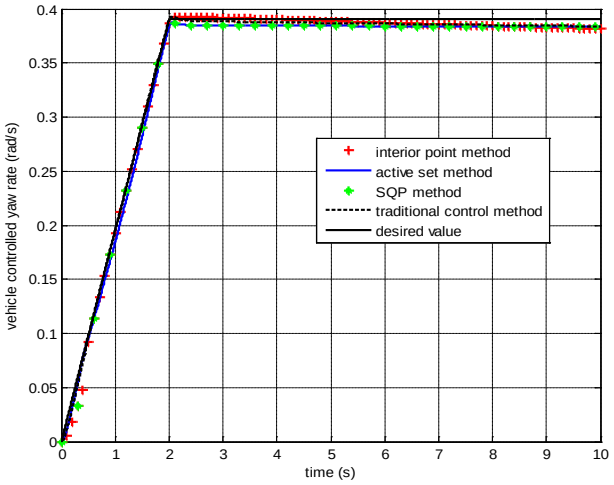

Figure VI-10. Vehicle controlled yaw rate in the second set of simulations.

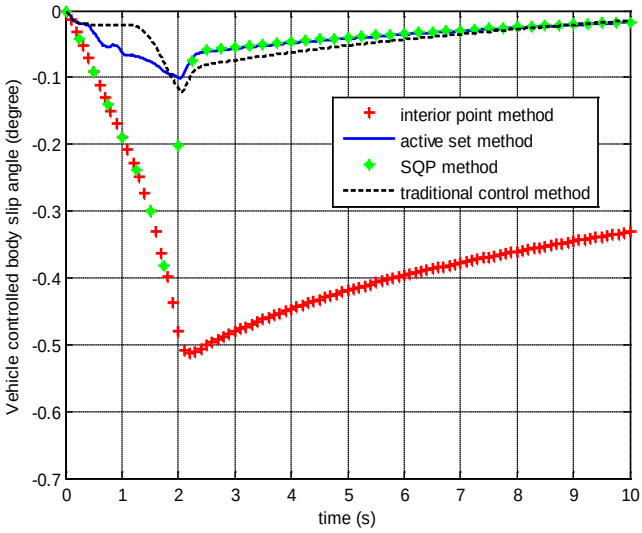

Figure VI-11. Vehicle controlled body slip angle in the second set of simulations.

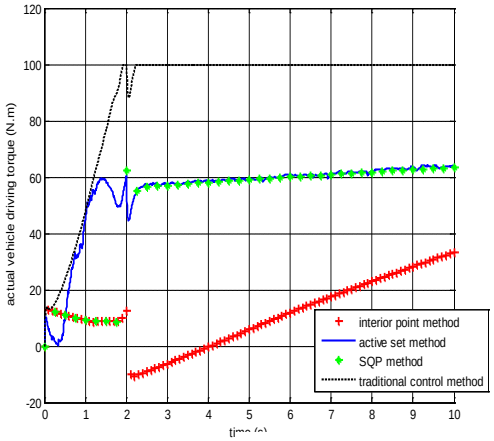

(a)

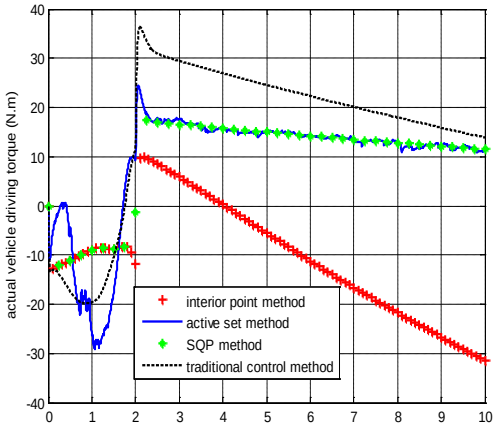

(b)

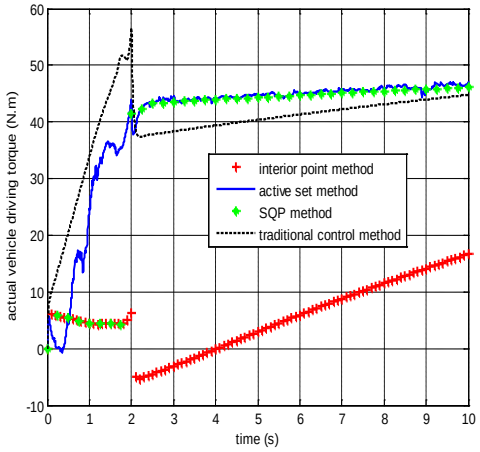

(c)

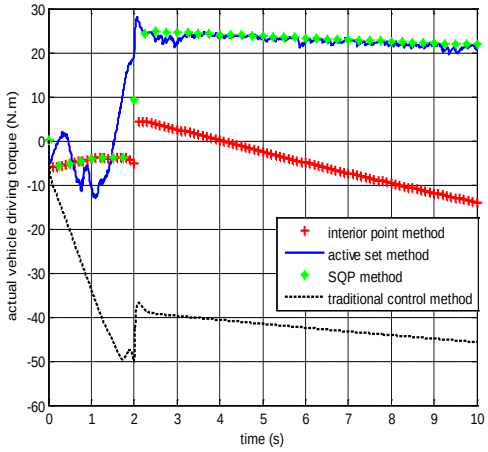

(d)

Figure VI-12. The distributed vehicle input driving torque of each wheel in the second simulation: (a) front left wheel (b) front right wheel (c) rear left wheel (d) rear right wheel.

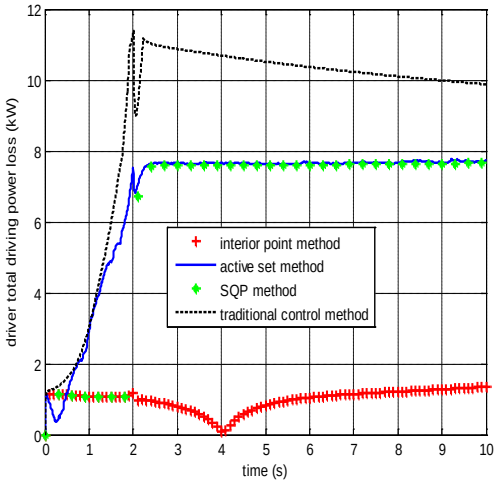

(a) total driving power loss

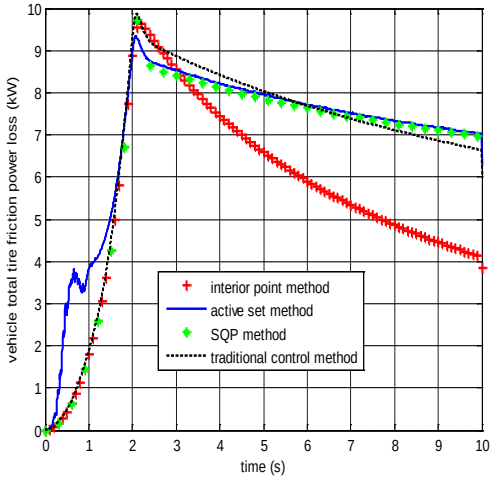

(b) total tyre friction loss

Figure VI-13. Total vehicle output power in the second simulation of cornering motion.

Figure VI-12 and Figure VI-13 present the individual tyre driving torque and total power output of the vehicle controlled by the proposed integrated control method and traditional control method. The integrated control method shows a large improvement in the total vehicle output power, which proves that the secondary control target of energy efficient control can be achieved. The 'interior point' algorithm in particular shows the obvious advantage in power saving compared with other algorithms. The 'SQP' method and the 'active set' method also save more on total power consumption compared with the traditional control method. This result has been clearly presented by the RMS value of the power consumption in Table VI-2.

In the third simulation, the motion of a double lane change is tested to prove the robustness of the proposed controller. The initial vehicle velocity is increased to 20 m/s. The friction coefficient is changed from 0.9 to 0.7 in 10 seconds in order to represent the changing of the road condition. The vehicle input steering angle is shown in Figure VI-14. According to Figure VI-15 and Figure VI-16, similar to the second set of simulations, the proposed integrated control method can achieve good yaw rate and body side-slip angle control performance. Particularly, the 'active set' method can achieve better body side-slip angle control performance compared with the 'interior point' method and the 'SQP' method.

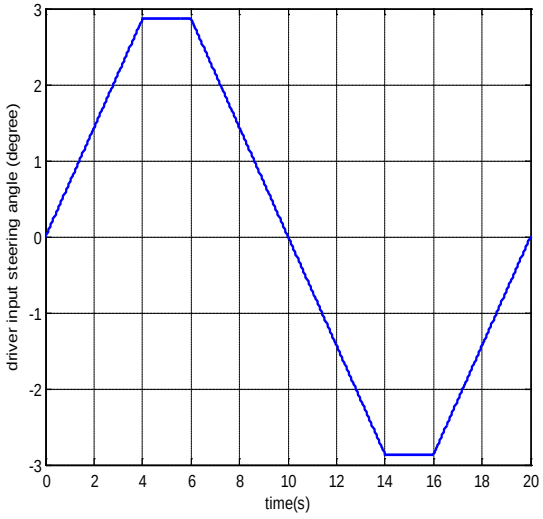

Figure VI-14. Driver's total input driving torque in the third simulation.

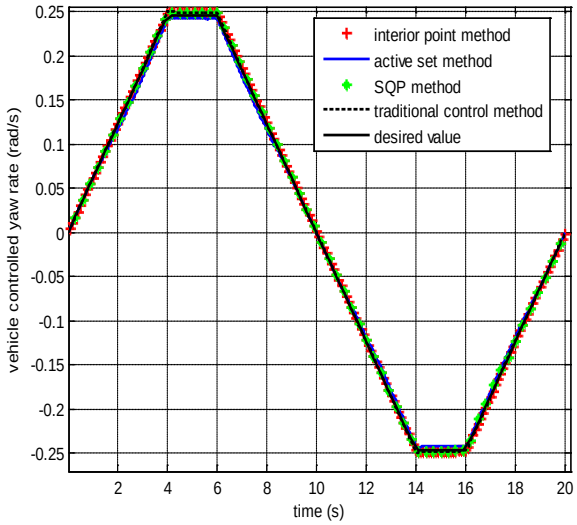

Figure VI-15. Vehicle controlled yaw rate in the third simulation.

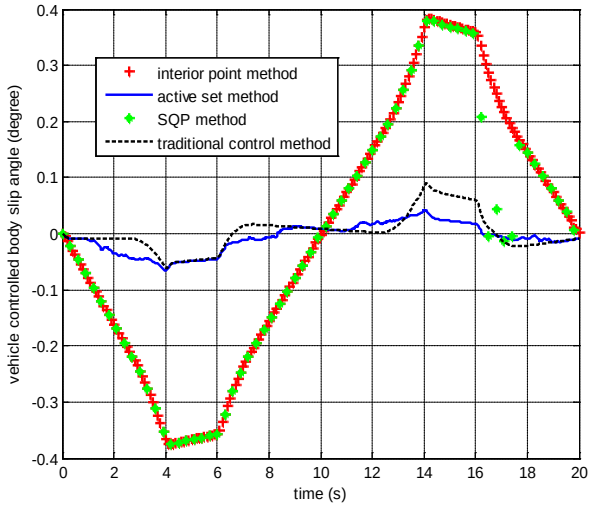

Figure VI-16. Vehicle controlled side-slip angle in the third simulation.

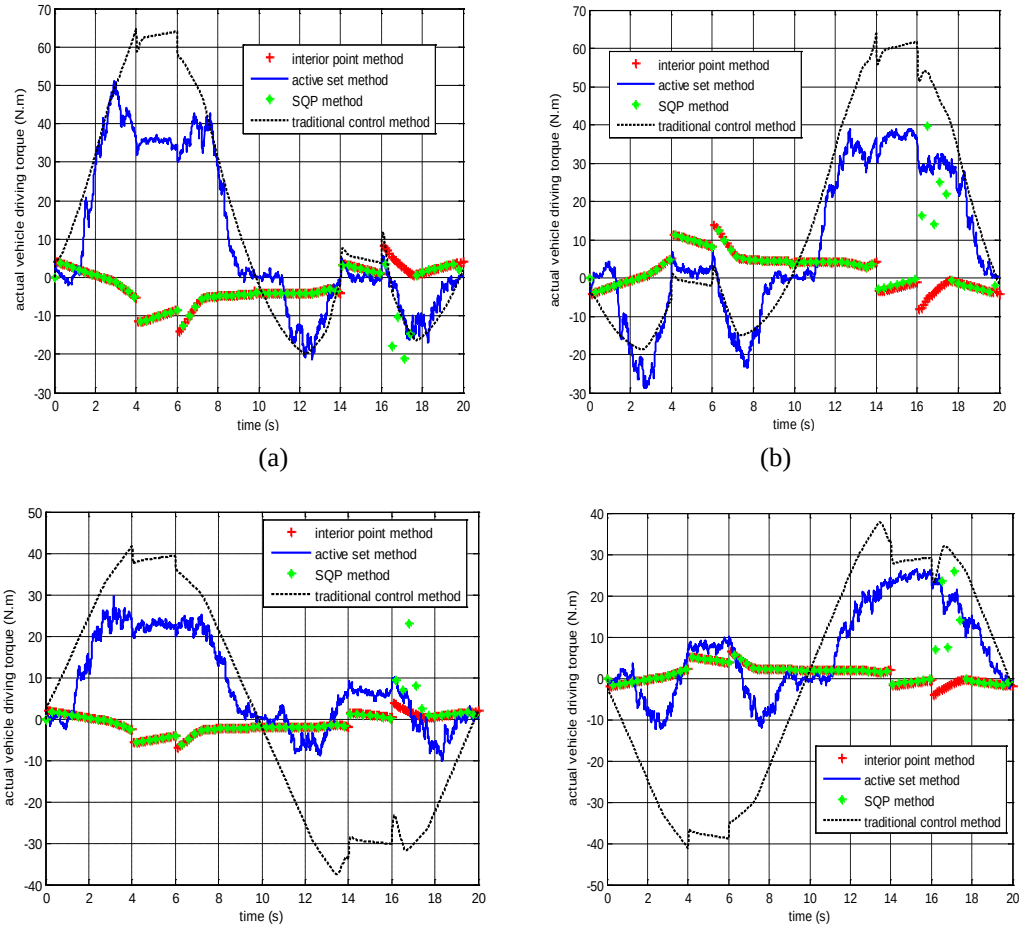

Figure VI-17. The distributed input driving torque of each wheel in the third simulation: (a) front left wheel (b) front right wheel (c) rear left wheel (d) rear right wheel.

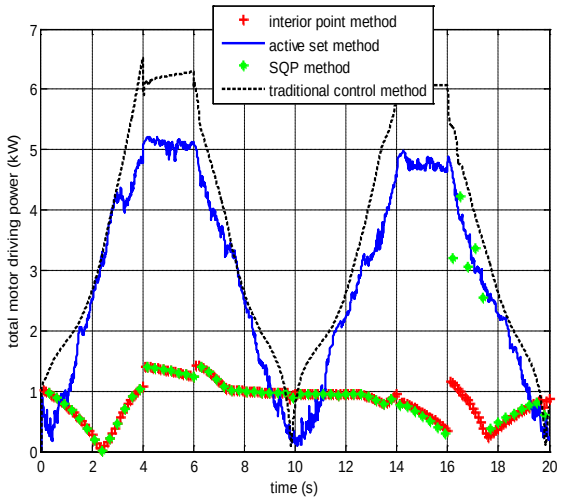

(a) total motor driving power

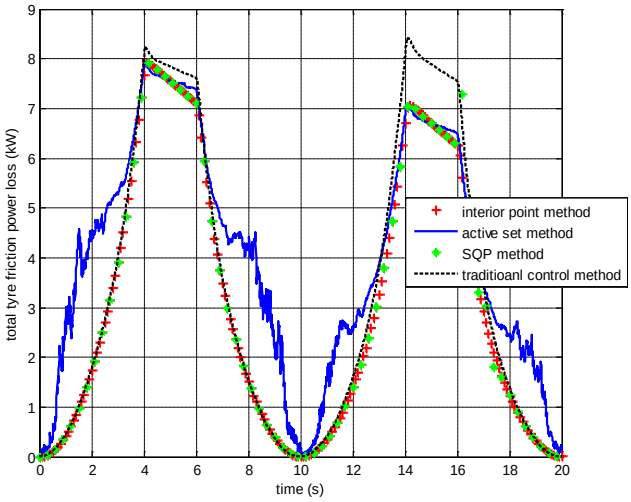

(b) total tyre friction power loss

Figure VI-18. The total output power of the vehicle in the third simulation.

Figure VI-17 shows the driving torque of each individual wheel. In Figure VI-18, the total motor driving power and total tyre friction power loss of each control method are compared. The 'interior point' method has better motor driving efficiency and less tyre friction loss compared both with other proposed methods and with the traditional control method. As can be seen in Table VI-2, the 'interior point' method also has the smallest total power consumption compared with other algorithms and the traditional control method.

Table VI-2. RMS value of the vehicle total power consumption

Vehicle moving scenarios			Motor driving power loss (kW)	Tyre friction power loss (kW)	Total power loss (kW)
Pure longitudinal motion	Large driving input	Interior point method	4.446	0.00982	4.456
		Active set method	4.479	0.00908	4.488
		SQP method	4.479	0.00908	4.488
		Traditional method	4.479	0.00908	4.488
	Small driving input	Interior point method	0.5119	7.06×10^{-5}	0.5120
		Active set method	0.7104	2.28×10^{-4}	0.7106
		SQP method	0.5512	6.12×10^{-5}	0.5513
		Traditional method	0.7204	3.85×10^{-5}	0.7204
Cornering motion	J-turn	Interior point method	1.034	5.991	7.025
		Active set method	7.045	7.283	14.33
		SQP method	6.829	7.161	13.99
		Traditional method	9.549	7.230	16.78
	Double line change	Interior point method	0.9060	4.107	5.013
		Active set method	3.307	4.654	7.961
		SQP method	1.251	4.130	5.381
		Traditional method	4.056	4.532	8.588
Combined pure longitudinal and cornering motion	Interior point method		2.111	8.933	11.04
	Active set method		15.43	13.30	28.73
	SQP method		14.15	12.03	26.18
	Traditional method		16.35	13.44	29.79

3) The simulation results of combined vehicle longitudinal motion and cornering motion

The fourth simulation is used to explore how to use Criterion 1 and Criterion 2 to detect the motion status and implement the corresponding control strategy. The input steering angle is shown in Figure VI-19(a) and the input driving torque is shown in Figure VI-19(b). In the first 4 seconds, the vehicle is under linear pure longitudinal motion, while the vehicle lateral motion starts after 4 seconds. In this way, this simulation can perform the changing of the control strategy from the pure longitudinal motion into the turning motion. The vehicle initial velocity is 17.5 m/s and friction coefficient is 0.9.

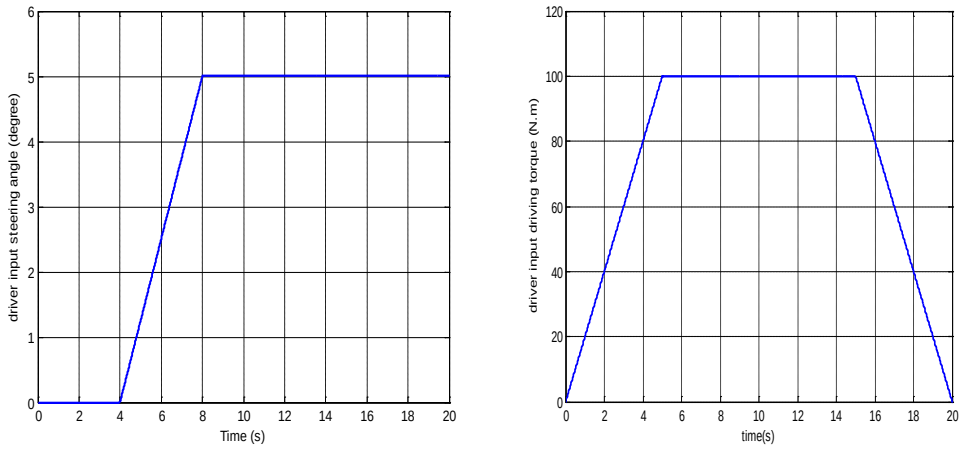

(a) (b)

Figure VI-19. Driver's (a) steering angle input and (b) total input driving torque in the fourth simulation.

Figure VI-20 and Figure VI-21 suggest the yaw rate and body side-slip angle responses in the whole simulation of changing from the linear pure longitudinal motion into the turning motion. At the beginning, the vehicle is moving under the conditions of linear pure longitudinal motion and only the driving energy-efficient controller is applied since Criterion 1 and Criterion 2 are both satisfied. After nearly 5 seconds, the vehicle starts turning and the vehicle is no longer performing linear pure longitudinal motion because Criterion 1 and Criterion 2 are not both satisfied. The stability controller and handling controller are implemented immediately by the designed switcher after 5 seconds to improve the yaw rate and body side-slip angle responses which are the primary control targets. Meanwhile, the driving actuator's energy efficiency is also improved due to the secondary control target. All three algorithms can roughly achieve the desired yaw rate and the controlled body side-slip angle of the 'interior point' method is larger than that of other proposed methods as well as the traditional control method.

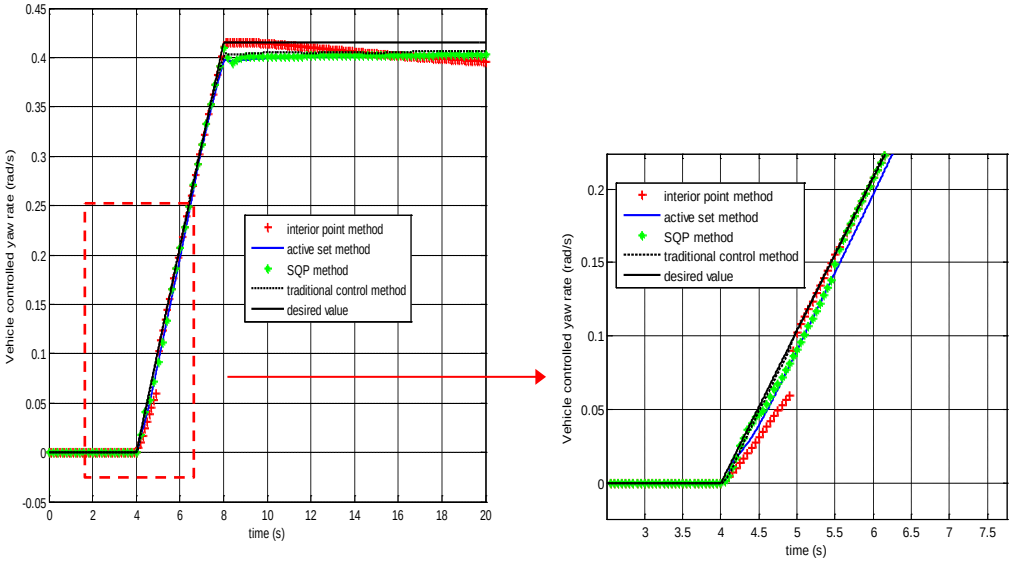

Figure VI-20. Vehicle controlled yaw rate in the fourth simulation.

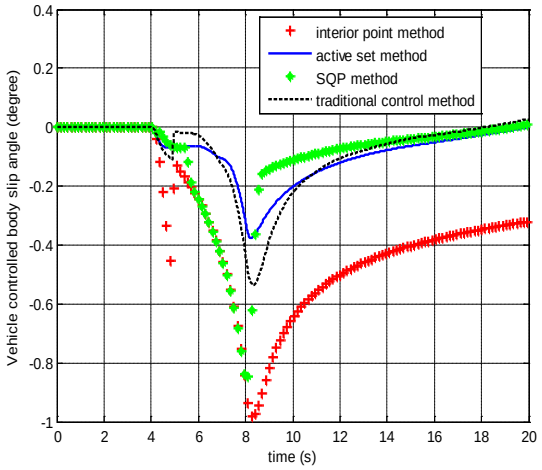

Figure VI-21. Vehicle controlled body slip angle in the fourth simulation.

Figure VI-22 and Figure VI-23 show the actual individual wheel driving torque and total actual output power in the whole simulation. In the first 5 seconds when the vehicle is under the condition of pure linear longitudinal motion, the driving toque is equally distributed among all four wheels. After 5 seconds, when the cornering motion starts, the 'interior point' method has the smallest motor driving power and tyre friction power loss compared with other algorithms and the traditional control method. The RMS value of the power consumption in Table VI-2 also verifies that the 'interior power' method has the best power saving performance.

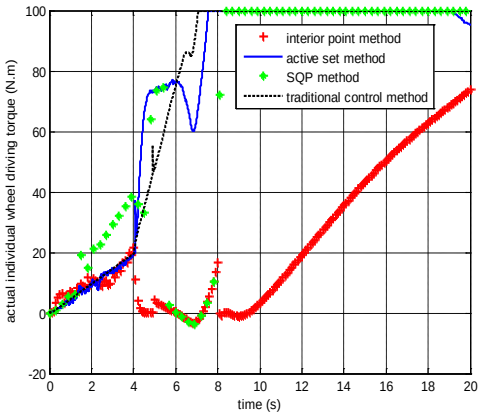

(a)

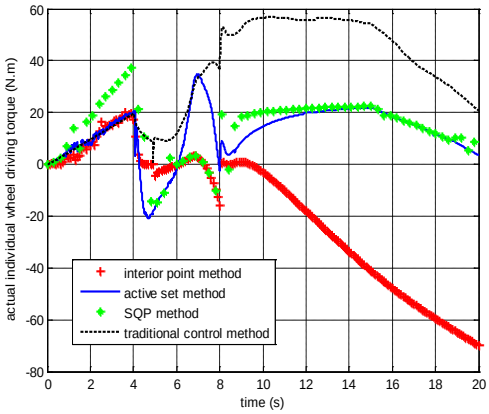

(b)

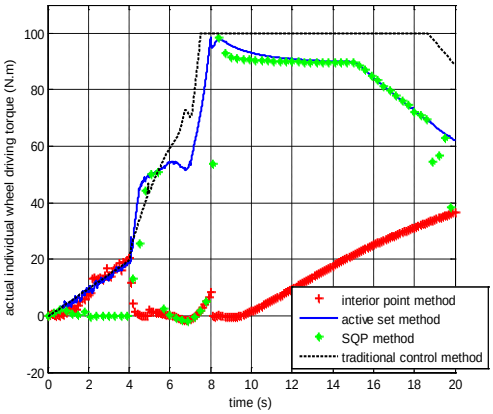

(c)

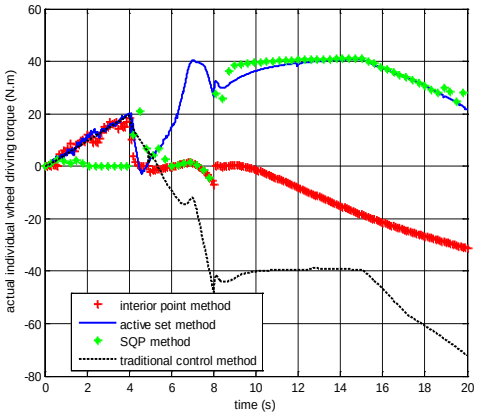

(d)

Figure VI-22. The actual driving torque of each wheel in the fourth simulation: (a) front left wheel (b) front right wheel (c) rear left wheel (d) rear right wheel.

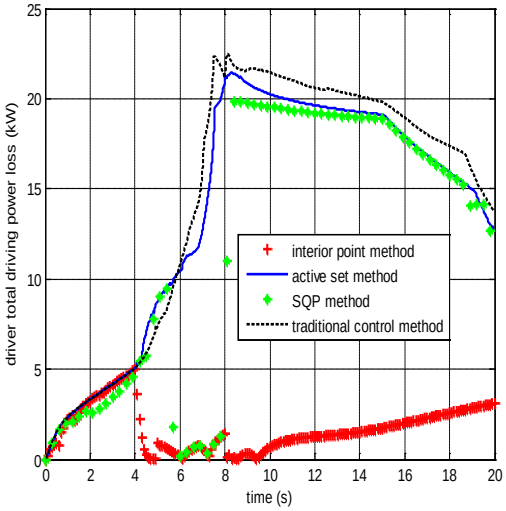

(a) total motor driving power

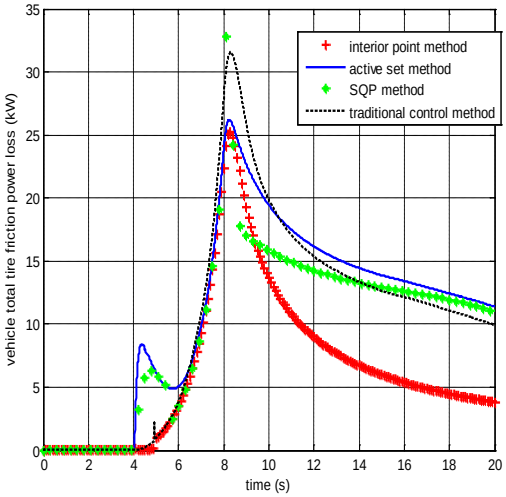

(b) total tyre friction power loss

Figure VI-23. The vehicle's total output power in the fourth simulation.

6. Summary

This chapter proposes an integrated dynamics control and energy efficiency optimisation method for both linear pure longitudinal motion and non-linear or turning motion. In the linear pure longitudinal motion, only the energy-efficient controller is proposed. In the vehicle non-linear motion or turning motion, the handling controller, stability controller and energy-efficient controller are all suggested. According to the simulation results, our findings can be summarised as follows:

In linear pure longitudinal motion, the simulation results suggest that the equal distribution of the driving torque and the braking torque of individual wheels is the optimal control allocation method during the medium-high torque demand. In the small torque demand, two specific wheels in the same axle are responsible for the major driving workload.

In both the pure cornering motion and combined traction and cornering motion, the simulation results suggest that the proposed integrated controller can successfully achieve the primary handling and stability control. In addition, the total output power of the driving toque is also optimised compared with the traditional dynamics control method. Particularly, although the body side-slip angle control performance is compromised, the ‘interior point’ algorithm of the integrated controller can achieve the best total power saving performance in most of the simulations. ‘Active set’ and ‘SQP’ algorithms have better body side-slip angle control but the total power efficiency improvement is limited. This is because the side-slip angle control needs more control efforts and energy consumption, so it is hard to balance the side-slip angle performance and the energy efficiency. This study suggests that the optimization algorithm should be chosen based on the priority: if the vehicle is moving smoothly and the energy efficiency is the primary issue, the ‘interior point’ algorithm can be implemented; if the vehicle is turning abruptly and the stability is more important, the ‘Active set’ and ‘SQP’ algorithms should be selected.

The proposed motion detection criteria are proved to successfully determine the transition point between the linear pure longitudinal motion and the non-linear motion or the cornering motion, and the control strategies can be switched by a designed switcher at this transition point.

In the following chapter, the application of the over-actuated controller on the fault-tolerant control will be focused.

VII. Application of the over-actuated control allocation method in the design of the fault-tolerant control

This chapter focuses on the fault-tolerant control method and the location of the specific faulty wheel is assumed to be known. This assumption is reasonable according to the literature [202] [216] [217] [173]. The newly proposed SMC fault-tolerant controller focuses primarily on 4WIS-4WID EVs. The main contribution of this paper is to solve the coupling effect of different control targets by grouping the actual driving actuators in fault-tolerant control of a 4WID vehicle. In addition, due to the fault of one specific wheel, the steering geometry of the whole vehicle will be re-arranged and the actual steering actuators will be adjusted in the 4WIS vehicle.

1. Steering geometry while wheel-fault happening

According to [80] [52], a complete steering model for an individual wheel of the electric vehicle can be presented by the following equation:

$$I_s\ddot{\delta}_i + c_s\dot{\delta}_i + k_s\delta_i = \tau_a + \tau_j + \tau_{act} \tag{124}$$

where τ_{act} is the actual steering torque generated from the steering motor. The output steering angle δ_i can be controlled by adjusting the actual steering torque τ_{act} according to the desired steering angle given by the driver. Therefore, the steering angle of an individual wheel δ_i is assumed to be known when all the wheels work well. However, when an individual steering motor cannot work, the actual steering torque is zero and the output steering angle is governed by the following equation:

$$I_s\ddot{\delta}_i + c_s\dot{\delta}_i + k_s\delta_i = \tau_a + \tau_j \tag{125}$$

It is suggested that the jacking torque does not play the important role when the vehicle longitudinal velocity is large and the tyre lateral force is large. In this study, the vehicle initial longitudinal velocity is 20 m/s or 15 m/s, which is quite large. Thus, the effect of jacking

torque can be neglected and the steering angle is determined by the total alignment moment τ_a:

$$\tau_a = -\left(t_m + t_{p0} - \frac{t_{p0} C_\alpha}{3\mu F_{zi}} |\tan \alpha_i|\right) F_{si} \tag{126}$$

where t_m is the mechanical trail and t_{p0} is the initial pneumatic trail.

If one wheel is faulty during vehicle turning, the steering angle of other three wheels must be adjusted according to the steering geometry in Figure VII-1 to maintain the turning. One simple method to realise the geometry in Figure VII-1 is shown as follows:

1) If the faulty wheel is the front wheel, the vehicle *ICR* is located on the extension cord of the front track. The steering angle of the healthy front wheel is zero and the steering angle of the front faulty wheel is determined by (125)(126). The steering angles of the rear left and rear right wheels can be calculated as [7]:

$$\delta_i = \tan^{-1}\left(D^T(x_i - x_{ICR}), -D^T(y_i - y_{ICR})\right) \tag{127}$$

where $x_{ICR} = l_f$ and $y_{ICR} = \frac{l_f + l_r}{\delta_d}$. $i = rl, rr$, which presents the rear left and rear right wheel, respectively. δ_d is the desired steering angle, which is determined by the driver. $(x_{rl}, y_{rl}) = \left(-l_r, \frac{b_f}{2}\right)$ and $(x_{rr}, y_{rr}) = \left(-l_r, -\frac{b_f}{2}\right)$ are the positions of the wheel centre. $D^T = 1$, if turning in an anti-clockwise direction; $D^T = -1$, if turning in a clockwise direction.

It should be noted that if the driver's desired steering centre is δ_d, the vehicle turning radius is $R = \frac{l_f + l_r}{\delta_d}$. The turning radius is the distance between the vehicle centre of gravity and the *ICR* but in this paper it is assumed that the distance between the front wheel centre (rear wheel centre) and the *ICR* is the turning radius. This assumption is reasonable because usually, the turn radius is much larger than the vehicle wheel base.

2) If the faulty wheel is the rear wheel, the vehicle *ICR* is located on the extension cord of the rear track. The steering angle of the rear healthy wheel is zero and the steering angle of the rear faulty wheel can be determined by equations (125) and (126). The steering angles of the front left and front right wheel can be calculated using equation (127). In equation (127),

$i = fl, fr$, which represents the front left and front right wheel, respectively. In addition, $x_{ICR} = -l_r$ and $y_{ICR} = \frac{l_f + l_r}{\delta_d}$. $(x_{rl}, y_{rl}) = \left(-l_r, \frac{b_f}{2}\right)$ and $(x_{rr}, y_{rr}) = \left(-l_r, -\frac{b_f}{2}\right)$ are positions of the wheel centre. $D^T = 1$, if the turning is anti-clockwise; $D^T = -1$, if the turning is clockwise.

The motor driver and in-wheel motor driving unit can be described by a control gain k_i, which is related to the in-wheel driving motor of each wheel.

$$k_i = \frac{T_i}{V_i} \tag{128}$$

where T_i is the driving torque of each wheel of the in-wheel motor and V_i is the input voltage of the in-wheel motor.

If the driving wheel is in a healthy condition, the normalised control gain k_i is assumed to be equal to 1. The value of k_i can be estimated by various fault diagnosis methods [202] [217]. The specific faulty wheel can be identified according to the estimation results of the control gain of driving torque k_i.

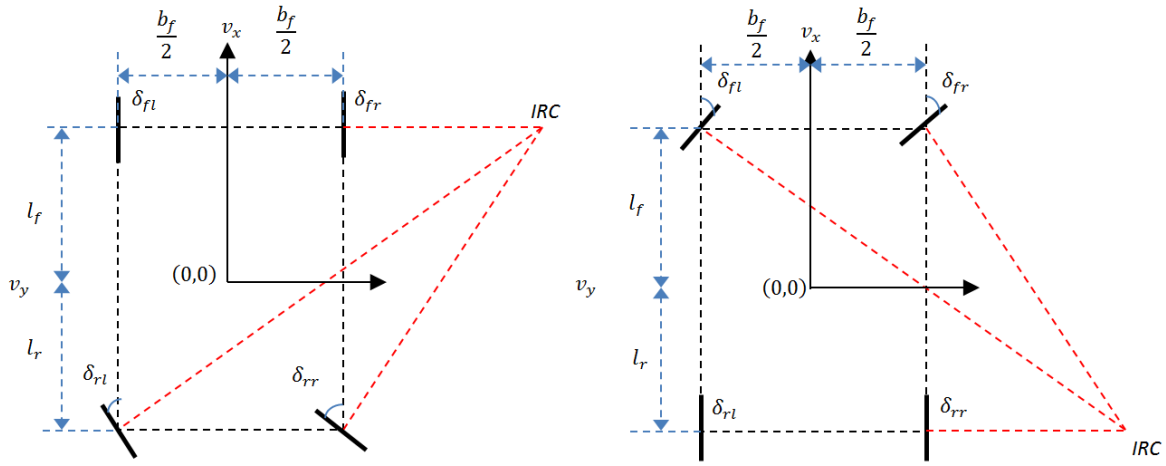

Figure VII-1. The vehicle steering geometry when one of the four wheels is the faulty wheel.

It should be noted that if the two front wheels of the vehicle cannot work during turning, the vehicle can move like a rear wheel steering vehicle. Similarly, if the two rear wheels of the vehicle are faulty during turning, the vehicle can move as a front wheel steering vehicle. However, if one of the front wheels and one of the rear wheels cannot work or more than three wheels are faulty, the vehicle cannot make a turn and must stop.

2. Sliding mode controller design

To evaluate the SMC, the vehicle dynamics equation can be simplified using the following equations [202]:

$$\dot{v}_x = v_y r + \frac{1}{m} F_x \quad \text{(a)}$$

$$\dot{v}_y = -v_x r + \frac{1}{m} F_y \quad \text{(b)}$$

$$\dot{r} = \frac{1}{I_z} M_z \quad \text{(c)}$$

(129)

where F_x, F_y and M_z are the total longitudinal force, lateral force and yaw moment.

$$F_x = F_{xfl} + F_{xfr} + F_{xrl} + F_{xrr} \quad \text{(a)}$$

$$F_y = F_{yfl} + F_{yfr} + F_{yrl} + F_{yrr} \quad \text{(b)}$$

$$M_z = l_f\left(F_{yfl} + F_{yfr}\right) - l_r\left(F_{yrl} + F_{yrr}\right) + \frac{b_f}{2}\left(F_{xfl} - F_{xfr}\right) + \frac{b_r}{2}\left(F_{xrl} - F_{xrr}\right) \quad \text{(c)}$$

(130)

According to [20], equation (129) can be rewritten as:

$$\begin{bmatrix} \dot{v}_x \\ \dot{v}_y \\ \dot{r} \end{bmatrix} = \begin{bmatrix} v_y r \\ -v_x r \\ 0 \end{bmatrix} + B_y(\delta_i)\boldsymbol{F_s} + B_x(\delta_i)\boldsymbol{F_t}$$

(131)

where $\boldsymbol{F_t} = [F_{tfl} \quad F_{tfr} \quad F_{trl} \quad F_{trr}]^{\boldsymbol{T}}$, $\boldsymbol{F_s} = [F_{sfl} \quad F_{sfr} \quad F_{srl} \quad F_{srr}]^{\boldsymbol{T}}$, which presents the tyre force along the wheel direction and perpendicular to the wheel direction, respectively.

$$B_x(\delta_i) = \begin{bmatrix} \frac{1}{m} & 0 & 0 \\ 0 & \frac{1}{m} & 0 \\ 0 & 0 & \frac{1}{I_z} \end{bmatrix} \begin{bmatrix} \cos\delta_{fl} & \cos\delta_{fr} & \cos\delta_{rl} & \cos\delta_{rr} \\ \sin\delta_{fl} & \sin\delta_{fr} & \sin\delta_{rl} & \sin\delta_{rr} \\ l_f \sin\delta_{fl} + \frac{b_f}{2}\cos\delta_{fl} & l_f \sin\delta_{fr} - \frac{b_f}{2}\cos\delta_{fr} & \frac{b_r}{2}\cos\delta_{rl} - l_r \sin\delta_{rl} & -\frac{b_r}{2}\cos\delta_{rr} - l_r \sin\delta_{rr} \end{bmatrix}$$

$$B_y(\delta_i)$$
$$= \begin{bmatrix} \frac{1}{m} & 0 & 0 \\ 0 & \frac{1}{m} & 0 \\ 0 & 0 & \frac{1}{I_z} \end{bmatrix} \begin{bmatrix} -\sin\delta_{fl} & -\sin\delta_{fr} & -\sin\delta_{rl} & -\sin\delta_{rr} \\ \cos\delta_{fl} & \cos\delta_{fr} & \cos\delta_{rl} & \cos\delta_{rr} \\ l_f\cos\delta_{fl} - \frac{b_f}{2}\sin\delta_{fl} & l_f\cos\delta_{fr} + \frac{b_f}{2}\sin\delta_{fr} & -\frac{b_r}{2}\sin\delta_{rl} - l_r\cos\delta_{rl} & \frac{b_r}{2}\sin\delta_{rr} - l_r\cos\delta_{rr} \end{bmatrix}$$

According to the wheel dynamics and equation (128), the individual tyre longitudinal force F_{ti} can be written as:

$$F_{ti} = \frac{k_i V_i - I_\omega \dot{\omega}_i}{R_\omega} \tag{132}$$

Therefore, the longitudinal tyre force can be presented by the following equation:

$$\boldsymbol{F_t} = \frac{1}{R_\omega}\begin{bmatrix} k_{fl} & 0 & 0 & 0 \\ 0 & k_{fr} & 0 & 0 \\ 0 & 0 & k_{rl} & 0 \\ 0 & 0 & 0 & k_{rr} \end{bmatrix}\begin{bmatrix} V_{fl} \\ V_{fr} \\ V_{rl} \\ V_{rr} \end{bmatrix} - \frac{I_\omega}{R_\omega}\begin{bmatrix} \dot{\omega}_{fl} \\ \dot{\omega}_{fr} \\ \dot{\omega}_{rl} \\ \dot{\omega}_{rr} \end{bmatrix} \tag{133}$$

Based on (133), vehicle model (131) can be rewritten as:

$$\begin{bmatrix} \dot{v}_x \\ \dot{v}_y \\ \dot{r} \end{bmatrix} = \begin{bmatrix} v_y r \\ -v_x r \\ 0 \end{bmatrix} + B_y(\delta_i)\boldsymbol{F_s} + \frac{B_x(\delta_i)}{R_\omega}\left(\begin{bmatrix} k_{fl} & 0 & 0 & 0 \\ 0 & k_{fr} & 0 & 0 \\ 0 & 0 & k_{rl} & 0 \\ 0 & 0 & 0 & k_{rr} \end{bmatrix}\begin{bmatrix} V_{fl} \\ V_{fr} \\ V_{rl} \\ V_{rr} \end{bmatrix} - I_\omega \begin{bmatrix} \dot{\omega}_{fl} \\ \dot{\omega}_{fr} \\ \dot{\omega}_{rl} \\ \dot{\omega}_{rr} \end{bmatrix}\right) \tag{134}$$

It is assumed that the lateral tyre force can be described by the following equation related to the side-slip angle if the linear relationship is assumed:

$$F_{si-linear} = C_a \alpha_i(v_x, v_y, r) \tag{135}$$

If the non-linear tyre characteristic is considered, the tyre lateral force can be presented as follows:

$$F_{si} = F_{si-linear} + \Delta F_{si} = C_a \alpha_i(v_x, v_y, r) + \Delta F_{si}$$

(136)

ΔF_{si} represents the additional lateral tyre force caused by the non-linear tyre characteristic.

In this way, equation (134) can be rewritten as equation (137) by neglecting the lateral tyre non-linear characteristics and acceleration of the wheel angular velocity. This simplification is reasonable because these neglected values can be compensated for by increasing the sliding mode gain.

$$\begin{bmatrix} \dot{v}_x \\ \dot{v}_y \\ \dot{r} \end{bmatrix} = \begin{bmatrix} v_y r \\ -v_x r \\ 0 \end{bmatrix} + B_y(\delta_i)\boldsymbol{F_{s-linear}} + \frac{1}{R_\omega}\begin{bmatrix} \frac{1}{m} & 0 & 0 \\ 0 & \frac{1}{m} & 0 \\ 0 & 0 & \frac{1}{I_z} \end{bmatrix}$$

$$\begin{bmatrix} \cos\delta_{fl}\,k_{fl} & \cos\delta_{fr}\,k_{fr} & \cos\delta_{rl}\,k_{rl} & \cos\delta_{rr}\,k_{rr} \\ \sin\delta_{fl}\,k_{fl} & \sin\delta_{fr}\,k_{fr} & \sin\delta_{rl}\,k_{rl} & \sin\delta_{rr}\,k_{rr} \\ \left(l_f\sin\delta_{fl} + \frac{b_f}{2}\cos\delta_{fl}\right)k_{fl} & \left(l_f\sin\delta_{fr} - \frac{b_f}{2}\cos\delta_{fr}\right)k_{fr} & \left(\frac{b_r}{2}\cos\delta_{rl} - l_r\sin\delta_{rl}\right)k_{rl} & \left(-\frac{b_r}{2}\cos\delta_{rr} - l_r\sin\delta_{rr}\right)k_{rr} \end{bmatrix}$$

$$\begin{bmatrix} V_{fl} \\ V_{fr} \\ V_{rl} \\ V_{rr} \end{bmatrix}$$

(137)

where $\boldsymbol{F_{s-linear}} = \begin{bmatrix} C_a\alpha_{fl}(v_x, v_y, r) \\ C_a\alpha_{fr}(v_x, v_y, r) \\ C_a\alpha_{rl}(v_x, v_y, r) \\ C_a\alpha_{rr}(v_x, v_y, r) \end{bmatrix}$

The SMC control law is evaluated according to equation (137):

$$\dot{v}_x = v_y r + B_{y1}\boldsymbol{F_{s-linear}} + \upsilon_1 \quad \text{(a)}$$

$$\dot{v}_y = -v_x r + B_{y2}\boldsymbol{F_{s-linear}} + \upsilon_2 \quad \text{(b)}$$

$$\dot{r} = B_{y3}\boldsymbol{F_{s-linear}} + \upsilon_3 \quad \text{(c)}$$

(138)

where $B_{y1} = \left[-\frac{\sin\delta_{fl}}{m} \quad -\frac{\sin\delta_{fr}}{m} \quad -\frac{\sin\delta_{rl}}{m} \quad -\frac{\sin\delta_{rr}}{m}\right]$, $B_{y2} = \left[\frac{\cos\delta_{fl}}{m} \quad \frac{\cos\delta_{fr}}{m} \quad \frac{\cos\delta_{rl}}{m} \quad \frac{\cos\delta_{rr}}{m}\right]$, $B_{y3} = \left[\frac{1}{I_z}\left(l_f\cos\delta_{fl} - \frac{b_f}{2}\sin\delta_{fl}\right) \quad \frac{1}{I_z}\left(l_f\cos\delta_{fr} + \frac{b_f}{2}\sin\delta_{fr}\right) \quad \frac{1}{I_z}\left(-\frac{b_r}{2}\sin\delta_{rl} - l_r\cos\delta_{rl}\right) \quad \frac{1}{I_z}\left(\frac{b_r}{2}\sin\delta_{rr} - l_r\cos\delta_{rr}\right)\right]$

The control law can be chosen such as:

$$\upsilon_1 = -v_y r - B_{y1}\boldsymbol{F_{s-linear}} + \dot{v}_{xr} - K_1 sgn(S_1) \quad \text{(a)}$$

$$\upsilon_2 = v_x r - B_{y2}\boldsymbol{F_{s-linear}} + \dot{v}_{yr} - K_2 sgn(S_2) \quad \text{(b)}$$

$$\upsilon_3 = -B_{y3}\boldsymbol{F_{s-linear}} + \dot{r}_r - K_3 sgn(S_3) \quad \text{(c)}$$

(139)

where v_{xr}, v_{yr} and r_r present the desired longitudinal velocity, lateral velocity and yaw rate. $\dot{v}_{xr}$, $\dot{v}_{yr}$ and $\dot{r}_r$ and the desired longitudinal acceleration, lateral acceleration and yaw acceleration. K_1, K_2 and K_3 are the control gains of SMC corresponding to υ_1, υ_2 and υ_3 respectively.

The sliding surface of each channel S_1, S_2 and S_3 can be defined as:

$$S_n = x_n - x_{nr}$$

(140)

where $n = 1,2,3$, x_{nr} is the vehicle state reference (v_{xr}, v_{yr}, r_r) and x_n is the vehicle state (v_x, v_y, r).

To prove the stability of the suggested control law, the Lyapunov method is used. The Lyapunov functions for the three channels can be chosen as:

$$V_n = \frac{1}{2}S_n^2$$

(141)

The time derivative of the above Lyapunov function is:

$$\dot{V}_1 = S_1\dot{S}_1 = S_1(\dot{v}_x - \dot{v}_{xr}) = S_1\left(v_y r + B_{y1}\boldsymbol{F_{s-linear}} + \upsilon_1 - \dot{v}_{xr}\right) \quad \text{(a)}$$

$$\dot{V}_2 = S_2\dot{S}_2 = S_2\left(\dot{v}_y - \dot{v}_{yr}\right) = S_2\left(-v_x r + B_{y2}\boldsymbol{F_{s-linear}} + \upsilon_2 - \dot{v}_{yr}\right) \quad \text{(b)}$$

$$\dot{V}_3 = S_3\dot{S}_3 = S_3(\dot{r} - \dot{r}_r) = S_3\left(B_{y3}\boldsymbol{F_{s-linear}} + \upsilon_3 - \dot{r}_r\right) \quad \text{(c)}$$

(142)

By applying the suggested control law in equation (139), equation (142) is rewritten as:

$$\dot{V}_1 = S_1\dot{S}_1 = -S_1K_1sgn(S_1) = -K_1|S_1| \quad \text{(a)}$$

$$\dot{V}_2 = S_2\dot{S}_2 = -S_2K_2sgn(S_2) = -K_2|S_2| \quad \text{(b)}$$

$$\dot{V}_3 = S_3\dot{S}_3 = -S_3K_3sgn(S_3) = -K_3|S_3| \quad \text{(c)}$$

(143)

According to equation (143), the time derivative of the above Lyapunov function is always negative, which proves the stability of the whole system.

To achieve the control law in equation (139), the actual driving torque of each wheel should be distributed according to equation (138):

$$\upsilon_1 = \frac{1}{R_\omega m}\left(\cos\delta_{fl}\,k_{fl}u_{fl} + \cos\delta_{fr}\,k_{fr}u_{fr} + \cos\delta_{rl}\,k_{rl}u_{rl} + \cos\delta_{rr}\,k_{rr}u_{rr}\right) = -v_y r - B_{y1}\boldsymbol{F_{s-linear}} + \dot{v}_{xr} - K_1sgn(S_1) \quad \text{(a)}$$

$$\upsilon_2 = \frac{1}{R_\omega m}\left(\sin\delta_{fl}\,k_{fl}u_{fl} + \sin\delta_{fr}\,k_{fr}u_{fr} + \sin\delta_{rl}\,k_{rl}u_{rl} + \sin\delta_{rr}\,k_{rr}u_{rr}\right) = v_x r - B_{y2}\boldsymbol{F_{s-linear}} + \dot{v}_{yr} - K_2sgn(S_2) \quad \text{(b)}$$

$$\upsilon_3 = \frac{1}{R_\omega I_z}\left(\left(l_f\sin\delta_{fl} + \frac{b_f}{2}\cos\delta_{fl}\right)k_{fl}u_{fl} + \left(l_f\sin\delta_{fr} - \frac{b_f}{2}\cos\delta_{fr}\right)k_{fr}u_{fr} + \left(\frac{b_r}{2}\cos\delta_{rl} - l_r\sin\delta_{rl}\right)k_{rl}u_{rl} + \left(-\frac{b_r}{2}\cos\delta_{rr} - l_r\sin\delta_{rr}\right)k_{rr}u_{rr}\right) = -B_{y3}\boldsymbol{F_{s-linear}} + \dot{r}_r - K_3sgn(S_3) \quad \text{(c)}$$

(144)

It is noted that the longitudinal velocity, lateral velocity and yaw rate are assumed to be available. Lateral tyre force $\boldsymbol{F_{s-linear}}$ can be estimated according to the linear tyre model and the side-slip angle of each individual wheel and the non-linear tyre characteristic is neglected. These assumptions are reasonable because the estimation of the longitudinal velocity, lateral velocity, longitudinal slip ratio, friction coefficient and lateral side-slip angle of the vehicle

has been done previously [61] [62] [27]. The actual vehicle yaw rate r can be measured by inertial measurement unit (IMU).

The function $sgn(x)$ used in SMC control law (144) will cause the serious chattering effect due to the abrupt change. In order to achieve continues and smooth switching control law, the saturation function $Sat(x)$ is used as follows instead of $sgn(x)$ in SMC:

$$Sat(x) = \begin{cases} 1 & if\ x > \varepsilon \\ sgn(x) & if\ -\varepsilon \le x \le \varepsilon \\ -1 & if\ x < -\varepsilon \end{cases} \tag{145}$$

where ε is the thickness of the boundary layer.

The desired longitudinal acceleration $\dot{v}_{xr}$ is determined by driver's desired driving input T_d, which is shown in equation (146). The desired longitudinal velocity v_{xr} can be determined by the integration of the desired longitudinal acceleration.

$$\dot{v}_{xr} = \frac{T_d}{mR_\omega} \tag{146}$$

The desired lateral velocity and lateral acceleration are assumed as zero. The lateral velocity is related to the vehicle body side-slip angle, which is an important value to present the vehicle stability. Boada et al. suggested the vehicle desired body side-slip angle is zero [100]:

$$\beta_d = 0 \tag{147}$$

The desired yaw rate can be calculated according to equation (**74**). The desired yaw acceleration is determined by the derivative of the desired yaw rate.

When a particular driving motor fails, the corresponding driving gain V_i can be reduced to reflect this failure. The vehicle handling and stability can be guaranteed by achieving the virtual control values v_1, v_2 and v_3 in SMC.

In the traditional SMC method, the distributed input voltage V_i of each driving motor can be solved by equation (144). However, there are four variables in three equations. Even if one of

the driving motors is faulty, we actually do not need to control all these three control targets under certain scenarios. For example, only control of the longitudinal velocity and yaw rate are required under normal driving conditions with a small steering angle. If the vehicle is turning with a large steering angle, only control of the yaw rate and body side-slip angle (related to the lateral velocity) is required.

Therefore, the SMC control system in equation (144) can be considered as an over-actuated control allocation problem. An allocation optimisation method can be proposed to minimise the control effort of each individual driving motor and meet the constraints of equation (144) at the same time. The constraints (144)(a), (144)(b) and (144)(c) can be chosen according to the actual scenarios. The cost function of the optimisation problem is:

$$J = \frac{1}{k_{fl}} u_{fl}^2 + \frac{1}{k_{fr}} u_{fr}^2 + \frac{1}{k_{rl}} u_{rl}^2 + \frac{1}{k_{rr}} u_{rr}^2$$

(148)

s.t. equations (148)(a), (148)(b) and (148)(c).

The cost function (148) can minimise the driving effort of individual wheels. Meanwhile, including the motor driving gain can counterbalance the large driving effort of a faulty wheel.

In addition, the practical limitation of the the maximum driving torque of the individual wheel for the electric vehicle T_{max} is 250 N.m [221]. Thus, the additional constraint of the control input is added into (148):

$$-T_{max} \leq k_i V_i \leq T_{max}$$

(149)

The allocated driving torque should also consider the effect of tyre force saturation. The actual total longitudinal tyre force and lateral tyre force generated by a specific tyre are limited by the vertical load of the wheel and the tyre-road friction coefficient. The following friction circle constraint is widely used in to describe the tyre force saturation:

$$F_{ti}^2 + F_{si}^2 \leq \mu F_{zi}^2$$

(150)

However, this non-linear constraint will greatly increase the computational effort. Castro et al. suggested this non-linear inequality can be approximated by the N half-spaces [252]:

$$C\begin{bmatrix} F_{ti} \\ F_{si} \end{bmatrix} \leq D\mu F_{zi}$$

(151)

where $C \in R^{N\times 2}$, $D \in R^N$ are matrices that characterise the half-spaces. One may see that, as the number of half-space N is increased, the friction circle constraints can be approximated with increasing accuracy. However, during the actual implementation of the controller, N cannot be too large, as the computational effort will greatly increase. To improve the computational efficiency, F_{ti} can be calculated from the driving torque (equation (152)) and F_{si} is equal to $\boldsymbol{F_{s-linear}}$.

$$F_{ti} = \frac{k_i V_i}{R_\omega}$$

(152)

The inequality (151) can be considered as another constraint of the optimisation problem (148).

3. Numerical comparison between SMC controller and other vehicle dynamics controllers

In this section, two sets of simulations are used to test the proposed SMC fault-tolerant controller. These simulation results are also compared with the traditional vehicle dynamics controller which does not consider the fault-tolerant problem. The traditional method uses the linear feedback method to adjust the four steering angles and four driving torques in order to achieve the desired yaw rate and body side-slip angle, which is similar to the method described in Section 5.1. We denote this as the linear feedback method in the following paragraph. In addition, the simulation results during the situation where no controller is applied are also presented in order to verify the SMC control performance. The vehicle parameters used in the simulations are listed in Table VII-1.

Table VII-1. Parameter values used in simulations. **[100] [80]**

t_m	Mechanical trail	0.028 m
t_{p0}	Initial pneumatic trail	0.05 m

k_s	Stiffness coefficient of kingpin	362 N.m/rad
I_s	Effective rotational inertia	4 Kg.m^2
b_s	Effective damping coefficient	88 N.m/(rad/s)

In the first set of simulations, the motion of a single lane change is examined. The driver's input steering angle is shown in Figure VII-2 and the friction coefficient is assumed as 0.9. The vehicle initial velocity is 20 m/s. It is assumed that the wheel fault first happens in the rear right wheel from 2 seconds to 2.5 seconds. The driver still wants to accelerate the vehicle and the desired total driving torque is shown in Figure VII-3. In the proposed SMC controller, only the longitudinal velocity control law v_1 and yaw rate control law v_3 are applied here. This is because the longitudinal velocity and yaw rate are primary control targets under normal driving conditions. The value of the allocated driving torque is determined by the control law v_1 to overcome the friction force and achieve the desired longitudinal velocity. In the linear feedback controller and no controller applied conditions, the desired driving torque in Figure VII-3 is equally distributed to two rear wheels.

Figure VII-4 suggests that the proposed SMC method and the linear feedback controller can both achieve the desired yaw rate accurately compared with when there is no controller applied. The SMC method shows robust control performance when the rear right wheel is faulty over a period of time. The linear feedback controller uses the driving torque to adjust the yaw rate. Under normal driving conditions, this control effort is small and the loss of working effort of one wheel will not significantly impair the yaw rate control performance. Figure VII-5 shows that the proposed SMC method can better achieve the desired longitudinal velocity compared with the linear feedback controller due to the applied control law v_1 (channel 1 of SMC).

Next, the wheel fault is assumed to occur in the two rear wheels from 2 seconds to 2.5 seconds. Figure VII-6 and Figure VII-7 also compare the control performance of yaw rate and longitudinal velocity between the proposed SMC method and the use of a linear feedback controller. The linear feedback controller has a serious error at 2.5 seconds and the simulation stops because the scenario that both the two rear wheels are faulty is more challenging than one faulty wheel scenario. The proposed SMC method can achieve the desired yaw rate even

if the two rear wheels cannot work properly from 2 seconds to 2.5 seconds. The desired longitudinal velocity can be also better achieved due to the applied control law v_1.

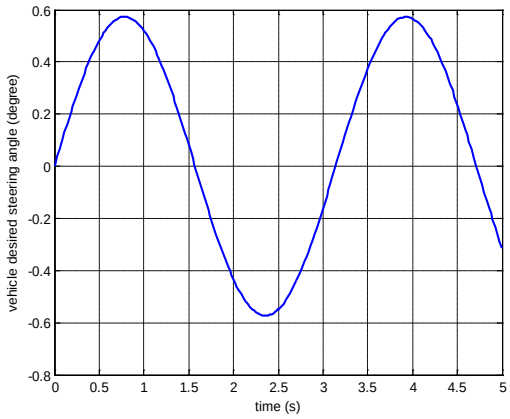

Figure VII-2. Driver's steering input during the motion of single lane change.

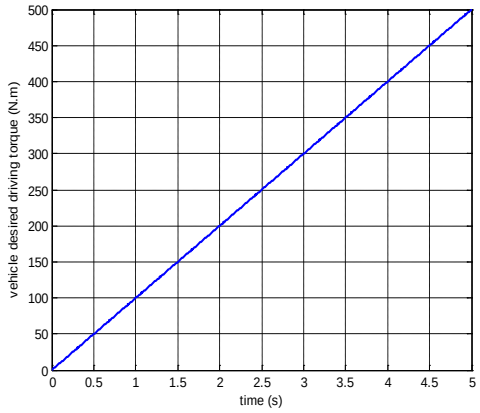

Figure VII-3. Driver's desired driving input during the motion of single lane change.

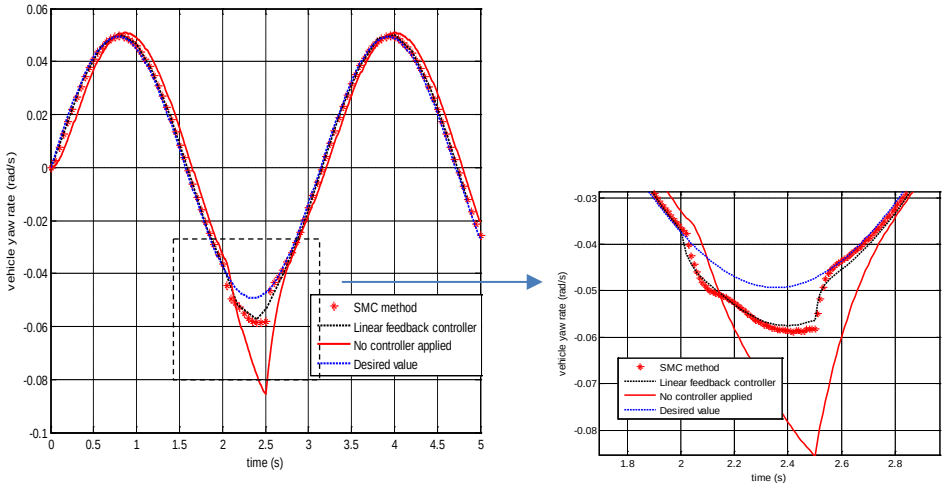

Figure VII-4. Vehicle controlled yaw rate during the motion of single lane change. (one faulty wheel)

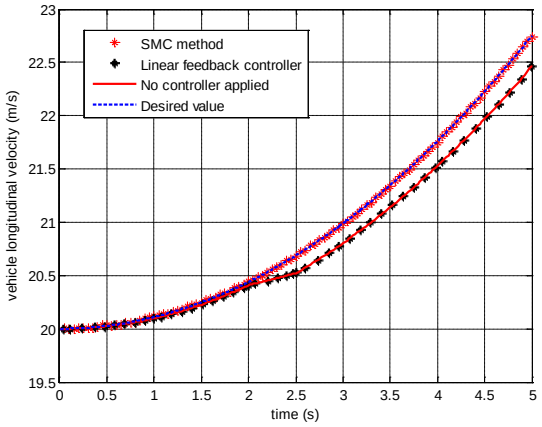

Figure VII-5. Vehicle longitudinal velocity during the motion of single lane change. (one faulty wheel)

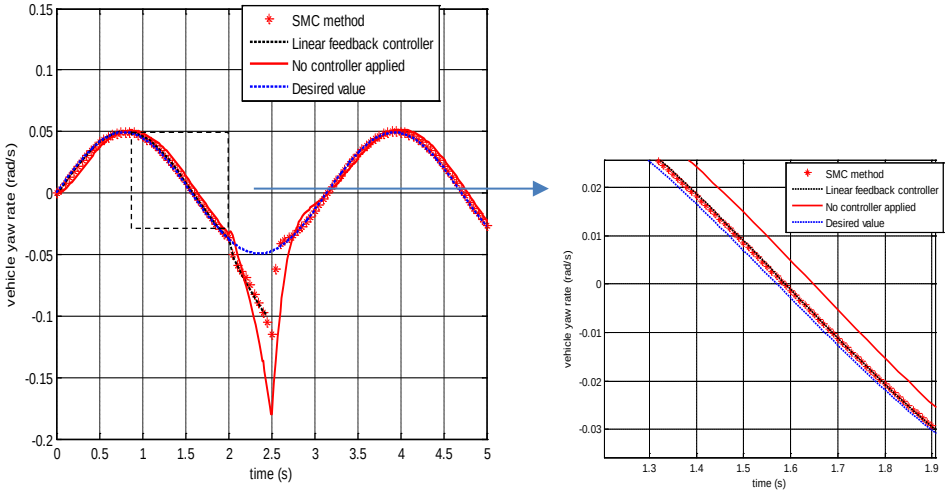

Figure VII-6. Vehicle controlled yaw rate during the motion of single lane change. (two faulty wheels)

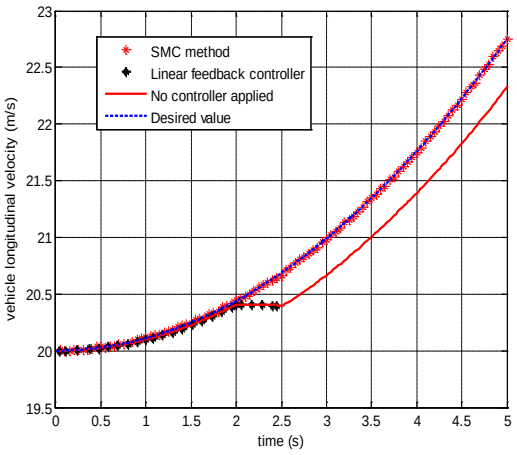

Figure VII-7. Vehicle longitudinal velocity during the motion of single lane change. (two faulty wheels)

In the second set of simulations, the vehicle is performing a simple J-turn motion and the input steering angle is shown in Figure VII-8. Vehicle initial velocity is 15 m/s and friction coefficient is 0.9. The rear right wheel is faulty from 2 seconds to 4 seconds. In this simulation, the steering angle is large and the primary control targets have changed into the yaw rate and vehicle body side-slip angle. Thus, in theory, control law v_2 and control law v_3 should be applied in this simulation. However, when the steering angle is large, there is a strong coupling effect between the control laws v_2 and v_3 and both the control performance of the yaw rate and the body side-slip angle will be negatively affected. Therefore, the simulation results of the application of yaw rate control law v_3 in SMC alone and the simulation results of the application of both control laws v_2 and v_3 in SMC are compared to show this strong coupling effect. In the next section, this problem is solved by grouping the driving control actuators. The detailed explanation of this and the simulation results can be found in the following sections.

It should be noted that the only application of yaw rate control law v_3 is briefly called yaw rate SMC and the application of both control laws v_2 and v_3 is called combined SMC in the following paragraph.

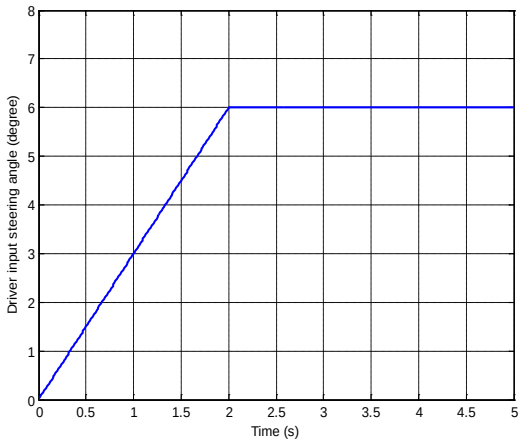

Figure VII-8. Driver's input steering angle during a J-turn manoeuvre.

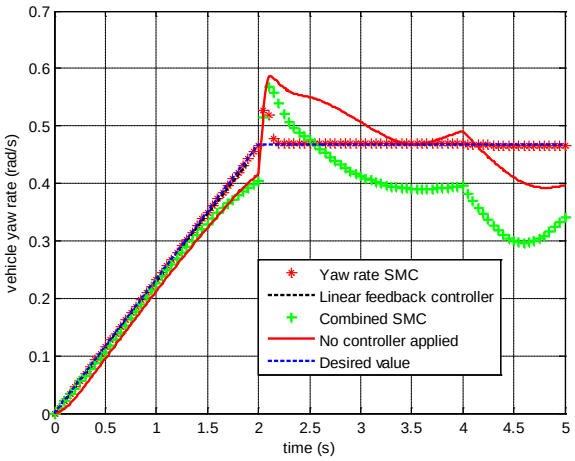

Figure VII-9. Vehicle controlled yaw rate during a J-turn manoeuvre. (one faulty wheel)

According to Figure VII-9, the yaw rate SMC method can track the desired yaw rate response perfectly even though the rear right wheel is faulty after 2 seconds. The yaw rate control performance of the combined SMC is compromised due to the coupling effect between control laws v_2 and v_3. The linear feedback controller also has a serious error during 2 seconds and the simulation stops at 2 seconds, which is obviously not suitable to the fault-tolerant control. In Figure VII-9, the simulation of the linear feedback control stops due to the wheel fault in 2 seconds. The combined SMC method shows even worse body side-slip angle response compared with the no controller applied situation and the yaw rate SMC method. Since the combined SMC shows no advantages over the yaw rate SMC, only yaw rate SMC is applied under the large steering angle turning condition in the following simulation. In the next section, the body side-slip angle performance when the SMC method is applied is improved by grouping the driving actuators.

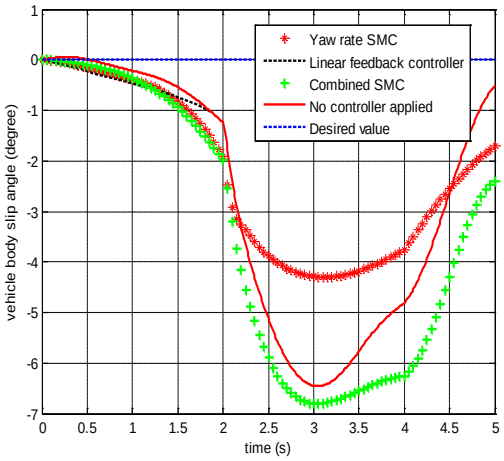

Figure VII-10. Vehicle body slip angle performance during J-turn manoeuvre. (one faulty wheel)

Figure VII-9 shows the yaw rate response and Figure VII-10 shows the body side-slip angle response when the two rear wheels are assumed to be faulty. From 2 seconds to 4 seconds, the rear right wheel of the electric vehicle is faulty. Moreover, the two rear wheels are faulty from 4 seconds to 5 seconds. The motor control gains of the two rear wheels are shown in Figure VII-11. In the simulation, the application of the linear feedback controller stops at 2 seconds. The yaw rate SMC method cannot achieve good control of the yaw rate and body side-slip angle after 4 seconds since all the two rear wheels lost the control. However, the control performance of SMC method is still better than no controller applied condition.

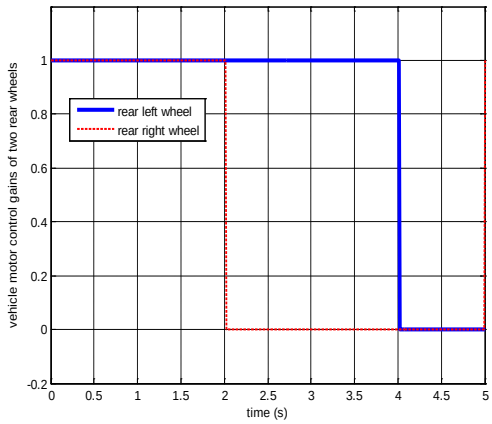

Figure VII-11. The motor control gains of two rear wheels during J-turn manoeuvre. (two faulty wheels)

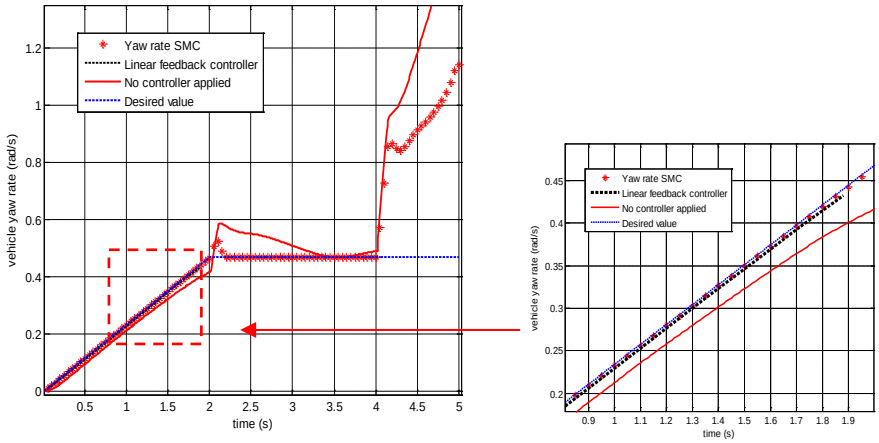

Figure VII-12. Vehicle controlled yaw rate during a J-turn manoeuvre. (two faulty wheels)

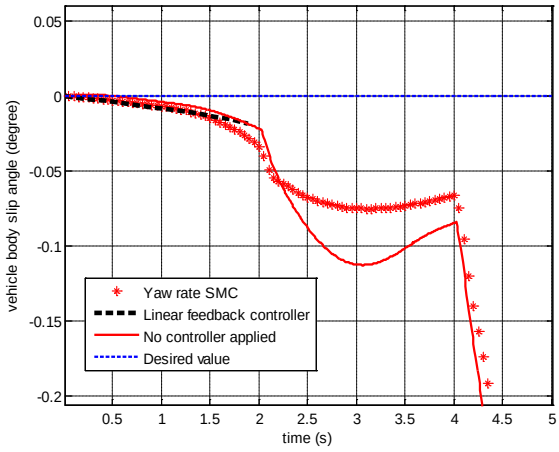

Figure VII-13. Vehicle body slip angle performance during J-turn manoeuvre. (two faulty wheels)

In this section, the simulation results prove that the proposed SMC controller can achieve better control under normal driving conditions and in a large steering angle J-turn manoeuvre than the linear feedback controller but the proposed SMC method still has some disadvantages. For instance, large sliding gains K_1,K_2 and K_3 are required in the above two sets of simulations in order to achieve good control performance. These large values will induce the chattering effects caused by frequent switching around the sliding surface. In addition, during the J-turn manoeuvre with a large steering angle, due to the strong coupling effect between the lateral velocity control v_2 and the yaw rate control v_3, only the yaw rate control v_3 is applied, and consequently the body side-slip angle response is compromised.

4. Innovative actuator-grouping SMC controller

In this section, some improved SMC methods are proposed to solve the two disadvantages of the SMC controller mentioned in the above section. Alipour et al. introduced the PISMC method, which included a proportional and integral controller into the SMC [221]:

$$v_1 = -v_y r - B_{y1}F_{si-linear} + \dot{v}_{xr} + K_{p1}(v_{xd} - v_x) + K_{i1}\int(v_{xd} - v_x) - K_1 Sat(S_1) \quad \text{(a)}$$

$$v_2 = v_x r - B_{y2}F_{si-linear} + \dot{v}_{yr} + K_{p2}\left(v_{yd} - v_y\right) + K_{i2}\int\left(v_{yd} - v_y\right) - K_2 Sat(S_2) \quad \text{(b)}$$

$$v_3 = -B_{y3}F_{si-linear} + \dot{r}_r + K_{p3}\left(v_{yd} - v_y\right) + K_{i3}\int\left(v_{yd} - v_y\right) - K_3 Sat(S_3) \quad \text{(c)}$$

(153)

where $K_{p1}, K_{i1}, K_{p2}, K_{i2}, K_{p3}, K_{i3}$ are determined online by the Levenberg Marquardt algorithm (LMA) algorithm, which aims to minimise the tracking error of the yaw rate or body side-slip angle. The detailed LMA algorithm can be found in [221]. In this study, the LMA algorithm is further revised by adding a threshold value of the yaw rate error or body side-slip angle error. This is because a too small yaw rate or body side-slip angle error will cause the singularity of the matrix and the LMA algorithm will not be accurate. On the other hand, a small yaw rate or body side-slip angle error means that the SMC method has tracked the desired values perfectly and the PI controller is no longer required.

The threshold value of the yaw rate error is defined as e_{r0} and the threshold value of the body side-slip angle is defined as $e_{\beta 0}$. If either the actual yaw rate error e_r or the body side-slip angle error e_β is larger than its threshold value, the PISMC will be actuated to control the vehicle. Otherwise, the traditional SMC is applied. The detailed structure of this threshold selection method is shown in Figure VII-14.

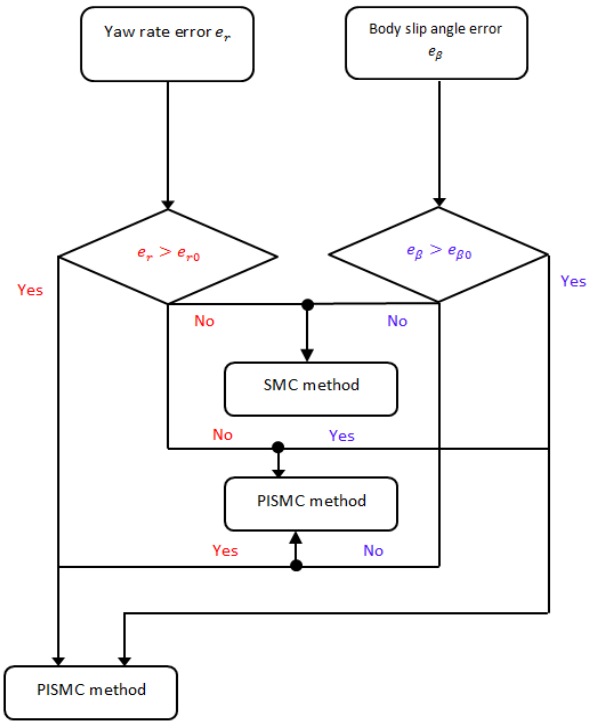

Figure VII-14. The flow chart of the threshold selection method of PISMC.

In the 4WID vehicle, there are four driving actuators which can be utilised if all the wheels are in the healthy condition. When there is a large steering angle during turning, the control targets are yaw rate and body side-slip angle. When all the four wheels are used simultaneously to control the yaw rate and body side-slip angle, there is a strong coupling effect on these two control targets. To solve this problem, the four driving motors are grouped into the class of the two front driving motors and the class of the two rear driving motors. If front wheels are steering wheels, the two front wheels are used to control the body side-slip angle and the two rear wheels are used to control the yaw rate. Similarly, if the rear wheels are steering wheels, the two rear wheels are used to control the body side-slip angle and the two front wheels are used to control the yaw rate. This is because only the steering wheel can generate enough vehicle lateral tyre force to control the vehicle body side-slip angle and all the four wheels can generate enough yaw moment to control the yaw rate. This control law can be considered as the revised SMC controller as follows:

$$v_1 = \frac{1}{R_\omega m}\left(\cos\delta_{fl}\, k_{fl} u_{fl} + \cos\delta_{fr}\, k_{fr} u_{fr} + \cos\delta_{rl}\, k_{rl} u_{rl} + \cos\delta_{rr}\, k_{rr} u_{rr}\right) = -v_y r - B_{y1} F_{si-linear} + \dot{v}_{xr} - K_1 Sat(S_1) \quad \text{(a)}$$

$$v_2 = \frac{1}{R_\omega m}\left(a_1 \sin\delta_{fl}\, k_{fl} u_{fl} + a_2 \sin\delta_{fr}\, k_{fr} u_{fr} + a_3 \sin\delta_{rl}\, k_{rl} u_{rl} + a_4 \sin\delta_{rr}\, k_{rr} u_{rr}\right) = v_x r - B_{y2} F_{si-linear} + \dot{v}_{yr} - K_2 Sat(S_2) \quad \text{(b)}$$

$$v_3 = \frac{1}{R_\omega I_z}\Big(b_1\left(l_f \sin\delta_{fl} + \frac{b_f}{2}\cos\delta_{fl}\right)k_{fl}u_{fl} + b_2\left(l_f \sin\delta_{fr} - \frac{b_f}{2}\cos\delta_{fr}\right)k_{fr}u_{fr} + b_3\left(\frac{b_r}{2}\cos\delta_{rl} - l_r \sin\delta_{rl}\right)k_{rl}u_{rl} + b_4\left(-\frac{b_r}{2}\cos\delta_{rr} - l_r \sin\delta_{rr}\right)k_{rr}u_{rr}\Big) = -B_{y3}F_{si-linear} + \dot{r}_r - K_3 Sat(S_3)$$

(c)

(154)

where if the vehicle is front wheel steering, $a_1 = a_2 = b_3 = b_4 = 1$ and $a_3 = a_4 = b_1 = b_2 = 0$. If the vehicle is rear wheel steering, $a_1 = a_2 = b_3 = b_4 = 0$ and $a_3 = a_4 = b_1 = b_2 = 1$.

If there is one faulty wheel among the four wheels, the front left wheel and rear right wheel can be put into a group, and front right wheel and rear left wheel can be put into a group. In this way, we can guarantee there are always two driving wheels being utilised to control the vehicle yaw rate, since one wheel is not enough to control the yaw rate. In equation (154), if the vehicle is front wheel steering and the faulty wheel is the rear left wheel, $a_2 = b_1 = b_4 = 1$ and $a_1 = a_4 = b_2 = 0$. If the vehicle is front wheel steering and the faulty wheel is the rear right wheel, $a_1 = b_2 = b_3 = 1$ and $a_2 = a_3 = b_1 = 0$. If the vehicle is rear wheel steering and the faulty wheel is the front left wheel, $a_4 = b_2 = b_3 = 1$ and $a_2 = a_3 = b_4 = 0$. If the vehicle is rear wheel steering and the faulty wheel is the front right wheel, $a_3 = b_1 = b_4 = 1$ and $a_1 = a_4 = b_3 = 0$.

If the two front wheels or two rear wheels of the vehicle are faulty, the vehicle can still perform the cornering motion. In this way, there are two wheels left to be controlled. In this situation, these two wheels are used to control the yaw rate and the vehicle body side-slip angle cannot be controlled due to the limited number of driving actuators. Therefore, equation (154) can be represented as follows:

If the two front wheels are faulty:

$$v_3 = \frac{1}{R_\omega I_z}\Big(b_3\left(\frac{b_r}{2}\cos\delta_{rl} - l_r \sin\delta_{rl}\right)k_{rl}u_{rl} + b_4\left(-\frac{b_r}{2}\cos\delta_{rr} - l_r \sin\delta_{rr}\right)k_{rr}u_{rr}\Big) = -B_{y3}F_{si-linear} + \dot{r}_r - K_3 Sat(S_3)$$

(155)

where $b_4 = b_3 = 1$.

If the two rear wheels are faulty:

$$v_3 = \frac{1}{R_\omega I_z}\left(b_1\left(l_f \sin\delta_{fl} + \frac{b_f}{2}\cos\delta_{fl}\right)k_{fl}u_{fl} + b_2\left(l_f \sin\delta_{fr} - \frac{b_f}{2}\cos\delta_{fr}\right)k_{fr}u_{fr}\right) = -B_{y3}F_{si-linear} + \dot{r}_r - K_3 Sat(S_3)$$

(156)

where $b_2 = b_1 = 1$.

5. Simulation results with actuator-grouping SMC controller

Section 7.3 shows the simulation results which proved that the proposed SMC method can achieve good control performance under normal driving conditions but the control performance of the body side-slip angle is compromised during turning when there is a large steering angle. In this section, the vehicle under extreme turning conditions is examined where the revised actuator-grouping SMC controller is expected to overcome the compromised control performance of the body side-slip angle. The simulation performance of PISMC is also tested in order to decrease the sliding mode control gain and decrease the driving control effort. Under extreme turning conditions, the yaw rate and body side-slip angle are the primary control targets.

In the first set of simulations, the vehicle is performing the simple J-turn motion and the input steering angle is the same as the value in Figure VII-8. The initial vehicle velocity is 15 m/s and the friction coefficient is 0.9. We assume the vehicle's rear right wheel is broken between 2 seconds to 4 seconds. First the PISMC method is used in order to attempt to improve the control performance of the traditional SMC method. The yaw rate SMC method is applied as the traditional SMC due to the strong coupling effect between control targets.

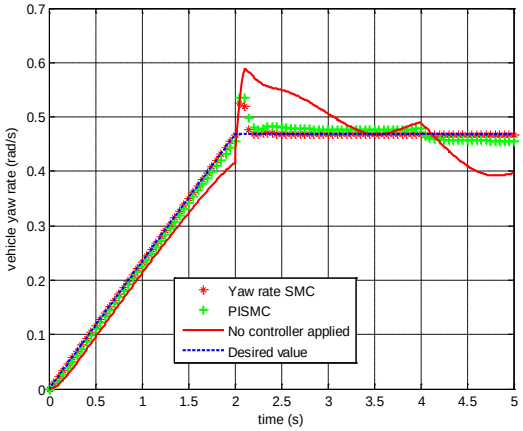

Figure VII-15. Vehicle yaw rate response during a J-turn manoeuvre when PISMC is applied.

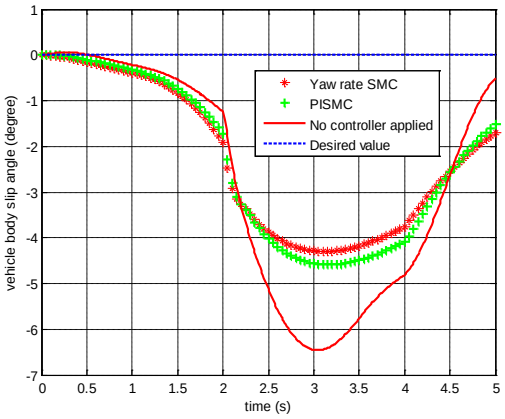

Figure VII-16. Vehicle body side-slip angle response during a J-turn manoeuvre when PISMC is applied

According to Figure VII-15 and Figure VII-16, when the PISMC is applied, the stability of the SMC can be improved and the sliding control gain, which is 500 in this simulation, can be decreased. (The default value of sliding mode control gain is 4000 for the traditional SMC method.) The control error of the yaw rate can be compensated for by the PI controller and less control effort is required, as shown in Figure VII-17 and Figure VII-18. The improvement in the vehicle body side-slip angle, however, is still not significant.

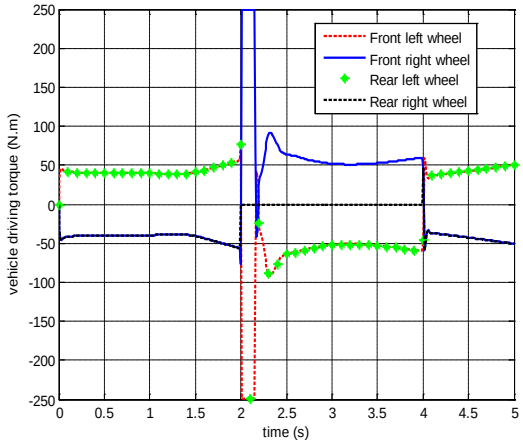

Figure VII-17. The input driving torque of each individual wheel when traditional SMC method is applied.

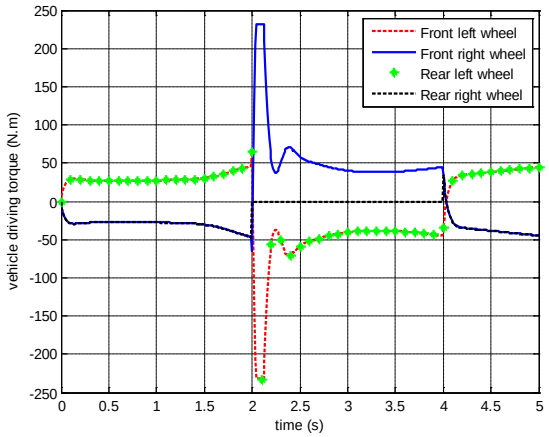

Figure VII-18. The input driving torque of each individual wheel when PISMC method is applied.

In the next set of simulations, the driver's input steering angle is shown in Figure VII-19 and all the other conditions remain unchanged. Figure VII-20 and Figure VII-21 show the vehicle yaw rate response and body side-slip angle response when the revised actuator-grouping SMC method is applied. In Figure VII-20, the yaw rate controlled by the traditional SMC method and revised actuator-grouping SMC method can both achieve the desired yaw rate accurately. According to Figure VII-21, the body side-slip angle control performance of the revised actuator-grouping SMC method is significantly better than the traditional SMC method and also better than the no controller applied condition. When no controller is applied, the yaw rate control performance is much worse than the controlled methods. The sharp increase of the yaw rate at 2 seconds is mainly because the rear right wheel is faulty and the steering angle is no longer controlled by the driver at this time. In addition, in order to comprehensively analyse the vehicle stability performance, the value of the vehicle body side-slip angle rate is also introduced and shown in Figure VII-22. In Figure VII-22, the actuator-grouping SMC also shows advantage over the traditional SMC.

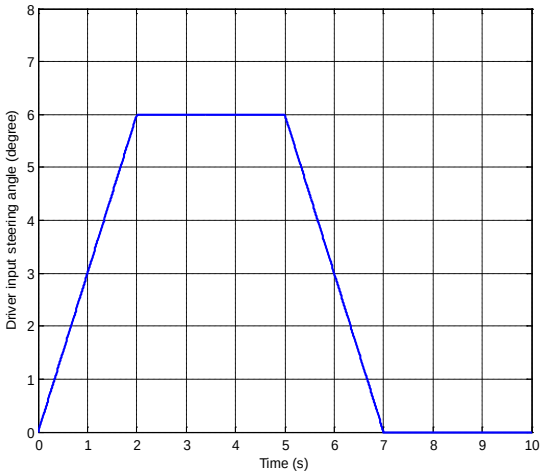

Figure VII-19. The driver's steering input when the revised actuator-grouping SMC controller is used.

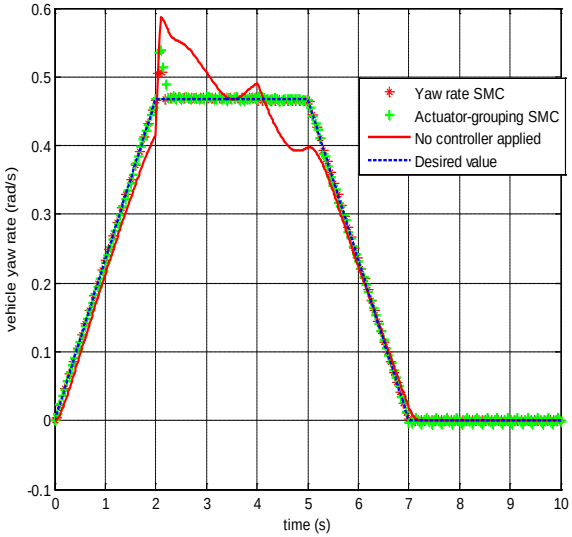

Figure VII-20. Vehicle yaw rate response when the revised actuator-grouping SMC controller is used. (one faulty wheel)

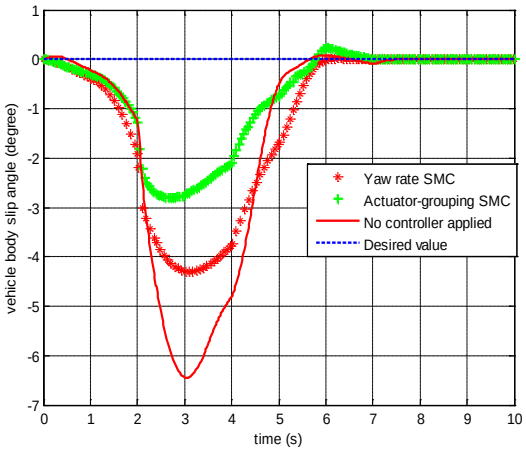

Figure VII-21. Vehicle body side-slip angle response when the revised actuator-grouping SMC controller is used. (one faulty wheel)

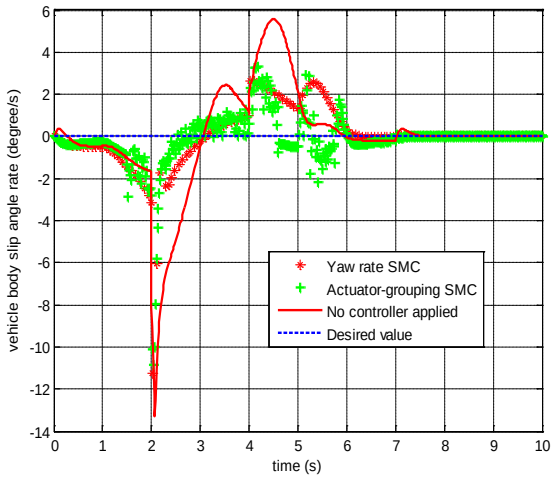

Figure VII-22. Vehicle body side-slip angle change rate when the revised actuator-grouping SMC controller is used. (one faulty wheel)

In the above simulations, it is assumed that only the rear right wheel cannot work between 2 to 4 seconds. In the following simulation, the rear right wheel can be assumed as the faulty wheel from 4 to 6 seconds. After that, the two rear wheels are both assumed to be faulty from 6 to 7 seconds and only the two front wheels can be steered and driven to maintain the vehicle dynamics performance. The motor control gains of the two faulty rear wheels are shown in Figure VII-23.

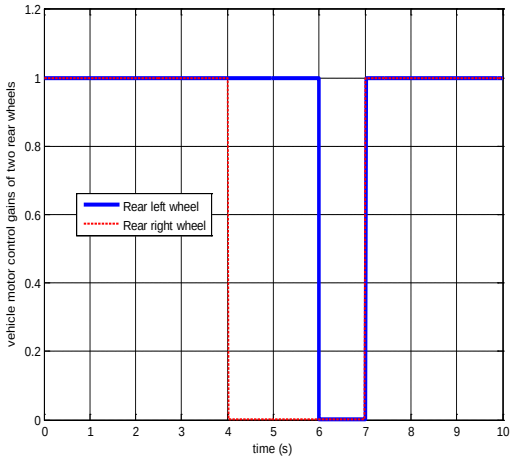

Figure VII-23. The motor control gains of two rear wheels. (two faulty wheels)

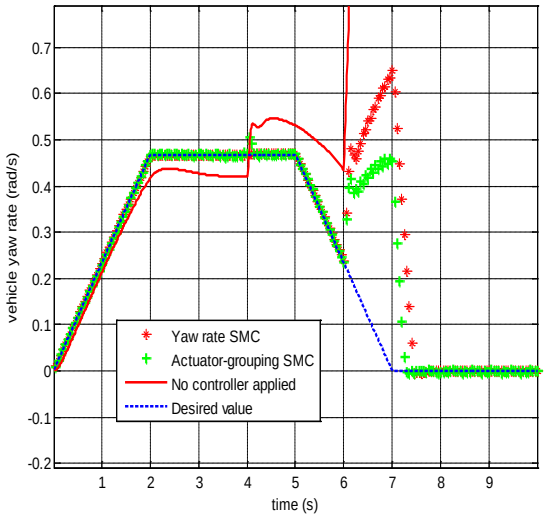

Figure VII-24. Vehicle yaw rate response when the revised actuator-grouping SMC controller is used. (two faulty wheels)

According to Figure VII-24, the traditional SMC method and the proposed actuator-grouping SMC method can achieve the desired yaw rate perfectly when only one wheel does not work or no fault happens. When two rear wheels are faulty, the yaw rate responses of two SMC methods increase sharply because the steering angles of two rear wheels are uncontrolled. The revised actuator-grouping SMC shows better yaw rate control performance than the traditional SMC and no controller applied condition. The body side-slip angle performance in Figure VII-25 and body side-slip angle change rate performance in Figure VII-26 are similar to Figure VII-21 and Figure VII-22, respectively and this proves that the proposed actuator-grouping SMC method can significantly improve the body side-slip angle response even when two rear wheels are faulty.

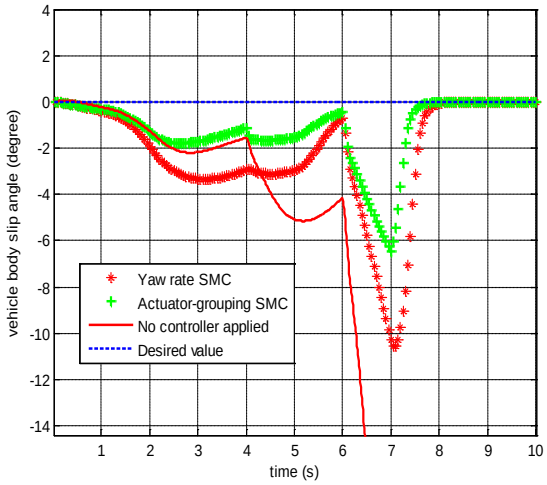

Figure VII-25. Vehicle body side-slip angle response when the revised actuator-grouping SMC controller is used. (two faulty wheels)

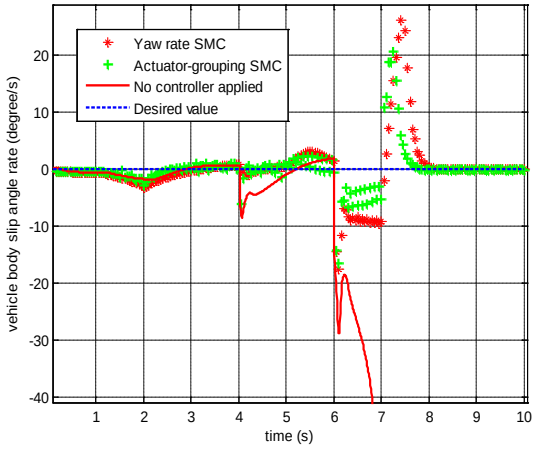

Figure VII-26. Vehicle body side-slip angle change rate when the revised actuator-grouping SMC controller is used. (two faulty wheels)

To better present and compare the simulation results of the vehicle yaw rate, body side-slip angle and longitudinal velocity, the RMS values of overall output response can be presented by the following equation:

$$RMS = R_1\sqrt{mean(v_{xd} - v_x)^2} + R_2\sqrt{mean(\beta_d - \beta)^2} + R_3\sqrt{mean(r_d - r)^2} \tag{157}$$

The term $mean(x)$ means the average value of the argument x. Each term is corresponding to one specific control target's RMS error value. R_1, R_2, R_3 are the scaling factors of each term. The default values of R_1, R_2 and R_3 are 1, which represents the equal weighting of each

term. If one specific control target is focused, the corresponding scaling factor can be increased. It has been suggested that the control targets can be different in different vehicle moving conditions and consequently the values of these scaling factors can be different. Particularly, in the normal driving condition, longitudinal velocity and yaw rate control are focused ($R_1 = 1, R_2 = 0, R_3 = 1$). In the vehicle J-turn motion, the vehicle body side-slip angle and yaw rate control are focused ($R_1 = 0, R_2 = 1, R_3 = 1$).

Table VII-2 and Table VII-3 summarise the RMS values of the body side-slip angle response and yaw rate response in the second and last set of simulations, which are corresponding to Figure VII-19 to Figure VII-26. These two sets of simulations are all J-turn motions and consequently the scaling factors $R_1 = 0, R_2 = 1, R_3 = 1$. Table VII-2 and Table VII-3 suggest that the proposed actuator-grouping SMC has much better overall control performance compared with yaw rate SMC and no controller applied condition in the simulation when only one wheel is faulty or in the simulation when two rear wheels are faulty.

Table VII-2. RMS values of control targets in the second set of simulations.

Control method	Longitudinal velocity error	Body slip angle error	Yaw rate error	Overall error
No controller applied	0	0.0452	0.0346	0.0798
Yaw rate SMC	0	0.0350	0.0057	0.0407
Actuator-grouping SMC	0	0.0215	0.0084	0.0299

Table VII-3. RMS values of control targets in the last set of simulations.

Control method	Longitudinal velocity error	Body slip angle error	Yaw rate error	Overall error
No controller applied	0	0.1333	0.3906	0.5239
Yaw rate SMC	0	0.0580	0.1609	0.2189
Actuator-grouping SMC	0	0.0324	0.1088	0.1412

6. Summary

This chapter first suggests some modifications to the traditional SMC method to achieve fault-tolerant control of a 4WIS-4WID electric vehicle. The steering geometry must be re-arranged according to the location of the faulty wheels. In addition, three SMC control laws (longitudinal velocity control, lateral velocity control and yaw rate control) can be selected freely based on the specific vehicle motion scenarios.

In Section 7.3, these modifications on the SMC method are compared with the linear feedback control method and the major findings can be summarised as follows:

1) Under normal driving conditions, the SMC method can achieve the desired yaw rate accurately when one or two wheels are faulty. The linear feedback method always has serious error and is not suitable for the fault tolerant control. In addition, the SMC method has better control performance over the longitudinal velocity compared with the linear feedback method due to the application of virtual control law v_1.

2) In the scenario of large steering angle turning, the SMC method can achieve the desired yaw rate when one of the front wheels or two front wheels are faulty, while the simulation of the linear feedback control method stops when the wheel fault happens. This proves the robustness of the SMC method. However, the vehicle body side-slip angle performance is compromised due to the coupling effect between different control targets.

To solve this problem, the driving actuators can be grouped and each group of actuators can be used to achieve the specific control target. This avoids the strong coupling effect between the individual control targets. The simulation in 7.5 still uses a large steering angle turning scenario to test the control performance of this revised actuator-grouping SMC method. The simulation results prove that both the body side-slip angle and the body side-slip angle rate are significantly improved compared with the traditional SMC method when one or two wheels are faulty.

In the next chapter, the application of over-actuated control allocation method on the autonomous vehicle control will be extensively focused.

VIII. Application of over-actuated control allocation method on the autonomous vehicle trajectory control

The primary control target of the autonomous vehicle control in this chapter is the desired vehicle trajectory. The over-actuated control allocation method is advantageous to achieve this primary control target, while also can achieve some secondary control targets, such as the vehicle stability and handling performance. In this chapter, the trajectory tracking method is first designed by strictly following the desired path. Then this method is improved by the potential field method which does not require to strictly track the desired path and the vehicle dynamics performance can be improved.

1. The autonomous vehicle trajectory controller by strictly tracking the desired path

This section focuses on the analysis of the comprehensive vehicle dynamics and control of the 4WIS-4WID vehicle in the overtaking scenario. It is assumed that the vehicle trajectory is known during the overtaking maneuverer. The four-wheel PID steering angle controller, four-wheel SMC steering controller, four-wheel SMC driving controller, and four-wheel combined yaw rate and longitudinal velocity SMC driving controller are proposed based on the 4WIS-4WID vehicle dynamics model. The proposed four-wheel combined yaw rate and longitudinal velocity SMC driving controller can achieve simultaneous control of the vehicle yaw rate and velocity due to the redundant control actuators of the 4WIS-4WID vehicle. In addition, the vehicle dynamics model also considers the load transfer effect that may cause the serious problem of vehicle rollover during the lane change of vehicle overtaking. The contribution of this paper can be summarised as follows: 1) Unlike most of the existing studies in literature which only used vehicle kinematic model or limited dynamics model to describe the vehicle motion in the overtaking scenario, this paper provides a comprehensive study on vehicle dynamic model based control of autonomous vehicle in the overtaking scenario. 2) This paper applies the advanced characteristics of 4WIS-4WID to the control of autonomous electric vehicle so that the optimal multi-objective control performance is achieved. 3) In this study, the autonomous control of the EV is achieved by separating the steering controller from the driving controller to alleviate the strong coupling effect between them.

1) Traditional autonomous vehicle trajectory controller

Until now, the trajectory control of the autonomous vehicle is based primarily on the control actuators of the front steering wheel and driving pedal. Petrov and Nashashibi proposed the kinematic modelling and adaptive control of the overtaking vehicle and overtaken vehicle [223]. In this study, however, only vehicle kinematic model is included and the dynamics model is not considered. A model predictive controller was developed to estimate the future position of the vehicle and an online objective function was optimised to minimise the error between the desired vehicle position and the estimated position [234]. Estimation of the future position of the vehicle may not be accurate, however, and the real-time feedback of the vehicle position is more reliable.

We assume that the optimal trajectory has been selected by various trajectory optimisation techniques in the literature [253] [237] [254]. To achieve this desired trajectory, vehicle steering input and driving torque input are utilised to separately control the lateral position and longitudinal position.

a) <u>Steering and lateral motion controller</u>

Traditionally, the steering angle of front wheel can be controlled by the simple PID controller as follows:

$$\delta_f = K_{p1}(y_d - y) + K_{i1}\int (y_d - y) + K_{d1}\frac{d(y_d - y)}{dt} \tag{158}$$

where y is the actual vehicle lateral position in real time, which is obtained by GPS. y_d is the desired lateral position in the desired vehicle trajectory.

K_{p1},K_{i1},K_{d1} are the PID control gains of the steering controller. For the linear control system, the fixed PID control gains can be used to design the controller. However, for the non-linear vehicle model and controller used in this study, these PID control gains should be updated in real-time to deal with the nonlinear characteristic. In this study, the adaptive law developed by [255] is utilised to tune the control gains in equation (158) in real-time.

In [255], the nonlinear lateral vehicle dynamics in equation (63) can be rewritten as the following equations:

$$v_y = \dot{y} \tag{a}$$

$$\dot{v}_y = -v_x r + \frac{F_{tfl}\sin\delta_f + F_{sfl}\cos\delta_f + F_{tfr}\sin\delta_f + F_{sfr}\cos\delta_f + F_{srl} + F_{srr}}{m} \tag{b}$$

(159)

When the vehicle steering angle is not too large, equation (159)(b) can be approximated as the following equation:

$$\dot{v}_y = F + G\delta_f(\theta)$$

(160)

where $F = -v_x r + \frac{F_{sfl}+F_{sfr}+F_{srl}+F_{srr}}{m}$, $G = \frac{F_{tfl}+F_{tfr}}{m}$, $\theta = \begin{bmatrix} K_{p1} \\ K_{i1} \\ K_{d1} \end{bmatrix}$.

Assume the desired input steering angle is:

$$\delta_f^* = G^{-1}\left(-F + \dot{v}_{yd} + k_0 e + k_1 \dot{e}\right)$$

(161)

where $e = y_d - y$, $\dot{e} = v_{yd} - v_y$. Substituting (161) into (160):

$$\ddot{e} + k_1\dot{e} + k_0 e = 0$$

(162)

where $\ddot{e} = \dot{v}_{yd} - \dot{v}_y$. If k_0 and k_1 satisfy that all the roots of the equation $s^2 + k_1 s + k_0 = 0$ are in the open left-half of the s-plane, then $e(t) \to 0$ as $t \to \infty$ in equation (162).

In the next step, a proper adaption law will be designed to online adjust the parameters of K_{p1},K_{i1},K_{d1} such that $\delta_f(\theta)$ in equation (159) can follow the desired steering angle δ_f^* based on the Lyapunov approach. Equation (160) can be rewritten as the following equation:

$$\dot{v}_y = F + G\delta_f(\theta) + G\delta_f^* - G\delta_f^* = G\delta_f(\theta) + \dot{v}_{yd} + kE - G\delta_f^*$$

(163)

where $k = \begin{bmatrix} k_1 \\ k_2 \end{bmatrix}$, $E = \begin{bmatrix} e \\ \dot{e} \end{bmatrix}$. From equation (163):

$$\ddot{e} = -k^T E + G\left(\delta_f^* - \delta_f(\theta)\right)$$

(164)

Equation (164) can be rewritten as:

$$\dot{E} = A_c E + B_c\left(\delta_f^* - \delta_f(\theta)\right)$$

(165)

where $A_c = \begin{bmatrix} 0 & 1 \\ -k_0 & -k_1 \end{bmatrix}$, $B_c = \begin{bmatrix} 0 \\ G \end{bmatrix}$.

The adaptive control law is designed to minimise the error defined by

$$w = \delta_f(\theta^*) - \delta_f^*$$

(166)

where θ^* represents the desired PID control gains. Combining equation (165) and (166) together:

$$\dot{E} = A_c E + B_c\left(\delta_f(\theta^*) - \delta_f(\theta)\right) - B_c w$$

(167)

To guarantee the stability of the designed control law, the following Lyapunov candidate function is suggested:

$$V = \frac{1}{2}E^T P E + \frac{1}{2\gamma}(\theta^* - \theta)^T(\theta^* - \theta)$$

(168)

where $\gamma > 0$ is a tuning rate determining the convergence speed. From (168):

$$\dot{V} \leq -\frac{1}{2}E^T Q E - \frac{1}{\gamma}(\theta^* - \theta)^T\left[\dot{\theta} - \gamma E^T P B_c \xi(e)\right] - E^T P B_c w$$

(169)

where P and Q are all positive definite symmetric matrices. $\xi(e) = \begin{bmatrix} e \\ \int e \\ \dot{e} \end{bmatrix}$. The detailed mathematical explanation from equations (168) to (169) can be found in [255].

If the control law is chosen by:

$$\dot{\theta} = \gamma E^T P B_c \xi(e) \tag{170}$$

Equation (169) can be rewritten as:

$$\dot{V} \leq -\frac{1}{2} E^T Q E - E^T P B_c w \tag{171}$$

In [255], it is proved that $-\frac{1}{2} E^T Q E - E^T P B_c w$ is always negative and the adaptive PID controller is stable.

It is noted that the vehicle lateral position error and lateral velocity error can be measured by the GPS. The vehicle tyre force is assumed to be known because a number of studies have proposed different vehicle tyre force estimation methods [21] [79].

b) *Driving and longitudinal motion controller*

Assume the vehicle is rear wheel driving vehicle and driving torque is equally distributed into the two rear wheels. The SMC is widely used to achieve the longitudinal motion control by tracking the desired velocity. The SMC law is evaluated according to the vehicle dynamics equation (63):

$$\dot{v}_x = v_y r + B_{y1} \boldsymbol{F_{s-linear}} + v_1 \tag{172}$$

where $B_{y1} = \begin{bmatrix} -\frac{\sin \delta_{fl}}{m} & -\frac{\sin \delta_{fr}}{m} & -\frac{\sin \delta_{rl}}{m} & -\frac{\sin \delta_{rr}}{m} \end{bmatrix}$ and $\boldsymbol{F_{s-linear}} = \begin{bmatrix} C_a \alpha_{fl}(v_x, v_y, r) \\ C_a \alpha_{fr}(v_x, v_y, r) \\ C_a \alpha_{rl}(v_x, v_y, r) \\ C_a \alpha_{rr}(v_x, v_y, r) \end{bmatrix}$.

The control law can be chosen such as:

$$\upsilon_1 = -v_y r - B_{y1}\boldsymbol{F_{s-linear}} + \dot{v}_{xd} - K_1 sgn(S_1)$$

(173)

where v_{xd} presents the desired longitudinal velocity and $\dot{v}_{xd}$ is the desired longitudinal acceleration. K_1 is the control gain of SMC corresponding to υ_1.

The sliding surface of channel S_1 can be defined as:

$$S_1 = v_x - v_{xd}$$

(174)

To prove the stability of the suggested control law, the Lyapunov method is used. The Lyapunov function for the sliding surface S_1 can be chosen as:

$$V_1 = \frac{1}{2}S_1^2$$

(175)

The time derivative of the above Lyapunov function is:

$$\dot{V}_1 = S_1\dot{S}_1 = S_1(\dot{v}_x - \dot{v}_{xr}) = S_1\left(v_y r + B_{y1}\boldsymbol{F_{s-linear}} + \upsilon_1 - \dot{v}_{xd}\right)$$

(176)

By applying the suggested control law in equation (173), equation (176) is rewritten as:

$$\dot{V}_1 = S_1\dot{S}_1 = -S_1 K_1 sgn(S_1) = -K_1|S_1|$$

(177)

According to equation (177), the time derivative of the above Lyapunov function is always negative. This proves the stability of the SMC control system.

To achieve the control law (173), the distributed torque of each rear wheel T_r is calculated by wheel dynamics equation (70):

$$\upsilon_1 = \frac{2T_r}{R_\omega m} = -v_y r - B_{y1}\boldsymbol{F_{s-linear}} + \dot{v}_{xr} - K_1 sgn(S_1)$$

$$T_r = \frac{R_\omega m}{2}\left(-v_y r - B_{y1}\boldsymbol{F_{s-linear}} + \dot{v}_{xr} - K_1 sgn(S_1)\right)$$

(178)

It is noted that because it is assumed that the steering angle of the two rear wheels are zero, $F_{ti} = F_{xi}$ in equation (178). The wheel rotation speed $\dot{\omega}_i$ is also neglected in equation (178). The actual vehicle longitudinal velocity v_x, lateral velocity v_y and yaw rate r can be measured by the GPS and inertial measurement unit (IMU).

In this section, the adaptive PID controller is applied to control the vehicle lateral motion and the SMC controller is proposed to achieve the vehicle longitudinal motion control. The overall stability of the whole system when these two kinds of controllers are applied together should be discussed. According to equation (160), when the desired steering angle is achieved, the desired lateral trajectory is satisfied. In addition, when the desired driving torque is achieved in equation (161), the desired longitudinal trajectory is satisfied.

$$\dot{v}_y = \dot{v}_y = F + G\delta_f^* = F + G\left[G^{-1}\left(-F + \dot{v}_{yd} + k_0 e + k_1 \dot{e}\right)\right]$$

$$\dot{v}_{yd} - \dot{v}_y + k_0 e + k_1 \dot{e} = 0 \quad \text{(a)}$$

$$\dot{v}_x = v_y r + B_{y1}\boldsymbol{F_{s-linear}} + v_1$$

$$= v_y r + B_{y1}\boldsymbol{F_{s-linear}} + \left(-v_y r - B_{y1}\boldsymbol{F_{s-linear}} + \dot{v}_{xd} - K_1 sgn(S_1)\right) = \dot{v}_{xd} \quad \text{(b)}$$

(179)

According to equation (179), if the desired steering angle δ_f^* and desired driving control law v_1 can be achieved simultaneously, the vehicle desired longitudinal and lateral position can be achieved and the stability of the whole system is guaranteed.

2) Innovative autonomous vehicle trajectory controller

The traditional dynamics control methods for autonomous vehicles only use one steering actuator and one driving actuator and this may hinder control. In this section, the 4WIS and 4WID EVs are utilised to realise autonomous control and a total of eight control actuators can be used. This control problem is actually the over-actuated control allocation problem and

redundant control actuators can be used to improve the control performance or achieve additional control targets.

a) *Steering and lateral motion controller*

In this section, the innovative steering controllers based on 4WIS EV are proposed. Two lateral steering controllers: the PID controller and the SMC controller are proposed.

(1) PID controller

Based on the steering controller (158), for the 4WIS vehicle, the steering angle of individual wheel can be calculated by the following equation:

$$\delta_i = \tan^{-1}\left(D^T(x_i - x_{ICR}), -D^T(y_i - y_{ICR})\right) \tag{180}$$

where $x_{ICR} = 0$ and $y_{ICR} = \frac{l_f + l_r}{\delta_d}$, which means that the turning radius is $\frac{l_f + l_r}{\delta_d}$. $i = fl, fr, rl, rr$, which represents the front left, front right, rear left and rear right wheel, respectively. $(x_{fl}, y_{fl}) = \left(l_f, \frac{b_f}{2}\right)$ and $(x_{fr}, y_{fr}) = \left(l_f, -\frac{b_f}{2}\right)$, $(x_{rl}, y_{rl}) = \left(-l_r, \frac{b_f}{2}\right)$ and $(x_{rr}, y_{rr}) = \left(-l_r, -\frac{b_f}{2}\right)$ are the positions of the wheel centre. δ_d is the desired steering angle, which is equal to δ_f in PID controller (158), which means that the desired total steering angle of the proposed four wheel steering controller is the same as the front wheel steering angle in the traditional method. $D^T = 1$, if turning in an anti-clockwise direction; $D^T = -1$, if turning in a clockwise direction.

(2) SMC controller

The SMC is utilised to achieve the steering and lateral motion control, which is robust to the model parameter uncertainty and non-linear characteristic of the model. The vehicle lateral motion dynamics equation can be described by the follows based on equation (63):

$$\ddot{y} = -v_x r + B_{y2}\boldsymbol{f}(\boldsymbol{v_2}) \tag{181}$$

where $f(v_2) = \left[\frac{\cos\delta_{fl}}{m} \quad \frac{\cos\delta_{fr}}{m} \quad \frac{\cos\delta_{rl}}{m} \quad \frac{\cos\delta_{rr}}{m}\right]$ and $B_{y2} = \begin{bmatrix} C_a\alpha_{fl}(v_x, v_y, r) \\ C_a\alpha_{fr}(v_x, v_y, r) \\ C_a\alpha_{rl}(v_x, v_y, r) \\ C_a\alpha_{rr}(v_x, v_y, r) \end{bmatrix}$.

Control input $\boldsymbol{v_2} = \begin{bmatrix} \delta_{fl} \\ \delta_{fr} \\ \delta_{rl} \\ \delta_{rr} \end{bmatrix}$.

The control law can be chosen such as:

$$B_{y2}\boldsymbol{f}(\boldsymbol{v_2}) = v_x r + \ddot{y}_d - \lambda\dot{\tilde{y}} - K_1 sgn(S_2) \tag{182}$$

The control target of steering SMC is the desired lateral position, so the sliding surface is chosen as sliding around the desired lateral position y_d:

$$S_2 = \dot{\tilde{y}} + \lambda\tilde{y} \tag{183}$$

where $\tilde{y} = y - y_d$.

To prove the stability of the suggested control law, the Lyapunov function of sliding surface S_2 is shown as follows:

$$V_2 = \frac{1}{2}S_2^2 \tag{184}$$

The time derivative of the above Lyapunov function is presented as follows by applying the control law (182):

$$\begin{aligned} \dot{V}_2 = S_2\dot{S}_2 = S_2\left(\ddot{\tilde{y}} + \lambda\dot{\tilde{y}}\right) = S_2\left(-v_x r + B_{y2}\boldsymbol{f}(\boldsymbol{v_2}) - \ddot{y}_d + \lambda\dot{\tilde{y}}\right) \\ = S_2\left(-v_x r + v_x r + \ddot{y}_d - \lambda\dot{\tilde{y}} - K_2 sgn(S_2) - \ddot{y}_d + \lambda\dot{\tilde{y}}\right) = -K_2|S_2| \end{aligned} \tag{185}$$

According to equation (185), the time derivative of the above Lyapunov function is always negative. This proves the stability of the SMC control system.

Equation (182) can be considered as the non-linear equality constraints of an over-actuated control allocation problem. The cost function of this control allocation problem is shown as follows, which aims to minimise the steering effort of individual wheel:

$$J_1 = \delta_{fl}^2 + \delta_{fr}^2 + \delta_{rl}^2 + \delta_{rr}^2$$

(186)

With the inequality constraint

$$-\frac{\pi}{2} \leq \delta_i \leq \frac{\pi}{2}$$

and the equality constraint (182).

3) Driving and longitudinal motion controller

To fully utilise the redundant driving actuators, the SMC suggested in Section 8.1.1 is extended into four-wheel driving control in this section to improve longitudinal control performance. Based on equations (70) and (161), control law (173) can be revised as follows:

$$\upsilon_1 = \frac{1}{R_\omega m}\left(\cos\delta_{fl}\,T_{fl} + \cos\delta_{fr}\,T_{fr} + \cos\delta_{rl}\,T_{rl} + \cos\delta_{rr}\,T_{rr}\right) = -v_y r - B_{y1}\boldsymbol{F_{s-linear}} + \dot{v}_{xr} - K_1 sgn(S_1)$$

(187)

where $T_{fl}, T_{fr}, T_{rl}, T_{rr}$ are vehicle driving torques of front left wheel, front right wheel, rear left wheel and rear right wheel.

The 4WID electric vehicle has the advantage to achieve the multiple control targets due to the more control actuators can be used. Thus, in addition to the vehicle longitudinal velocity, the vehicle yaw rate can be controlled by SMC. Specifically, the vehicle yaw dynamics can be described by the following equation according to equation (63):

$$\dot{r} = B_{y3}\boldsymbol{F_{s-linear}} + \upsilon_3$$

(188)

Where

$$B_{y3} = \frac{1}{I_z}\left[l_f\cos\delta_{fl} - \frac{b_f}{2}\sin\delta_{fl} \quad l_f\cos\delta_{fr} + \frac{b_f}{2}\sin\delta_{fr} \quad -\frac{b_r}{2}\sin\delta_{rl} - l_r\cos\delta_{rl} \quad \frac{b_r}{2}\sin\delta_{rr} - l_r\cos\delta_{rr}\right]$$

The control law υ_3 can be chosen that:

$$\upsilon_3 = -B_{y3}\boldsymbol{F_{s-linear}} + \dot{r}_d - K_3 sgn(S_3)$$

(189)

where $\dot{r}_d$ is the desired yaw acceleration. The desired yaw rate r_d is determined by the derivative of the desired yaw angle φ_d. Desired yaw angle φ_d can be calculated by the following equation:

$$\varphi_d = atan\frac{y_d(t) - y_d(t-1)}{x_d(t) - x_d(t-1)}$$

(190)

where $y_d(t)$ suggests the desired lateral position in current time step and $y_d(t-1)$ presents the desired lateral position in the previous time step. $x_d(t)$ presents the desired longitudinal position in current time step and $x_d(t-1)$ suggests the desired longitudinal position in the previous time step. The control target of SMC is the desired yaw rate, so the sliding surface is chosen as sliding around the desired yaw rate r_d:

$$S_3 = r - r_d$$

(191)

To prove the stability of the suggested control law, the Lyapunov function of sliding surface S_3 is shown as follows:

$$V_3 = \frac{1}{2}S_3^2$$

(192)

The time derivative of the above Lyapunov function is presented as follows by applying the control law (189):

$$\dot{V}_3 = S_3\dot{S}_3 = S_3(\dot{r} - \dot{r}_d) = S_3\left(B_{y3}\boldsymbol{F_{s-linear}} - B_{y3}\boldsymbol{F_{s-linear}} + \dot{r}_d - K_3 sgn(S_3) - \dot{r}_d\right)$$

$$= -K_3|S_3|$$

(193)

According to equation (193), the time derivative of the above Lyapunov function is always negative. This proves the stability of the SMC control system.

To achieve the control law (189), the distributed torque of each wheel T_i is calculated by wheel dynamics equation (70) and (63):

$$v_3 = \frac{1}{R_\omega I_z}\Bigg(\left(l_f \sin\delta_{fl} + \frac{b_f}{2}\cos\delta_{fl}\right)T_{fl} + \left(l_f \sin\delta_{fr} - \frac{b_f}{2}\cos\delta_{fr}\right)T_{fr} + \left(\frac{b_r}{2}\cos\delta_{rl} - l_r \sin\delta_{rl}\right)T_{rl} + \left(-\frac{b_r}{2}\cos\delta_{rr} - l_r \sin\delta_{rr}\right)T_{rr}\Bigg) = -B_{y3}\boldsymbol{F_{s-linear}} + \dot{r}_d - K_3 sgn(S_3)$$

(194)

Equations (187) and (194) can be considered as the equality constraints of an over-actuated optimal control allocation problem. The cost function of this control allocation problem is shown as follows, which aims to minimise the driving effort of individual wheel:

$$J_2 = T_{fl}^2 + T_{fr}^2 + T_{rl}^2 + T_{rr}^2$$

(195)

With the inequality constraints

$$-|T_{max}| \le T_i \le |T_{max}|$$

and the equality constraints (187) and (194).

The practical limitation of the maximum driving torque of the individual wheel for the electric vehicle T_{max} is 250 N.m [221].

It should be noted that equality constraint (187) is the longitudinal velocity controller and constraint (194) is the yaw rate. Therefore, the proposed longitudinal motion controller can be named as the integrated velocity and yaw rate SMC driving controller.

In addition, the function $sgn(x)$ used in SMC will cause the serious chatting effect due to the abrupt change. In order to achieve continues and smooth switching control law, the saturation function $Sat(x)$ is used as follows instead of $sgn(x)$ in SMC:

$$Sat(x) = \begin{cases} 1 & if\ x > \varepsilon \\ x & if\ -\varepsilon \le x \le \varepsilon \\ -1 & if\ x < -\varepsilon \end{cases}$$

(196)

where ε is the thickness of the boundary layer, which should be chosen as a small value and is assumed as 0.05 in this study [243].

4) Simulation results

In this section, the traditional autonomous vehicle controllers and innovative vehicle controllers are compared. For the purpose of simplification, the traditional PID steering controller is called ‘2 wheel PID steering’ and the four wheel steering PID controller is called ‘4 wheel PID steering’ in this section. The four wheel SMC steering controller is called ‘4 wheel SMC steering’. In addition, the traditional two wheel SMC longitudinal velocity controller and four wheel SMC velocity controller are called ‘2 wheel SMC driving’ and ‘4 wheel SMC driving’. The combined longitudinal velocity SMC controller and yaw rate SMC controller is called ‘4 wheel combined SMC driving’. The simulation parameters are shown in Table VIII-1. It should be noted that the different steering controllers and driving controllers are combined together as different integrated controllers, which is shown in

Table VIII-1. Parameter values used in simulations. [100]

K_1	Sliding mode control gain for the longitudinal velocity control	4000
K_2	Sliding mode control gain for the lateral position control	9
K_3	Sliding mode control gain for the yaw rate control	4000
ε	Thickness of boundary layer	0.05
γ	Tuning rate of the PID adaptive controller	0.01

Table VIII-2. Different integrated controllers

Integrated controllers	Steering controller	Driving controller
Traditional controller	*Two-wheel PID steering*	*Two-wheel SMC driving*
The first improved controller	*Four-wheel PID steering*	*Four-wheel SMC driving*
The second improved controller	*Four-wheel SMC steering*	*Four-wheel combined SMC driving*

In the first set of simulations, it is assumed that the overtaking vehicle is moving behind the overtaken vehicle in the same track and the initial velocity of these two vehicles is both 20 m/s. During the vehicle overtaking, the overtaking vehicle is assumed to have a lane change manoeuvre to the right track, and then the overtaking vehicle speeds up in order to go ahead of the overtaken vehicle. After that, the overtaking vehicle takes another lane change manoeuvre in order to go back to the left track. Thus, the desired vehicle trajectory of the overtaking can be determined by the following equation:

$$y_d = \begin{cases} 0 & if\ x_d < 100 \\ -\left(R - \sqrt{R^2 - (x_d - 100)^2}\right) & if\ 100 \le x_d < 200 \\ -5 & if\ 200 \le x_d < 300 \\ \left(R - \sqrt{R^2 - (x_d - 300)^2}\right) - 5 & if\ 300 \le x_d < 400 \\ 0 & if\ x_d \ge 400 \end{cases} \tag{197}$$

where R is the turning radius, which is assumed as 1000 in this study. The turning radius of the desired trajectory is chosen as a large value since the longitudinal velocity is relatively high. The width of the lane of normal road is approximately 5 meters, so the desired lateral displacement is chosen as 5 meters. The desired longitudinal position x_d is determined by the vehicle desired longitudinal velocity v_{xd}. It is assumed that the longitudinal velocity remains constant value of 20 m/s before and during the first lane change manoeuvre. Then the vehicle speeds up gradually from 20 m/s into 30 m/s in the right track and the vehicle maintains this

speed in the second lane change manoeuvre. In this way, the overtaking vehicle can avoid the collision with the overtaken vehicle if the overtaken vehicle maintains its initial velocity.

The desired vehicle trajectory during the vehicle overtaking is shown in Figure VIII-1 (a) and the desired longitudinal velocity is shown in Figure VIII-1 (b). The friction coefficient is 0.9 in the simulations of this whole section.

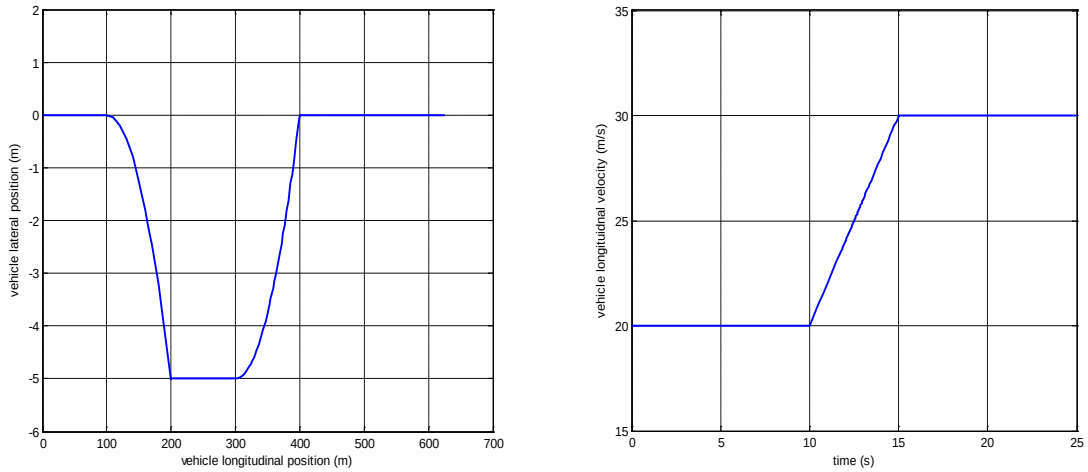

(a) desired vehicle trajectory (b) desired vehicle longitudinal velocity

Figure VIII-1. Vehicle desired trajectory in the first set of simulations.

In this set of simulation, the results of different steering controllers and driving controllers are compared in the following figures:

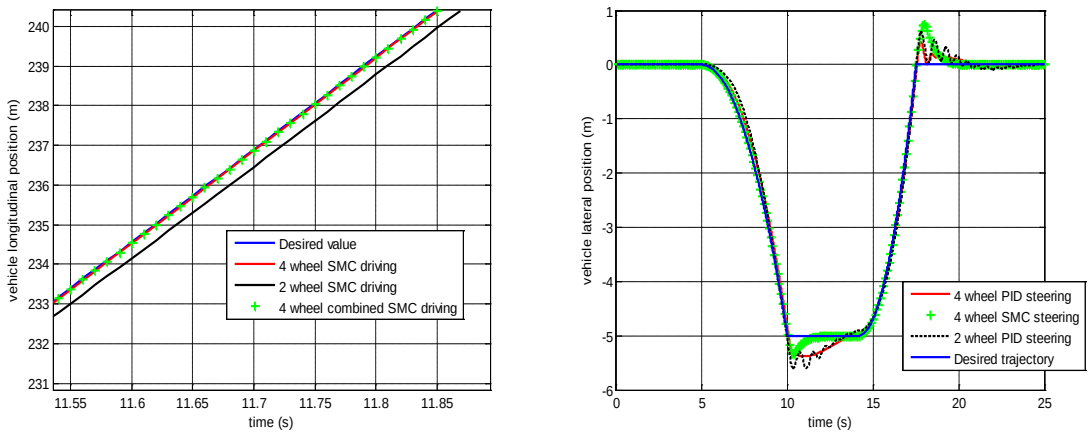

(a) longitudinal position vs time (b) lateral position vs time

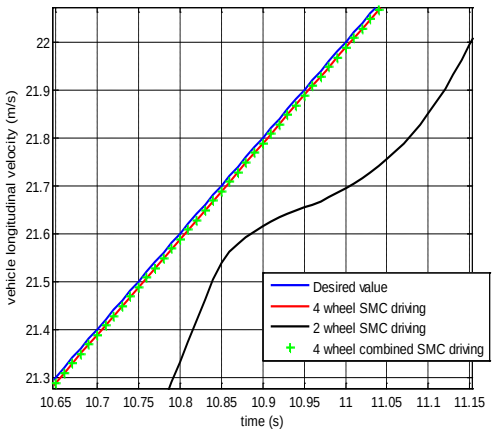

(c) longitudinal velocity vs time

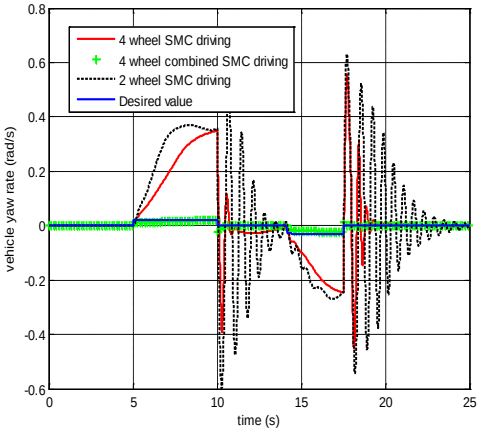

(d) yaw rate vs time

Figure VIII-2. Comparison between the vehicle desired dynamics response and the actual response in the first set of simulations.

Figure VIII-2 (b) shows that the proposed four-wheel PID steering controller has better control performance compared with two-wheel PID steering controller due to the 4WIS, but the problem of oscillation still exists. The SMC steering controller is more stable than the PID controller and has better control performance. Simulations show that all the desired longitudinal position and longitudinal velocity can be perfectly tracked for all of the three methods. This is because the desired longitudinal velocity is easy to achieve and the more difficult longitudinal driving scenario must be considered. The normal size figures of the longitudinal position and longitudinal velocity response of the three control methods are not shown because all the controlled results converge into the same line. Instead of that, the enlarged figures of the longitudinal position and velocity response are presented in Figure VIII-2 (a) and (c). From Figure VIII-2 (a) and (c), it can still be seen that the traditional two-wheel SMC driving has slightly worse control compared with the proposed four-wheel SMC driving controller and four-wheel combined SMC driving controller.

Figure VIII-2 (d) compares the yaw rate response of different driving control methods. The yaw rate responses of the traditional two-wheel SMC driving controller and the four-wheel SMC driving controller are highly unstable, but the yaw rate controlled by the four-wheel combined SMC driving controller is greatly improved and close to the desired value. This proves that the proposed four-wheel combined SMC controller can achieve the control targets of yaw rate and longitudinal velocity simultaneously and also shows the advantage of the 4WID vehicle.

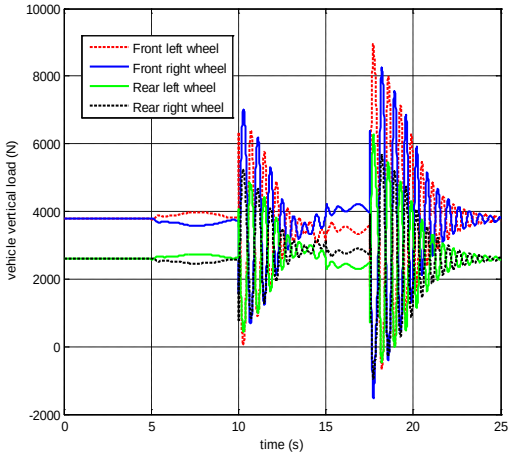

(a) traditional controller applied

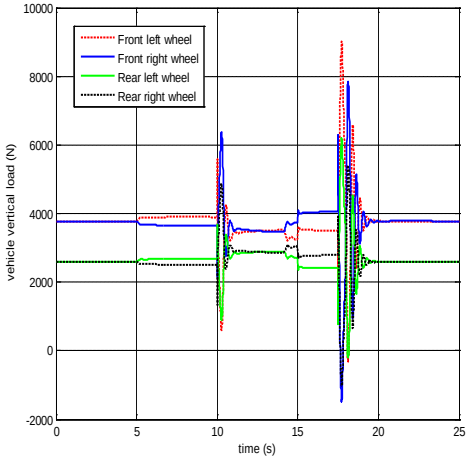

(b) the first improved controller

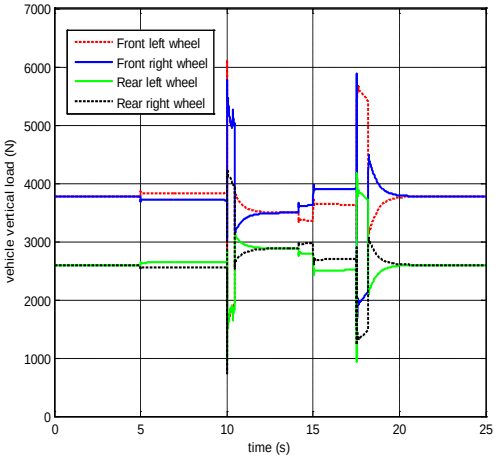

(c) the second improved controller

Figure VIII-3. Vehicle vertical load of each wheel in the first set of simulations

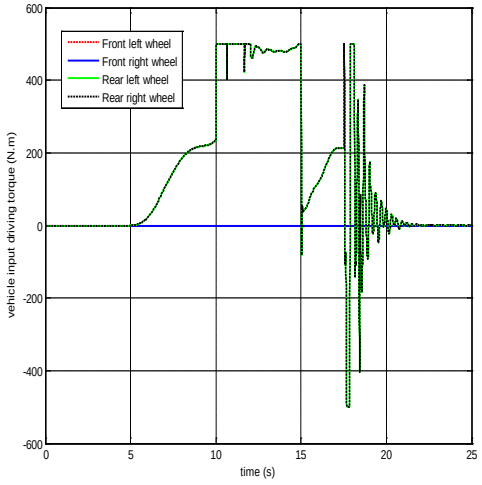

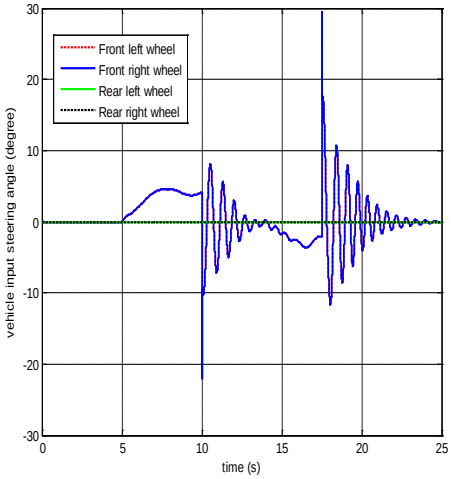

(a) traditional controller applied

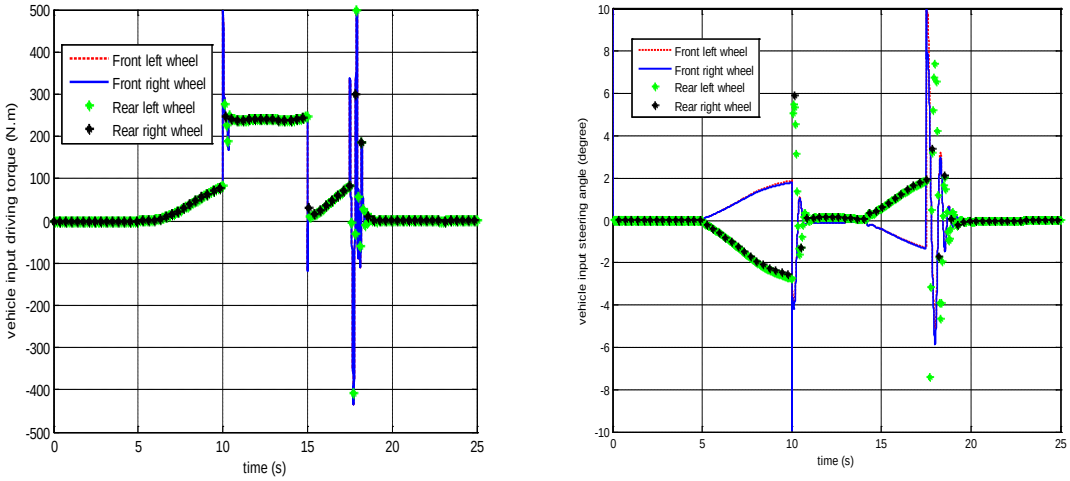

(b) the first improved controller

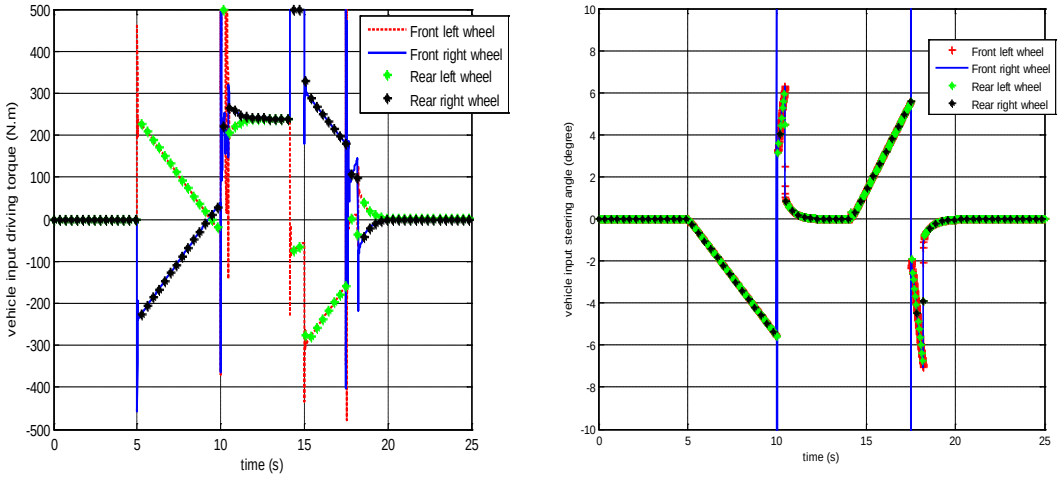

(c) the second improved controller

Figure VIII-4. Vehicle steering and driving inputs in the first set of simulations

Figure VIII-3 shows the load transfer effect of the combined lateral and longitudinal dynamics controller on the vehicle load. When the traditional controller is used as in Figure VIII-3 (a), the vertical load oscillates widely at 10 seconds and 17 seconds when the vehicle is starting to turn. These oscillations are so large that the vertical load is less than zero and the vehicle may roll over. When the first improved controller is applied in Figure VIII-3 (b), the vehicle vertical load oscillation is significantly alleviated due to the 4WIS. Figure VIII-3 (c) suggests that the rollover problem is not showing when the second improved controller is

applied. However, at 10 second and 17 second, when the vehicle is in the transit time between turning and straight moving, the load transfer effect is still quite significant.

In Figure VIII-4, due to the application of the 4WID and 4WIS, the first improved controller costs less steering and driving control effort compared with the traditional two-wheel controller. The second improved controller needs more driving torque compared with the first improved controller because the additional control target of yaw rate is achieved.

In the second set of simulations, in order to make the overtaking scenario more challenging, the desired vehicle trajectory is changed according to the following equation, which is shown in Figure VIII-5 (a):

$$y_d = \begin{cases} 0 & if\ x_d < 150 \\ -\left(R - \sqrt{R^2 - (x_d - 150)^2}\right) & if\ 150 \le x_d < 300 \\ -11.3 & if\ 300 \le x_d < 450 \\ \left(R - \sqrt{R^2 - (x_d - 450)^2}\right) - 11.3 & if\ 450 \le x_d < 600 \\ 0 & if\ x_d \ge 600 \end{cases} \tag{198}$$

In addition, the desired longitudinal velocity is increased to the values in Figure VIII-5 (b).

Figure VIII-6 (b) shows that oscillation problem of the two-wheel PID and four-wheel PID steering controllers is more serious than the first scenario with the increase of vehicle velocity. This suggests the disadvantage of the PID steering controller when the longitudinal velocity is large. The four-wheel SMC steering controller shows good control compared with the other methods. Figure VIII-6 (a) and (c) show that the two-wheel SMC driving and four-wheel SMC driving cannot work properly after 11 seconds and the four-wheel combined SMC driving controller has good control. Figure VIII-6 (d) suggests that the proposed four wheel combined SMC driving controller can better achieve the desired yaw rate compared with other methods.

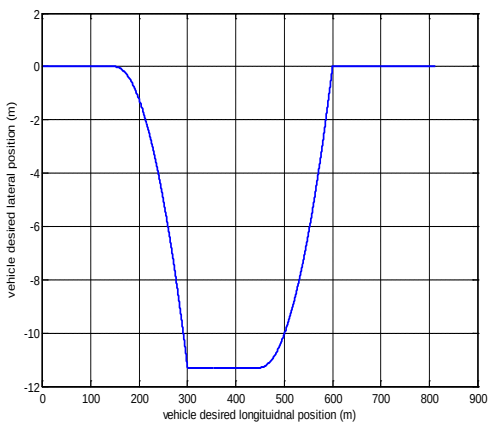

(a) vehicle desired trajectory

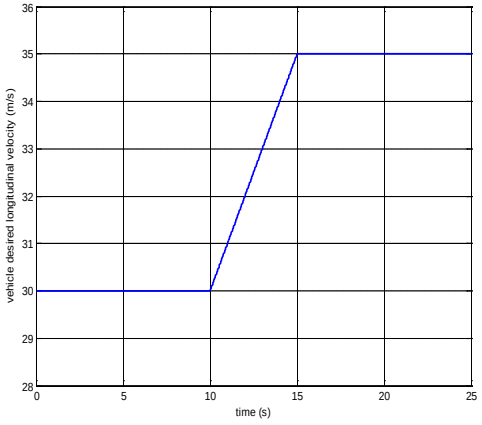

(b) vehicle desired velocity

Figure VIII-5. The desired vehicle trajectory in the second set of simulations.

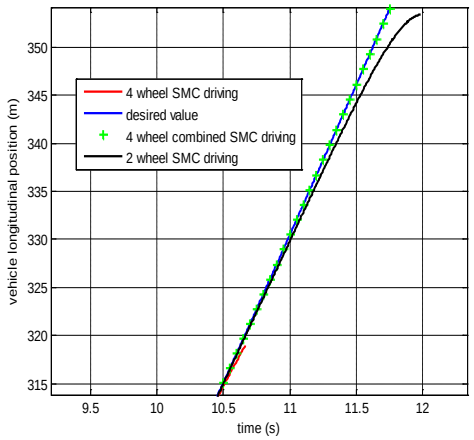

(a) longitudinal position vs time

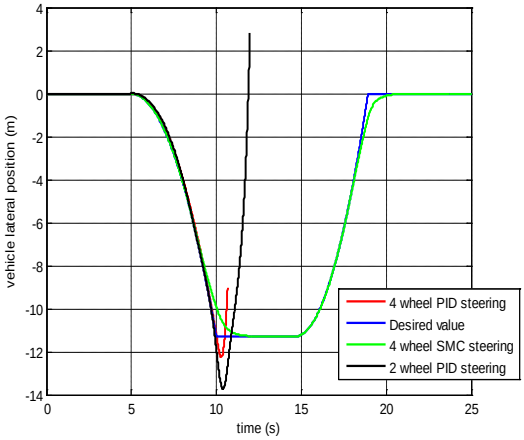

(b) lateral position vs time

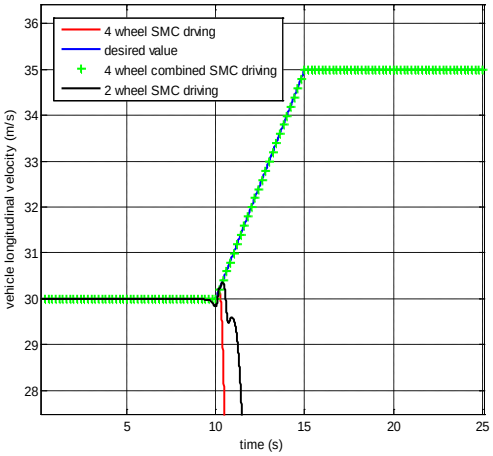

(c) longitudinal velocity vs time

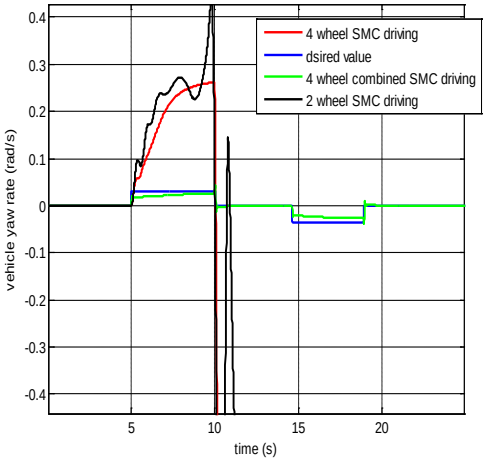

(d) yaw rate vs time

Figure VIII-6. Comparison between the desired dynamics response and the actual response in the second set of simulations.

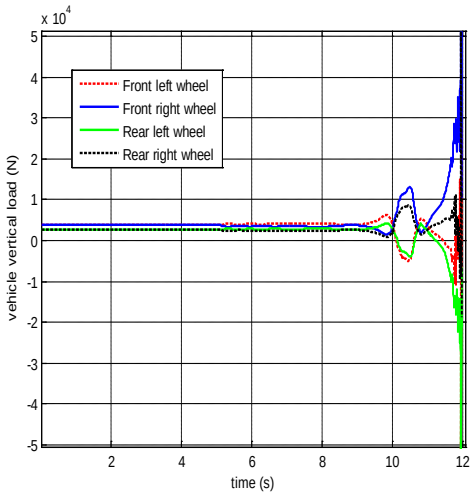

(a) traditional controller applied

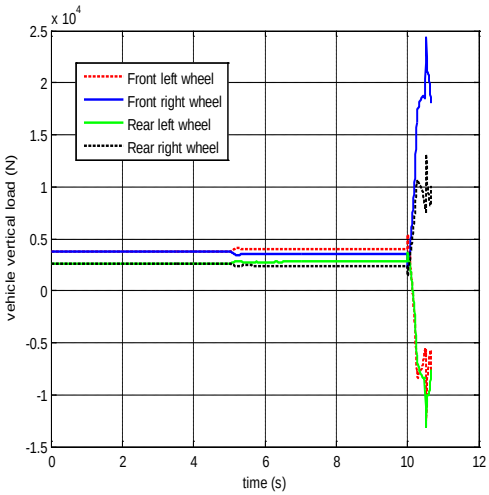

(b) the first improved controller

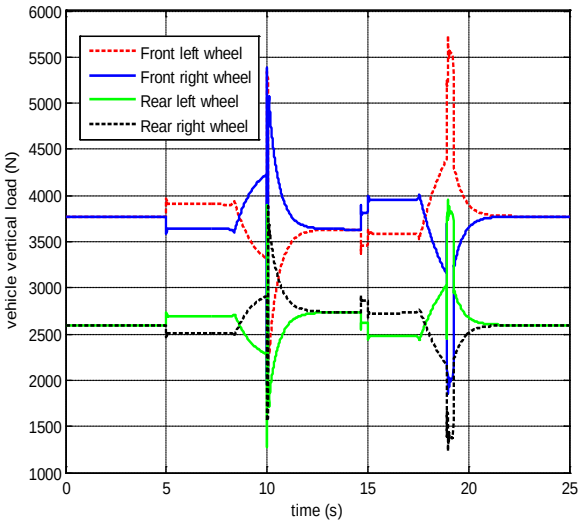

(c) the second improved controller

Figure VIII-7. Vehicle vertical load of each wheel in the second set of simulations.

Figure VIII-7 proves that although the second improved controller has a more significant load transfer effect than the situation in the first scenario, it still has much better control performance than the other two methods. Figure VIII-8 presents the input steering angle and driving torque of the second improved controller. The driving and steering inputs of the traditional controller and the first improved controller are not presented here because the simulation is failure after 11 second.

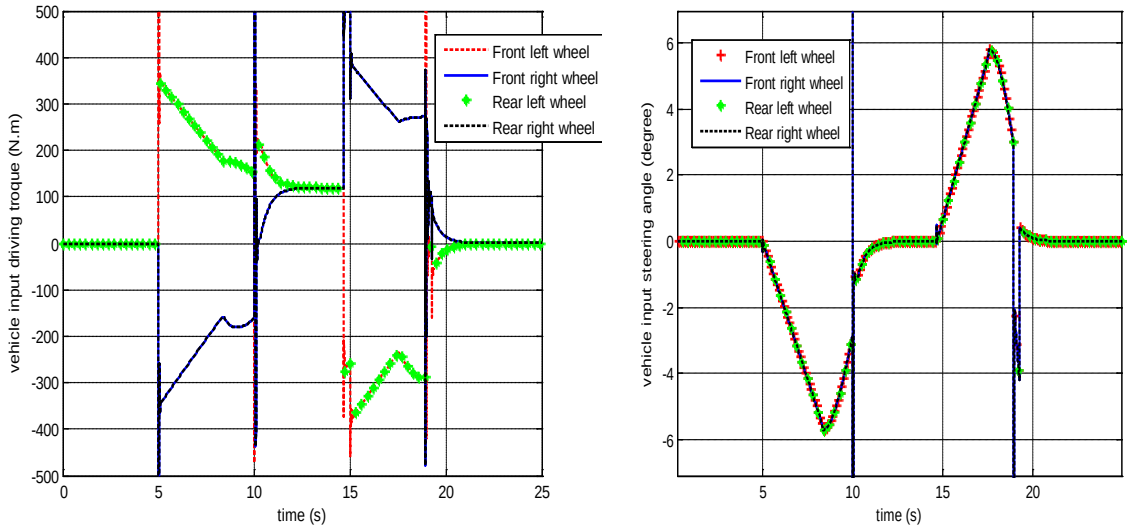

Figure VIII-8. Vehicle steering and driving inputs of the second improved controller in the second set of simulations.

Thus, it can be concluded that the proposed combined four-wheel SMC steering controller and four-wheel combined SMC driving controller can achieve better trajectory and dynamics control performance than other methods.

5) Conclusion

Most of the existing studies on the autonomous control of vehicle overtaking motion applied the vehicle kinematic model or the limited dynamics model to describe the vehicle motion, which is only suitable at low speed and in-doors. This section, however, proposes a comprehensive vehicle dynamics control of the on-road autonomous EV with high velocity by utilising the redundant control actuators from 4WIS-4WID characteristics. Moreover, unlike the holonomic omni-directional robot, strong coupling effect between the longitudinal motion, lateral motion and yaw motion is a great challenge for the autonomous vehicle motion control. In this section, the autonomous control of the overtaking motion of the EV is achieved by separating the steering controller (to achieve the desired lateral position) from the driving controller (to achieve the desired longitudinal position and yaw rate) to alleviate the strong coupling effect between them. Specifically, this paper proposes a four-wheel PID steering controller and a four-wheel SMC steering controller which are based on the traditional two wheel steering controller. In addition, based on the traditional two-wheel

driving controller, this section suggests a four-wheel SMC driving controller and a four-wheel combined yaw rate and longitudinal velocity SMC driving controller. Simulation has shown:

1) When the four-wheel SMC steering controller and four-wheel combined yaw rate and longitudinal velocity SMC driving controller are used together, the controlled vehicle can achieve most of the control targets. This proves that the control method based on 4WID and 4WIS vehicles can achieve much better control performance than the traditional methods.

2) When the four-wheel PID steering controller and four-wheel SMC driving controller are used together, the controlled vehicle can achieve better control performance compared with the traditional method. This good performance can be achieved, however, when the longitudinal velocity is not too high. The higher the velocity, the higher the oscillation will be.

3) The four-wheel combined yaw rate and longitudinal velocity SMC driving controller can achieve both the desired yaw rate and the longitudinal velocity simultaneously. This suggests that using over-actuated control allocation can achieve multiple control targets.

The trajectory tracking control of the autonomous EV is a complex and challenge task and this section is only a small step. This paper only considers the pre-defined road centre line to be followed in the vehicle trajectory tracking. In the potential field method proposed in the next section, the road boundary instead of a simple centre line of the road should be considered and the desired trajectory can be optimised within the road boundary based on different control targets (such as the minimum traveling time or the smooth of the vehicle trajectory). In addition, the situation when the static or moving obstacles on the road is considered and the obstacle avoiding control is implemented.

2. Potential field method based autonomous vehicle trajectory control

In this study, an innovative potential field method aiming to achieve the vehicle trajectory control based on yaw angle control is proposed. This potential filed method includes the attractive potential function, repulsive potential function and the yaw angle potential function that minimises the yaw angle change rate. Instead of using the relative positions, this paper uses the difference between the desired velocity and the actual velocity to describe the

attractive potential function since the vehicle lateral velocity is directly related to the yaw angle. The repulsive potential function is proposed to guarantee the actual vehicle position is constrained by the upper and lower boundary. The vehicle dynamics motion is described by the time-derivative equations and these equations should be transferred into the position-dependent equations that describe the vehicle actual trajectory to guarantee the satisfaction of the road boundary. In addition, the yaw angle potential function is suggested in this paper to minimise the yaw angle change rate and improve the handling and stability of the vehicle. These potential functions can be minimised to determine the real-time desired yaw angle. Then according to the desired yaw angle, a two-level vehicle trajectory controller is suggested to track this desired yaw angle and the desired trajectory. In the upper level, the desired vehicle total longitudinal force, total lateral force and yaw moment are determined according to the desired yaw angle and desired longitudinal velocity. In the lower level, the controlled values of individual steering and driving actuator are optimally allocated in the 4WIS-4WID EV to achieve the desired total longitudinal force, lateral force and yaw moment.

The main contributions of this section can be summarised as follows: 1) an innovative yaw-angle based potential field function is proposed to achieve the desired road trajectory within the certain road boundary and minimise the yaw angle change rate. 2) a two-level vehicle dynamics trajectory controller is proposed to optimally distribute the individual control actuator.

1) Potential Field Method

In the autonomous vehicle steering control, the potential field includes the component that guides the vehicle towards the desired path and the obstacle potentials induced by the road curb or other vehicles in the traffic. The total potential energy function can be presented by the following equation:

$$U = U_{att} + U_{rep} + U_s \tag{199}$$

where U_{att} is the attractive potential that guides the vehicle towards the desired path and U_{rep} is the repulsive potential that guides the vehicle away from the obstacle. U_s is the potential

function that minimise the yaw angle change rate, which can improve the vehicle handling and stability performance:

$$U_s = c\big(\varphi(k+1) - \varphi(k)\big)^2$$

(200)

where $\varphi(k)$ and $\varphi(k+1)$ present the yaw angle in the kth time step and $(k+1)th$ time step. c is the scaling factor.

The attractive potential U_{att} can be presented by equation (201) according to [235]:

$$U_{att} = \alpha_p \|p_{tar}(k) - p(k)\|^r + \alpha_v \|v_{tar}(k) - v(k)\|^n$$

(201)

where $p(k)$ and $p_{tar}(k)$ denote the position of the vehicle and the desired path at time t. $v_{tar}(k)$ and $v(k)$ present the actual velocity of the vehicle and the desired velocity of the trajectory at time step k, which includes the longitudinal velocity and lateral velocity. α_p and α_v are scalar positive parameters. r and n are positive parameters. In the actual vehicle dynamics control, the vehicle velocity can be easily controlled by achieving the desired longitudinal velocity and yaw angle. However, the vehicle position error is hard to be controlled for the on-road vehicle. The control of the lateral and longitudinal position tracking error requires the control of the longitudinal and lateral forces. For the in-door robot such as the holonomic omni-directional robot, the orientation and position can be controlled independently and consequently the longitudinal position and lateral position can be perfectly tracked without interfering with the yaw angle. However, for the autonomous EV, the longitudinal force and lateral force will have strong couple effect on the yaw angle of the vehicle during the position tracking due to the limitation of the vehicle mobility. Therefore, in this study, the desired trajectory is only tracked by the desired vehicle velocity and equation (201) can be rewritten as follows by assuming $n = 2$:

$$U_{att} = \alpha_v \|v_{tar}(k) - v(k)\|^2 = \alpha_v\big(v_x(k)\tan\varphi(k) - v_{yd-g}(k)\big)^2$$

(202)

where v_x is the longitudinal velocity in the vehicle body-fixed coordinate system, and this value is transferred into the global coordinate system as the lateral velocity by multiplying $\tan\varphi$. v_{yd-g} is the desired vehicle lateral velocity of the central line of the desired trajectory

in the global coordinate system, and this value is obtained according to the derivative of the lateral position of the central line of the trajectory. The actual vehicle longitudinal velocity is assumed to track the desired value accurately due to the application of the trajectory controller in Section 8.2.2, so it is not included in equation (202).

In addition, to determine the repulsive potential function of the road, the road boundary trajectory should be determined at first. The on-board sensors and camera can obtain the information of the road boundary ahead of the vehicle [233]. In addition, the real-time vehicle states (such as longitudinal velocity, lateral velocity and yaw rate) are assumed to be known or measurable since a number of studies and Chapter 3 of this thesis have proposed various vehicle state estimation methods [61] [62]. The road boundary can be described by the line of the upper boundary and the line of the lower boundary:

$$Y_{ub} = f_1(X) \tag{a}$$

$$Y_{lb} = f_2(X) \tag{b}$$

(203)

where X is the longitudinal position and $Y_{ub}(Y_{lb})$ is the lateral position of the boundary in the global coordinate system.

This road boundary position function depends on the position. In order to guarantee the vehicle is moving within the road boundary, the repulsive potential function is determined by the distance between the current vehicle lateral position and lateral positions of the corresponding upper and lower boundary when their longitudinal positions are same. However, the vehicle motion equations are usually described by the function depending on time in the vehicle body-fixed coordinate system. Thus, the following equations are used to transfer the time-dependent vehicle motion equation in the body-fixed coordinate system into the position-dependent vehicle motion equation in the global coordinate system:

$$X(k+1) = X(k) + \Delta t\big(v_x\,(k)\cos\varphi(k) - v_y(k)\sin\varphi(k)\big) \tag{a}$$

$$Y(k+1) = Y(k) + \Delta t\big(v_x(k)\sin\varphi(k) + v_y(k)\cos\varphi(k)\big) \tag{b}$$

(204)

where k presents the number of time step. Δt is the length of each time step and can be presented by the difference between the time value of the next time step $t(k+1)$ and the current time step $t(k)$:

$$\Delta t = t(k+1) - t(k) \tag{205}$$

v_x is the longitudinal velocity in the vehicle body-fixed coordinate system and v_y is the lateral velocity in the vehicle body-fixed coordinate system.

The boundary condition of the vehicle motion can be presented by the following equation:

$$Y_{ub}\big(X(k+1)\big) \le Y(k+1) \le Y_{lb}\big(X(k+1)\big) \tag{206}$$

Thus, the repulsive potential function can be determined according to the boundary condition (206). When the vehicle lateral position is between the central line and upper boundary, the repulsive potential function is as follows:

$$U_{rep} = \frac{b_1}{\Big(Y(k+1) - Y_{ub}\big(X(k+1)\big)\Big)^2} \tag{207}$$

When the vehicle lateral position is between the central line and the lower boundary, the repulsive potential function is as follows:

$$U_{rep} = \frac{b_2}{\Big(Y(k+1) - Y_{lb}\big(X(k+1)\big)\Big)^2} \tag{208}$$

where b_1, b_2 are the scaling factors.

In addition to the road boundary, vehicles ahead and below the controlled vehicle can also be considered as the obstacles in the actual traffic condition. Assume the real-time velocities of the front vehicle (ahead the controlled vehicle) and rear vehicle (below the controlled vehicle) are v_1 and v_2, respectively. In order to prevent the controlled vehicle from the collisions, the controlled vehicle velocity v_x should be constrained between v_1 and v_2.

The optimal control of vehicle motion can be achieved by choosing the optimal value of desired yaw angle to minimise the total potential energy function U. Thus, the cost function of the optimisation problem can be presented as follows:

$$J_{1min,\varphi_d} = a_0(v_{xd} - v_x)^2 + \alpha_v \left(v_x \tan\varphi_d(k+1) - v_{yd-g}(k+1)\right)^2 + \frac{b_1}{\left(Y(k+1) - Y_{ub}\left(X(k+1)\right)\right)^2} + \frac{b_2}{\left(Y(k+1) - Y_{lb}\left(X(k+1)\right)\right)^2} + c\left(\varphi_d(k+1) - \varphi_d(k)\right)^2 \tag{209}$$

s.t.

$$-\frac{\pi}{2} \leq \varphi_d \leq \frac{\pi}{2} \tag{a}$$

$$\mathrm{v}_2 \leq \mathrm{v}_\mathrm{x} \leq \mathrm{v}_1 \tag{b}$$

where $X(k+1)$ and $Y(k+1)$ can be determined by equation (204). a_0 is the scaling factor related to the term of achieving the desired longitudinal velocity. This optimisation problem can be solved by various algorithms. In this paper, the Matlab embedded function 'fmincon' is applied to solve this problem and obtain the desired yaw angle φ_d. In the next section, the vehicle dynamics trajectory controller is proposed to track this desired yaw angle.

2) Vehicle Trajectory Controller

Based on the desired vehicle longitudinal velocity and desired yaw angle of the trajectory, the autonomous vehicle motion can be controlled. The vehicle tracking error dynamics equation can be presented by the following equation based on [12]:

$$\dot{\tilde{e}}_y = v_x \sin(\tilde{\varphi} + \varphi_d) + v_y \cos(\tilde{\varphi} + \varphi_d) \tag{a}$$

$$\tilde{v}_x = \left[v_x \cos(\tilde{\varphi} + \varphi_d) - v_y \sin(\tilde{\varphi} + \varphi_d)\right] - v_{xd} \tag{b}$$

$$\tilde{\varphi} = \varphi_{act} - \varphi_d \tag{c}$$

(210)

where φ_{act} and φ_d are the vehicle's actual and desired yaw angles, respectively. $\dot{\tilde{e}}_y$ is the derivative of the lateral position error in the global coordinate system. $\tilde{v}_x$ is the error between the vehicle actual longitudinal velocity and the desired value v_{xd} tangential to the path in the global coordinate system.

The vehicle trajectory controller includes two parts: the feedforward controller and the feedback controller. The feedforward force and moment demands are calculated with the assumption that vehicle follows the desired trajectory:

$$F_{t,feedforward} = m\dot{v}_{xd} \tag{a}$$

$$F_{n,feedforward} = mv_{xd}\dot{\varphi}_d \tag{b}$$

$$M_{z,feedforward} = I_z\ddot{\varphi}_d \tag{c}$$

(211)

where $F_{t,feedforward}$ is the total force demand in the global coordinate frame tangential to the path in the feedforward controller. $F_{n,feedforward}$ is the total force demand in the global coordinate frame norm to the path in the feedforward controller. $M_{z,feedforward}$ is the total yaw moment required to achieve the desired vehicle motion in the feedforward controller. The feedforward controller (211) requires the perfectly tracking of the desired trajectory, which is unrealistic in the actual vehicle control.

To compensate the tracking error in the feedforward control, the feedback controller is proposed. The feedback force and moment demands are calculated by the following equations:

$$F_{t,feedback} = -m\dot{\tilde{e}}_y\dot{\varphi}_d - K_1\tilde{v}_x \tag{a}$$

$$F_{n,feedback} = m\tilde{V}\dot{\varphi}_d - K_{2d}\dot{\tilde{e}}_y - K_{2p}\tilde{e}_y \tag{b}$$

$$M_{z,feedback} = -K_{3d}\dot{\tilde{\varphi}} - K_{3p}\tilde{\varphi} \tag{c}$$

(212)

where $K_1, K_{2d}, K_{2p}, K_{3d}, K_{3p}$ are feedback control gains. $F_{t,feedback}$ is the total force demand in the global coordinate frame tangential to the path in the feedback controller. $F_{n,feedback}$ is the total force demand in the global coordinate frame norm to the path in the feedback controller. $M_{z,feedback}$ is the total yaw moment required to achieve the desired vehicle motion in the feedback controller.

When the vehicle is perfectly tracking the desired path, the total feedforward and feedback force tangential to the path $F_{t,total} = F_{t,feedforward} + F_{t,feedback}$ should be equal to the total longitudinal force of the vehicle $F_{x,total}$ and the total feedforward and feedback force norm to the path $F_{n,total} = F_{n,feedforward} + F_{n,feedback}$ should be equal to the total lateral force of the vehicle $F_{y,total}$. When the tracking error is considered, however, the total demand forces in the global coordinate frame should be transferred into the vehicle body-fixed coordinate frame by the following equations:

$$F_{x,total} = F_{t,total}\cos\tilde{\varphi} + F_{n,total}\sin\tilde{\varphi} \quad \text{(a)}$$

$$F_{y,total} = -F_{t,total}\sin\tilde{\varphi} + F_{n,total}\cos\tilde{\varphi} \quad \text{(b)}$$

$$M_{z,total} = M_{z,feedford} + M_{z,feedback} \quad \text{(c)}$$

(213)

In this section, in order to achieve the trajectory tracking control, the vehicle position error is described in the global coordinate frame at first. After that, according to the position error, the demand total longitudinal force and lateral force should be transferred from the global coordinate frame into the vehicle body-fixed coordinate frame. This is because that the vehicle dynamics control can only be achieved in the body-fixed coordinate system. In the following section, the steering and driving actuators are controlled to achieve the desired total longitudinal force, the total lateral force and yaw moment.

3) Optimal actuator control allocation method

In this study, the 4WIS-4WID EV is used to achieve the desired trajectory control. This 4WIS-4WID EV has the advantage of using redundant control actuators to achieve better control performance.

In this section, the control targets of the actuator control allocation method are the desired total longitudinal tyre force, the desired total lateral tyre force and desired yaw moment determined in the upper level trajectory controller in the last section. In addition, the individual allocated tyre forces are minimised to guarantee each tyre has been used sufficiently. The cost function of this actuator control allocation problem is shown as follows:

$$J_{2min,F_{ti},F_{si}} = \frac{F_{tfl}^2 + F_{sfl}^2}{\mu^2 F_{zfl}^2} + \frac{F_{tfr}^2 + F_{sfr}^2}{\mu^2 F_{zfr}^2} + \frac{F_{trl}^2 + F_{srl}^2}{\mu^2 F_{zrl}^2} + \frac{F_{trr}^2 + F_{srr}^2}{\mu^2 F_{zrr}^2}$$

(214)

subject to:

$$F_{tfl}\cos\delta_{fl} + F_{tfr}\cos\delta_{fr} + F_{trl}\cos\delta_{rl} + F_{trr}\cos\delta_{rr} - F_{sfl}\sin\delta_{fl} - F_{sfr}\sin\delta_{fr} - F_{srl}\sin\delta_{rl} - F_{srr}\sin\delta_{rr} = F_{x,total} - K_{s1}Sat\left(F_x - F_{x,total}\right)$$

(a)

$$F_{tfl}\sin\delta_{fl} + F_{tfr}\sin\delta_{fr} + F_{trl}\sin\delta_{rl} + F_{trr}\sin\delta_{rr} + F_{sfl}\cos\delta_{fl} + F_{sfr}\cos\delta_{fr} + F_{srl}\cos\delta_{rl} + F_{srr}\cos\delta_{rr} = F_{y,total} - K_{s2}Sat\left(F_y - F_{y,total}\right)$$

(b)

$$\begin{aligned} &F_{tfl}\left(l_f\sin\delta_{fl} + 0.5b_f\cos\delta_{fl}\right) + F_{tfr}\left(l_f\sin\delta_{fr} - 0.5b_f\cos\delta_{fr}\right) \\ &+ F_{trl}(-l_r\sin\delta_{rl} + 0.5b_r\cos\delta_{rl}) + F_{trr}(-l_r\sin\delta_{rr} - 0.5b_r\cos\delta_{rr}) \\ &+ F_{sfl}\left(l_f\cos\delta_{fl} - 0.5b_f\sin\delta_{fl}\right) + F_{sfr}\left(l_f\cos\delta_{fr} + 0.5b_f\sin\delta_{fr}\right) \\ &+ F_{srl}(-l_r\cos\delta_{rl} - 0.5b_r\sin\delta_{rl}) + F_{srr}(-l_r\cos\delta_{rr} + 0.5b_r\sin\delta_{rr}) \\ &= M_{z,total} - K_{s3}Sat\left(M_z - M_{z,total}\right) \end{aligned}$$

(c)

where F_x, F_y are the actual total longitudinal tyre force and lateral tyre force. $M_z = I_z\dot{r}$ is the actual yaw moment of the vehicle.

$$F_{ti}^2 + F_{si}^2 \le \mu F_{zi}^2 \quad \text{(d)}$$

$$-\frac{T_{bmax}}{R_\omega} \le F_{ti} \le \frac{T_{dmax}}{R_\omega} \quad \text{(e)}$$

The constraints (214)(a), (b) and (c) are applied here to achieve the desired longitudinal tyre force, lateral tyre force and yaw moment. To overcome the distribution error due to the non-linear characteristic of the vehicle dynamics model, the SMC is proposed in constraints (214)(a), (b) and (c) to accurately tracking the desired values. The effect of tyre friction circle is considered in (214)(d) and the constraint of the individual wheel driving/braking actuator is shown in (214)(e). In this study, an in-wheel brushless DC electric motor is applied. It has been suggested that the maximum driving torque T_{dmax} is 100 N.m and the maximum regenerated brake torque T_{bmax} is 80 N.m [15]. The optimization problem (214) can also be solved by the Matlab embedded function 'fmincon' and the detailed analysis of the optimization algorithm is beyond the scope of this study.

When the individual tyre forces have been allocated in (214), the controlled value of individual actuator can be mapped from the individual tyre force by equation (98)(99):

The practical limitation of the steering angle is considered between -90 degrees and 90 degrees ($\delta_{max} = 90$), which is larger than the traditional vehicle [115]. Thus,

$$-\delta_{max} \leq \delta_i \leq \delta_{max}$$

The whole control structure of the proposed potential field based trajectory tracking controller is shown in Figure VIII-9.

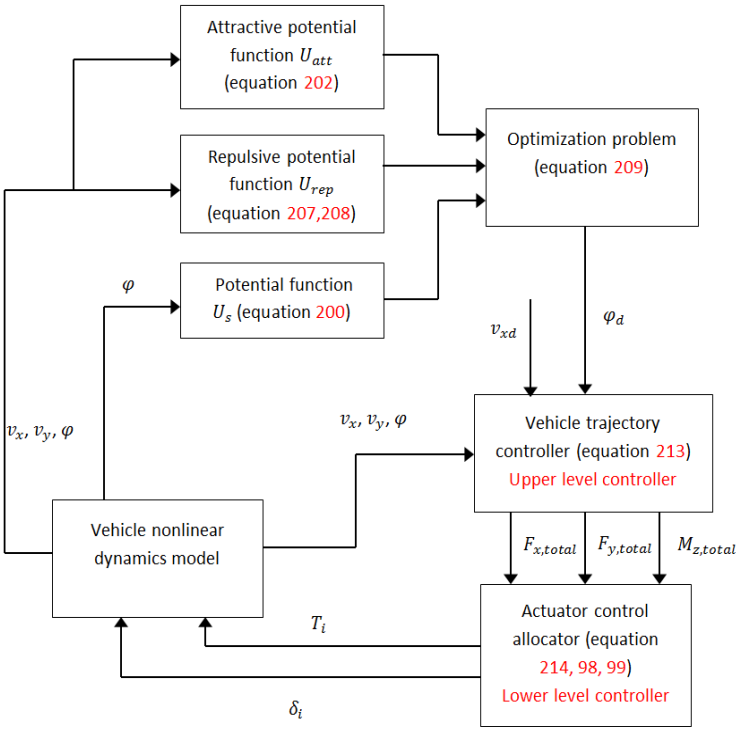

Figure VIII-9. The whole control structure of the proposed potential field based trajectory controller.

4) Stability analysis

In this study, the vehicle trajectory tracking controller and the actuator allocation method are proposed together as the hierarchy structure. The desired total tyre forces and moment from the upper level trajectory tracking controller are the control targets of the actuator allocation method in the lower level. Thus, the control performance of the upper level controller can directly affect the control performance of the lower level and the combined stability analysis of the two controllers is required.

When both the feedforward and feedback controllers in the trajectory tracking controller are applied, the vehicle dynamics equations of the body-fixed coordinate system are shown as follows by substituting (211), (212) and (213) into vehicle dynamics model (63):

$$m\dot{v}_x = mv_y r + \left[\left(m\dot{v}_{xd} - m\dot{\tilde{e}}_y\dot{\varphi}_d - K_1\tilde{v}_x\right)\cos\tilde{\varphi} + \left(mv_{xd}\dot{\varphi}_d + m\tilde{v}_x\dot{\varphi}_d - K_{2p}\tilde{e}_y\right)\sin\tilde{\varphi}\right] \quad \text{(a)}$$

$$m\dot{v}_y = -mv_x r + \left[-\left(m\dot{v}_{xd} - m\dot{\tilde{e}}_y\dot{\varphi}_d - K_1\tilde{v}_x\right)\sin\tilde{\varphi} + \left(mv_{xd}\dot{\varphi}_d + m\tilde{v}_x\dot{\varphi}_d - K_{2p}\tilde{e}_y\right)\cos\tilde{\varphi}\right] \quad \text{(b)}$$

$$I_z\dot{r} = I_z\ddot{\varphi}_d - K_{3p}\tilde{\varphi} \quad \text{(c)}$$

(215)

In equation (215)(c), when $\tilde{\varphi} \to 0$, $\varphi \to \varphi_d$, the actual yaw moment $I_z\dot{r}$ is approaching to the desired value $I_z\ddot{\varphi}_d$. We can obtain $r \to \dot{\varphi}_d$ by integrating (215)(c). (215)(a) and (215)(b) can be rewritten as:

$$m\dot{v}_x - m\dot{v}_{xd} + K_1\tilde{v}_x = mv_y r - mv_y\dot{\varphi}_d + mv_{yd}\dot{\varphi}_d \quad \text{(a)}$$

$$m\dot{v}_y = -mv_x r + mv_{xd}\dot{\varphi}_d + m(v_x - v_{xd})\dot{\varphi}_d - K_{2p}\tilde{e}_y \quad \text{(b)}$$

(216)

In (216)(a), when $\tilde{v}_x \to 0$, $v_x \to v_{xd}$ and the desired lateral velocity $v_{yd} = 0$. Thus $m\dot{v}_x - m\dot{v}_{xd} = 0$ and the vehicle longitudinal acceleration converges into the desired value. In (216)(b), when $\tilde{e}_y \to 0$, $m\dot{v}_y = 0$. The vehicle lateral acceleration converges into zero. This proves the stability of the trajectory tracking controller.

Equation (213) can be satisfied only when the desired total longitudinal force, total lateral force and total yaw moment can be accurately achieved in the lower level actuator distribution controller. Thus, the stability analysis of the lower level actuator controller is required to guarantee the accurate tracking of the desired tyre forces and moment.

When the vehicle non-linear dynamics is considered, constraints (214)(a), (214)(b) and (214)(c) can be rewritten as the follows:

$$\begin{aligned}
&\left(\frac{T_{fl}}{R_\omega} + \Delta F_{tfl}\right)\cos(\delta_{fl} + \Delta\delta_{fl}) + \left(\frac{T_{fr}}{R_\omega} + \Delta F_{tfr}\right)\cos(\delta_{fr} + \Delta\delta_{fr}) + \left(\frac{T_{rl}}{R_\omega} + \Delta F_{trl}\right)\cos(\delta_{rl} + \Delta\delta_{rl}) + \left(\frac{T_{rr}}{R_\omega} + \Delta F_{trr}\right)\cos(\delta_{rr} + \Delta\delta_{rr}) \\
&\quad - \left(C_\alpha\left(\delta_{fl} - \frac{l_f r}{v_x}\right) + \Delta F_{sfl}\right)\sin(\delta_{fl} + \Delta\delta_{fl}) - \left(C_\alpha\left(\delta_{fr} - \frac{l_f r}{v_x}\right) + \Delta F_{sfr}\right)\sin(\delta_{fr} + \Delta\delta_{fr}) \\
&\quad - \left(C_\alpha\left(\delta_{rl} + \frac{l_r r}{v_x}\right) + \Delta F_{srl}\right)\sin(\delta_{rl} + \Delta\delta_{rl}) - \left(C_\alpha\left(\delta_{rr} + \frac{l_r r}{v_x}\right) + \Delta F_{srr}\right)\sin(\delta_{rr} + \Delta\delta_{rr}) \\
&\quad = F_{x,total} - K_{s1}Sat(F_x - F_{x,total})
\end{aligned} \tag{a}$$

$$\begin{aligned}
&\left(\frac{T_{fl}}{R_\omega} + \Delta F_{tfl}\right)\sin(\delta_{fl} + \Delta\delta_{fl}) + \left(\frac{T_{fr}}{R_\omega} + \Delta F_{tfr}\right)\sin(\delta_{fr} + \Delta\delta_{fr}) + \left(\frac{T_{rl}}{R_\omega} + \Delta F_{trl}\right)\sin(\delta_{rl} + \Delta\delta_{rl}) + \left(\frac{T_{rr}}{R_\omega} + \Delta F_{trr}\right)\sin(\delta_{rr} + \Delta\delta_{rr}) \\
&\quad + \left(C_\alpha\left(\delta_{fl} - \frac{l_f r}{v_x}\right) + \Delta F_{sfl}\right)\cos(\delta_{fl} + \Delta\delta_{fl}) + \left(C_\alpha\left(\delta_{fr} - \frac{l_f r}{v_x}\right) + \Delta F_{sfr}\right)\cos(\delta_{fr} + \Delta\delta_{fr}) \\
&\quad + \left(C_\alpha\left(\delta_{rl} + \frac{l_r r}{v_x}\right) + \Delta F_{srl}\right)\cos(\delta_{rl} + \Delta\delta_{rl}) + \left(C_\alpha\left(\delta_{rr} + \frac{l_r r}{v_x}\right) + \Delta F_{srr}\right)\cos(\delta_{rr} + \Delta\delta_{rr}) \\
&\quad = F_{y,total} - K_{s2}Sat(F_y - F_{y,total})
\end{aligned} \tag{b}$$

$$\begin{aligned}
&\left(\frac{T_{fl}}{R_\omega} + \Delta F_{tfl}\right)\left(l_f\sin(\delta_{fl} + \Delta\delta_{fl}) + 0.5b_f\cos(\delta_{fl} + \Delta\delta_{fl})\right) + \left(\frac{T_{fr}}{R_\omega} + \Delta F_{tfr}\right)\left(l_f\sin(\delta_{fr} + \Delta\delta_{fr}) - 0.5b_f\cos(\delta_{fr} + \Delta\delta_{fr})\right) \\
&\quad + \left(\frac{T_{rl}}{R_\omega} + \Delta F_{trl}\right)\left(-l_r\sin(\delta_{rl} + \Delta\delta_{rl}) + 0.5b_r\cos(\delta_{rl} + \Delta\delta_{rl})\right) \\
&\quad + \left(\frac{T_{rr}}{R_\omega} + \Delta F_{trr}\right)\left(-l_r\sin(\delta_{rr} + \Delta\delta_{rr}) - 0.5b_r\cos(\delta_{rr} + \Delta\delta_{rr})\right) \\
&\quad + \left(C_\alpha\left(\delta_{fl} - \frac{l_f r}{v_x}\right) + \Delta F_{sfl}\right)\left(l_f\cos(\delta_{fl} + \Delta\delta_{fl}) - 0.5b_f\sin(\delta_{fl} + \Delta\delta_{fl})\right) \\
&\quad + \left(C_\alpha\left(\delta_{fr} - \frac{l_f r}{v_x}\right) + \Delta F_{sfr}\right)\left(l_f\cos(\delta_{fr} + \Delta\delta_{fr}) + 0.5b_f\sin(\delta_{fr} + \Delta\delta_{fr})\right) \\
&\quad + \left(C_\alpha\left(\delta_{rl} + \frac{l_r r}{v_x}\right) + \Delta F_{srl}\right)\left(-l_r\cos(\delta_{rl} + \Delta\delta_{rl}) - 0.5b_r\sin(\delta_{rl} + \Delta\delta_{rl})\right) \\
&\quad + \left(C_\alpha\left(\delta_{rr} + \frac{l_r r}{v_x}\right) + \Delta F_{srr}\right)\left(-l_r\cos(\delta_{rr} + \Delta\delta_{rr}) + 0.5b_r\sin(\delta_{rr} + \Delta\delta_{rr})\right) \\
&\quad = M_{z,total} - K_{s3}Sat(M_z - M_{z,total})
\end{aligned}$$

(c)

(217)

where ΔF_{ti} and ΔF_{si} are the additional tyre forces caused by tyre non-linear characteristic. $\Delta\delta_i$ presents the changed steering value of each wheel in the each simulation time step due to the steering actuator controller applied.

Substituting the actual allocated actuators values in equation (98)(99) into equation (217):

$$\begin{aligned}F_x - F_{x,total} = {} & \left(\Delta F_{tfl}\cos\delta_{fl} + (\Delta F_{tfl} + F_{tfl})\cos\Delta\delta_{fl}'\right) + \left(\Delta F_{tfr}\cos\delta_{fr} + (\Delta F_{tfr} + F_{tfr})\cos\Delta\delta_{fr}'\right) + (F_{trl} + \Delta F_{trl})(\cos\delta_{rl} + \cos\Delta\delta_{rl}') \\ & + (\Delta F_{trr}\cos\delta_{rr} + (F_{trr} + \Delta F_{trr})\cos\Delta\delta_{rr}') - \left(\Delta F_{sfl}\sin\delta_{fl} + \left(F_{sfl} + \Delta F_{sfl}\right)\sin\delta_{fl}'\right) \\ & - \left(\Delta F_{sfr}\sin\delta_{fl} + \left(F_{sfr} + \Delta F_{sfr}\right)\sin\delta_{fr}'\right) - (\Delta F_{srl}\sin\delta_{rl} + (F_{srl} + \Delta F_{srl})\sin\delta_{rl}') \\ & - \left(\Delta F_{srr}\sin\delta_{fl} + (F_{srr} + \Delta F_{srr})\sin\delta_{rr}'\right) = -K_{s1}Sat\left(F_x - F_{x,total}\right)\end{aligned}$$

(a)

$$\begin{aligned}F_y - F_{y,total} = {} & \left(\Delta F_{tfl}\sin\delta_{fl} + (\Delta F_{tfl} + F_{tfl})\sin\Delta\delta_{fl}'\right) + \left(\Delta F_{tfr}\sin\delta_{fr} + (\Delta F_{tfr} + F_{tfr})\sin\Delta\delta_{fr}'\right) \\ & + (\Delta F_{trl}\sin\delta_{rl} + (\Delta F_{trl} + F_{trl})\sin\Delta\delta_{rl}') + (\Delta F_{trr}\sin\delta_{rr} + (\Delta F_{trr} + F_{trr})\sin\Delta\delta_{rr}') \\ & + \left(\Delta F_{sfl}\cos\delta_{fl} + (\Delta F_{sfl} + F_{sfl})\cos\Delta\delta_{fl}'\right) + \left(\Delta F_{sfr}\cos\delta_{fr} + (\Delta F_{sfr} + F_{sfr})\cos\Delta\delta_{fr}'\right) \\ & + (\Delta F_{srl}\cos\delta_{rl} + (\Delta F_{srl} + F_{srl})\cos\Delta\delta_{rl}') + (\Delta F_{srr}\cos\delta_{rr} + (\Delta F_{srr} + F_{srr})\cos\Delta\delta_{rr}') = -K_{s2}Sat\left(F_y - F_{y,total}\right)\end{aligned}$$

(b)

$$\begin{aligned}M_z - M_{z,total} = {} & \left(l_f\left(\Delta F_{tfl}\sin\delta_{fl} + (\Delta F_{tfl} + F_{tfl})\sin\Delta\delta_{fl}'\right) + 0.5b_f\left(\Delta F_{tfl}\cos\delta_{fl} + (\Delta F_{tfl} + F_{tfl})\cos\Delta\delta_{fl}'\right)\right) \\ & + \left(l_f\left(\Delta F_{tfr}\sin\delta_{fr} + (\Delta F_{tfr} + F_{tfr})\sin\Delta\delta_{fr}'\right) - 0.5b_f\left(\Delta F_{tfr}\cos\delta_{fr} + (\Delta F_{tfr} + F_{tfr})\cos\Delta\delta_{fr}'\right)\right) \\ & + \left(-l_r(\Delta F_{trl}\sin\delta_{rl} + (\Delta F_{trl} + F_{trl})\sin\Delta\delta_{rl}') + 0.5b_r(\Delta F_{trl}\cos\delta_{rl} + (\Delta F_{trl} + F_{trl})\cos\Delta\delta_{rl}')\right) \\ & + \left(-l_r(\Delta F_{trr}\sin\delta_{rr} + (\Delta F_{trr} + F_{trr})\sin\Delta\delta_{rr}') - 0.5b_r(\Delta F_{trr}\cos\delta_{rr} + (\Delta F_{trr} + F_{trr})\cos\Delta\delta_{rr}')\right) \\ & + \left(l_f\left(\Delta F_{sfl}\cos\delta_{fl} + (\Delta F_{sfl} + F_{sfl})\cos\Delta\delta_{fl}'\right) - 0.5b_f\left(\Delta F_{sfl}\sin\delta_{fl} + \left(F_{sfl} + \Delta F_{sfl}\right)\sin\delta_{fl}'\right)\right) \\ & + \left(l_f\left(\Delta F_{sfr}\cos\delta_{fr} + (\Delta F_{sfr} + F_{sfr})\cos\Delta\delta_{fr}'\right) + 0.5b_f\left(\Delta F_{sfr}\sin\delta_{fr} + \left(F_{sfr} + \Delta F_{sfr}\right)\sin\delta_{fr}'\right)\right) \\ & + \left(-l_r(\Delta F_{srl}\cos\delta_{rl} + (\Delta F_{srl} + F_{srl})\cos\Delta\delta_{rl}') - 0.5b_r(\Delta F_{srl}\sin\delta_{rl} + (F_{srl} + \Delta F_{srl})\sin\delta_{rl}')\right) \\ & + \left(-l_r(\Delta F_{srr}\cos\delta_{rr} + (\Delta F_{srr} + F_{srr})\cos\Delta\delta_{rr}') + 0.5b_r(\Delta F_{srr}\sin\delta_{rr} + (F_{srr} + \Delta F_{srr})\sin\delta_{rr}')\right) \\ & = -K_{s3}Sat\left(M_z - M_{z,total}\right)\end{aligned}$$

(c)

(218)

In equation (218), $\Delta F_{ti,}\, \Delta F_{si}$ and F_{ti}, F_{si} are bounded if the vehicle tyre is working under the stability region (linear and non-linear region) and $\sin\theta$ and $\cos\theta$ are also bounded functions. Thus, the SMC can guarantee the rewritten constraints (217)(a-c) are satisfied by choosing

the large enough sliding mode gains K_{s1}, K_{s2}, K_{s3}. This leads to $F_x \rightarrow F_{x,total}$, $F_y \rightarrow F_{y,total}$ and $M_z \rightarrow M_{z,total}$.

5) Simulation Results

In this section, two sets of simulations are used to test the effectiveness of the proposed vehicle trajectory controller. In the first set of simulations, the road boundary is wide enough and the boundary constraints can be neglected. The control targets are the tracking of the road central line and minimising of the yaw angle change rate to guarantee the smoothness of the trajectory. In the second set of simulations, the road boundary is much narrow than the first set of simulations and the boundary avoiding control is the primary control target. In the third and fourth set of simulations, the desired vehicle path and road boundary are changing with the actual traffic condition. The simulation parameters are shown in Table III-1.

In the first set of simulations, the upper level boundary, road centre line and lower level boundary of vehicle desired trajectory are presented in Figure VIII-10. In this simulation, the vehicle initial velocity is 20 m/s and the tyre-road friction coefficient is 0.9. It should be noted that the upper and lower boundaries in the simulation indicate the constraints of the vehicle C.G. point and the vehicle geometric length is neglected here.

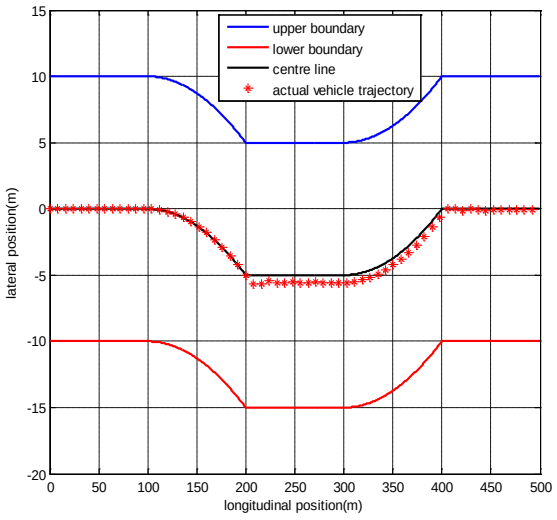

Figure VIII-10. The actual vehicle trajectory when the desired trajectory is strictly followed in the first set of simulations.

Figure VIII-10 presents the simulation results when the road centre line is strictly followed. This means $c = b_1 = b_2 = 0, a_v = 100, a_0 = 0$ in the optimal control law (209). In Figure VIII-11, the vehicle trajectory is optimised by the minimising of the position error and the minimising of the desired yaw rate. This means that $b_1 = b_2 = 0$ and $a_0 = 0, a_v = 1, c = 80000$ in the optimal control law (**209**). In Figure VIII-11, the road centre line is roughly followed by the actual vehicle and the vehicle trajectory is much smoother than the trajectory in Figure VIII-10. Figure VIII-12 and Figure VIII-13 compare vehicle longitudinal velocity, body slip angle responses and yaw rate responses when the desired trajectory is strictly followed (Figure VIII-10) and when the vehicle trajectory is optimised (Figure VIII-11). It can be found that if the centre line of the path is strictly followed, the actual vehicle body slip angle is large and the yaw rate and longitudinal velocity oscillate significantly. The vehicle handling and stability performance would be significantly impaired and the vehicle is moving in a dangerous condition. When the actual trajectory is optimised, vehicle body slip angle is much smaller and the vehicle yaw rate and longitudinal velocity response are more stable. This proves that the proposed potential field method can successfully improve the vehicle handling and stability performance, which are generally defined in terms of vehicle yaw rate and body slip angle.

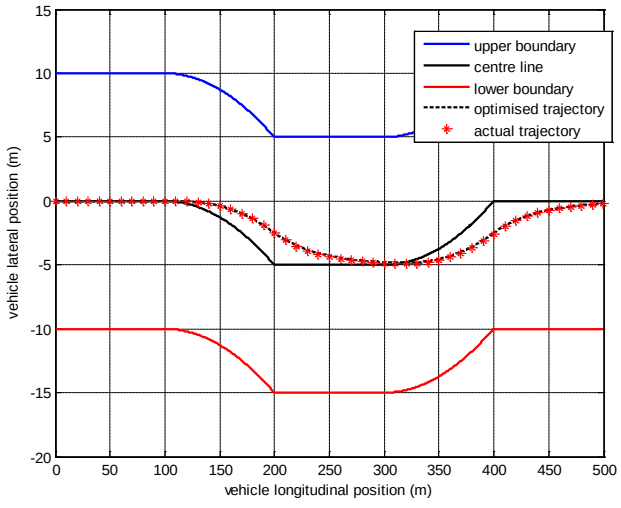

Figure VIII-11. The actual vehicle trajectory when the trajectory of the path is optimised in the first set of simulations.

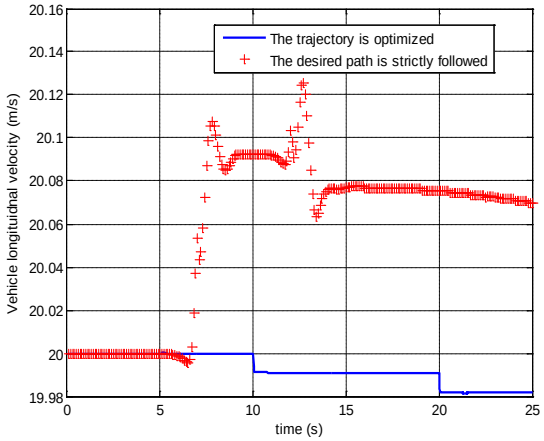

Figure VIII-12. The actual vehicle velocity in the first set of simulations.

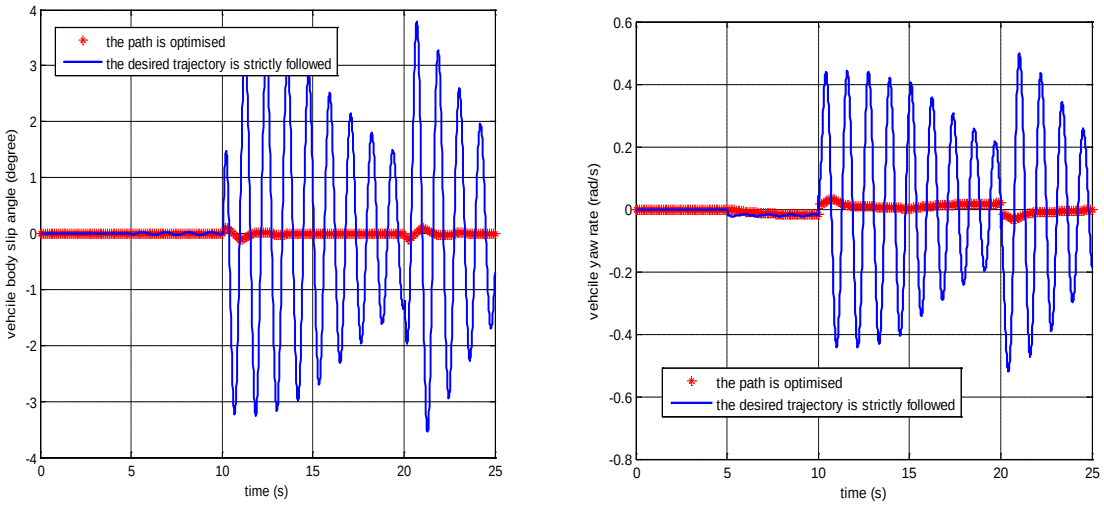

(a) (b)

Figure VIII-13. The actual vehicle responses (a) body slip angle (b) yaw rate in the first set of simulations.

In the second set of simulations, the vehicle initial velocity and tyre-road friction coefficient remain unchanged. According to Figure VIII-14, the desired trajectory and road boundary are more challenge than the first set of simulation. This path simulates the situation when the vehicle is trying to avoid the obstacle by doing the double lane change.

The results in Figure VIII-14 demonstrate the potential field method can successfully avoid the road boundary in the narrow moving space by minimising the yaw rate and not strictly

following the road centre line. In this case, $a_0 = 0, a_v = 0.5, b_1 = b_2 = 2000, c = 20000$ are used in the optimal law (209). This is quite different from the simple trajectory-following method as shown in Figure VIII-15. It can be found in Figure VIII-15 that the vehicle hits the lower boundary after the first turning and this is a serious problem that the vehicle may have an accident.

Figure VIII-16 and Figure VIII-17 compare the actual vehicle longitudinal velocity, body slip angle responses and yaw rate responses when the desired path is strictly followed and when the trajectory is optimised. When the desired path is strictly followed, the vehicle body slip angle is very large, the longitudinal velocity decreases rapidly and the yaw rate is highly unstable when the vehicle hits the lower boundary. The main reason for the instability of the vehicle in Figure VIII-15 is that the only control target for the strict path-following method is that the desired yaw angle and longitudinal velocity must strictly follow the desired path. When the vehicle is turning in a narrow angle, the large change rate of the yaw angle is required if the desired path is strictly followed. This large change rate of yaw angle as shown in Figure VIII-17 (b) results in the instability of the vehicle. When the proposed potential field method is applied to optimise the vehicle trajectory, the vehicle body slip angle and yaw rate performance are much improved.

Table VIII-3 summaries the maximum vehicle longitudinal velocity when the vehicle is turning with certain turning radius without hitting the road boundary and this value is obtained by a number of simulation tests. According to Table VIII-3, the vehicle maximum velocity increases when the turning radius increases. In addition, the boundary optimisation gains (b_1, b_2) also increase and play an important role when the turning radius is small.

It should be noted that the scaling factor a_0 in the optimisation problem (209) is assumed as zero in the first two sets of simulations because the longitudinal velocity is not required to achieve the certain value and the controller tries to maintain the initial velocity. In addition, the velocity constraint (209) is also neglected here since there is no front and rear vehicles.

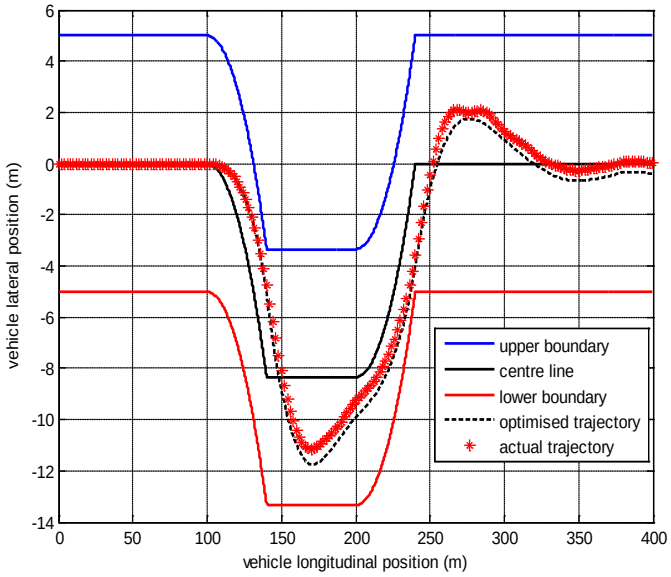

Figure VIII-14. The actual vehicle trajectory when the trajectory of the path is optimised in the second set of simulations.

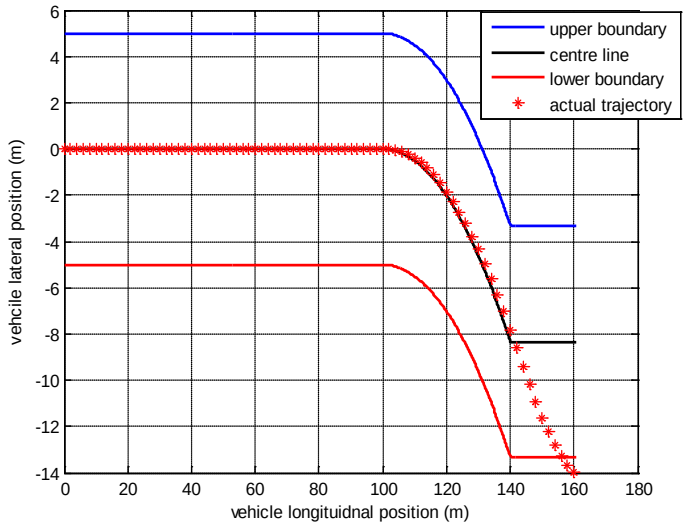

Figure VIII-15. The actual vehicle trajectory when the desired trajectory is strictly followed in the second set of simulations.

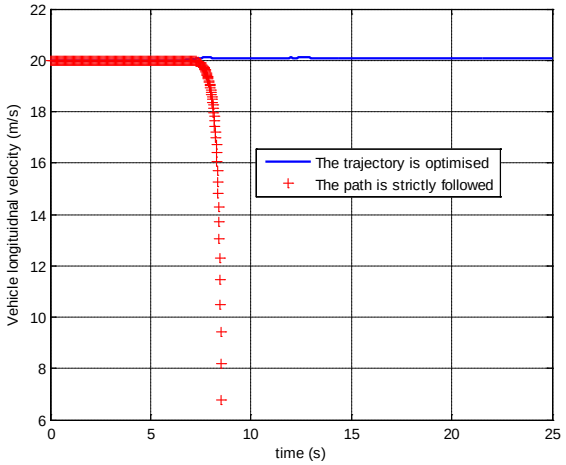

Figure VIII-16. The actual vehicle longitudinal velocity in the second set of simulations.

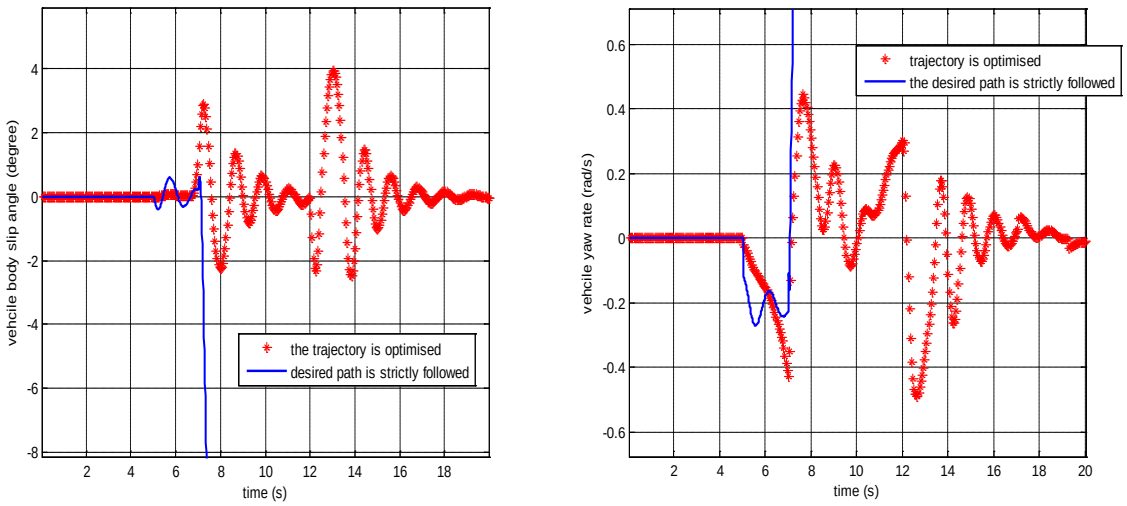

(a) (b)

Figure VIII-17. The actual vehicle responses (a) body slip angle (b) yaw rate in the second set of simulations.

Table VIII-3. Vehicle maximum longitudinal velocity during vehicle turning

Turn radius (m)	Maximum longitudinal velocity (m/s)	Optimization control gains
1000	>50	$b_1 = b_2 = 0$ and $a_v = 1, c = 80000, a_0 = 0$
200	25	$a_v = 0.5, b_1 = b_2 = 0, c = 20000, a_0 = 0$
100	20	$a_v = 0.5, b_1 = b_2 = 2000, c = 20000, a_0 = 0$

In the third set of the simulations, the impacts of the surrounding traffic of the controlled autonomous vehicle are considered. The vehicle initial velocity and tyre-road friction coefficient remain unchanged. The vehicle is assumed to move along the desired path with wide boundary as Figure VIII-10 at the beginning. After 200 meters in the longitudinal direction, the road boundary is narrower than the boundary at the beginning due to the effect of the surrounding traffic. In addition, it is assumed that there exists a vehicle in front of the controlled vehicle and a vehicle behind the controlled vehicle along the path, which is quite common in the real situation. The controlled vehicle velocity is constrained by the longitudinal velocity of the front vehicle (20 m/s~18m/s) and rear vehicle (18m/s~15m/s) in the body-fixed coordinate system. In this simulation, $a_0 = 0, a_v = 0.5, b_1 = b_2 = 0, c = 20000$ are used in the optimal law (209).

Figure VIII-18 suggests that the vehicle is controlled within the road boundary. Figure VIII-19 presents that the longitudinal velocity of the controlled vehicle in the body-fixed coordinate system is within the velocity constraints of the front and rear vehicle. The above simulation results prove that the controlled vehicle can satisfy all the boundary constraints and velocity constraints and the desired trajectory is successfully achieved. Figure VIII-20 suggests that the vehicle yaw rate and body slip angle change abruptly during the turning.

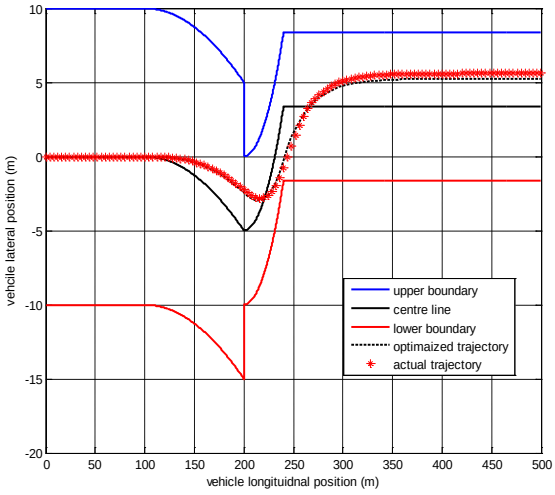

Figure VIII-18. Vehicle actual trajectory when the surrounding traffic is considered in the third set of simulations.

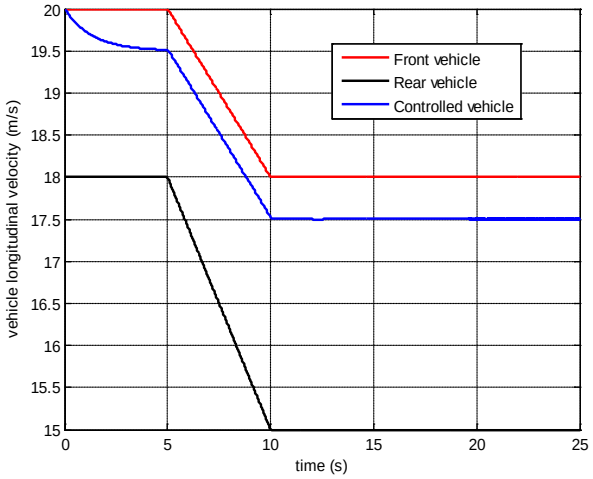

Figure VIII-19. Vehicle longitudinal velocity when the surrounding traffic is considered in the third set of simulations.

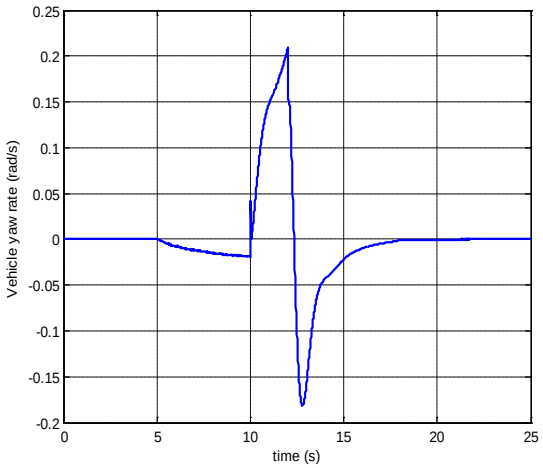

(a)

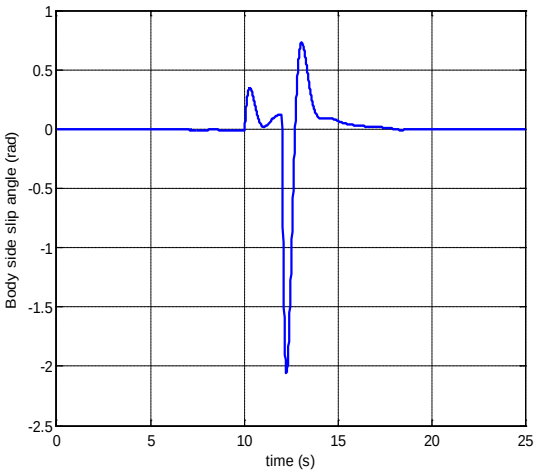

(b)

Figure VIII-20. The actual vehicle responses (a) body slip angle (b) yaw rate in the third set of simulations.

In the fourth set of simulations, the proposed potential field controller is applied in the actual traffic condition of overtaking and lane change. The tyre-road friction coefficient is assumed to be unchanged. At the beginning, the controlled vehicle is assumed to move on the bottom lane of the highway with the longitudinal velocity of 18 m/s, while another vehicle is moving on the top lane of the highway with velocity of 20 m/s. In order to overtake the vehicle in the top lane at 5 seconds, the controlled vehicle should turn on the left-turning signal, and then start to increase the speed into 20 m/s and make the lane change. At the same time of 5 seconds, when the driver of the top lane vehicle notices the left-turning signal of overtaking vehicle, he may push the brake pedal and decrease the vehicle velocity for safety reason. Figure VIII-21 presents the changed longitudinal velocity of the overtaken vehicle and overtaking vehicle. Figure VIII-22 shows the path boundary of the overtaking vehicle and this boundary is determined by the position of the overtaken vehicle and boundary of top lane and bottom lane. The upper and lower boundary (blue line and red line in Figure VIII-22) is actually changed with the relative longitudinal position between the overtaking vehicle and overtaken vehicle. If the longitudinal position of the controlled overtaking vehicle is behind the overtaken vehicle, the overtaking vehicle is constrained within the bottom lane. If the longitudinal position of the overtaking vehicle is in front of the overtaken vehicle with a certain safety distance d, the overtaking vehicle starts to make a lane change with the following boundary condition:

$$X_1 > X_2 + d \tag{219}$$

where X_1 and X_2 are the longitudinal position of the controlled overtaking vehicle and overtaken vehicle, respectively. It should be noted that the safety distance d is changing with vehicle velocity in reality. In this study, however, this value is assumed as constant due to the velocity is not changed significantly.

According to Figure VIII-22, the actual vehicle trajectory is roughly constrained by the road boundary and this proves that the proposed controller can successfully control the vehicle motion in the actual traffic condition of overtaking. In this case, $a_0 = 2, a_v = 0.5, b_1 = b_2 =$

$2000, c = 20000$ are used in the optimal law (209). Figure VIII-23 also suggests that the vehicle yaw rate and body slip angle change abruptly during the overtaking.

It is noted the actual vehicle trajectory when the desired path is strictly followed would hit the road boundary in the third and fourth set of simulations and is not presented here.

According to the four sets of simulations, the major limitations of the potential field method is the requirement of the manually tuning of the optimization scaling factors in different scenarios, which is possibly time-consuming. In addition, the proposed method cannot handle too extreme situations, such as turning abruptly with very fast speed.

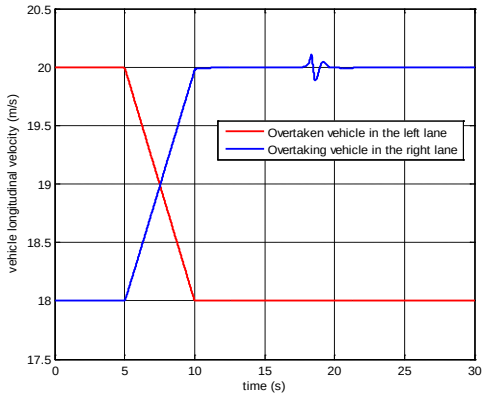

Figure VIII-21. Vehicle longitudinal velocity of the overtaking vehicle and overtaken vehicle in the fourth set of simulations.

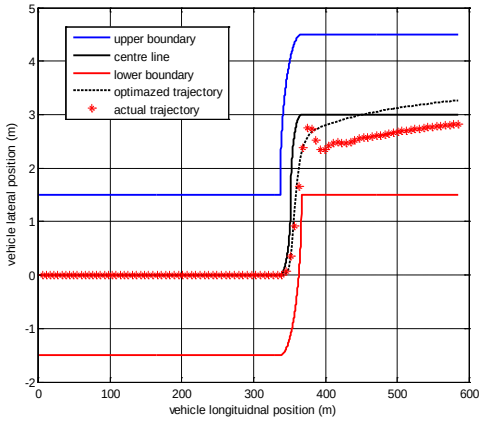

Figure VIII-22. Vehicle actual trajectory of the controlled overtaking vehicle when the path is optimized in the fourth set of simulations.

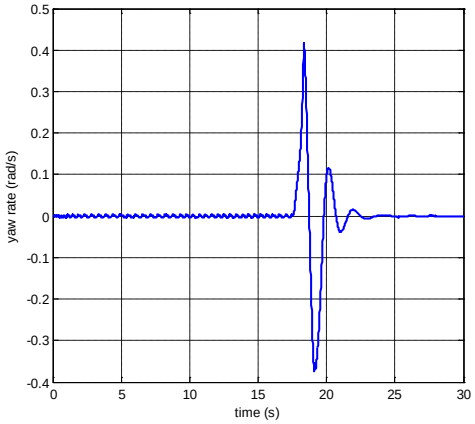

(a)

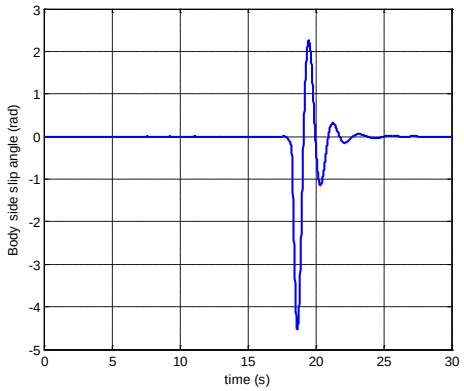

(b)

Figure VIII-23. Vehicle (a) yaw rate and (b) body slip angle response in the fourth set of simulation.

6) Conclusions

The potential field method is widely applied in the trajectory control of the mobile robot. This section extends the potential field method into a more challenge research area – the trajectory control of the autonomous on-road vehicle that has less mobility and higher velocity compared with the mobile robot. An innovative potential field function that includes the attractive potential, the repulsive potential and the potential that minimises yaw angle change rate is proposed in this study to determine the desired yaw angle. Then according to the desired yaw angle, the two-level vehicle trajectory controller is proposed to control the actual vehicle trajectory. The simulation results verified the suggested controller and the major findings are listed below:

1) Compared with the method exactly tracking the road centre line, the proposed potential field method that constraints the actual vehicle trajectory in a certain road boundary has better handling and stability performance.

2) In the narrow road boundary condition, the vehicle controlled by proposed potential field method can successfully avoid the upper and lower boundaries.

3) When the road boundary is changed in real-time due to the actual traffic condition or when the controlled vehicle tries to make the lane change and overtake other vehicles, the proposed method can still successfully control the vehicle.

This study only suggests some useful findings of the application of the potential field method into the autonomous vehicle control. In the future, the more advanced controller should be proposed to deal with more complex autonomous control problem in the macro view, such as the vehicle control in the intersection.

3. Summary

In this chapter, the application of the over-actuated control allocation method on the autonomous vehicle trajectory control is extensively focused. Two different trajectory control methods, the direct tracking method and the potential energy method, are proposed in this chapter and the potential energy method shows the improvement of the vehicle trajectory control performance and dynamics control performance.

IX. Experiment validation of the vehicle mass and road slope estimator based on a scaled electric vehicle

In previous chapters, the design of the over-actuated control allocation method for various control targets is focused and the designed controller is verified by the simulation results in Matlab Simulink. However, the simulation validation is not enough to present the actual performance of the proposed over-actuated controller.

Research on vehicle dynamics is often limited to software simulation purposes because the full-sized vehicle tests can be dangerous and expensive. The evaluation of vehicle dynamics and safety control system, however, cannot only rely on the software simulation, because the critical practical issues in the real-world vehicle dynamics cannot be considered without the real experiments. Thus the scaled vehicle test platform has been extensively studied in the current literature. Using the fixed road surface for the scaled vehicle test is widely implemented in the research area, but the interfacing and sensing problems are induced by the moving vehicles. Some of the researches are focusing on the scaled robot vehicle platform [256] [257] and the research on narrow tilting vehicle and the car-trailer system can also utilise the scaled vehicle platform [258] [259]. For the on-road scaled automobile test experiment, Katzourakis et al. and Reuter et al. developed the low-cost scaled automobile platform for research and education in vehicle dynamics and control, especially for the ESC system [260] [261]. Then Grepl et al. developed the novel 4WIS/4WID experimental vehicle platform for the research and education in mechatronics [262].

In this chapter, the parameter estimation and system identification of the vehicle longitudinal motion is focused and vehicle lateral motion is neglected. A four-wheel driving scaled electric vehicle is built to verify the mathematical modelling of vehicle dynamics and compared with the software simulation results. According to measured values from sensors, the unknown parameters of the vehicle dynamics model can be identified (such as vehicle mass and road slope) and vehicle states in real-time such as the longitudinal velocity and the longitudinal tyre force can be estimated. All these vehicle parameters and states are valuable values in the vehicle stability and control system, such as vehicle stability control [263] [39] and antilock braking system [264] [265].

In this chapter, the real experiment is implemented based on a 1:10 scaled electric vehicle to verify the proposed two-layer parameter estimator in Section 3.3. The hardware implementation is introduced at first. Then the experimental results of the estimated slowly changed parameter - vehicle mass in the first layer of the estimator is presented. When the vehicle mass is assumed to be available from the first layer, the experimental results of the estimated fast changed parameter – road slope in the second layer estimator is presented. The RMS error of the estimated vehicle mass and road slope is also presented as an estimation performance index.

1. Hardware implementation

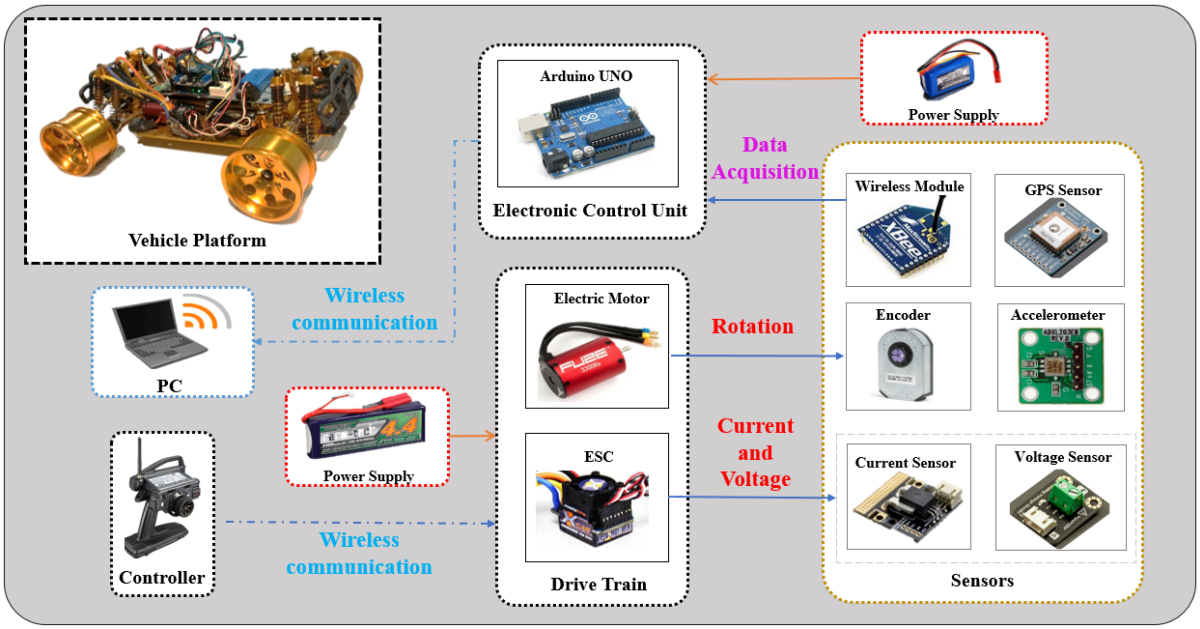

Figure IX-1. The function structure of scaled electric vehicle.

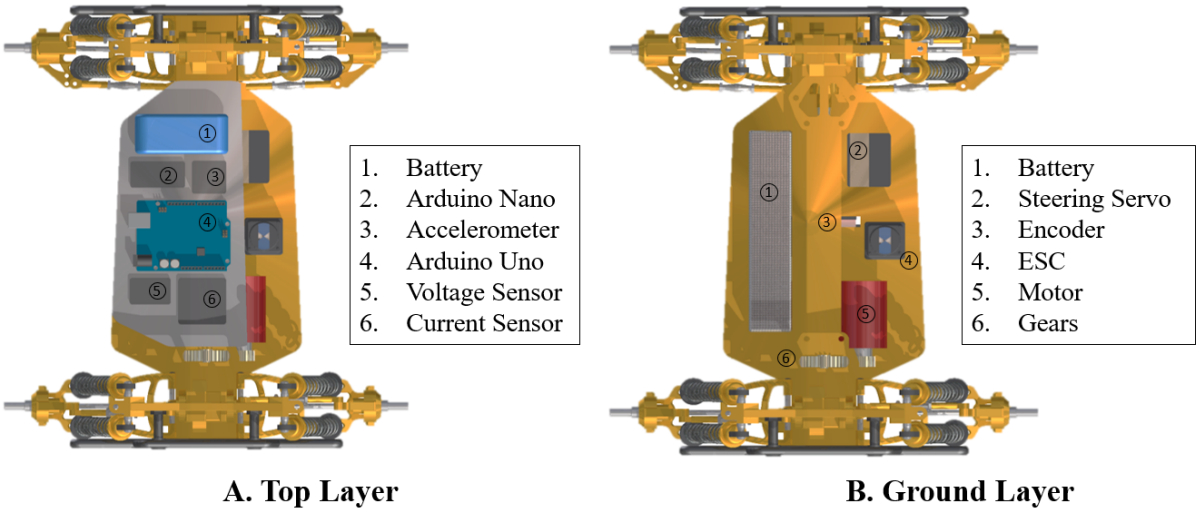

Figure IX-2. Electronics components on vehicle chassis.

The function structure of the scaled electric vehicle is shown in Figure IX-1. The system of the vehicle testing platform in this study consists of 6 sections, namely vehicle chassis, electronic control unit, drive train, sensors, battery and PC.

A 1:10 4WD metal vehicle chassis is used in the scaled electric vehicle test platform, which consists of front-and-rear suspension, transmission shaft and front-and-rear differentials. The vehicle chassis is the main mechanical body of the vehicle and allows all other components to be installed on-board as shown in Figure IX-2. On the top layer, Arduino UNO powdered by an external battery is used as the electronic control unit to control all electronic sensors and communicate with PC by wireless modular XBee. On the ground layer, the vehicle is driven by the drivetrain system which consists of a 3300KV motor and a 45A Electronic Speed Controller (ESC). Driving power is transferred from the motor to the transmission shaft by the transmission gear. Encoder is mounted on the transmission shaft to count the number of cycles that the shaft has rotated.

An Arduino UNO is used as the electronic control unit for data acquisition of all on-board electronic components and can send the analogue voltages measured by the sensing equipment to the PC. Specifically, the Arduino has been programmed to collect data from a current sensor, voltage sensor, accelerometer, encoder and wireless sensor. After collecting these data, the Arduino will communicate with the PC to estimate vehicle mass and road slope.

The drivetrain system consists of a Dynamite Fuze 540 four-pole brushless motor and a 45A ESC. To ensure a constant acceleration is maintained throughout experiments, a remote control joystick is used with the function setting of constant throttle. Multiple sensors including encoder, current sensor, voltage sensor, accelerometer and wireless module are installed on vehicle chassis. All the measured data from sensors is collected by Arduino UNO and sent to PC through wireless module.

1) Sensor

To successfully estimate the parameters of vehicle mass and road slope, the measurement values of the wheel angular velocity, the driving torque and the vehicle longitudinal acceleration are required.

In this scaled vehicle, AMT102 encoder is mounted on the transmission shaft to count the number of cycle that the shaft has rotated. In this way, the wheel speed of the vehicle and the rotation speed of the shaft of the electric motor are measured.

A linear ACS758 50A current module is used in this study to measure the power consumption of the motor to calculate the driving torque. The vehicle total driving torque T can be approximated by the following equation:

$$T = \frac{9600}{\omega_e} \times Power = \frac{9600}{\omega_e} \times I \times V \tag{220}$$

where ω_e is the rotation speed of the output shaft of the electric motor. I is the measured current from the motor and V is the measured voltage from the battery.

To obtain the real-time information of vehicle longitudinal acceleration, the two-axis accelerometer – ADXL203 is used. This kind of accelerometer can measure the vehicle longitudinal and lateral acceleration simultaneously in real-time.

2) Data collection and analysis

The measured data from voltage sensor, current sensor and accelerometer is the analogy signal, while the encoder uses interrupt digital signal to detect the rotation of transmission shaft. The interrupt from encoder greatly affects the data collection from other sensors with analogy measured data. Thus, it is necessary to separate the data collection of the encoder from the data collection of the other sensors. In this study, Arduino Nano is used to collect the interrupt signal from encoder since it is relatively small and is only used for encoder. Then Arduino Nano will send the collected data from encoder to Arduino Uno. The communication between Arduino Uno and Arduino Nano is achieved by Serial Peripheral Interface (SPI), which is a synchronous serial data protocol used by microcontrollers for communicating with other devices.

2. Estimation of the vehicle mass

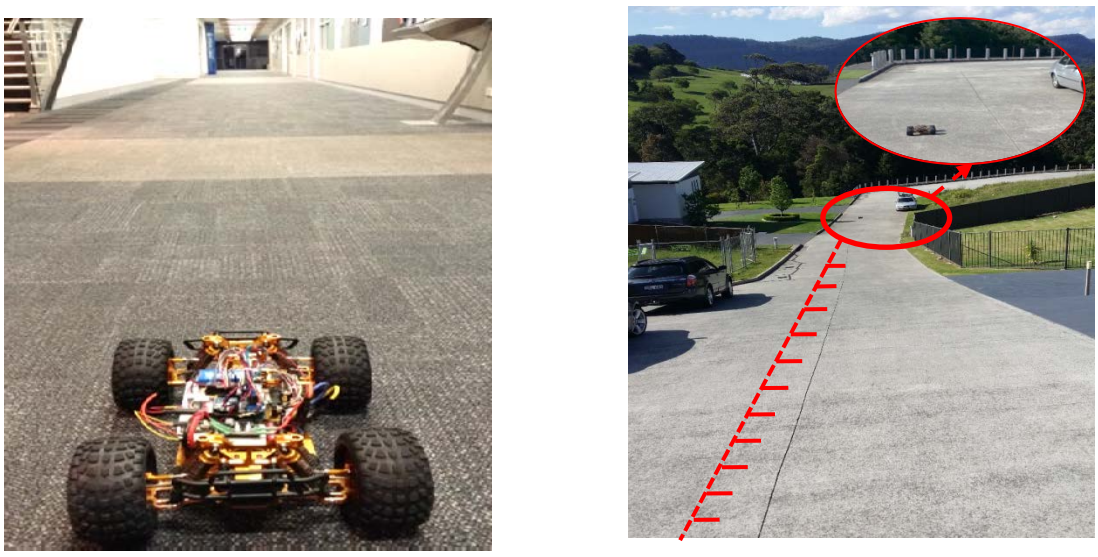

(a) Estimation of the vehicle mass (b) Estimation of road slope

Figure IX-3. The photo of different scenarios of the vehicle test.

Table IX-1. Scaled vehicle parameters

Vehicle mass (kg)	m	3.2 (4)
Wheel radius (m)	R_ω	0.0625
Wheel moment of inertial (m/s^2)	I_ω	0

In the experiments of mass estimation, the scaled vehicle is accelerating along the straight line on the carpet inside the building by assuming the zero road slope condition, which is shown in Figure IX-3(a). In this set of experiments, the vehicle mass is estimated by the proposed first layer estimator. The parameter of the wheel moment of inertial is too small for the 1:10 scaled electric vehicle and consequently this value is assumed to be zero in the experiment. Table IX-1 shows some actual scaled vehicle parameters for the reference and comparison.

In this section, the first experiment is the mass estimation test of the scaled vehicle without the adding load (3.2 kg) and the second experiment is the mass estimation test of the vehicle with the adding load (4 kg). According to Section 3.3, the mass estimation method requires the measured values of wheel angular velocity, driving torque and longitudinal acceleration. Figure IX-4 shows the vehicle measured wheel speed, driving torque and acceleration and Figure IX-5 presents the estimated vehicle mass in the first experiment. Then the vehicle measured states and the estimated mass of the vehicle in the second experiment are shown in Figure IX-6 and Figure IX-7 respectively. It is noted in Figure IX-4(c) and Figure IX-6(c), the calculated vehicle acceleration according to the vehicle dynamics model and estimated vehicle mass is compared with the actual measured acceleration to present the estimation performance. The estimated vehicle mass is shown to fit well with the actual values in Figure IX-5 and Figure IX-7, which proves the effective of the proposed first layer estimator. However, there is still obvious noise existing in the mass estimation and this is mainly due to significant measured noise of the acceleration. In addition, the scaled vehicle has relative small mass and the vibration of the vehicle chassis may impair the estimation performance. Thus, the estimation results can be improved by a heavier scaled vehicle and a more accurate accelerometer.

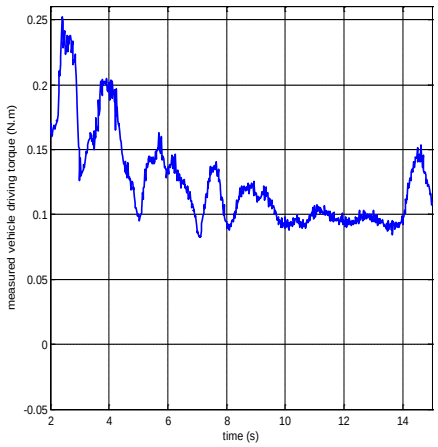

(a)

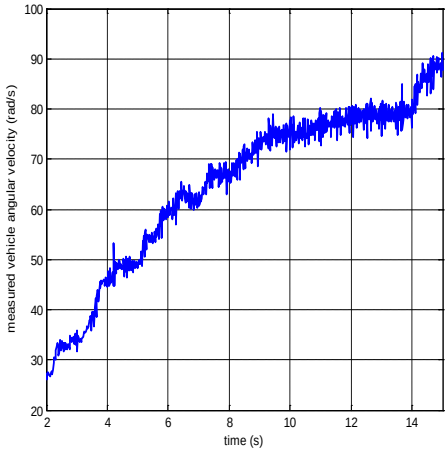

(b)

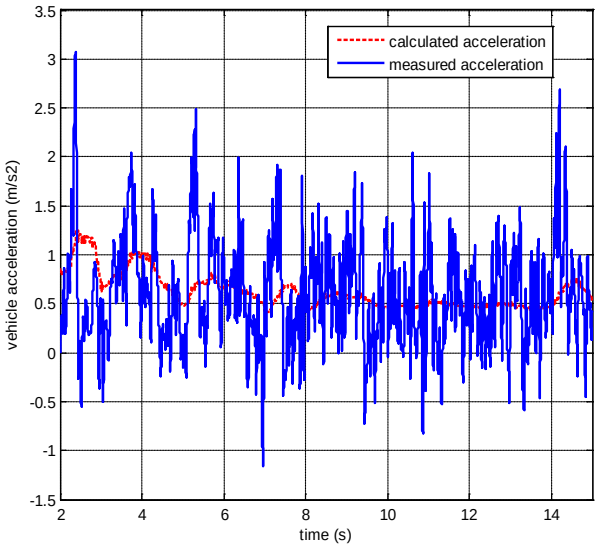

(c)

Figure IX-4. Vehicle measured states in the first experiment.

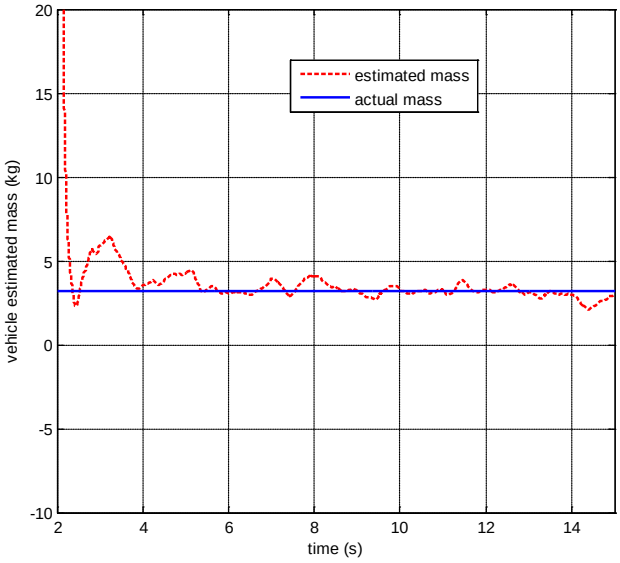

Figure IX-5. Vehicle estimated mass in the first experiment.

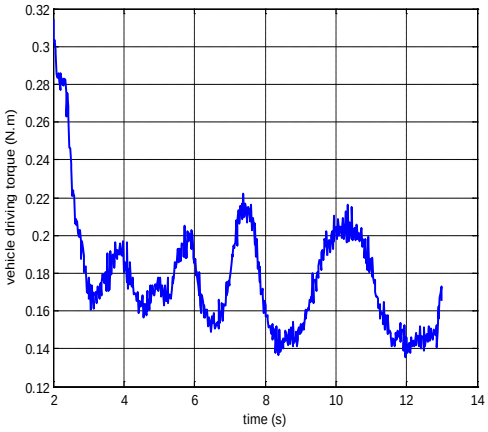

(a)

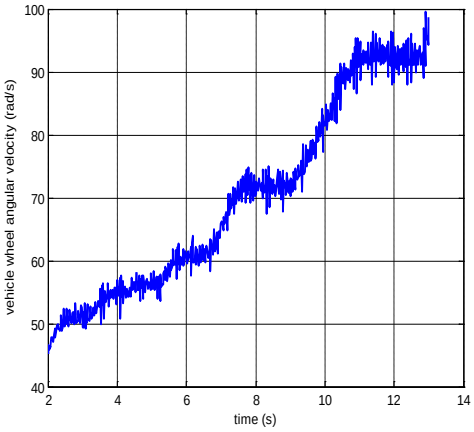

(b)

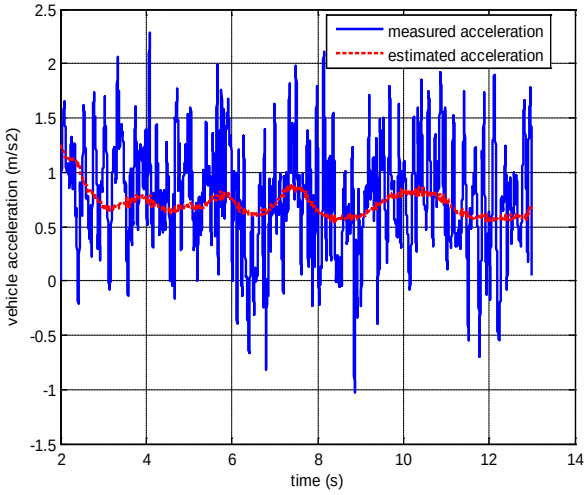

(c)

Figure IX-6. Vehicle measured states in the second experiment.

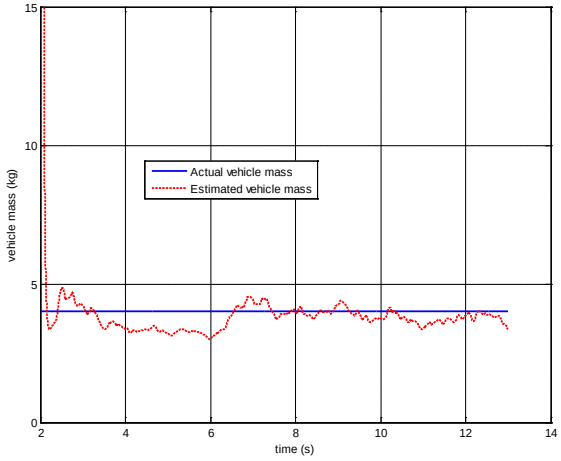

Figure IX-7. Vehicle estimated mass in the second experiment.

3. Estimation of the real-time road slope

When the vehicle mass is assumed to be available in the first layer, the adaptive velocity observer in the second layer is applied to estimate the real-time road slope. The experiment of road slope estimation is testing on the cement road as shown in Figure IX-3(b). The value of the slope is defined as negative because the force generated by the slope can be considered as the resistance force for the vehicle motion. The actual road slope is measured by a level and the curve fitting results of the relationship between the actual slope value and the distance is shown in Figure IX-8.

Three tests are carried out on the same road slope condition in the experiment. According to Section 3.3, the road slope estimation method only requires the measured values of wheel angular velocity and input driving torque during the smooth road condition such as the cement road in this experiment. The measured vehicle wheel angular velocity, driving torque and the estimated road slope in each test are shown in Figure IX-9-Figure IX-11. These figures show that the estimated slope values generally match the actual values. However, significant disturbance exists in the results. This is mainly due to several reasons: (1) vehicle swaying during climbing up the slope causes the large noise on the sensors; (2) the measured

driving torque is approximated by the battery power, but a significant proportion of battery power is consumed by the steering servo motor in order to keep the vehicle running straight when the road slop is changing; (3) parts of the scaled vehicle get loose after many times of experiment and this causes the friction loss of the transmission system. It should be noted that the estimated road slope is fluctuating much after the longitudinal position 20 metres. This is because that the road slope is much larger after 20 metres and more serious swaying of the vehicle during climbing up the large road slope may occur. This would lead to the larger disturbance in the estimation results.

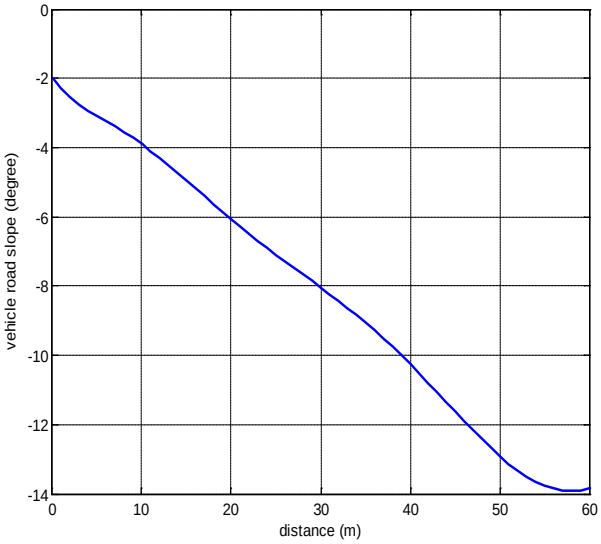

Figure IX-8. The actual road slope value.

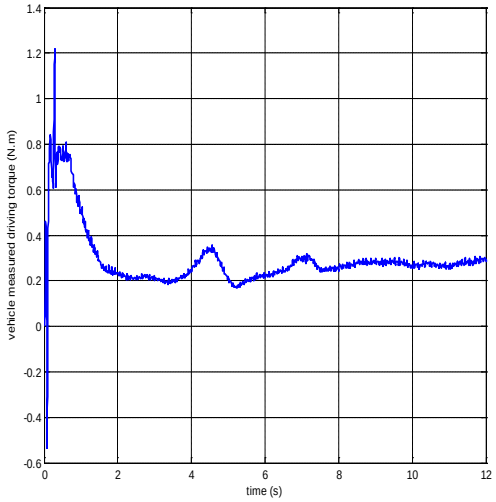

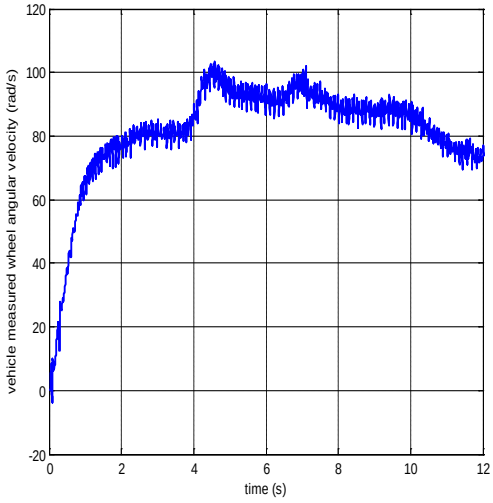

(a) measured driving torque (b) measured wheel angular velocity

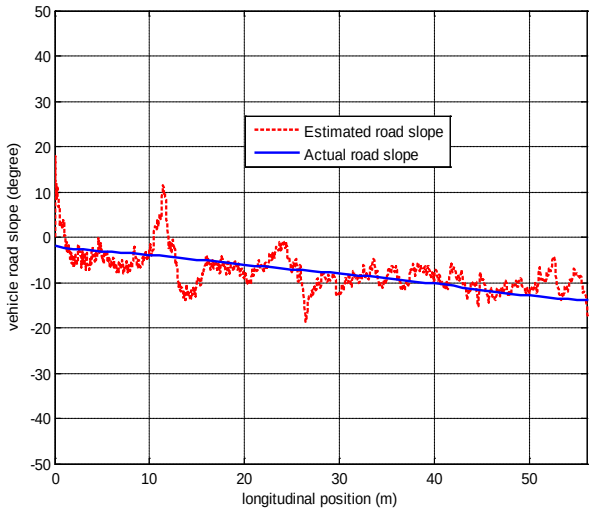

(c) estimated vehicle road slope

Figure IX-9. The vehicle simulation results in the first test of road slope simulation.

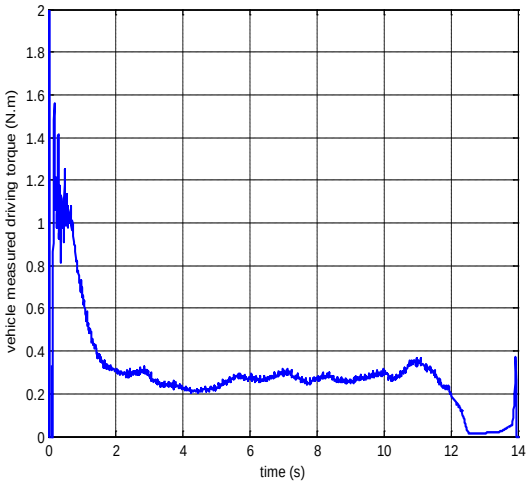

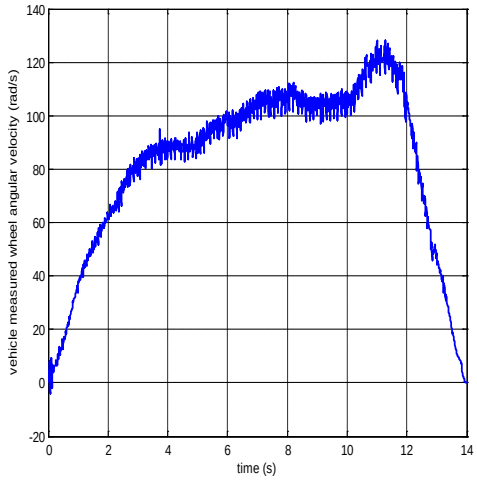

(a) measured driving torque (b) measured wheel angular velocity

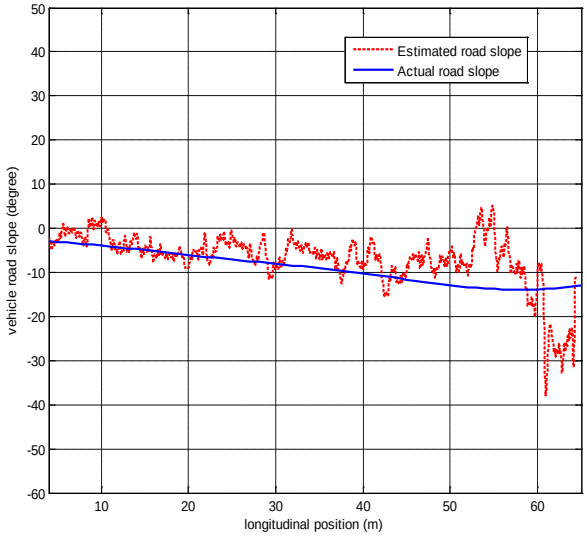

(c) estimated vehicle road slope

Figure IX-10. The vehicle simulation results in the second test of road slope simulation.

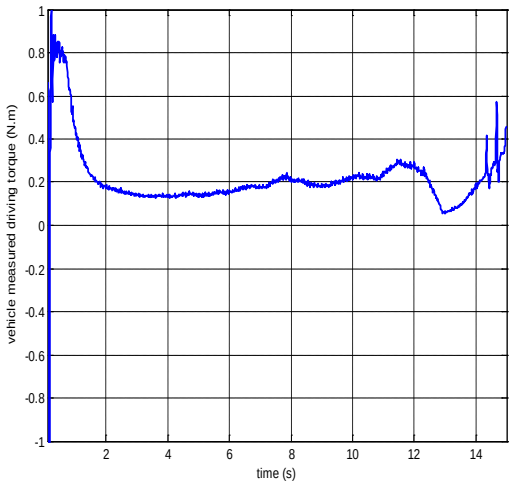

(a) measured driving torque

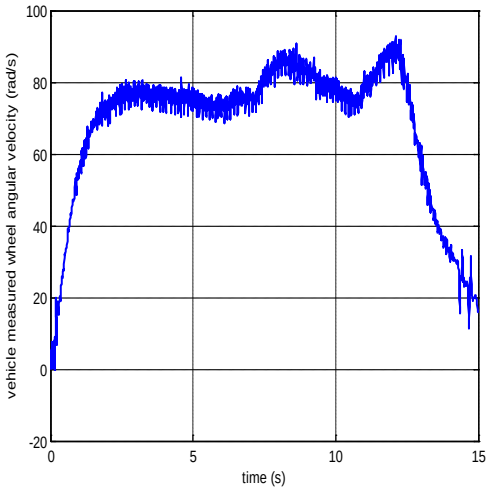

(b) measured wheel angular velocity

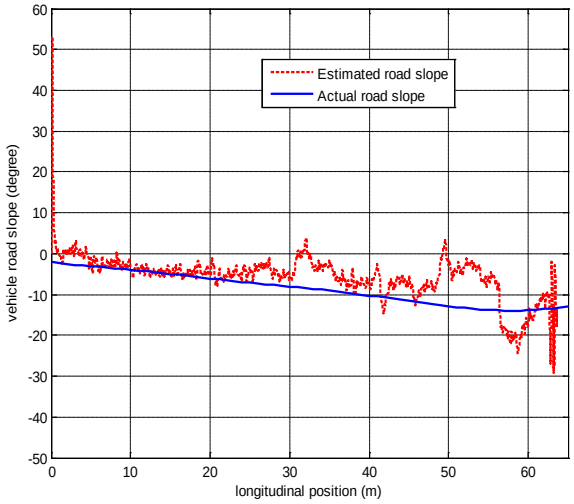

(c) estimated vehicle road slope

Figure IX-11. The vehicle simulation results in the third test of road slope simulation.

Finally, in order to clearly present the estimation error of the mass estimation and road slope estimation in the experiment, the RMS values of the estimation error are shown in Table IX-2. In Table IX-2, the RMS error value of the mass estimation is large due to the big error at the beginning of the vehicle motion. The first road slope estimation experiment has the smallest RMS error and the best estimation performance compared with other two experiments. In Figure IX-9-Figure IX-11, the first test also shows to have the best estimation performance.

Table IX-2. RMS value of the estimation error.

Mass estimation experiment	
First test	11.8159
Second test	11.4506
Road slope estimation experiment	
First test	4.6195
Second test	6.8118
Third test	7.9488

4. Summary

The experiment equipment of scaled electric vehicle is proved to be a useful experimental testbed for the study of the vehicle dynamics and control. Particularly in this chapter, the scaled vehicle is proved to successfully estimate the vehicle parameters by measuring some vehicle input values.

There is still noise existing in the estimated mass and road slope in the experiment. This is mainly due to the vibration of vehicle chassis and the measured noise of the accelerometer. This problem can be solved by increasing the weight of the scaled vehicle and using accurate accelerometers. The scaled vehicle still has the limitation of that it cannot fully reflect the dynamics performance of the full-sized vehicle, although the vehicle parameters have been scaled. For instance, the wind drag force and wheel rolling resistant force are neglected in the parameter estimation of the scaled vehicle. In addition, the scaled vehicle can only travel a short distance on the road compared with full-sized vehicle.

X. Summary of the whole thesis

This thesis mainly focuses on solving of the over-actuated control allocation problem in the 4WIS-4WID EVs, and this innovative EV has redundant control actuators with advantages to achieve multiple control targets simultaneously.

First of all, various vehicle state estimation methods are proposed for the 4WIS-4WID EV, such as the side-slip angle estimator, the longitudinal velocity estimator, the slip ratio estimator, friction-coefficient estimator, mass estimator and road slope estimator. These estimated vehicle states are important feedback values for the design of the over-actuated control allocation method. Then the comprehensive vehicle body dynamics model, tyre model, steering model and driving model are developed for the 4WIS-4WID EV, which can be used to describe the actual vehicle motion. These above studies can be considered as the preliminary studies of the over-actuated control of the 4WIS-4WID EV.

Based on the above preliminary studies, the linear feedback control allocation method for the stability and handling control of the 4WIS-4WID EV is proposed. In this method, the simulation suggests the yaw rate feedback controller (based on controlling the additional yaw moment) is proved to be able to accurately track the desired yaw rate, but the body side-slip angle response is compromised. Thus, a body side-slip angle feedback controller (based on controlling additional total lateral tyre force) is proposed and combined together with the yaw rate controller. This combined controller can achieve better overall control performance. Furthermore, a non-linear control allocation method based on the GA algorithm is also suggested to achieve the stability and handling control. This non-linear control method includes the individual wheel side-slip angle controller and slip ratio controller where the controller gains can be automatically tuned by GA algorithm. The simulations in this method suggest that this non-linear control allocation method is robust to the non-linear tyre characteristic and consequently the controlled values track the desired values more accurately in all the simulations of the J-turn, lane change and combined traction and J-turn manoeuvres.

In addition to the primary control targets of the vehicle handling and stability, this thesis also applies the over-actuated control allocation method into the energy-efficient control, fault-tolerant control and autonomous vehicle trajectory control.

An integrated vehicle dynamics and energy-efficient controller is proposed at first. In the linear pure longitudinal motion of the energy-efficient controller design, the simulation results suggest that the equal distribution of the driving torque and the braking torque of individual wheels can achieve the optimal energy-efficient performance during the medium-high torque demand. In the small torque demand, when two specific wheels in the same axle are responsible for the major driving workload, the optimal energy-efficient performance is achieved. In both the pure cornering motion and combined traction and cornering motion, the simulation results suggest that the proposed integrated controller can successfully achieve the primary control targets of handling and stability control and the secondary control target of energy-efficient control.

For the design of the fault-tolerant controller, under normal driving conditions, the SMC method can achieve the desired yaw rate accurately when one or two wheels are faulty. In addition, the SMC method has better control performance on the longitudinal velocity compared with the linear feedback method. In the scenario of large steering angle turning, the SMC method can achieve the desired yaw rate when one of the front wheels or two front wheels are faulty. This proves the robustness of the SMC method. However, the vehicle body side-slip angle performance is compromised due to the coupling effect between different control targets. To solve this problem, the driving actuators can be grouped and each group of actuators can be used to achieve the specific control target.

In the overtaking scenario of autonomous vehicle trajectory controller design, when the four-wheel SMC steering controller and four-wheel combined yaw rate and longitudinal velocity SMC driving controller are used together, the controlled vehicle can strictly follow the desired trajectory and achieve most of the control targets. This proves that the control method based on 4WID and 4WIS vehicles can achieve much better control performance than the traditional methods. In addition, a potential field method is also proposed to achieve the trajectory control of autonomous vehicle. Compared with the method that exactly tracking the road centre line, the proposed potential field method that constraints the actual vehicle trajectory in a certain road boundary has better handling and stability performance. In the

narrow road boundary condition, the vehicle controlled by proposed potential field method can successfully avoid the upper and lower boundaries.

Finally, a scaled EV is applied to test and verify the proposed vehicle mass and road slope estimator, which is proved to be a useful experimental testbed for the study of the vehicle dynamics and control.

In the future, more advanced nonlinear control allocation and optimization algorithm should be developed, such as the PID turned SMC control algorithm, nonsingular terminal SMC or other intelligent control techniques incorporating the deep learning or machine learning in the area of computer science. In addition, the full-sized electric vehicle test platform with four in-wheel motors installed should be built to more clearly present and validate the designed estimators and controllers.

References

[1] "Key world energy statistics," International Energy Agency, 2014.

[2] "World energy outlook," International Energy Agency, 2012.

[3] M. Peden, R. Scurfield, D. Sleet, D. Mohan, A. Hyder and E. Jarawan, "World report on road traffic injury prevention," World Health Organization, Geneva, Switzerland, 2004.

[4] Y. Furukawa, N. Yuhara, S. Sano, H. Takeda and Y. Matsushita, "A review of four-wheel steering studies from the viewpoint of vehicle dynamics and control," *Vehicle System Dynamics,* vol. 18, pp. 151-186, 1989.

[5] Y. Shibahata, N. Irie, H. Ito and K. Nakamura, "The development for an experimental four-wheel-steering vehicle," *SAE Paper 860623.*

[6] N. Hata, S. Hasegawa, S. Takahashi, K. Ito and T. Fujishiro, "A control method to decrease rea-end projection of 4WS vehicle," *Proceedings of JSAE (in Japanese),* vol. No.882105, 1988.

[7] T. Lam, H. Qian and Y. Xu, "Omnidirectional steering interface and control for a four-wheel independent steering vehicle," *IEEE/ASME Trans.Mechatronics,* vol. 15, pp. 329-338, 2010.

[8] N. Mutoh and Y. Nakano, "Dynamics of front-and-rear-wheel-independent-drive-type electric vehicles at the time of failure," *IEEE Transactions on Industrial Electronics,* vol. 59, no. 3, pp. 1488-1499, 2012.

[9] M. Demirci and M. Gokasan, "Adaptive optimal control allocation using Lagrangian neural networks for stability control of a 4WS-4WD electric vehicle," *Transactions of the Institute of*

Measurement and Control, vol. 35, no. 8, pp. 1139-1151, 2013.

[10] E. Ono, Y. Hattori, Y. Muragishi and K. Koibuchi, "Vehicle dynamics integrated control for four-wheel-distributed steering and four-wheel-distributed traction/braking systems," *Vehicle System Dynamics*, vol. 44, no. 2, pp. 139-151, 2006.

[11] M. Segawa, K. Nishizaki and S. Nakano, "A study of vehicle stability control by steer by wire system," in *Proceedings of AVEC 2000*, Ann Arbor, MI, 2000.

[12] K. Matsuno, R. Nitta, K. Inoue, K. Ichikawa and Y. Hiwatashi, "Development of a new all-wheel-drive control system," in *Proceedings of FISITA 2000*, Seoul, 2000.

[13] M. Abe, Y. Kano, K. Suzuki, Y. Shibihata and Y. Furukawa, "Side-slip control to stabilize vehicle lateral motion to direct yaw moment," *JSAE Review*, vol. 22, pp. 413-419, 2001.

[14] M. Nagai, Y. Hirano and S. Yamanaka, "Integrated control of active rear wheel steering and direct yaw moment control," *Vehicle Systems Dynamics*, vol. 27, pp. 357-370, 1997.

[15] Chen, Y. and J. Wang, "Design and experimental evaluations on energy efficient control allocation methods for overactuated electric vehicles: Longitudinal motion case," *IEEE Transactions on Mechatronics*, vol. 19, no. 2, pp. 538-548, 2014.

[16] R. H. Senger and W. Kortum, "Investigations on state observer for the lateral dynamics of four-wheel steered vehicles," in *Proc. 11th Int. Association for Vehicle System Dynamics Symp.*, Kingston, Ontario, Canada, 1989.

[17] H. E. Tseng, B. Ashrafi, D. Madau, T. A. Brown and D. Recker, "The development of vehicle stability control at ford," *IEEE/ASME Trans. Mechatronics*, vol. 4, no. 3, pp. 223-234, 1999.

[18] U. Kiencke and A. Daiss, "Observation of lateral vehicle dynamics," *Control Engineering Practise*, vol. 5, no. 8, pp. 1145-1150, 1997.

[19] L. Li and J. Song, "Linear subsystem model for real-time control of vehicle stability control system," in *2006 IEEE Int. Conf. Robotics, Automation&Mechatronics*, 2006.

[20] L. R. Ray, "Nonlinear state and tire force estimation for advanced vehicle control," *IEEE Trans. Control Syst. Technol.*, vol. 3, no. 1, pp. 117-124, 1995.

[21] L. Ray, "Nonlinear tire force estimation and road friction identification: simulation and experiments," *Automatica*, vol. 33, no. 10, pp. 1819-1833, 1997.

[22] M. A. Wilkin, D. C. Crolla, M. C. Levesley and W. J. Manning, "Design of a robust tyre force estimator using an extended Kalman filter," *SAE paper*, Vols. Rep. 2005-01-0402, 2005.

[23] M. Doumiati, A. Victorino, A. Charara and D. Lechner, "Estimation of vehicle lateral tire-road forces: a comparison between extended and unscented Kalman _ltering," in *ECC 09*, Hungary, 2009.

[24] X.-Y. Z. and W.-W. D., “Study on Velocity Estimation for Four-Wheel Independent Drive Electric Vehicle by UKF,” in *Measuring Technology and Mechatronics Automation (ICMTMA), 2013 Fifth International Conference on. IEEE*, 2013.

[25] L. Imsland, T. A. Johansen, T. I. Fossen, H. F. Grip, J. C. Kalkkuhl and A. Suissa, “Vehicle velocity estimation using nonlinear observers,” *Automatica,* vol. 42, no. 12, pp. 2091-2103, 2006.

[26] L. Zhao, Z. Liu and H. Chen, “Design of a Nonlinear Observer for Vehicle Velocity Estimation and Experiments,” *IEEE Transactions on Control System Technology,* vol. 19, no. 3, pp. 664-672, 2011.

[27] L. Li, J. Song, L. Kong and Q. Huang, “Vehicle velocity estimation for real-time dynamic stability control,” *International Journal of Automotive Technology,* vol. 10, no. 6, pp. 675-685, 2009.

[28] S. Y. Ko, . J. W. Ko, S. M. Lee and et al., “Vehicle velocity estimation using effective inertia for an in-wheel electric vehicle,” *International Journal of Automotive Technology,* vol. 15, no. 5, pp. 815-821, 2014.

[29] X. Xin, W. Zhang, C. Shen and et al., “Control strategy of four-wheel independent drive electric vehicle based on vehicle velocity estimation and switchover,” *Transactions of the Institute of Measurement and Control,* vol. 0142331215625767, 2016.

[30] J. Ryu, E. Rossetter and J. Gerdes, “Vehicle sideslip and roll parameter estimation using GPS,” in *Proceedings of the International Symposium on Advanced Vehicle Control (AVEC),* Hiroshima, Japan, 2002.

[31] D. Bevly, J. Ryh and J. Gerdes, “Integrating INS sensors with GPS measurements for continues estimation of vehicle sideslip, roll and tire cornering stiffness,” *IEEE Trans. Intelligent Transportation System,* vol. 7, no. 4, pp. 483-493.

[32] R. Daily and D. Bevly, “The use of GPS for vehicle stability control system,” *IEEE Trans. Industrial Electronics,* vol. 51, no. 2, pp. 270-277.

[33] Y. Fukada, “Estimation of vehicle slip-angle with combination method of model observer and direct integration,” in *Int. Symp. Adv. Veh. Control (AVEC)*, Nagoya, Japan, 1998.

[34] A. Van Zanten, “Bosch ESP systems: 5years of experience,” *SAE Paper No. 2000-01-1633,* 2000.

[35] K. Park, S. Heo and I. Baek, “Controller design for improving lateral vehicle dynamic stability,” *JSAE Review,* vol. 22, pp. 481-486.

[36] B. Chen and F. Hsieh, “Sideslip angle estimation using extended Kalman filter,” *Vehicle System Dynamics (Supplement),* vol. 46, pp. 353-364.

[37] U. Kiencke and A. Daib, “Observation of lateral vehicle dynamics,” *Control Eng. Pract.,* vol. 5,

no. 8, pp. 1145-1150, 1997.

[38] . P. Venhovens and K. Naab, “Vehicle dynamics estimation using Kalman Filters,” *Vehicle System Dynamics*, vol. 32, pp. 171-184, 1999.

[39] J. Stephant, . A. Charara and D. Meizel, “Virtual sensor: Application to vehicle sideslip angle and transversal forces,” *IEEE Trans. Ind. Electron.*, vol. 51, no. 2, pp. 278-289, 2004.

[40] A. Hac and M. Simpson, “Estimation of vehicle sideslip angle and yaw rate,” *SAE Paper No. 2000-10-0696*, 2000.

[41] T. Hiraoka, H. Kumamoto and O. Nishihara, “Sideslip angle estimation and active front steering system based on lateral acceleration data at centers of percussion with respect to front/rear wheels,” *JSAE Review*, vol. 25, pp. 37-42.

[42] J. Stéphant, A. Charara and D. Meizel, “Evaluation of a sliding mode observer for sideslip angle,” *Control Eng. Pract.*, vol. 15, no. 7, pp. 803-812, 2007.

[43] D. Piyabongkarn, R. Rajamani, J. Grogg and J. Lew, “Development and experimental evaluation of a slip angle estimator for vehicle stability control,” *Proc. PACC*, pp. 366-371.

[44] Y. Fukada, “Slip-angle estimation for vehicle stability control,” *Vehicle System Dynamics*, pp. 375-388, 1999.

[45] D. Pi, N. Chen, J. Wang and B. Zhang, “Design and evaluation of sideslip angle observer for vehicle stability control,” *International Journal of Automotive Technology*, vol. 12, no. 3, pp. 391-399.

[46] G. Baffet , A. Charara and D. Lechner , “Estimation of vehicle sideslip, tire force and wheel cornering stiffness,” *Control Engineering Practice*, vol. 17, no. 11, pp. 1255-1264, 2009.

[47] K. Nakajima, M. Kurishige, M. Endo and T. Kifuku, “A vehicle state detection method based on estimated alignment torque using EPS,” *SAE*, Vols. Paper No. 2005-01-1265, 2005.

[48] E. Ono, K. Asano and K. Koibuchi, “Estimation of tire grip margin using electric power steering system,” in *the 18th Int. Association for Veh. Syst. Dyn. (IAVSD) Symp.*, Kanagawa, Japan, 2003.

[49] Y. Yasui, W. Tanaka, Y. Muragishi, E. Ono, M. Momiyama, H. Katoh, H. Aizawa and Y. Imoto, “Estimation of lateral grip margin based on self-aligning torque for vehicle dynamics enhancement,” *SAE Paper No. 2004-01-1070*, 2004.

[50] M. Endo, K. Ogawa and M. Kurishige, “Cooperative control of active front steering and electric power steering based on self-aligning torque,” in *the Int. Symp. Adv. Veh. Control (AVEC)*, Taipei, Taiwan, 2006.

[51] Y. J. Hsu, S. Laws, C. D. Gadda and J. C. Gerdes, “A Method to Estimate the Friction Coefficient and Tire Slip Angle Using Steering Torque,” in *Proceedings of 2006 ASME*

International Mechanical Engineering Congress and Exposition, Chicago, Illinois, USA, 2006.

[52] Y. J. Hsu, S. Laws and J. C. Gerdes, "Estimation of Tire Slip Angle and Friction Limits Using Steering Torque," *IEEE Transactions on Control Systems Technology,* vol. 18, no. 4, pp. 896-907, 2010.

[53] P. Yih, J. Ryu and J. C. Gerdes, "Vehicle state estimation using steering torque," in *Proceeding of the 2004 American Control Conference*, 2004.

[54] R. Williams, B. Carter, P. Gallina and G. Rosati, "Dynamic model with slip for wheeled omnidirectional robots," *IEEE Transactions on Robotics and Automation,* vol. 18, pp. 285-293, 2002.

[55] H. E. Tseng, D. Madau, B. Ashrafi, T. Brown and D. Recker, "Technical challenges in the development of vehicle stability control system," in *Proc. IEEE Int.Conf.Control Applications*, HI, 1999.

[56] A. T. van Zanten, "Bosch ESP systems: 5 years of experience," in *Proc. SAE Automotive Dynamics and Stability Conf.*, Troy. MI, 2000.

[57] A. Nishio, K. Tozu, H. Yamaguchi, K. Asano and Y. Amano, "Development of vehicle stability control system based on vehicle sideslip angle estimation," *SAE Paper, No. 2001-01-0137,* 2001.

[58] L. Austin and D. Morrey, "Recent advances in antilock braking systems and traction control systems," *Proc.Inst.Mech.Eng.D,* vol. 214, no. 6, pp. 625-638, 2000.

[59] K. Yi and J. Taeyoung, "Observer based estimation of tire-road friction for collision warning algorithm adaptation," *JSME Int.J.Series C,* vol. 41, no. 1, pp. 116-124, 1998.

[60] G. Erdogan, L. Alexander and R. Rajamani, "Friction coefficient measurement system for autonomous winter road maintenance," *Vehicle System Dynamics*, vol. 47, no. 4, pp. 497-512, 2009.

[61] J. Wang, L. Alexander and R. Rajamani, ""Friction estimation on high-way vehicles using longitudinal measurements," *ASME J. Dyn. Syst.,Meas. Control,* vol. 126, no. 2, pp. 265-275, 2004.

[62] R. Rajamani, G. Phanomchoeng, D. Piyabongkarn and J. Y. Lew, "Algorithms for Real-Time Estimation of Individual Wheel Tire-Road Friction Coefficients," *IEEE/ASME Transactions on Mechatronics*, vol. 17, no. 6, pp. 1183-1195, 2012.

[63] B. Breuer, U. Eichhorn and J. Roth, "Measurement of Tyre-Road Friction Ahead of the Car and inside the Tyre," in *Proc. Int. Symp. Advanced Vehicle Control*, 1992.

[64] U. Eichhorn and J. Roth, "Prediction and Monitoring of Tyre-Road Friction," in *in Proc. FISITA*, London, 1992.

[65] T. Uno, Y. Sakai, J. Takagi and T. Yamashita, “Road Surface Recognition Method Using Optical Spatial filtering,” in *in Proc. AVEC*, 1994.

[66] “Intelligent Tyre for Accident-Free Traffic,” Apollo Consortium, APOLLO Final Report, Finland, 2005.

[67] L. Li, F. Wang and Q. Zhou, “Integrated longitudinal and lateral tire/road friction modelling and monitoring for vehicle motion control,” *IEEE Transactions on Intelligent Transportation system*, vol. 7, no. 1, 2006.

[68] F. Napolitano, T. Gaiffe, Y. Cottreau and et al., “PHINS: The first inertial navigation system based on fiber optic gyroscopes,” in *Proc. St. Petersburg Int. Conf. Navigation System*, St. Petersburg, Russia, 2002.

[69] R. Usui and A. Ohno, “Resent progress of fiber optic gyroscope and application at JAE,” in *Optical Fiber Sensors Conf. Tech. Dig.*, Portland, OR, 2002.

[70] E. Nebot, S. Sukkarieh and H. Durrant-Whyte, “Inertial navigation aided with GPS information,” in *Proc. 4th Annu. Conf. Mechatronics and Machine Vision Practice*, Toowoomba, Qld., Australia, 1997.

[71] F. Cao, D. K. Yang, A. Xu and et al., “Low cost SINS/GPS integration for land vehicle navigation,” in *Proc. IEEE 5th Int. Conf. Intelligent Transportation System*, Singapore, 2002.

[72] C. Chan, “Magnetic sensing as a position reference system for ground vehicle control,” *IEEE Trans. Instrum. Meas.*, vol. 51, no. 1, pp. 43-52, 2002.

[73] J. Hernandez and C. Kuo, “Steering control of automated vehicles using absolute positioning GPS and magnetic markers,” *IEEE Trans. Veh. Technol.*, vol. 52, no. 1, pp. 150-161, 2003.

[74] S. M. Donecker, T. Lasky and B. Ravani, “A mechatronic sensing system for vehicle guidance and control,” *IEEE/ASME Trans. Mechatronics*, vol. 8, no. 4, pp. 500-510, 2003.

[75] F. Gustaffson, “Slip-Based Tire-Road Friction Estimation,” *Automatica*, vol. 33, no. 6, pp. 1087-1099, 1997.

[76] S. Müller, M. Uchanski and H. Karl, “Slip-Based Tire-Road Friction Estimation During Braking,” in *Proceedings of 2001 ASME International Mechanical Engineering Congress and Exposition*, New York, 2001.

[77] R. Rajamani, D. Piyabongkarn, J. Lew and J. Grogg, “Algorithms for Real-Time Estimation of Individual Wheel Tire-Road Friction Coefficient,” in *Proceedings of the 2006 American Control Conference*, Minnesota, 2006.

[78] L. R. Ray, “Nonlinear estimation of vehicles state and tire forces,” in *American Control Conference*, Chicago, 1992.

[79] J. Dakhlallah, S. Glaser, S. Mammar and Y. Sebsadji, “Tire-Road Forces Estimation Using Extended Kalman Filter and Side slip Angle Evaluation,” in *2008 American Control*

Conference, USA, 2008.

[80] C. Ahn, H. Peng and H. Tseng, "Robust estimation of road friction coefficient using lateral and longitudinal vehicle dynamics," *Vehicle System Dynamics*, vol. 50, no. 6, pp. 961-985, 2012.

[81] C. Ahn, H. Peng and H. Tseng, "Robust estimation of road frictional coefficient," *IEEE Transactions on Control Systems Technology*, vol. 21, no. 1, 2013.

[82] R. Wang and J. Wang, "Tire-road friction coefficient and tire cornering stiffness estimation based on longitudinal tire force difference generation"," *Control Engineering Practice*, 2012.

[83] G. Xu, K. Xu and W. Li, "Novel estimation of tyre–road friction coefficient and slip ratio using electrical parameters of traction motor for electric vehicle," *Int J Veh Autonomous Syst*, vol. 11, no. 2/3, pp. 261-278, 2013.

[84] J. Yang, J. Na, Y. Guo and X. Wu, "Adaptive estimation of road gradient and vehicle parameters for vehicular systems," *IET Control Theory Appl.*, vol. 9, no. 6, pp. 935-943, 2015.

[85] M. I. J. A. e. a. E. Hellström, "Look-ahead control for heavy trucks to minimize trip time and fuel consumption," *Control Engineering Practice*, vol. 17, no. 2, pp. 245-254, 2009.

[86] a. H. F. Y. Saboohi, "Model for developing an eco-driving strategy of a passenger vehicle based on the least fuel consumptio," *Applied Energy*, vol. 86, no. 10, pp. 1925-1932, 2009.

[87] H. Bae, J. Ryu and J. Gerdes, "Road grade and vehicle parameter estimation for longitudinal control using GPS," in *in Proc. IEEE ITSC*, 2001.

[88] V. Winstead and I. Kolmanovsky, "Estimation of road grade and vehicle mass via model predictive control," in *in Proc. IEEE CCA*, 2005.

[89] P. Sahlholm and K. Johansson, "Road grade estimation for look-ahead vehicle control using multiple measurement runs," *Control Eng. Pract.*, vol. 18, no. 11, pp. 1328-1341, 2010.

[90] P. Lingman and B. Schmidtbauer, "Road slope and vehicle mass estimation using Kalman filtering," *Vehicle System Dynamics*, vol. 37, no. 1, pp. 12-23, 2002.

[91] S. Mangan and J. Wang, "Development of a novel sensorless longitudinal road gradient estimation method based on vehicle can bus data," *IEEE/ASME Trans. Mechatronics*, vol. 12, no. 3, pp. 375-386, 2007.

[92] S. Mangan, J. Wang and Q. Wu, "Measurement of the road gradient using an inclinometer mounted on a moving vehicle," in *in Proc. IEEE Int. Symp. Comput. Aided Contr. Syst.* , 2002.

[93] A. S. H. P. A. Vahidi, "Recursive least squares with forgetting for online estimation of vehicle mass and road grade: theory and experiments," *Vehicle System Dynamics*, vol. 43, no. 1, pp. 31-55, 2005.

[94] P. Ioannou and J. Sun, Robust Adaptive Control, Upper Saddle River, NJ: Pentice Hall, 1996.

[95] V. Adetola and M. Guay, “Finite-time parameter estimation in adaptive control of nonlinear systems,” *IEEE Transactions on Automatic Control,* vol. 53, no. 3, pp. 807-811, 2008.

[96] V. Adetola and M. Guay, “Performance improvement in adaptive control of linearly parameterized nonlinear system,” *IEEE Transactions on Automatic Control,* vol. 55, no. 9, pp. 2182-2186, 2010.

[97] M. N. Mahyuddin, J. Na, G. Herrmann, X. Ren and P. Barber, “Adaptive observer-based parameter estimation with application to road gradient and vehicle mass estimation,” *IEEE Transactions on Industrial Electronics,* vol. 61, no. 6, 2014.

[98] M. Abe, Vehicle handling Dynamics: Theory and Application, UK: Elsevier, 2009.

[99] D. Karnopp, Vehicle stability, New York : Marcel Dekker, 2004.

[100] B. Boada, M. Boada and V. Díaz, “Fuzzy-logic Applied to Yaw Moment Control for Vehicle Stability,” *Vehicle System Dynamics,* vol. 43, no. 10, pp. 753-770, 2005.

[101] H. Pacejka, Tire and vehicle dynamics, Warrendale, Pa.: Published on behalf of Society of Automotive Engineers, 2006.

[102] J. Deur, N. Kranjčević, O. Hofmann, J. Asgari and D. Hrovat, “Analysis of Lateral Tyre Friction Dynamics,” *Vehicle System Dynamics,* vol. 47, no. 7, pp. 831-850, 2009.

[103] T. Uil, “Tyre models for steady-state vehicle handling analysis,” Master’s Thesis, Eindhoven University of Technology, Department of Mechanical Engineering, Dynamics and Control Group, Eindhoven, 2007.

[104] H. Dugoff, . P. Fancher and L. Segel, “An analysis of tire traction properties and their influence on vehicle dynamic performance”,” *SAE 700377,* pp. 1219-1243.

[105] K. Guo and D. Lu, “UniTire: unified tire model for vehicle dynamic simulation,” *Vehicle System Dynamics,* vol. 45, pp. 79-99, 2007.

[106] N. Xu, D. Lu and S. Ran, “A Predicted Tire Model for Combined Tire Cornering and Braking Shear Forces Based on the Slip Direction,” in *2011 International Conference on Electronic & Mechanical Engineering and Information Technology*, 2011.

[107] J. Zhou, J. Wong and R. Sharp, “A Multi-Spoke, Three Plane Tyre Model for Simulation of Transient Behaviour,” *Vehicle System Dynamics,* vol. 31, pp. 35-45, 1999.

[108] J. Lacombe, “Tire Model for Simulations of Vehicle Motion on High and Low Friction Road Surface,” in *Proceedings of the 2000 Winter Simulation Conference*, 2000.

[109] C. Canudas, M. Petersen and A. Shiriaev, “A New Nonlinear Observer for Tire/Road Distributed Contact Friction,” in *Proceedings of the 42nd IEEE Conference on Decision and Control Maui,* Hawaii USA, 2003.

[110] S. Yamazaki, O. Furukawa and T. Suzuki, “Study on Real Time Estimation of Tire to Road Friction,” *Vehicle System Dynamics Supplement,* vol. 27, pp. 225-233, 1997.

[111] J. Reid, D. Boesch and R. Bielenberg, “Detailed tire modelling for crash applications,” *TCRS 2007,* vol. 12, no. 5, pp. 521-529, 2007.

[112] X. Lu, K. Guo, D. Lu and Y. Wang, “Effect of tire camber on vehicle dynamic simulation for extreme corning,” *Vehicle System Dynamics Supplement,* vol. 44, pp. 39-49, 2006.

[113] T. Shim, D. Margolis and C. Belltawn, “An Analytical tire mode! for vehicle simulation in normal driving conditions,” *SAE Paper #2000-01-0356,* 2000.

[114] K. Guo and L. Ren, “A unified semi-empirical tire model with higher accuracy and less parameters,” *SAE Technical Paper Series 1999-01-0785,* 1999.

[115] M. Best, “Identifying tyre models directly from vehicle test data using an extended Kalman filter,” *Vehicle System Dynamics,* vol. 48, no. 2, pp. 171-187, 2010.

[116] G. Dihua, S. Jin and L. Yam, “Modeling of Tyre Cornering Properties with Experimental Modal Parameters,” *SAE paper no 1999-01-0784,* 1999.

[117] P. Bolzern, F. Cheli, G. Falciola and F. Resta, “Estimation of the Non-Linear Suspension Tyre Cornering Forces from Experimental Road Test Data,” *Vehicle System Dynamics,* vol. 31, pp. 23-34, 1999.

[118] S. Laws, C. Gadda, S. Kohn, P. Yih, . J. Gerdes and J. Milroy, “Steer-by-wire suspension and steering design for controllability and observability,” in *presented at the IFAC World Congress,* Prague, 2005.

[119] N. Cavina , F. Ponti and G. Rizzoni , “Fast algorithm for on-board torque estimation,” in *SAE International Congress Exposition,* Detroit, MI., 1999.

[120] T. Svensson , I. Moore and R. Daniels , “Method for operating a hydraulic brake system of a motor vehicle and a hydraulic braking system,” US Patent, app.13/733,041, 2013.

[121] T. Johansen and T. I. Fossen, “Control allocation—a survey,” *Automatica,* vol. 49, no. 5, pp. 1087-1103, 2013.

[122] K. Bordignon and W. Durham, “Closed-form solution to constrained control allocation problem,” *Journal of Guidance Control and Dynamics,* vol. 18, pp. 1000-1007, 1995.

[123] W. Durham, “Constrained control allocation,” *Journal of Guidance Control and Dynamics,* vol. 16, pp. 717-725, 1993.

[124] T. Fossen and S. Sagatun, “Adaptive control of nonlinear systems: a case study of underwater robotic systems,” *Journal of Robotic Systems,* vol. 8, pp. 393-412, 1991.

[125] J. Virnig and D. Bodden , “Multivariable control allocation and control law conditioning when control effectors limit,” in *Proc. aiaa guidance, navigation and control conf.,* Scottsdale, AZ.,

1994.

[126] J. Shi, W. Zhang, G. Li and X. Liu, “Research on allocation efficiency of the redistributed pseudo inverse algorithm,” *Science China Information Sciences,* vol. 53, pp. 271-277, 2010.

[127] R. Adams, J. Buffington, A. Sparks and S. Banda, Robust multivariable flight control, London: Springer-Verlag., 1994.

[128] J. Buffington and D. Enns, “Lyapunov stability analysis of daisy chain control allocation,” *Journal of Guidance Control and Dynamics,* vol. 19, pp. 1226-1230, 1996.

[129] M. Oppenheimer, D. Doman and M. Bolender, “Control allocation,” in *The control handbook, control system applications,* 2010.

[130] W. C. Durham, “Constrained control allocation,” *Journal of Guidance Control and Dynamics,* vol. 16, pp. 717-725, 1993.

[131] . J. A. Paradiso, “Adaptable method of managing jets and aerosurfaces for aerospace vehicle control,” *Journal of Guidance, Control, and Dynamics,* vol. 14, pp. 44-50, 1991.

[132] M. Bodson, “Evaluation of optimization methods for control allocation,” *Journal of Guidance Control and Dynamics,* vol. 25, pp. 703-711, 2002.

[133] I. Lindfors, “Thrust allocation method for the dynamic positioning system,” in *In Proc. 10th ship control symposium,* 1993.

[134] M. Bodson and S. A. Frost, “Control allocation with load balancing,” *Journal of Guidance Control and Dynamics,* vol. 34, pp. 380-387, 2011.

[135] J. Nocedal and S. J. Wright, Numerical optimization, Springer, 1999.

[136] O. Härkegård, “Efficient active set algorithms for solving constrained least squares problems in aircraft control allocation,” in *In Proc. IEEE conf. decision and control,* Las Vegas, NV, 2002.

[137] J. Petersen and M. Bodson, “Interior-point algorithms for control allocation,” *Journal of Guidance, Control, and Dynamics,* vol. 28, pp. 471-480, 2005.

[138] J. A. M. Petersen and M. Bodson, “Constrained quadratic programming techniques for control allocation,” *IEEE Transactions on Control Systems Technology,* vol. 14, pp. 91-98, 2006.

[139] J. J. Burken, P. Lu, Z. L. Wu and C. Bahm, “Two reconfigurable flight control design methods: robust servomechanisms and control allocation,” *Journal of Guidance Control and Dynamics,* vol. 24, pp. 482-493, 2001.

[140] S. Millsap and E. Law, “Handling enhancement due to an automotive variable ratio electric power steering system using model reference robust tracking control,” in *Proceedings of SAE 1996,* Detroit, MI, 1996.

[141] W. Kramer and M. Hackl, “Potential functions and benefits of electronic steering assistance,” in *Proceedings of FISITA96 World Congress*, Prague, 1996.

[142] J. Ackermann, “Robust control prevents car skidding,” *IEEE Control Systems Magazine 17*, pp. 17-31, 1997.

[143] T. Kojo, M. Suzumara, K. Fukui, T. Sugawara, M. Matsuda and J. Kawamuro, “Development of front steering control system,” in *Proceedings of AVEC 2002*, Hiroshima, 2002.

[144] R. McCann, “Variable effort steering for vehicle stability enhancement using an electric power steering system,” in *Proceedings of SAE 2000*, Detroit, MI, 2000.

[145] S. Matsumoto, H. Yamaguchi, H. Inoue and Y. Yasuno, “Braking force distribution control for improved vehicle dynamics,” in *Proceedings of AVEC 92*, Yokohoma, 1992.

[146] E. Donges, “Supporting drivers by chassis control systems,” in *Smart vehicles*, Swets and Zeitlinger, 1996, pp. 276-296.

[147] H. Leffler, “Electronic brake management EBM – a possible approach for brake and control system integration,” in *Proceedings of FISITA96 World Congress*, Prague, 1996.

[148] H. Leffler, R. Auffhammer , R. Heyken and H. Roth, “New driving stability control system with reduced technical effort and medium class passenger cars,” in *Proceedings of SAE 1998*, Detroit, MI, 1998.

[149] H. Leffler , H. Krusche, R. Auffhammer, H. Roth and H. Vieler, “Accident prevention by driving stability control for compact passenger cars,” in *Proceedings of FISITA 1998*, Paris, 1998.

[150] A. Straub, “DSC (dynamic stability control) in BMW 7 series cars,” in *Proceedings of AVEC96*, 1996, 547-557.

[151] G. Naito, E. Yaguchi and K. Ozaki, “Improving vehicle dynamics by torque split control system,” in *Proceedings of AVEC 92*, Yokohoma, 1992.

[152] S. Motoyama, H. Uki, K. Isoda and H. Yuasa, “Effect of traction force distribution control on vehicle dynamics,” *Vehicle System Dynamics*, vol. 22, pp. 455-464, 1993.

[153] H. Smakman, “Functional integration of active suspension with slip control for improved lateral vehicle dynamics,” in *Proceedings of AVEC 2000*, Ann Arbor, MI, 2000.

[154] K.-H. Senger and W. Schwartz, “The influence of a four wheel steering system on the stability behaviour of a vehicle–driver system,” *Vehicle System Dynamics Supplement*, vol. 17, 1987.

[155] J. Whitehead, “Four wheel steering: maneuverability and high speed stabilisation,” in *Proceedings of the SAE 1988*, Detroit, MI, 1988.

[156] J. Whitehead , “Rear wheel steering dynamics compared to front steering,” *Transactions of the*

ASME 112, pp. 88-93, 1990.

[157] X. Xia and E. Law, "Nonlinear dynamic response of four wheel steering automobiles to combined braking and steering commands in collision avoidance maneuvers," in *Proceedings of SAE 1990*, Detroit, MI, 1990.

[158] Y. Shibihata, K. Shimida and T. Tomari, "Improvement of vehicle maneuverability by direct yaw moment control," in *Proceedings of AVEC 92*, Yokohoma, 1992.

[159] S. Inagaki, I. Kshiro and M. Yamamoto, "Analysis on vehicle stability in critical cornering using the phase-plane method," in *Proceedings of AVEC94*, Tsukuba, 287-292.

[160] M. Selby, PhD thesis, School of Mechanical Engineering, University of Leeds, 2003.

[161] J. He , PhD thesis, School of Mechanical Engineering, University of Leeds, 2005.

[162] M. Abe, Y. Kano, Y. Shibihata and Y. Furukawa, "Improvement of vehicle handling safety with vehicle sideslip control by direct yaw moment," in *Proceedings of the 16th IAVSD*, 1999.

[163] M. Abe , Y. Kano, K. Suzuki, Y. Shibihata and Y. Furukawa , "An experimental validation of side-slip control to compensate for a loss of stability due to nonlinear tyre characteristics," in *Proceedings of Proceedings of AVEC 2000,* Ann Arbor, MI, 2000.

[164] M. Abe , Y. Shibihata and Y. Shimuzu , "Analysis of steering gain and vehicle handling performance with variable gear-ratio steering system (VGS)," in *Proceedings of FISITA 2000*, Seoul, 2000.

[165] Y. Furukawa and M. Abe , "On-board-tire-model reference control for cooperation of 4WS and direct yaw moment control for improving active safety of vehicle handling," in *Proceedings of AVEC 1996*, Aachen, 1996.

[166] S. Mammar and V. Baghdassarian , "Two-degree-of-freedom formulation of vehicle handling improvement by active steering," in *Proceedings of the American Control Conference*, 2000.

[167] S. Mammar and D. Koenig, "Vehicle handling improvement by active steering," *Vehicle System Dynamics*, vol. 38, pp. 211-242, 2002.

[168] M. Nagai, Y. Hirano and S. Yamanaka, "Integrated robust control law of active rear wheel steering and direct yaw moment control," *Vehicle Systems Dynamics Supplement*, vol. 28, pp. 416-421, 1998.

[169] M. Nagai, M. Shino and F. Gao , "Study on integrated control of active front steer angle and direct yaw moment," *JSAE Review*, vol. 23, pp. 309-315, 2002.

[170] S. Kleine and J. Van Niekerk, "Modelling and control of a steer-by-wire vehicle," *Vehicle System Dynamics Supplement*, vol. 28, pp. 114-142, 1998.

[171] N. Cooper, W. Manning , D. Crolla and M. Levesley, "Study of the integration of roll control

and torque distribution," in *Proceedings of AVEC 2004*, Arnhem, 2004.

[172] Y. Chen and J. Wang, "Design and Evaluation on Electric Differentials for Overactuated Electric Ground Vehicles with Four Independent In-wheel Motors," *IEEE Transactions on Vehicular Technology*, vol. 61, no. 4, pp. 1534-1542, 2012.

[173] R. Wang and J. Wang, "Passive actuator fault-tolerant control for a class of overactuated nonlinear systems and applications to electric vehicles," *IEEE Transactions on Vehicular Technology*, vol. 62, no. 3, pp. 972-985, 2013.

[174] Z. Shuai, H. Zhang, J. Wang, J. Li and M. Ouyang, "Lateral motion control for four-wheel-independent-drive electric vehicles using optimal torque allocation and dynamic message priority scheduling," *Control Engineering Practice*, vol. 24, pp. 55-66, 2014.

[175] Z. Shuai, H. Zhang, J. Wang , J. Li and M. Ouyang, "Network control of vehicle lateral dynamics with control allocation and dynamic message priority assignment," in *ASME 2013 Dynamics Systems and Control Conference*, Palo Alto, California, USA, 2013.

[176] N. Ando and H. Fujimoto, "Yaw-rate control for electric vehicle with active front/rear steering and driving/braking force distribution of rear wheels," in *The 11th IEEE International Workshop on Advanced Motion Control*, Nagaoka, Japan, 2010.

[177] S. Beiker, "Verbbesserungsmoglichkeiten des Fahrverhalten von Pkw durch zusammenwirkende Regelsysteme," *Fortschritt-Berichte VDI*, vol. 12, 2000.

[178] A. Trächtler, "Integrierte fahrdynamikregelung mit ESP, akitiver lenkung und aktivem fahrwerk," *Automatisierungstechnik*, vol. 53, pp. 11-19, 2005.

[179] R. Orend, "Modelling and control of a vehicle with single-wheel chassis actuators," in *Proceedings of 16th IFAC World Congress*, Prague, 2005.

[180] J. Fredriksson , J. Andreasson and L. Laine, "Wheel force distribution for improved handling in a hybrid electric vehicle using nonlinear control," in *43rd IEEE Conference on Decision and Control*, Atlantis, Paradise Island, Bahamas, 2004.

[181] J. Andreasson and T. Bünte , "Global chassis control based on inverse vehicle dynamics models," *Vehicle System Dynamics supplement*, vol. 44, pp. 321-328, 2006.

[182] N. Bajcinca and Y. Kouhi, "Distributed optimization for feedforward global chassis control," in *IFAC Symposium on Advances in Automotive Control*, Munich, 2010.

[183] N. Bajcinca, "Fault-tolerant distributed feedback global chassis control," in *2013 XXIV International Conference on Information, Communication and Automation Technologies (ICAT)*, Sarajevo, Bosnia and Herzegovina, 2013.

[184] R. Kizu, H. Harada and H. Minabe, "Electronic control of car chassis present status and future perspective," in *International Congress on Transportation Electronics, Convergence88*, Detroit, USA, 1988.

[185] H. Tanaka, H. Inoue and H. Iwata, “Development of a vehicle integrated control system,” *SAE Paper 925049,* 1992.

[186] P. Rieth and R. Schwarz, “ESC II-ESC with active steering intervention,” *SAE Paper 2004-01-0260,* 2004.

[187] A. van Zanten, R. Erhardt and G. Pfaff, “VDC, The Vehicle Dynamics Control System of Bosch,” *SAE Technical Paper 950759,* 1995.

[188] F. Yu, D. Li and D. Crolla, “Integrated vehicle dynamics control – State of the art review,” in *IEEE Vehicle Power and Propulsion Conference (VPPC)*, Harbin, China, 2008.

[189] . T. Ohgke, . K. Schirmer, A. Schuster and E. Wrle, “Kraftfahrzeugsteuersystem,” patent number: DE 10107949 B4.

[190] L. Fang, J. Jung, J. Hong and J. Lee, “Study on high-efficiency performance in interior permanent magnet synchronous motor with double-layer PM design,” *IEEE Trans. Magnetics,* vol. 44, no. 11, pp. 4393-4396.

[191] G. Cvetkovski and L. Petkovska, “Efficiency maximisation in structural design optimization of permanent magnet synchronous motor,” in *Proc. 18th Int. Conf. Electrical Machines*, 2008.

[192] S. Morimoto, Y. Tong, Y. Takeda and . T. Hirasa, “Less minimization control of permanent magnet synchronous motor drives,” *IEEE Trans. Industrial Electronics,* vol. 41, no. 5, pp. 511-517, 1994.

[193] C. Cavallaro, . A. O. Ditommaso, R. Miceli, A. Raciti, G. R. Galluzzo and M. Trapanese, “Efficiency enhancement of permanent-magnet synchronous motor drives by online loss minimization approaches,” *IEEE Trans. Industrial Electronics,* vol. 52, no. 4, pp. 1153-1160, 2005.

[194] R. Wai, R. Duan, J. Lee and L. Liu, “High efficiency fuel-cell power inverter with soft-switching resonant technique,” *IEEE Trans. Energy Conversion,* vol. 20, no. 2, pp. 485-492, 2005.

[195] J. S. Lai, R. W. Yong, G. W. J. Ott and J. W. McKeever, “Efficiency modelling and evaluation of a resonant snubber based soft-switching inverter for motor drive applications,” in *Proc. 26th Annual IEEE Power Electronics Specialists Conf.*.

[196] R. Wang, Y. Chen, D. Feng , X. Huang and J. Wang , “Development and performance characterization of an electric ground vehicle with independently actuated in-wheel motors,” *J. Power Sources,* vol. 196, no. 8, pp. 3962-3971.

[197] J. Gu, M. Ouyang, D. Lu , J. Li and L. Lu , “Energy efficiency optimization of electric vehicle driven by in-wheel motors,” *International Journal of Automotive Technology,* vol. 14, no. 5, pp. 763-772, 2013.

[198] L. De Novellis, A. Sorniotti and P. Gruber, “Wheel torque distribution criteria for electric vehicles with torque-vectoring differentials,” *IEEE Transactions on Vehicular Technology,* vol.

63, no. 4, pp. 1593-1602, 2014.

[199] A. Pennycott, L. De Novellis, A. Sabbatini, P. Gruber and A. Sorniotti , “Reducing the motor power losses of a four-wheel drive, fully electric vehicle via wheel torque allocation,” *Proc IMechE Part D: J Automobile Engineering*, vol. 228, no. 7, pp. 830-839, 2014.

[200] A. Pennycott, L. De Novellis, P. Gruber and A. Sorniotti, “Enhancing the energy efficiency of fully electric vehicles via the minimization of motor power loss,” in *in IEEE International Conference on Systems, Man, and Cybernetics*, Manchester, UK, 2012.

[201] Y. Chen and J. Wang, “Adaptive energy-efficient control allocation for planar motion control of over-actuated electric ground vehicles,” *IEEE Transactions on Control System Technology*, vol. 22, no. 4, 2014.

[202] R. Wang and J. Wang, “Fault-tolerant control for electric ground vehicles with independently-actuated in-wheel motors,” *Journal of Dynamic Systems, Measurement, and Control*, vol. 134, 2012.

[203] H. Fujimoto, T. Saito and T. Noguchi, “Motion stabilization control of electric vehicle under snowy conditions based on yaw-moment observer,” in *in Proceedings of IEEE international workshop on advanced motion control*, Kawasaki, Japan, 2004.

[204] S. Sakai and Y. Hori, “Advantage of electric motor for anti-skid control of electric vehicle,” *European Power Electronics Journal*, vol. 11, pp. 26-32, 2001.

[205] T. Saito, H. Fujimoto and T. Noguchi, “Yaw-moment stabilization control of small electric vehicle,” in *in Proceedings of the IEEJ technical meeting on industrial instrumentation and control*, Tokyo, Japan, 2002.

[206] D. Yin and Y. Hori, “A new approach to traction control of EV based on maximum effective torque estimation,” in *in Proceedings of the 34th annual conference of the IEEE industrial electronics society*, Florida, USA, 2008.

[207] J. Hu, D. Yin and Y. Hori, “Fault-tolerant traction control of electric vehicles,” *Control Engineering Practice*, vol. 19, pp. 204-213, 2011.

[208] H. Niemann and J. Stoustrup , “Passive fault tolerant control of a double inverted pendulum – a case study,” *Control Engineering Practise*, vol. 13, no. 8, pp. 1047-1059, 2005.

[209] D. Espinoza and D. Campos-Delgado, “Active fault tolerant scheme for variable speed drives under actuator and sensor faults,” in *in Proc. IEEE Int.Conf.ControlAppl.*, San Antonio, TX, USA, 2008.

[210] K. Zhou, “A new controller architecture for high performance, robust, and fault tolerant control,” *IEEE Trans. Autom. Control*, vol. 46, no. 10, pp. 1613-1618, 2001.

[211] A. Raisemche, M. Boukhnifer, C. Larouci and D. Diallo, “Two active fault-tolerant control schemes of induction-motor drive in EV or HEV,” *IEEE Transactions on Vehicular*

Technology, vol. 63, no. 1, 2014.

[212] A. Chamseddine and H. Noura, "Control and Sensor Fault Tolerance of Vehicle Active Suspension," *IEEE Trans. Control Syst. Technol.,* vol. 16, no. 3, pp. 416-433, 2008.

[213] R. Jayabalan and B. Fahimi, "Monitoring and Fault Diagnosis of Multi-converter Systems in Hybrid Electric Vehicles," *IEEE Trans. Veh. Technol.,* vol. 55, no. 5, pp. 1475-1484, 2006.

[214] M. Oudghiri , M. Chadli and A. Hajjaji, "Robust Observer-based Fault-tolerant Control for Vehicle Lateral Dynamics," *Int. J. Veh. Des.,* vol. 48, no. 3/4, pp. 173-189, 2008.

[215] O. Wallmark, L. Harnefors and O. Carlson , "Control Algorithms for a Fault-tolerant PMSM Drive," *IEEE Trans. Ind. Electron. Control Instrum.,* vol. 54, no. 4, pp. 1973-1980, 2007.

[216] M. Muenchhof, M. Beck and R. Isermann, "Fault-tolerant Actuators and Drives – Structures, Fault Detection Principles and Applications," *Annu. Rev. Control,* vol. 33, no. 2, pp. 136-148, 2009.

[217] R. Wang and J. Wang, "Fault-tolerant Control with Active Fault Diagnosis for Four-wheel Independently Driven Electric Ground Vehicles," *IEEE Transactions on Vehicular Technology*, vol. 60, no. 9, pp. 4276-4287, 2011.

[218] H. Shimizu, J. Harada and L. Chan, "Development of a high performance electric vehicle," in *Proceedings of the 1996 IEEE IECON 22nd International Conference*, 1996.

[219] W. C., Y. L., Y. H. and K. L., "Rule-based traction system failure control of distributed electric drive vehicle," *Journal of Mechanical Engineering,* vol. 48, no. 10, pp. 90-95, 2012.

[220] X. Xin, H. Zheng, H. Xu and G. Qin, "Control strategies for four in-wheel driven electric vehicles when motor drive system fail," in *2014 American Control Conference (ACC)*, Portland, Oregon, USA, 2014.

[221] H. Alipour, M. B. B. Sharifian and M. Sabahi , "A Modified Integral Sliding Mode Control to Lateral Stabilisation of 4-Wheel Independent Drive Electric Vehicle," *Vehicle System Dynamics*, vol. 52, no. 12, pp. 1584-1606, 2014.

[222] P. Song, M. Tomizuka and C. Zong, "A novel integrated chassis controller for full drive-by-wire vehicles," *Vehicle System Dynamics,* vol. 53, no. 2, pp. 215-236, 2015.

[223] P. Petrov and F. Nashashibi, "Modelling and nonlinear adaptive control for autonomous vehicle overtaking," *IEEE Transactions on Intelligent Transportation System,* vol. 15, no. 4, pp. 1643-1656, 2014.

[224] S. Shladover, "The GM-PATH platoon scenario," *Intellimotion,* vol. 6, no. 3, pp. 2-3, 1997.

[225] R. Kianfar, B. Augusto, A. Ebadighajari and et al., "Design and experimental validation of a cooperative driving system in the grand cooperative driving challenge," *IEEE Trans. Intell. Transp. Syst.,* vol. 13, no. 3, pp. 994-1007, 2012.

[226] E. van Nunen, M. Kwakkernaat, J. Ploeg and B. Netten, “Cooperative competition for future mobility,” *IEEE Trans. Intell Transp. Syst.*, vol. 13, no. 3, pp. 1018-1025, 2012.

[227] M. Nieuwenhuijze , T. van Keulen, S. Oncu, B. Bonsen and H. Nijmeijer, “Cooperative driving with a heavy-duty truck in mixed traffic: Experimental results,” *IEEE Trans. Intell. Transp. Syst.*, vol. 13, no. 3, pp. 1026-1032, 2012.

[228] T. Fraichard, “CyberCar: L’alternative a la voiture particuliere,” *Navigation*, vol. 53, no. 209, pp. 53-75, 2009.

[229] S. Hima, S. Glaser, A. Chaibet and B. Vanholme, “Controller design for trajectory tracking of autonomous passenger vehicles,” in *in Proc. IEEE Conf. Intell. Transp. Syst.*, Washington, DC, 2011.

[230] J. Alonso, E. Vidal, A. Rotter and M. Muhlenberg, “Lane-change decision aid system based on motion-driven vehicle tracking,” *IEEE Trans. Veh. Technol.*, vol. 57, no. 5, pp. 2736-2746, 2008.

[231] J. E. Naranjo, C. Gonzalez, R. Garcia, T. de Pedro and R. E. Haber, “Power-steering control architecture for automatic driving,” *IEEE Trans. Intell. Transp. Syst.*, vol. 6, no. 4, pp. 406-415, 2005.

[232] J. Pérez, V. Milanés and E. Onieva, “Cascade architecture for lateral control in autonomous vehicles,” *IEEE Transactions on Intelligent Transportation System*, vol. 12, no. 1, pp. 73-82, 2011.

[233] S. Glaser, B. Vanholme,, S. Mammar, D. Gruyer and L. Nouveliére, “Maneuver-based trajectory planning for highly autonomous vehicles on real road with traffic and driver interaction,” *IEEE Transactions on Intelligent Transportation systems*, vol. 11, no. 3, pp. 589-606, 2010.

[234] C. Lin, J. Juang and K. Li, “Active collision avoidance system for steering control of autonomous vehicles,” *IET Intelligent Transport Systems*, vol. 8, no. 6, pp. 550-557, 2014.

[235] S. Ge and Y. Cui, “Dynamic motion planning for mobile robots using potential field method,” *Autonomous Robots*, vol. 13, pp. 207-222, 2002.

[236] M. A. K. Jaradat, M. H. G. Garibeh and E. A. Feilat, “Autonomous mobile robot dynamic motion planning using hybrid fuccy potential field,” *Soft Comput*, vol. 16, pp. 153-164, 2012.

[237] O. Khatib, “Real-time obstacle avoidance for manipulators and mobile robot,” *The International Journal of robotic Research*, vol. 5, no. 1, pp. 90-98, 1986.

[238] Z. Pan, J. Li, K. Hu and H. Zhu, “Intelligent vehicle path planning based on improved artificial potential field method,” *Applied Mechanics and Materials*, vol. 742, pp. 349-354, 2015.

[239] H. Park and J. C. Gerdes, “Optimal tyre force allocation for trajectory tracking with an over-actuated vehicle,” in *2015 IEEE Intelligent Vehicles Symposium (IV)*, Seoul, Korea, 2015.

[240] N. Cavina, F. Ponti and G. Rizzoni, “Fast algorithm for on-board torque estimation,” in *SAE Int. Congr. Expo.*, Detroit, MI, 1999.

[241] T. Svensson, I. Moore and R. Daniels, “Method for operating a hydraulic brake system of a motor vehicle and a hydraulic braking system,” US Patent, app.13/733,041, 2013.

[242] R. Rajamani, D. Piyabongkarn, J. Y. Lew, K. Yi and G. Phanomchoeng, “Tire-Road Friction-Coefficient Estimation,” *IEEE Control System Magazine*, pp. 54-69, 2010.

[243] F. Jiang and Z. Gao, “An Adaptive Nonlinear Filter Approach to the Vehicle Velocity Estimation for ABS,” in *Proceedings of the 2000 IEEE International Conference on Control Applications*, USA, 2000.

[244] P. Simionescu and D. Beale , “Optimum synthesis of the four-bar function generator in its symmetric embodiment: the Ackermann steering linkage,” *Mechanism and Machine Theory*, vol. 37, pp. 1487-1504, 2002.

[245] Y. Zhao and J. Zhang , “Yaw stability control of a four-independent-wheel drive electric vehicle,” *Int. J. Electric and Hybrid Vehicles*, vol. 2, no. 1, pp. 64-76, 2009.

[246] S. Yim, J. Choi and K. Yi, “Coordinated control of hybrid 4WD vehicles for enhanced manoeuvrability and lateral stability,” *IEEE Transactions on Vehicular Technology*, vol. 61, no. 4, pp. 1946-1950, 2012.

[247] Y. Suzuki, Y. Kano and M. Abe, “A study on tyre force distribution controls for full drive-by-wire electric vehicle,” *Vehicle System Dynamics*, 2014.

[248] V. Roberge, M. Tarbouchi and G. Labonté, “Comparison of Parallel Genetic Algorithm and Particle Swarm Optimization for Real-Time UAV Path Planning,” *IEEE Transactions on Industrial Informatics*, vol. 9, no. 1, pp. 132-141, 2013.

[249] Y. Hori, Y. Toyoda and Y. Tsuruoka , “Traction control of electric vehicle: basic experimental results using the test EV ‘UOT Electric March’,” *IEEE Transactions on Industry Applications*, vol. 34, no. 5, pp. 1131-1138, 1998.

[250] R. Hebden, C. Edwards and S. Spurgeon, “Automotive steering control in a split-μ manoeuvre using an observer-based sliding mode controller,” *Vehicle System Dynamics*, vol. 41, no. 3, pp. 181-202, 2004.

[251] M. Mirzaei, “A new strategy for minimum usage of external yaw moment in vehicle dynamic control system,” *Transportation Research Part C: Emerging Technology*, vol. 18, no. 2, pp. 213-224, 2010.

[252] R. de Castro, M. Tanelli, R. Araújo and S. Savaresi, “Design of safety-oriented control allocation strategies for overactuated electric vehicles,” *Vehicle System Dynamics*, vol. 52, no. 8, pp. 1017-1046, 2014.

[253] J. Barraquand, B. Langlois and J. Latombe, “Nemerical potential field techniques for robot path

planning," *IEEE Trans. Syst., Man, Cybern.*, vol. 22, no. 2, pp. 224-241, 1992.

[254] S. Quinlan and O. Khatib, "Elastic bands: Connecting path planning and control," in *in Proc. IEEE Conf. Robot. Autom.*, Atlanta, GA, 1993.

[255] W. Chang, R. Hwang and J. Hsieh, "A self-turning PID control for a class of nonlinear systems based on the Lyapunov approach," *Journal of Process Control*, vol. 12, pp. 233-242, 2002.

[256] M. Sampei, T. Tamura, T. Kobayashi and N. Shibui, "Arbitrary path tracking control of articulated vehicles using nonlinear control theory," *IEEE Trans. Contr. Syst. Technol.*, vol. 3, no. 1, pp. 125-131, 1995.

[257] R. Woodley and L. Acar, "A testbed system for nonlinear or intelligent control," in *Proceedings of the American Control Conference*, San Diego, CA, 1999.

[258] J. Gohl, R. Rajamani, L. Alexander and P. Starr, "The development of tilt-controlled narrow ground vehicles," in *Proceedings of the American Control Conference*, Anchorage, AK, 2002.

[259] A. Divelbiss and J. Wen, "Trajectory tracking control of a car-trailer system," *IEEE Trans. Contr. Syst. Technol.*, vol. 5, no. 3, pp. 269-278, 1997.

[260] D. Katzourakis and et al., "An Open-Source Scaled Automobile Platform for Fault -Tolerant Electronic Stability Control," *IEEE Transactions on Instrumentation and Measurement*, pp. 2303-2314, 2010.

[261] S. Reuter, H. Diab, S. Kowalewski, E. Hauck and S. Jeschke, "Design and implementation of a vehicle dynamics control system by means of torque vectoring for an autonomous vehicle," in *Proceedings of the 2012 IEEE International Conference on Robotics and Biomimetics*, Guangzhou, China, 2012.

[262] R. Grepl, J. Vejlupek, V. Lambersky, M. Jasansky, F. Vadlejch and P. Coupek, "Development of 4WS/4WD Experimental Vehicle: Platform for Research and Education in Mechatronics," in *Proceedings of the 2011 IEEE International Conference on Mechatronics*, Istanbul, Turkey, 2011.

[263] R. Daily and D. Bevly, "The use of GPS for vehicle stability control system," *IEEE Trans. Ind. Electron.*, vol. 51, no. 2, pp. 270-277, 2004.

[264] Y. Hori, "Future vehicle driven by electricity and control-research on four-wheel-motored 'UOT electric march II'," *IEEE Trans. Ind. Electron.*, vol. 51, no. 5, pp. 954-962, 2004.

[265] W. Wang, I. Li, M. Chen, S. Su and S. Hsu, "Dynamic slip-ratio estimation and control of autilock braking systems using an observer-based direct adaptive fuzzy-neural controller," *IEEE Trans. Ind. Electron.*, vol. 56, no. 5, pp. 1746-1756, 2009.

[266] S.-B. Lu, C. Lim and Y.-B. He , "Steering-based fault-tolerant control for the braking failures of an independent driving electric vehicle," *Proc ImechE Part D: J Automobile Engineering*, 2014.

[267] R. Wang and J. Wang, “Tire-road friction coefficient and tire cornering stiffness estimation based on longitudinal tyre force difference generation,” *Control Engineering Practice*, vol. 21, no. 1, pp. 65-75, 2013.